Studies on High-Gain Millimeter Wave Antennas for 5G and Non-Terrestrial Network (NTN) Applications

Ph.D. Thesis

By

Priyank Mishra

DISCIPLINE OF ELECTRICAL ENGINEERING

INDIAN INSTITUTE OF TECHNOLOGY INDORE

November 2025

Studies on High-Gain Millimeter Wave Antennas for 5G and Non-Terrestrial Network (NTN) Applications

A THESIS

Submitted in partial fulfillment of the
requirements for the award of the degree
of
DOCTOR OF PHILOSOPHY

by

PRIYANK MISHRA

DISCIPLINE OF ELECTRICAL ENGINEERING
INDIAN INSTITUTE OF TECHNOLOGY INDORE
November 2025

INDIAN INSTITUTE OF TECHNOLOGY INDORE

I hereby certify that the work which is being presented in the thesis entitled **Studies on High-Gain Millimeter Wave Antennas for 5G and Non-Terrestrial Network (NTN) Applications** in the partial fulfillment of the requirements for the award of the degree of **Doctor of Philosophy** and submitted in the **Department of Electrical Engineering, Indian Institute of Technology Indore**, is an authentic record of my own work carried out during the time period from August 2020 to November 2025 under the supervision of Dr. Saptarshi Ghosh, Associate Professor, Indian Institute of Technology Indore, Indore, India.

The matter presented in this thesis has not been submitted by me for the award of any other degree of this or any other institute.

30.11.2025

Signature of the student with date
(Priyank Mishra)

This is to certify that the above statement made by the candidate is correct to the best of my knowledge.

Saptarshi Ghosh 19/03/26
Signature of Thesis Supervisor with date
(Dr. Saptarshi Ghosh)

Priyank Mishra has successfully given his Ph.D. Oral Examination held on **19 March 2026**.

Saptarshi Ghosh 19/03/26
Signature of Thesis Supervisor with date
(Dr. Saptarshi Ghosh)

ACKNOWLEDGEMENTS

I would like to express my sincere appreciation to all those who have significantly contributed to making this period of learning not only productive but also deeply fulfilling.

Foremost, I extend my profound gratitude to my supervisor, Dr. Saptarshi Ghosh, for his unwavering support, insightful guidance, and inspirational leadership throughout my research journey. His vision and encouragement have shaped the trajectory of my work and instilled in me a sense of purpose and academic rigor. I am truly indebted to him for his constant motivation and patience, which have been instrumental in the successful completion of this thesis.

I am deeply thankful to Prof. Abhirup Dutta and Prof. Swaminathan Ramabadran, members of my Research Progress Committee, for their valuable time, constructive feedback, and thoughtful suggestions during various stages of this work. Their insights have greatly enriched the quality and depth of my research. My sincere thanks are also due to the Head, Department of Electrical Engineering, for the constant support and academic environment that fostered my research. I would like to acknowledge Prof. Suhas Joshi, Director, Indian Institute of Technology Indore, for providing me with the opportunity and resources to pursue my doctoral studies at this esteemed institute. I am also grateful to the dedicated Institute staff for their consistent assistance and cooperation.

I wish to express my sincere gratitude to my employers, Coal India Limited (Ministry of Coal, Government of India) and the Ministry of Home Affairs, Government of India, for sponsoring my Ph.D. research and for their continued support and encouragement throughout this journey.

I take this opportunity to thank my lab mates — Dr. Maharana Pratap Singh, Mr. Patinavalasa Sainadh, Mr. Akhila Gouda, Mr. Praneet Jain, Mr. Deepak Kaushik, Mr. Munna Aziz, Dr. Mohammad Ameen, Dr. Anil Kumar Nayak, and Dr. Poonam Tiwari — for their cooperation, valuable discussions, and camaraderie that made the lab environment both productive and enjoyable. I am also thankful to my colleagues — Mr. M.C.S. Rao, Major Kirpal Singh, Mr. P.N. Murthy, Mr. C.P. Kabra, Ms. Mahalaxmi, Mr. A.C. Singh, Mr. Mohammad Sabir, Mr. Sanjay Wairagade, Mr. Aditya Ajgaonkar, and Dr. Rahul Nawani — for their guidance, encouragement, and friendship beyond the academic realm.

I would also like to express my deep spiritual gratitude to Neem Karoli Baba, whose blessings and grace have been a guiding light through moments of uncertainty and reflection. I am equally grateful to Sadhguru for his profound insights, which have helped me maintain clarity, balance, and purpose throughout this demanding journey. I bow in reverence to the divine grace experienced at Shri Venkateshwara Temple and Ayyappa Swami Temple (RK Puram, New Delhi), Jagannath Mandir (Hauz Khas, New Delhi), Shri Mahalakshmi Jagdamba Mandir (Koradi, Nagpur), Mahakali Temple (Chandrapur), Shri Kundeshwar Temple

(Tikamgarh), Shri Ramraja Temple (Orchha), and Baba Balak Nath Temple (Kasauli), where I found inner peace and spiritual renewal during this period.

I have also drawn immense inspiration from nature. The diverse mountain landscapes of Jammu & Kashmir, Himachal Pradesh, Uttarakhand, and the stark grandeur of the Leh and Spiti valleys have shaped my deepest sense of awe. Equally grounding have been the calm strength of the Satpura and Melghat forests along the sacred flow of the Narmada River, the mist-laden valleys of Meghalaya, and the green stretches around Chandrapur, Indore, Nagpur, and New Delhi. The majestic stillness of these varied landscapes has continually reminded me of endurance, humility, and the vastness of exploration. My journeys of biking and trekking through these terrains have been a source of clarity and balance, shaping the patience and perseverance essential for this long research journey.

Finally, and most importantly, I express my heartfelt gratitude to my family members for their unconditional love, patience, and belief in me throughout this long academic pursuit. A special word of love goes to my twin daughters, Rishika and Ridhvika, who arrived as a blessing during the final stage of this journey. Their arrival marks a beautiful new beginning, one that makes this achievement even more meaningful.

Priyank Mishra

This thesis is lovingly dedicated to Neem Karoli Baba (Maharaj ji), whose simple yet profound teachings of love, service and remembrance of the Divine continue to guide my journey. His grace has been a silent companion throughout the exploration of knowledge, both in the lab and within. May this work honour his light and reflect the spirit of selfless devotion he embodied.

SYNOPSIS

Name of Student: Priyank Mishra **Roll Number**: 2001102004

Degree for which submitted: Ph.D. **Department**: Electrical Engineering

Thesis Title: Studies on High-Gain Millimeter Wave Antennas for 5G and Non-Terrestrial Network (NTN) Applications

Name of Thesis Supervisor: Dr. Saptarshi Ghosh

Month and Year of Submission: November, 2025

The continuous advancement in wireless communication technologies has significantly accelerated the need for high-speed, low-latency, and reliable data transmission. With the emergence of the fifth generation (5G) and upcoming 6G mobile communication systems, the pressure on the existing frequency spectrum has intensified. To accommodate the increasing user demands and enable massive device connectivity, the industry has turned toward the millimeter-wave (mm-wave) frequency bands, particularly around 28 GHz and 38 GHz, which offer significantly larger bandwidths compared to sub-6 GHz counterparts.

However, mm-wave communication introduces several inherent challenges. These include high free-space path loss, poor material penetration, short communication range, and susceptibility to atmospheric absorption. To overcome these limitations and ensure robust system performance, antenna systems operating in this spectrum must be carefully designed to deliver high gain, compact size, low mutual coupling in MIMO configurations, efficient beam directionality, and radiation safety especially for applications involving wearable and body-mounted devices.

Antennas, being critical transducers between guided and radiated waves, have evolved substantially to meet these challenges. From early wire and patch antennas to modern high-frequency implementations involving metamaterials, artificial magnetic conductor (AMC) surfaces, Fabry Perot cavities, and reflectarrays, the scope of antenna design has widened significantly. In the context of 5G and non-terrestrial networks (NTNs), antennas are no longer

passive radiators but active enablers of system performance, enabling MIMO diversity, beamforming, spatial multiplexing, and safe interaction with human users and environments.

This thesis is devoted to the development of compact, high-performance, and application-specific antenna systems targeting both terrestrial and non-terrestrial mm-wave communications. The work is organized into six original research contributions, each solving a specific set of challenges associated with mm-wave antenna design. The first two contributions present split ring resonator (SRR)-loaded and AMC-backed dual-band antennas for wearable and body-centric 5G communication. These are followed by a CSRR-loaded MIMO antenna that offers a dual-band operation with compact size and improved gain. The fourth design explores a Fabry–Perot cavity-backed MIMO antenna to enhance gain and aperture efficiency without increasing the system complexity. Building on this, the fifth contribution introduces a five-port MIMO antenna that achieves simultaneous polarization and pattern diversity using a unique combination of circularly and linearly polarized elements. Finally, the thesis culminates with a beam-steerable 3-bit reflectarray antenna designed for NTN platforms such as LEO/GEO satellites and high-altitude platforms (HAPs), offering wideband high-gain operation with mechanical beam steering.

Across all designs, key antenna parameters such as S-parameters, gain, and efficiency have been rigorously evaluated through both simulation and experimental validation. MIMO-specific performance metrics, such as envelope correlation coefficient (ECC), total active reflection coefficient (TARC), and channel capacity loss (CCL) are assessed wherever applicable. Safety evaluations, including specific absorption rate (SAR) and power density analysis using body phantoms, are conducted for relevant wearable configurations. All prototypes have been fabricated on standard substrates and benchmarked against contemporary mm-wave antenna systems.

Overall, this thesis offers a unified design framework that begins with on-body MIMO antennas for wearable networks and progresses toward high-gain reflectarrays for NTN deployment. The outcomes collectively demonstrate the potential of these antennas in enabling compact, safe, and high-performance wireless systems for 5G and beyond.

Dual-Band SRR-Loaded Printed Monopole MIMO Antenna

The first work of this thesis presents a compact dual-band antenna system for mm-wave applications. In Stage I, a printed monopole antenna loaded with an SRR, and an annular slot geometry is designed on a Rogers RO4003™ substrate to operate at 28 GHz and 38 GHz.

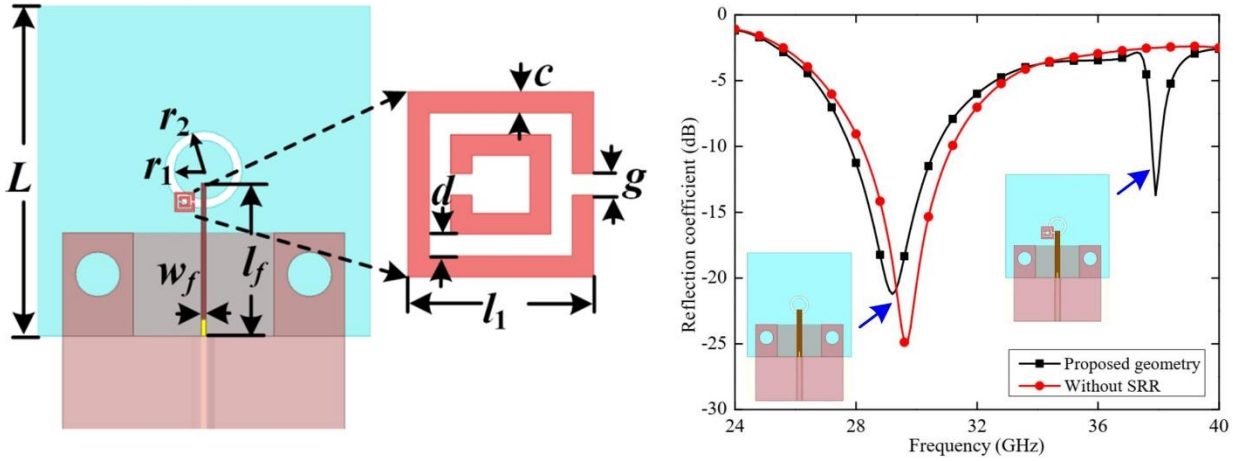

(a) (b)

Figure 1: SRR loaded annular slot monopole antenna. (a) Schematic diagram, and (b) comparison of simulated reflection coefficient (S_{11}) of the proposed single-band antenna design with and without the SRR geometry. The dimensions are L= 15, l_f = 6.8, w_f = 0.7, r_1= 1.0, r_2= 1.3, l_1 = 1.74, d = 0.2, c = 0.2, and g = 0.2 (units: mm).

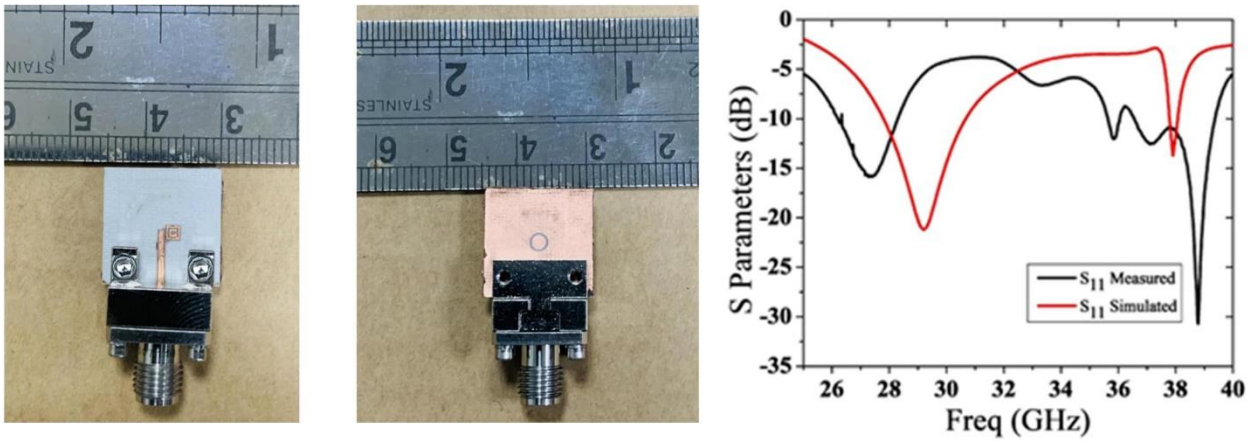

(a) (b)

Figure 2: (a) Photograph (top and bottom layer) of the fabricated prototype. (b) Simulated and measured S_{11} response of the proposed single antenna.

The antenna configuration is illustrated in Figure 1(a), while the simulated reflection coefficient (S_{11}) comparison with and without SRR loading is shown in Figure 1(b), highlighting the generation of an additional resonance due to the SRR. The fabricated prototype is presented in Figure 2(a), and its measured and simulated S_{11} responses confirm dual-band operation with −10 dB bandwidths of 26.2–28.3 GHz and 35.6–39.37 GHz, and peak broadside gains of 6.21 dBi and 6.49 dBi, respectively.

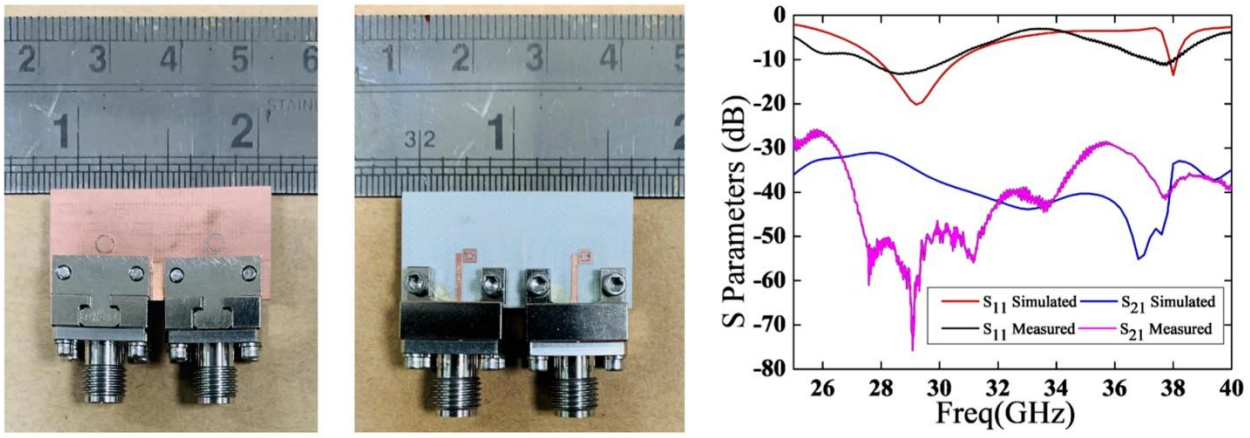

(a) (b)

Figure 3: (a) Photograph (bottom and top layer) of the fabricated prototype of two port MIMO. (b) Simulated and measured S_{11} and S_{21} response of the proposed two port MIMO antenna.

In Stage II, the antenna is extended to a two-port MIMO configuration with an inter-element spacing of 15 mm, as shown in Figure 3(a). The simulated and measured S-parameters in Figure 3(b) demonstrate high isolation (>28 dB) and preservation of dual-band behavior. Several MIMO performance metrics, including ECC < 0.1, TARC < -10 dB, and CCL < 0.5 bps/Hz, validate the antenna's suitability for compact, high-isolation mm-wave 5G MIMO systems.

AMC Backed Four-Port MIMO Antenna

Building upon the annular-slot-based monopole antenna developed in Stage I of Work 1, the next work focuses on enhancing the radiation safety and extending the design into a four-port MIMO configuration tailored for wearable 5G mm-wave wireless body area network (WBAN) applications. While the earlier dual-band MIMO antenna achieved broadside radiation and dual-band operation at 28 GHz and 38 GHz, its performance was constrained by limited isolation and a relatively large footprint due to the side-by-side arrangement of antenna elements. Additionally, it did not address on-body radiation concerns, which are critical for wearable use.

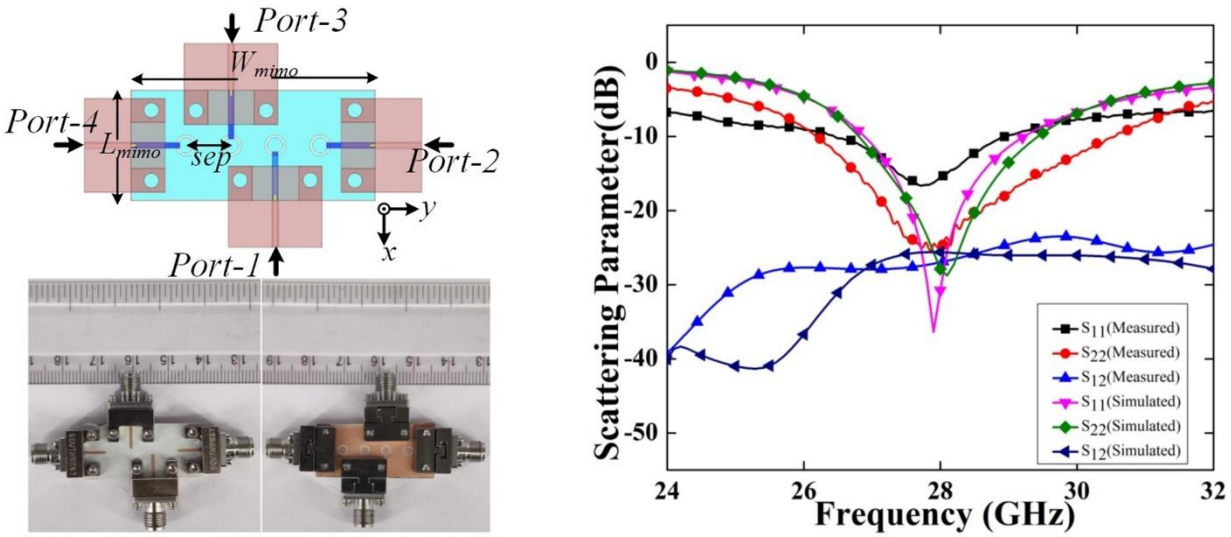

(a) (b)

Figure 4. (a) Geometry and fabricated prototype (top and bottom layer) of the proposed 4 port MIMO antenna with *sep* = 6.1, L_{mimo} = 15, W_{mimo} = 33.2 (units: mm). (b) Simulated and measured S-parameter plots of the proposed 4-port MIMO antenna. The optimized dimensions are: L=W= 15, r_1 = 1.08, r_2 = 1.38, w_f = 0.7, l_f = 6.6, l_s = 7.5 (units: mm).

To overcome these challenges, the same annular-slot antenna element is employed as the base radiator and arranged in a mutually orthogonal four-element layout to reduce mutual coupling and improve spatial compactness. Furthermore, a custom-designed AMC surface is integrated beneath the antenna to suppress back-lobe radiation and enhance gain. The layout and fabricated prototype of the complete four-port configuration are shown in Figure 4(a), with corresponding simulated and measured S-parameters presented in Figure 4(b).

The AMC surface comprises a 10×7 unit-cell array, whose geometry and periodic simulation setup are illustrated in Figure 5(a), and its in-phase reflection behavior near 28 GHz is confirmed by the reflection phase plot in Figure 5(b). The assembled configuration, including the fabricated AMC and four-port antenna mounted above it with a 3.4 mm separation, is shown in Figure 5(c), and its S-parameter results are depicted in Figure 5(d).

Compared to the standalone MIMO design, the AMC-backed antenna demonstrates a 4.83 dBi gain improvement, up to 66% better isolation, and a bandwidth extension of 0.65 GHz. Safety performance is evaluated using a three-layer human body phantom, confirming reduced back radiation and compliance with power density limits. Overall, the proposed configuration

achieves enhanced gain, compactness, and user safety, making it well-suited for high-performance 5G wearable WBAN systems.

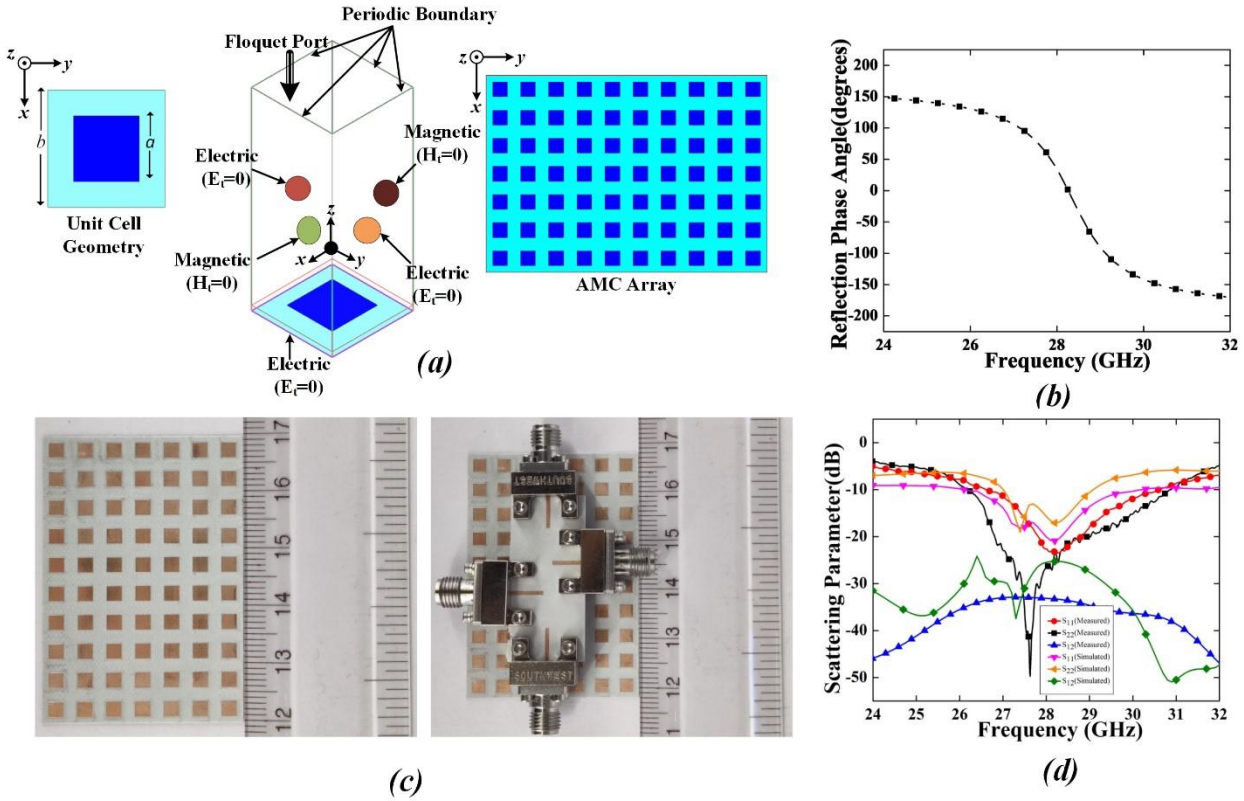

Figure 5. (a) The unit cell geometry of the proposed AMC with dimensions: a = 2.6, b=5 (units: mm), periodic boundary set up for simulation, and the AMC array (10×7 unit cells). (b) Simulated reflection phase characteristics of the AMC unit cell. (c) Fabricated prototype of the proposed AMC array (10 × 7) and 4 port MIMO antenna placed on top of AMC at the separation of 3.4 mm. (d) Simulated and measured S-parameter responses of the proposed MIMO antenna with AMC.

CSRR-Loaded Dual-Band MIMO Antenna Array

The third work of the thesis introduces a CSRR-loaded dual-band MIMO antenna array for millimeter-wave WBAN applications, operating at 28.2 GHz and 38.8 GHz (n257 and n260 bands). The design builds conceptually on Work 1, which has used the SRR loading to achieve dual-band operation in a printed monopole configuration. However, Work 1 has suffered from limited isolation and relatively low gain due to the side-by-side single-element arrangement. Additionally, while Work 2 has an enhanced radiation safety due to the use of AMC, it has been restricted to a single-band operation and increased the overall thickness of the structure.

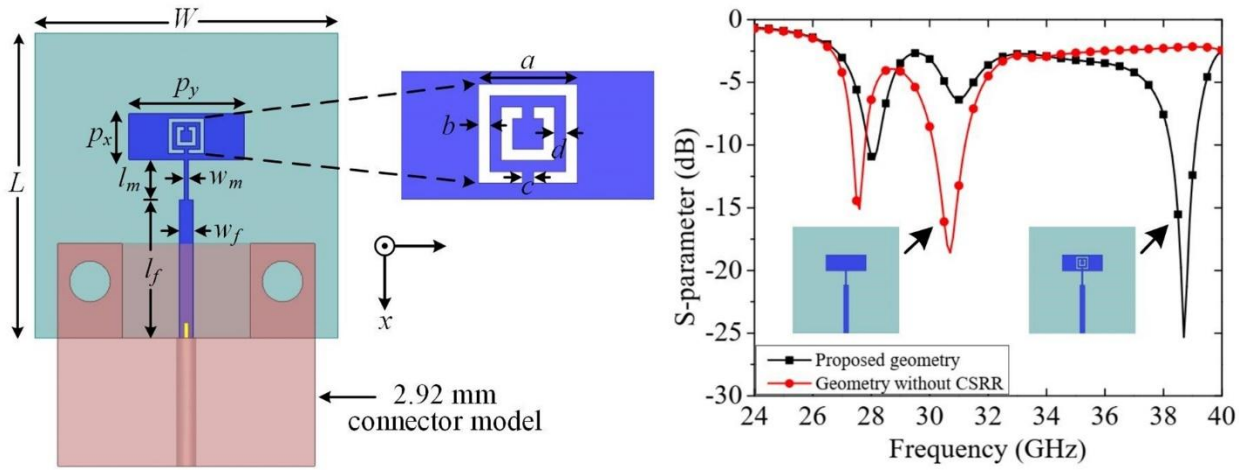

(a) (b)

Figure 6. (a) Proposed single antenna geometry with the connector model, and (b) simulated reflection coefficients (S_{11}) of the antenna topology with and without CSRR loading. The geometric dimensions are: $L = W = 15$, $l_f = 15$, $w_f = 0.7$, $l_m = 2$, $w_m = 0.2$, $p_x = 2.25$, $p_y = 5.7$, $a = 1.74$, and $b = c = d = 0.2$ (unit: mm).

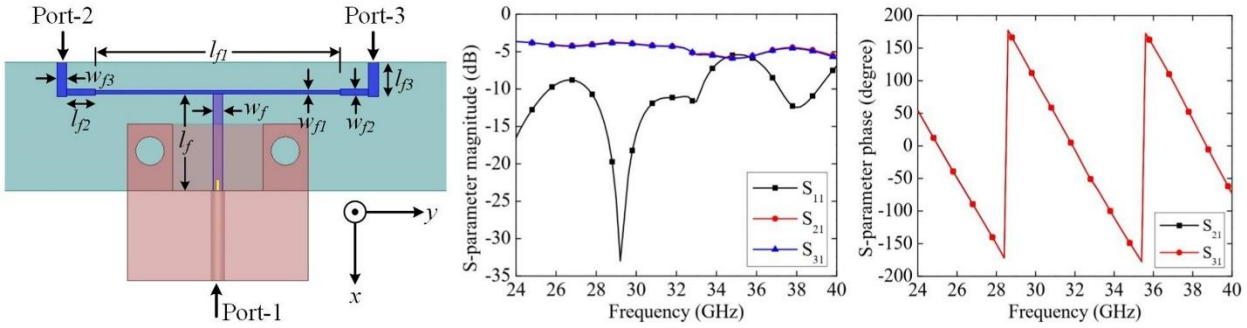

(a) (b) (c)

Figure 7. (a) Proposed 1× 2 power divider design. Simulated S-parameters of the power divider: (b) amplitude characteristics, and (c) phase characteristics. The geometric dimensions are as follows: $l_f = 6.8$, $w_f = 0.7$, $l_{f1} = 17.2$, $w_{f1} = 0.23$, $l_{f2} = 2$, $w_{f2} = 0.46$, $l_{f3} = 2.4$, $w_{f3} = 0.7$ (units: mm).

To address these gaps, the proposed design uses a patch-based geometry with CSRR loading to realize dual-band response in a two-port MIMO array. As shown in Figure 6(a), the antenna integrates CSRRs to improve impedance matching and enable resonance at both target frequencies. The impact of the CSRR is demonstrated in Figure 6(b). A dual-band T-junction power divider, as depicted in Figure 7(a), is used to ensure proper feeding to the array network, with balanced amplitude and phase responses validated in Figures 7(b) and 7(c), respectively.

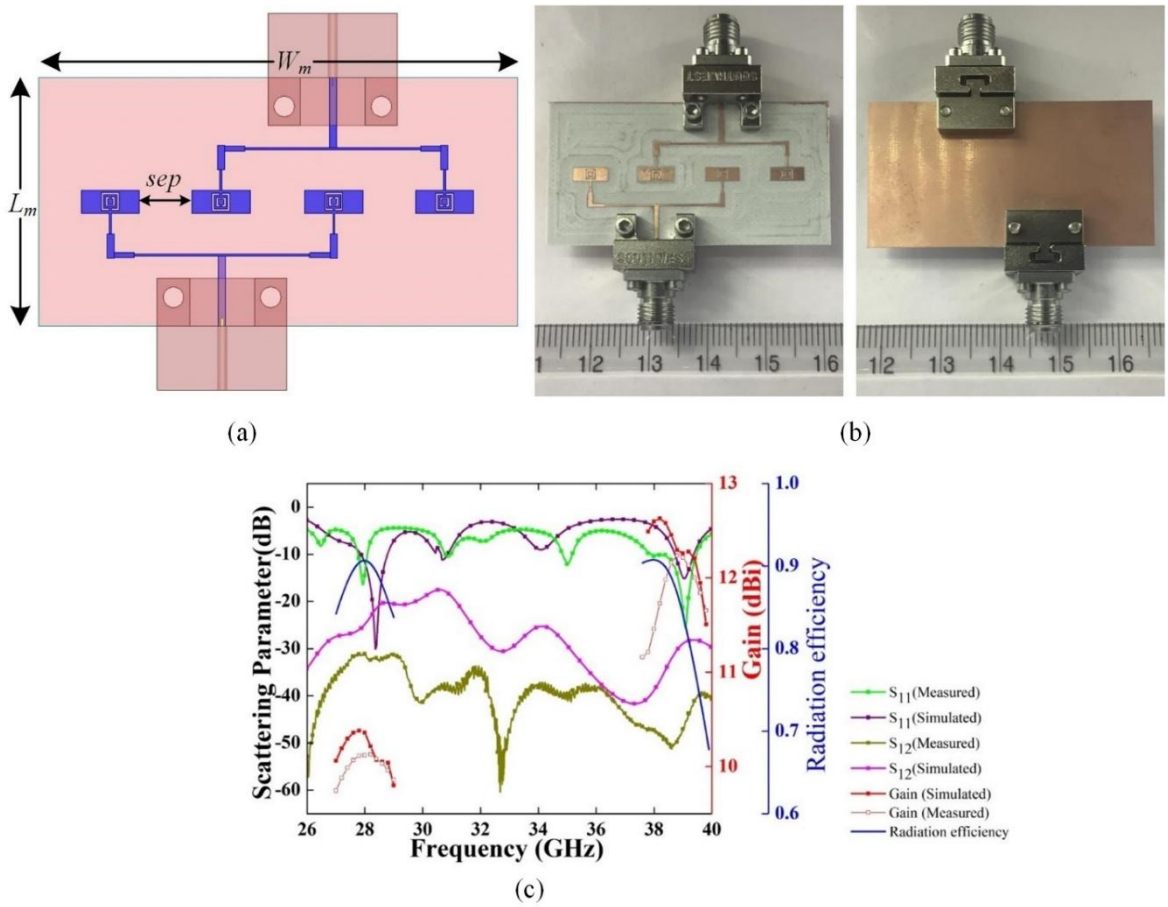

Figure 8. (a) Schematic representation and (b) fabricated prototype (top and bottom views) of the of the proposed two-port MIMO two-element antenna array. (c) Simulated and measured scattering parameter responses (S_{11}, S_{12}), gain, and radiation efficiency for the proposed geometry.

To further improve the antenna performance, the two-port MIMO antenna is expanded to a two-element antenna array configuration, as illustrated in Figure 8(a), with its fabricated prototype presented in Figure 8(b). The simulated and measured performances in Figure 8(c) confirm high isolation (>20 dB), dual-band coverage, and broadside radiation with peak gain exceeding 10 dBi due to the array configuration. While the array's footprint ($0.21\lambda_o \times 0.53\lambda_o \times 0.028\lambda_o$) is comparable to Work 1, the gain is significantly enhanced. Importantly, the safety analysis using a three-layer body phantom confirms compliance with power density norms and low back radiation, comparable to the AMC-based design in Work 2, but without requiring additional layers. This design therefore combines dual-band functionality (from Work 1), improved radiation safety (approaching Work 2), and significantly higher gain, offering a balanced solution for high-performance, on-body 5G mm-wave MIMO communication systems.

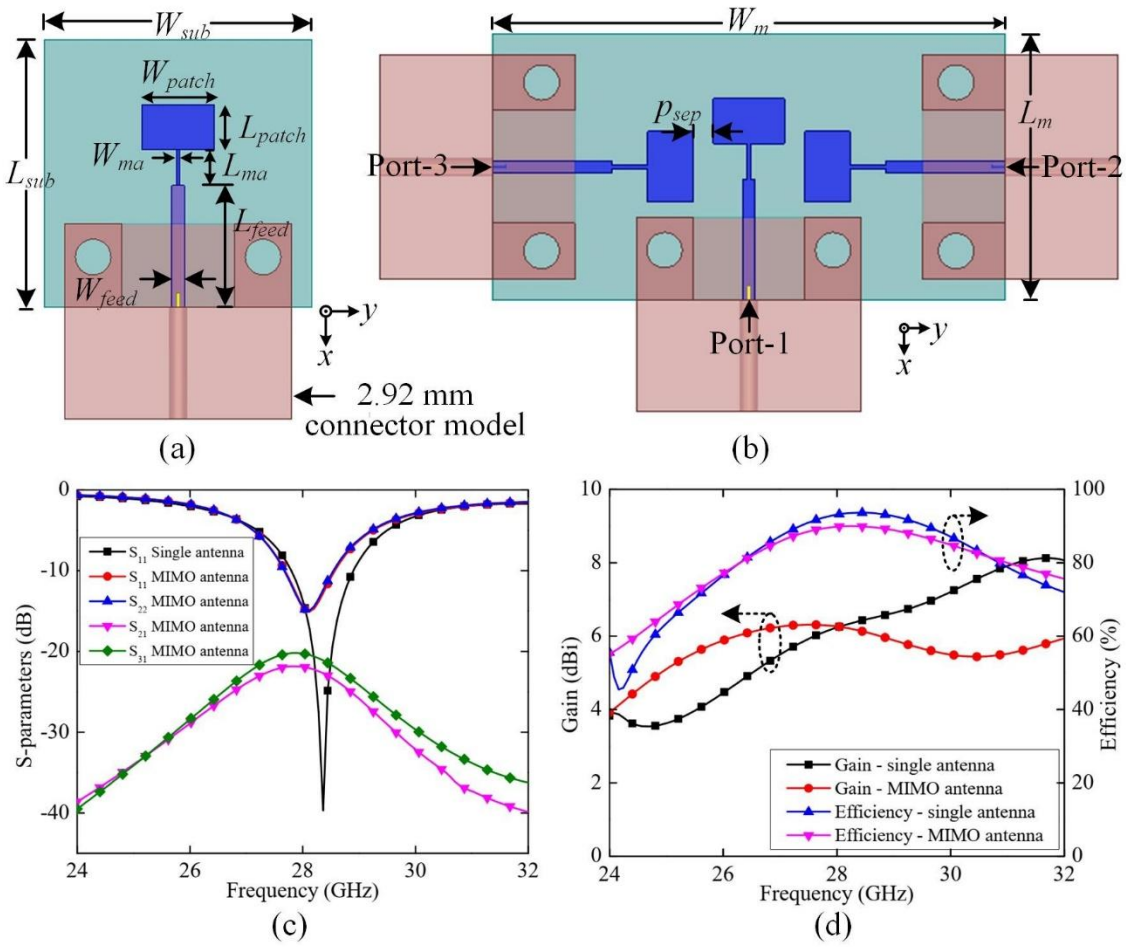

Figure 9. Schematic diagrams of the proposed (a) antenna element along with the connector model, and (b) its 3-port MIMO antenna configuration. Simulated responses of both antenna element and MIMO antenna: (c) scattering parameters, (d) gain and efficiencies. The geometric dimensions are: $L_{sub} = W_{sub} = 15$, $L_{patch} = 2.54$, $W_{patch} = 4$, $L_{ma} = 2$, $W_{ma} = 0.2$, and $L_{feed} = 6.8$, $W_{feed} = 0.7$ $W_m = 29$, $L_m = 15$, $p_{sep} = 1.16$ (unit: mm).

Fabry–Perot Cavity-Based MIMO Antenna

Building on the prior development of compact dual-band MIMO antennas using CSRR loading (Work 3) and AMC-backed wearable MIMO systems (Work 2), the fourth work advances toward designing a high-gain, aperture-efficient mm-wave MIMO antenna for 28 GHz 5G (n257 band) applications. The key objective is to significantly improve directivity and aperture efficiency while maintaining strong MIMO performance within a compact form factor.

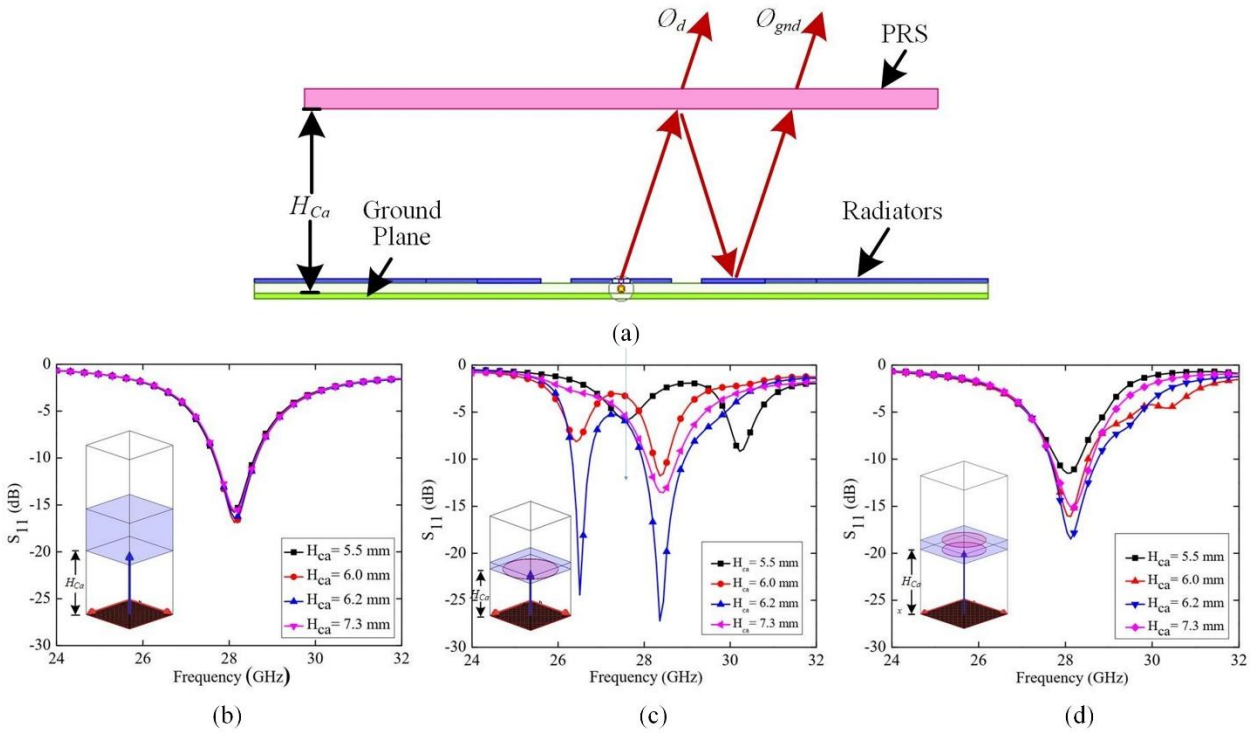

Figure 10. (a) Radiation mechanism in FP Cavity; Simulated parametric variation of S_{11} with respect to height of the cavity (H_{ca}), when a single antenna element is loaded with (b) an unprinted PRS, (c) a 3×3 single-side printed PRS array, and (d) a 3×3 double-side printed PRS array.

The proposed antenna consists of three orthogonally placed rectangular microstrip patch elements forming a three-port MIMO system without any external decoupling structures. The schematic of a single antenna element and the full MIMO layout are illustrated in Figures 9(a) and 9(b), respectively. The simulated S-parameters, gain, and efficiency for both single and multi-port configurations are shown in Figures 9(c) and 9(d), demonstrating adequate isolation, good impedance matching, and stable radiation characteristics.

To enhance the antenna performance, a Fabry–Perot cavity is implemented by placing a superstrate approximately at half-wavelength above the antenna geometry. To choose the optimum Fabry–Perot cavity for the proposed MIMO antenna, three different configurations are investigated: (i) an unprinted dielectric, (ii) a single-side printed partially reflecting surface (PRS), and (iii) a double-side printed PRS. Their responses are parametrically varied and the most suitable configuration is chosen for improving the performance of the MIMO antenna.

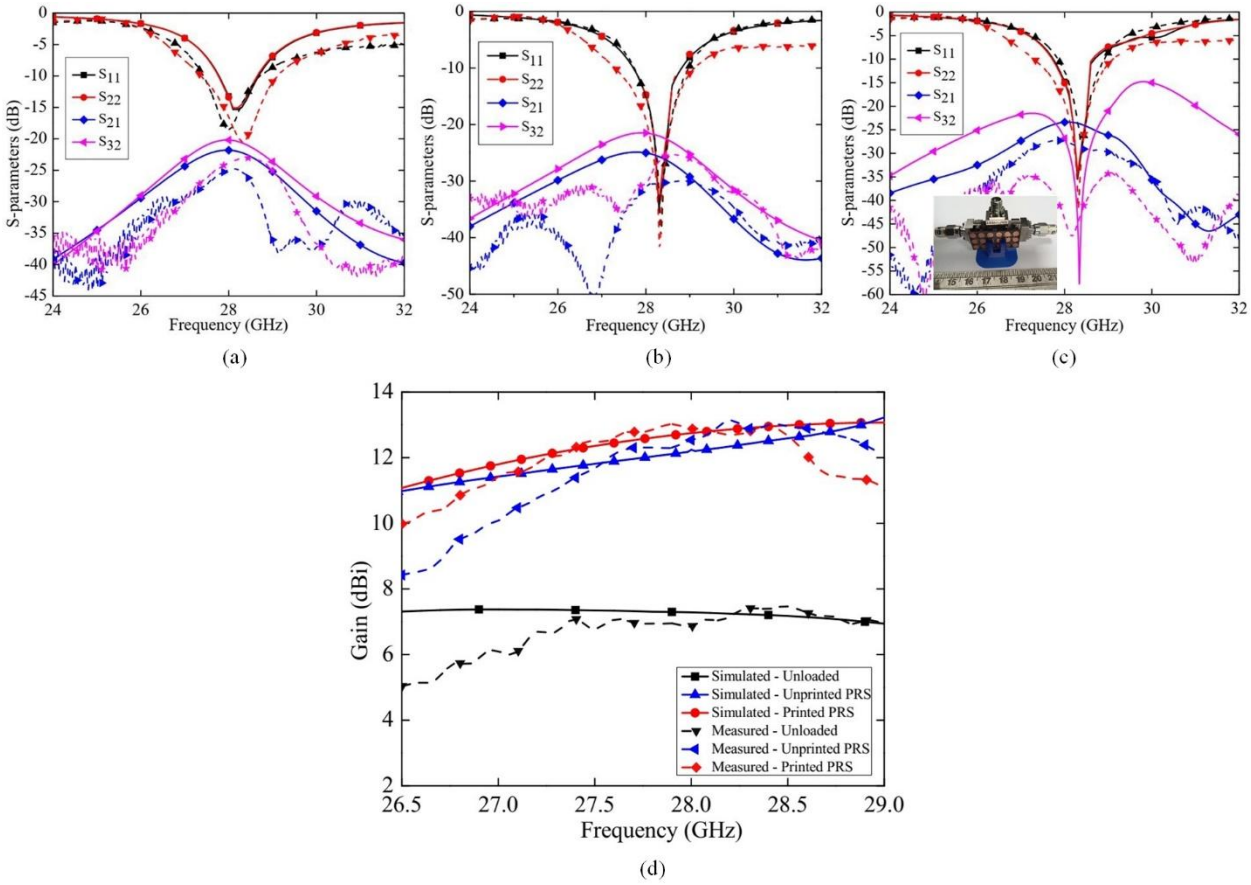

Figure 11. Simulated and measured S-parameters of the proposed MIMO antenna for different cases: (a) without loading any PRS (i.e. only antenna geometry), (b) loaded with a unprinted PRS array, and (c) loaded with a double-side printed PRS array. The solid and dashed lines represent simulated and measured responses, respectively. (d) Simulated and measured broadside gain of the proposed MIMO antenna (Port 1) for all cases (i.e., unloaded, loaded with unprinted PRS, and loaded with double-side printed PRS array).

The underlying radiation mechanism and the effect of cavity height (H_{ca}) on the S_{11} performance are analyzed in Figures 10(a)–10(d), confirming constructive wave interference due to Fabry–Perot resonance. The simulated and measured S-parameters for all three superstrate configurations are shown in Figures 11(a)–11(c), revealing enhanced bandwidth and inter-port isolation compared to the unloaded case. The corresponding gain improvements are presented in Figure 11(d), highlighting performance enhancement with each superstrate.

Performance comparison across different configurations reveals a peak gain of 12.74 dBi and 91.5% aperture efficiency with the double-side PRS, followed by 12.24 dBi / 87.9% for the

unprinted dielectric, and 11.84 dBi / 78.1% with the single-side PRS. In all cases, the ECC remains below 0.01, ensuring strong MIMO diversity performance. The measured results closely align with simulations, validating the design accuracy.

This work represents a logical progression from the CSRR-loaded, dual-band compact MIMO system (Work 3) and the AMC-based, single-band wearable antenna (Work 2), toward a high-efficiency Fabry–Perot cavity-backed architecture. The combination of enhanced gain, aperture efficiency, low mutual coupling, and compact structure makes the proposed antenna highly suitable for high-data-rate, long-range 5G MIMO deployments.

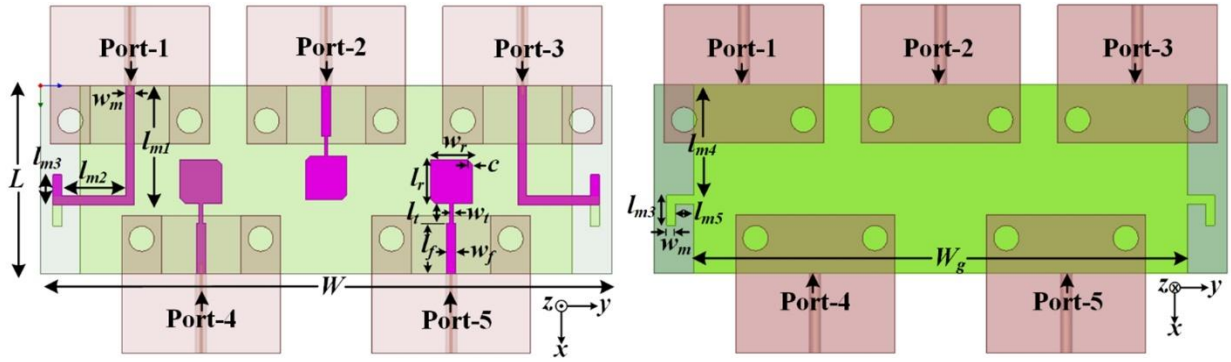

Figure 12. Illustration of the proposed 5-port MIMO antenna design: (a) top view, and (b) bottom view. The optimized dimensions are as follows: $l_f = 4$, $w_f = 0.77$, $l_t = 1.6$, $w_t = 0.2$, $l_r = 3.5$, $w_r = 3.35$, c = 0.55, $l_{m1} = 9.5$, $w_m = 0.7$, $l_{m2} = 5.1$, $l_{m3} = 2.4$, $l_{m4} = 8.8$, $l_{m5} = 1.45$, and $W_g = 23$ (units: mm).

Five-Port MIMO Antenna with Polarization and Pattern Diversity

The fifth work presents the design and demonstration of a compact five-port mm-wave MIMO antenna system offering simultaneous polarization and pattern diversity, specifically aimed at 28 GHz 5G wireless communication. The schematic top and bottom views of the proposed antenna are illustrated in Figures 12(a) and 12(b), respectively, with optimized geometric parameters detailed therein. The measured S-parameter responses for individual port excitations are shown in Figures 13(a)–(b), while the axial ratio characteristics of the circularly polarized ports are provided in Figure 13(c).

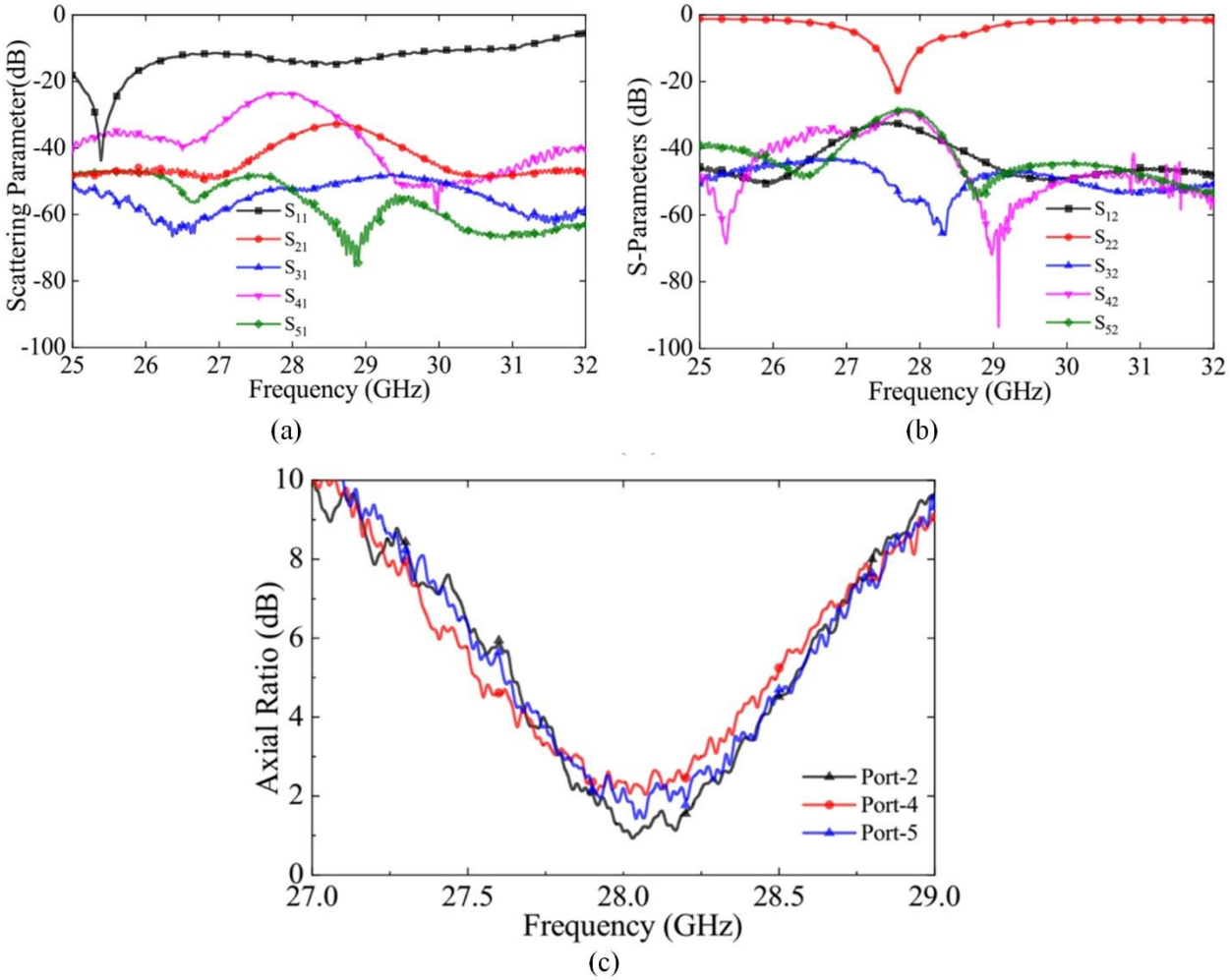

Figure 13. The measured S-parameters of the fabricated MIMO antenna system, when: (a) Port-1 and (b) Port-2, are individually excited. (When one port is excited, others are terminated with matched loads). (c) Measured axial ratio, when Ports 2, 4, and 5 are individually excited.

Evolving from Work 2 to Work 4, this design (fifth work) shifts from gain and safety optimization toward enhanced spatial and polarization diversity. While earlier designs have improved performance through AMC backing, dual-band CSRR loading, and FP cavity superstrates, they remain limited to broadside radiation and lacked polarization diversity. Work 5 addresses these gaps, ensuring robust operation in dynamic multipath environments.

The proposed antenna integrates three chamfered rectangular patch elements (Ports 2, 4, and 5) producing circular polarization (CP) responses—two right-hand CP (RHCP) and one left-hand CP (LHCP)—all radiating in the broadside direction. Additionally, two printed dipole

antennas (Ports 1 and 3) provide linearly polarized (LP) radiation in the end-fire direction. This hybrid configuration enables the system to support multiple signal orientations and paths, thereby improving resilience to user motion and channel variation.

Despite incorporating five elements with diverse radiation patterns, the design maintains a compact footprint ($1.4\lambda_0 \times 4.26\lambda_0$), high isolation (22–61 dB), and radiation efficiency between 89–97%, all without any external decoupling structures. Experimental validation confirms peak gains up to 9.05 dBi and adequate bandwidth across all ports.

By combining RHCP, LHCP, and LP elements in a single platform and achieving both broadside and end-fire radiation, this work provides a well-balanced and compact solution that meets the practical demands of high-capacity, resilient, and spatially diverse 5G MIMO systems.

Reflectarray for mm-wave Non-Terrestrial Networks

This sixth and final work presents the development of a wideband, high-gain reflectarray antenna operating at 28 GHz for Ka-band mm-wave Non-Terrestrial Network (NTN) applications.

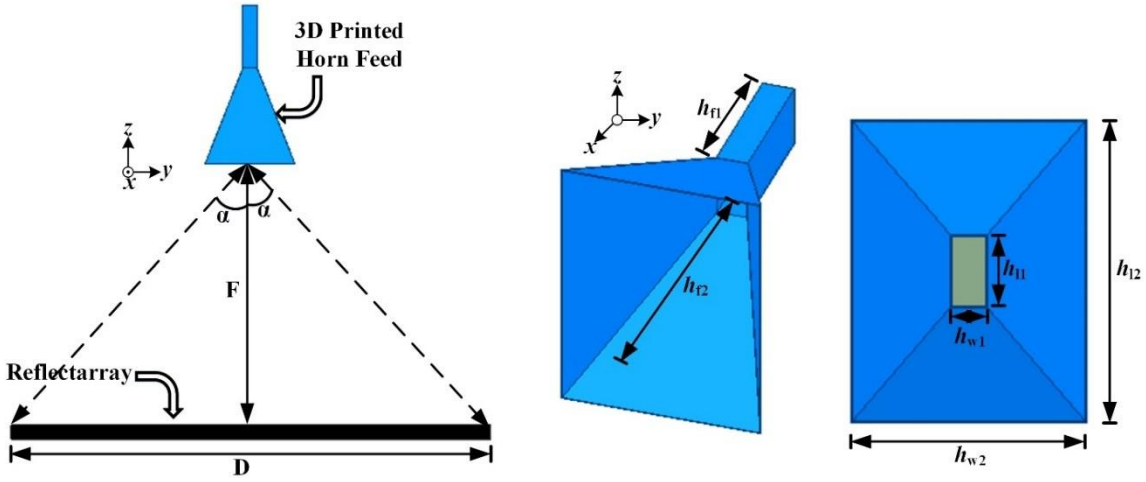

Figure 14. (a) General setup of the proposed Reflectarray antenna fed by a horn antenna. (b) Schematics of the designed 3D printed horn antenna, with dimensions: h_{f1} = 13.05, h_{f2} = 19.89, h_{l1} = 5.6, h_{l2} = 24, h_{w1} = 3, and h_{w2} = 18.53 (units: mm).

The planar reflectarray is a two-dimensional geometry composed of sub-wavelength square-ring unit cell resonators, arranged to produce a highly directional beam in the desired direction when illuminated by a feed source placed at a specific focal position. The fundamental configuration of the reflectarray antenna, fed by a 3D-printed pyramidal horn antenna, is shown in

Figure 14(a), where *D* represents the aperture dimension and *F* denotes the focal distance from the feed to the array. The detailed schematic of the horn antenna, with optimized dimensions is presented in Figure 14(b).

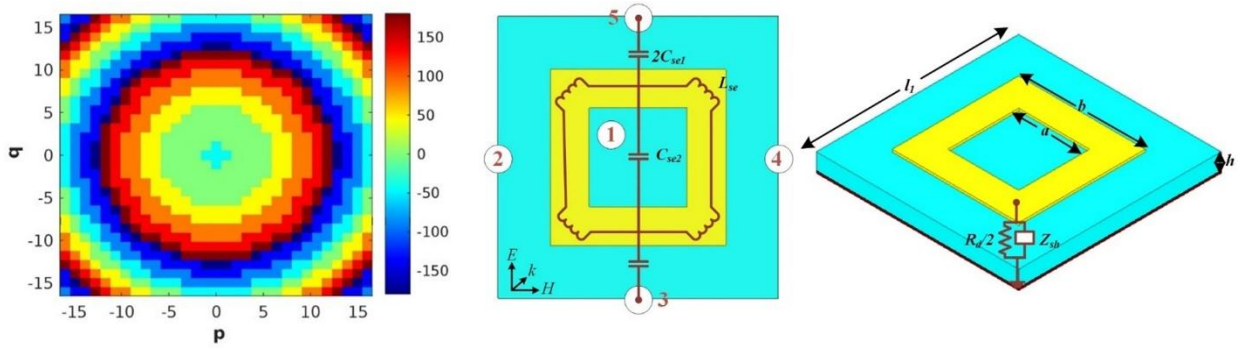

(a) (b) (c)

Figure 15. (a) Required 3-bit discrete reflection phase distribution plot for the radiated beam at θ = 0° and φ = 0°. (b) Top view and (c) isometric view of the proposed unit cell along with its equivalent circuit diagram. The dimensions are: l_1 = 3.2 mm, h = 0.797 mm. C_{se1} and C_{se2} represent coupling capacitances, L_{se} denotes the inductance of the metallic square ring, R_d is resistance associated with substrate loss, and Z_{sh} represents vertical coupling capacitance or inductance.

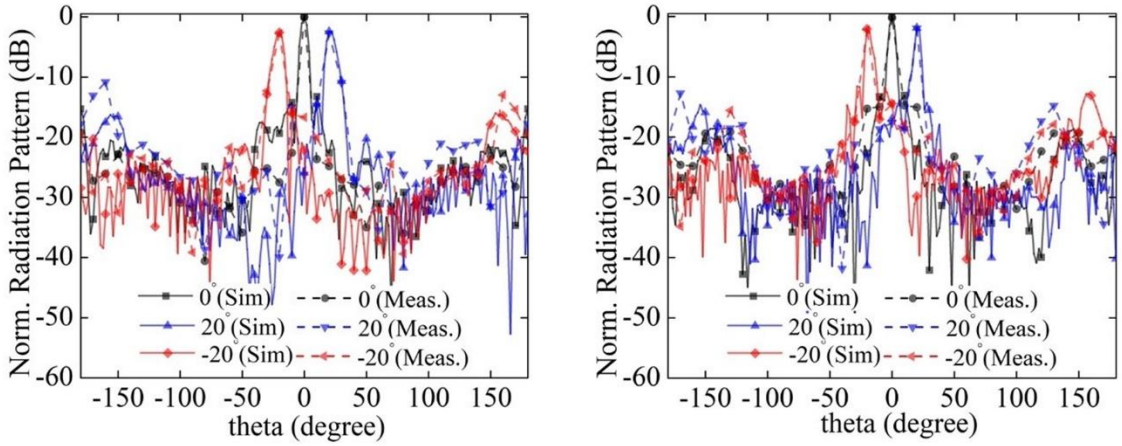

(a) (b)

Figure 16. Measured and simulated far-field radiation pattern for radiated beam at 0°, 20°, -20° in YZ-plane at (a) 26.7 GHz and (b) 38 GHz.

The reflectarray consists of a 31 × 31 planar grid of 3-bit quantized unit cells, each engineered to impart discrete phase shifts by varying the dimensions of the metallic square ring. The required continuous reflection phase distribution for generating a broadside beam (θ = 0°, φ = 0°) is shown in Figure 15(a). The geometry of the proposed square-ring unit cell in top and isometric views, along with its equivalent circuit model, are presented in Figures 15(b)-(c). This design achieves a full 360° reflection phase range with low insertion loss (< 0.8 dB).

Far-field radiation patterns for beams steered at 0°, 20°, and −20° in the YZ-plane are shown in Figures 16(a) and 16(b) for 26.7 GHz and 38 GHz, respectively, confirming stable beam shaping and minimal distortion across steering angles. The gain and aperture efficiency versus frequency are presented in Figure 17(a) and 17(b), respectively, indicating a peak gain of 27.8 dBi, maximum aperture efficiency of 56.1%, and a wide 3-dB gain bandwidth of 54.6%.

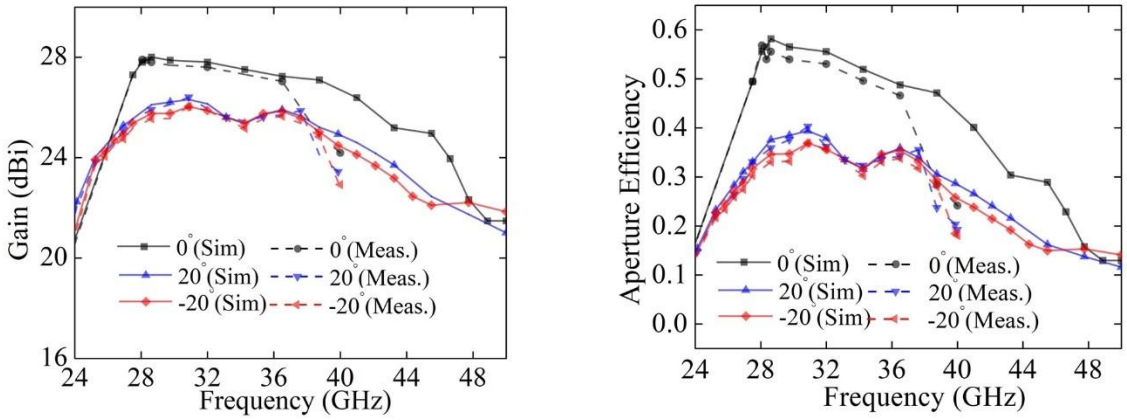

(a) (b)

Figure 17. Simulated and measured (a) gain and (b) aperture efficiency of the proposed reflectarray.

In summary, this thesis presents a systematic progression from compact wearable MIMO antennas to high-gain, beam-steerable reflectarrays, covering 28 GHz and 38 GHz 5G applications. The designs employ SRR/CSRR loading, AMC integration, Fabry–Perot cavities, and polarization–pattern diversity to enhance bandwidth, gain, isolation, and deployment versatility. The final reflectarray solution demonstrates scalability from terrestrial to non-terrestrial networks, offering a unified framework for next-generation mm-wave communications.

Contents

List of Figures

List of Tables

List of Abbreviations and Acronyms

1G: First generation

2G: Second generation

3G: Third generation

4G: Fourth generation

5G: Fifth generation

B5G: Beyond fifth generation

MIMO: Multiple-input multiple-output

NTN: Non-Terrestrial Network

RAN: Radio Access Network

3GPP: 3rd Generation Partnership Project

mm-wave: Millimeter-wave

IoT: Internet of Things

AR: Axial Ratio

LP: Linear Polarization

CP: Circular Polarization

LHCP: Left-hand Circular Polarization

RHCP: Right-hand Circular Polarization

RL: Return Loss

ARBW: Axial Ratio Bandwidth

PRS: Partially reflective surface

FPC: Fabry–Perot cavity

ECC: Envelope Correlation Coefficient

DG: Diversity Gain

DO: Diversity Order

DM: Diversity Measure

TARC: Total Active Reflection Coefficient

CCL: Channel Capacity Loss

ME: Multiplexing Efficiency

MEG: Mean effective gain

WBAN: Wireless Body Area Network

PEC: Perfect Electric Conductor

AMC: Artificial Magnetic Conductor

Chapter 1

Introduction

The relentless pursuit of higher data rates, greater reliability, and lower latency has been the principal driving force behind the evolution of wireless communication technologies. Since the mid-1980s, wireless systems have advanced from the analog, voice-centric first generation (1G), through the digital revolution of second generation (2G), to the multimedia capabilities of third generation (3G) networks. These early systems primarily supported voice communication, while data-intensive services such as video streaming or file transfer remained dependent on wired connections. The arrival of fourth generation (4G) systems marked a turning point, enabling the convergence of mobile broadband and the Internet, with technologies like multiple-input multiple-output (MIMO) dramatically enhancing channel capacity without requiring additional spectrum.

Building on this foundation, fifth-generation (5G) networks have already been rolled out, with sub-6 GHz deployments delivering improved capacity and coverage. However, while these systems provide important enhancements over 4G, they fall short of meeting the full spectrum of emerging requirements. Bandwidth-intensive applications such as augmented reality (AR), 3D media, and ultra-high-definition (8K) video streaming demand peak data rates on the order of 10 Gbit/s and beyond, coupled with ultra-low latency and massive connectivity. Meeting these targets necessitates moving beyond sub-6 GHz solutions toward millimeter-wave (mm wave) frequency bands, which offer the wide bandwidths required to realize the ambitious vision of 5G and beyond-5G (B5G) communications [1].

The mm-wave spectrum (30–300 GHz) provides vast bandwidth for multi-Gbps data rates and remains under-utilized compared to sub-6 GHz bands. Regulatory bodies such as the ITU and FCC have allocated key 5G bands—most notably 28 GHz and 38 GHz—owing to their low atmospheric attenuation and proven suitability for terrestrial and indoor communications [2]. However, operation at mm-wave frequencies presents unique challenges. The free-space path loss increases with frequency, leading to significantly higher attenuation than in sub-6 GHz systems—for instance, the path loss at 28 GHz is about 15 dB higher than at 5 GHz for the same distance. Additional losses arise from atmospheric absorption (notably at 60 GHz due to oxygen resonance), rain attenuation, and scattering. These factors restrict mm-wave communications primarily to short-range links and small-cell architectures. Mitigation requires

the use of high-gain, and highly directive antennas. When such antennas are employed at both the transmitter and the receiver, they can partially offset free-space losses, enhance the signal-to-noise ratio (SNR), and support reliable line-of-sight (LOS) links.

Antenna design is therefore a critical enabling factor in the success of mm-wave systems. Antennas serve as the transducers coupling guided RF energy to free space, and their physical dimensions scale inversely with operating frequency—allowing compact form factors at mm-wave bands. Modern consumer devices often conceal microstrip antennas beneath their outer casings, where thin metallic patches on dielectric substrates provide efficient low-profile radiation. For mm-wave operation, common high-gain antenna types include reflectors, lenses, and horns, but these are often impractical for compact, handheld, or wearable devices due to their bulk size and cost. Instead, printed circuit antennas, such as microstrip patches or dipole arrays, offer a manufacturable, low-cost, and integration-friendly alternative.

At 28 GHz, achieving reliable high-capacity links necessitates careful consideration of beam directivity and scanning capability. Highly directive antennas (e.g., 20 dBi gain) exhibit half-power beamwidths as narrow as 16°, making even minor transmitter–receiver misalignments detrimental to link quality [3]. Beam-steerable or switched-beam arrays can counteract this by dynamically adjusting the radiation direction to maintain connectivity. Furthermore, practical radiation patterns differ from idealized models—side lobes, main-lobe degradation under misalignment, and polarization effects must be factored into both antenna and system design.

The use of MIMO architectures further enhances mm-wave performance by exploiting spatial dimensions to boost capacity without extra spectrum or power [4]. The short wavelength enables large-array integration, allowing hybrid spatial multiplexing and beamforming—jointly improving throughput, SNR, and link robustness in diverse channel conditions.

However, at mm-wave frequencies, MIMO antenna design presents distinct challenges arising from the extremely small wavelength. The reduced wavelength facilitates the integration of large antenna arrays within compact spaces; however, it simultaneously imposes stringent requirements on element isolation, MIMO performance, and fabrication precision. Inadequate control of these parameters can lead to increased mutual coupling between closely spaced elements, thereby deteriorating overall system performance. Precise array calibration and low-loss feeding networks are critical to maintain phase coherence across elements for effective beamforming and spatial multiplexing. Hybrid antenna architectures, combining subarray-based analog beamforming with digital precoding, can help reduce hardware

complexity while retaining directional gain. Techniques such as element pattern optimization, use of low-loss substrates, and incorporation of reconfigurable or adaptive antenna elements further enhance MIMO performance, enabling robust links even in dynamic mm-wave environments.

In addition to terrestrial applications, mm-wave technology is rapidly expanding into the domain of Non-Terrestrial Networks (NTNs), envisioned as a critical extension of the 5G and beyond-5G ecosystems. NTNs leverage spaceborne and airborne platforms to deliver seamless global coverage, especially in areas where terrestrial networks face deployment limitations or reliability challenges. The spaceborne segment primarily includes geosynchronous and non-geosynchronous satellite constellations such as Low Earth Orbit (LEO) and Geostationary Earth Orbit (GEO) systems, while the airborne segment encompasses Uncrewed Aerial Vehicles (UAVs), Uncrewed Aerial Systems (UAS), and High-Altitude Platforms (HAPs). Together, these advanced platforms can effectively bridge connectivity gaps, extend network reach, and provide resilient communication services in remote or disaster-affected regions where terrestrial infrastructure is sparse or non-functional.

From a Radio Access Network (RAN) perspective, the significance of NTNs within the 5G framework lies in their ability to overcome spatial, economic, and deployment constraints inherent to ground-based systems. By establishing wide-area coverage through aerial and satellite-based links, NTNs play a vital role in ensuring continuous connectivity for mobile broadband and Internet of Things (IoT) applications, particularly in rural areas. This hybrid integration of terrestrial and non-terrestrial components forms a comprehensive communication ecosystem capable of meeting diverse service demands—from broadband access and vehicular communication to remote sensing and emergency response [5].

Recognizing their strategic potential, the 3rd Generation Partnership Project (3GPP) has incorporated NTN integration into the 5G standardization roadmap. Specifically, 3GPP Releases 17 and 18 focus on harmonizing NTN with the terrestrial 5G architecture by defining interworking protocols, mobility management procedures, and interoperability frameworks between satellite, aerial, and ground segments. Release 17 formally includes LEO satellite constellations and high-altitude platforms as NTN use cases, laying the groundwork for unified global coverage. Figure 1.1 shows the standard 3GPP management system integrated with the satellite management system. These advances mark a step toward realizing an interconnected communication infrastructure that transcends traditional terrestrial boundaries [7]-[8].

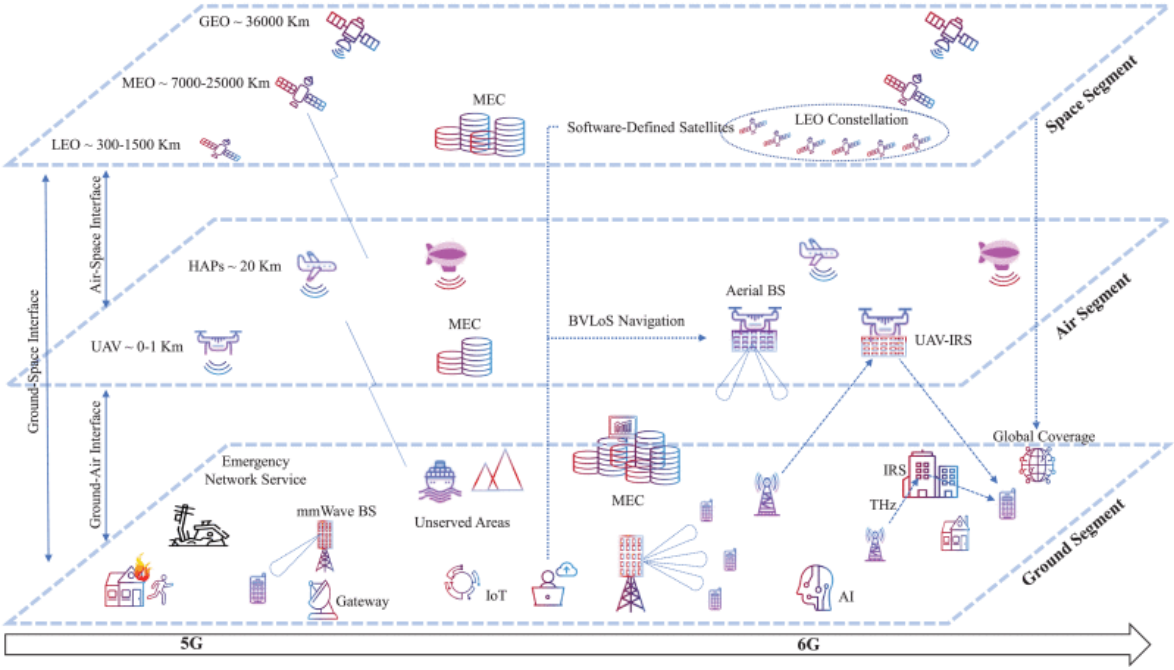

Figure 1.1: The evolution of integrated terrestrial and non-terrestrial networks [6].

To support the high-gain, wide-bandwidth, and beam-agile requirements of NTN links, antenna technologies must evolve to deliver efficient, lightweight, and steerable solutions. Reflectarray antennas have emerged as particularly promising candidates in this context, combining the high-gain characteristics of parabolic reflectors with the planar form factor of phased arrays. By introducing electronically or mechanically controlled phase shifts, they enable dynamic beam steering while maintaining a low-profile and cost-effective structure. Such attributes make reflectarrays well-suited for next-generation NTN applications involving LEO/GEO satellites, UAVs, and HAPs, where compactness, power efficiency, and adaptive coverage are essential for maintaining robust mm-wave communication links over vast and dynamic environments. As wireless communication systems continue to diversify and demand increasingly specialized performance, antenna engineering has moved away from a one-size-fits-all paradigm toward highly optimized designs tailored to specific operational contexts. Each environment introduces its own challenges—ranging from the compact form factors required by portable and wearable devices, to proximity effects near the human body, operation at extreme frequencies, and the need to maintain high mobility with dynamic coverage. Addressing these challenges necessitates innovations not only in antenna geometry, but also in the integration of advanced materials, engineered surfaces, and multi-antenna configurations.

Within this evolving landscape, the research presented in this thesis situates itself at the intersection of these demands, aiming to bridge the gap between diverse application

requirements and practical mm-wave antenna solutions. Specifically, the thesis focuses on the design and realization of compact, high-performance, and application-specific mm-wave antenna systems for both terrestrial and non-terrestrial communications. The work follows a logical progression—beginning with integration strategies for wearable and portable platforms, where size, efficiency, and user proximity are key constraints, and advancing toward the development of high-gain, beam-steerable architectures capable of meeting the stringent requirements of NTN links.

1.1 Millimeter Wave Spectrum

Millimeter-wave (mm-wave) frequencies offer exceptionally wide bandwidths, making it possible to achieve multi-gigabit data rates well beyond those of conventional wireless systems. For an additive white Gaussian noise (AWGN) channel, the channel capacity (C) is linearly dependent on the available bandwidth (B) as [9]:

$$C = B\ log_2(1 + SNR) \tag{1.1}$$

where, *SNR* is the signal to noise ratio. Since the transmitted power at mm-wave frequencies is capped by regulatory and safety limits, these links are generally suited to small-cell deployments rather than wide-area coverage. Even within this constraint, mm-wave systems offer several notable advantages. The short wavelengths allow for dense frequency reuse, enabling many cells to coexist efficiently within a limited geographic area. The abundant available bandwidth makes it possible to achieve data rates approaching those of fibre-optic links, supporting high-capacity applications. Moreover, the technology benefits from decades of use in secure communication systems, providing a mature foundation for wireless networks.

Interest in mm-wave technology is not new — experimental work at these frequencies dates back over a century [10]— but modern fabrication techniques, signal processing advances, and new spectrum policies have made them viable for widespread deployment. With the abundance of spectrum available, significant research efforts have focused on developing mm-wave wireless networks and standards such as IEEE 802.11ad Wi-Fi operating at 60 GHz. Figure 1.2 illustrates the mm-wave spectrum earmarked for future mobile communication. The total available bandwidth exceeds 150 GHz (excluding absorption bands), and unutilized mm-wave bands have already attracted significant research interest.

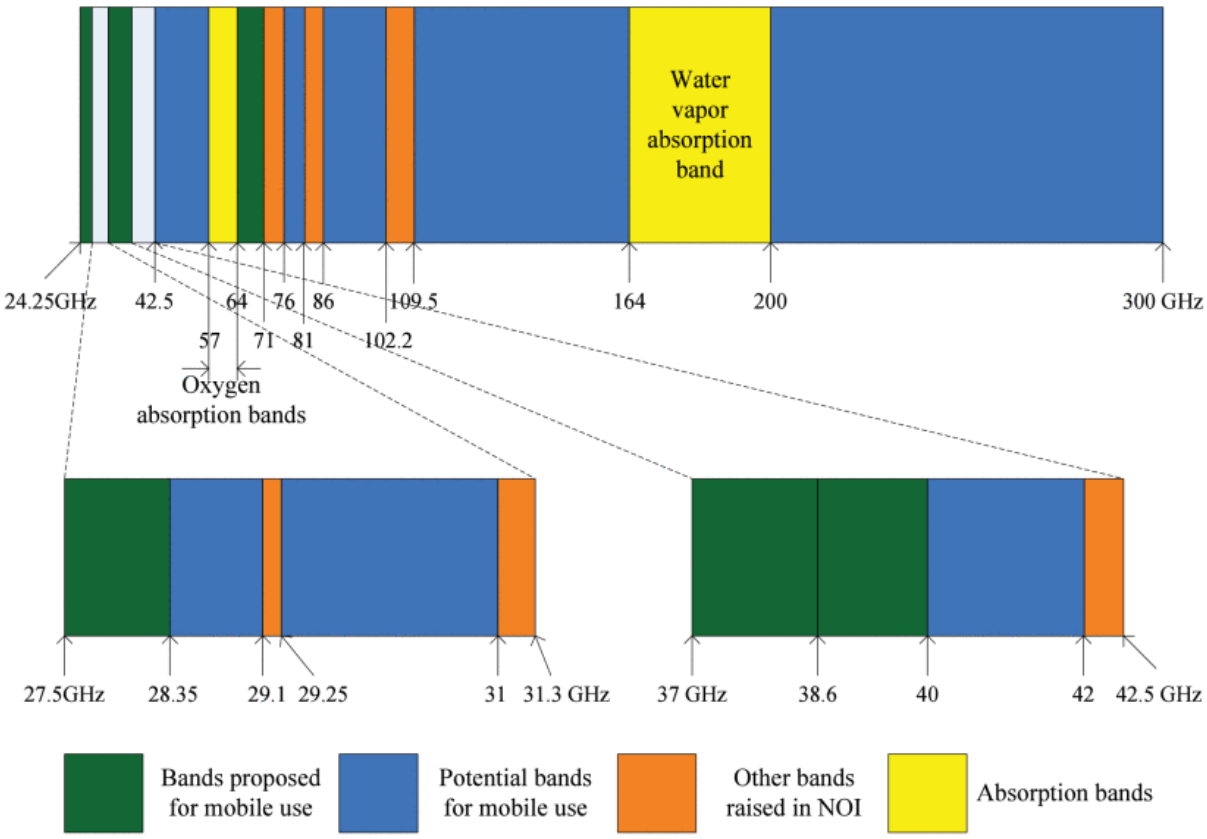

Figure 1.2: Millimeter-wave spectrum earmarked for future mobile communication [11].

Today, mm-wave spectrum is increasingly recognized as a cornerstone of high-capacity, low-latency 5G and future-generation wireless systems. International bodies such as 3GPP and the ITU have adopted a phased rollout strategy—beginning with frequencies below 40 GHz for early deployments, and gradually expanding into higher bands. At WRC-19, new allocations for 5G includes 24.5–27.5 GHz, 37–43.5 GHz, 45.5–47 GHz, 47.2–48.2 GHz, and 66–71 GHz [12]. Among these, the 28 GHz, 38 GHz, and 73 GHz bands have gained prominence for long-distance links because of their relatively low oxygen absorption, in contrast to the heavily attenuated 60 GHz band. Such globally coordinated allocations are fostering economies of scale in both device manufacturing and network infrastructure.

In India, the mm-wave journey has picked up pace. Reliance Jio holds substantial mm-wave allocation around the 26 GHz band across all major areas, enabling enterprise-grade and fixed wireless broadband services [13]. The Telecom Regulatory Authority of India (TRAI) has recommended expanding auctions into the 37–40 GHz bands to support high-capacity 5G deployments in dense urban zones. The regulator has, however, held off from auctioning the 42.5–43.5 GHz band due to the current lack of device support. These moves reflect India's

effort to adopt globally aligned mm-wave bands while allowing for careful rollout aligned with ecosystem maturity.

In recent years, mm-wave has also become a key enabler for NTNs, which include satellite-based and aerial communication platforms. The latest 3GPP specifications define dedicated NTN bands in the upper Ka-band range, with uplink channels around 27.5–30 GHz and downlink channels extending from roughly 17.7 to 30 GHz [14]. These allocations are intended to deliver high-capacity, wideband links between spaceborne or high-altitude platforms and ground terminals. However, using mm-wave in NTNs is far from straightforward: signal attenuation due to atmospheric absorption, precise beam alignment for moving platforms, and Doppler effects at high relative velocities all present engineering challenges.

1.2 High-Gain Millimeter Wave Antennas

Mitigating propagation losses at mm-wave frequencies necessitates the deployment of high-gain and highly directive antennas. At mm Wave frequencies, high gain is typically realized through an increased effective aperture or through the collective radiation of multiple elements in an array. By concentrating radiated energy into narrow beams, the antennas can effectively compensate for severe free-space attenuation and atmospheric absorption. When directional antennas are employed at both the transmitter and receiver, the received power increases significantly, resulting in an improved SNR and enhanced link reliability—particularly for LOS communication scenarios.

The gain of an antenna represents its capability to focus radiated power in a preferred direction relative to an isotropic radiator. Since received power diminishes rapidly with increasing frequency due to higher path loss, the use of high-gain antennas at both link terminals becomes essential for sustaining efficient mm-wave communication links over extended distances. The maximum gain (G_{max}) achievable by an antenna aperture (A_{eff}) can be calculated as:

$$G_{max} = \frac{4\pi A_{eff}\epsilon}{\lambda^2} \tag{1.2}$$

where, ϵ is the radiation efficiency of the antenna. Increasing the aperture size or the operating frequency enhances gain, but practical constraints—such as limited space and integration requirements—often restrict physical aperture expansion.

One of the ways to improve the gain of an antenna is by arranging multiple radiating elements into an array configuration. The use of antenna arrays remains a classical and widely adopted method, where the collective radiation of several elements enhances the overall

directivity and gain. However, at mm-wave frequencies, array implementations face significant challenges such as increased feed network losses, mutual coupling between closely spaced elements, elevated side-lobe levels, and radiation leakage at feed-line junctions—all of which deteriorate overall efficiency and performance.

In recent years, several innovative gain enhancement approaches have been explored as alternatives to traditional array networks. Among them, resonant cavity antennas (RCAs)—including Fabry–Perot cavity (FPC) and bandgap resonator antennas (BRA) based on partially reflective surfaces (PRSs) —have gained notable attention. While PRS-based antennas [15] achieve substantial gain improvements, their impedance bandwidths are limited by the spacing between the radiating surface and the PRS, typically around $\lambda_o/2$ (where λ_o is the free-space wavelength). This constraint often increases the overall height and reduces aperture efficiency.

To mitigate these issues, alternative materials and configurations have been investigated. Dielectric slabs with phase-compensating holes have been proposed [16], though their gain enhancement remains modest (~2.3 dB). Other studies have introduced epsilon-near-zero (ENZ) and mu-near-zero (MNZ) metamaterials [17] to manipulate electromagnetic (EM) wave propagation and enhance directional radiation. While these materials can achieve gain improvement in specific planes (E- or H-plane), they often narrow the impedance bandwidth and are highly sensitive to fabrication tolerances and permittivity variations near zero. Furthermore, ensuring impedance matching between the antenna and the metamaterial layer remains a critical challenge.

Another promising strategy involves near-field phase correction, which provides gain enhancement by tailoring the phase distribution across the antenna aperture without relying on bulky lenses. This approach utilizes arrays of miniature phase-delay unit cells to locally modify the phase of the transmitted wavefront [18]. Although early implementations suffered from limited aperture efficiency (≈30%) due to single-frequency phase shifters, subsequent wideband designs [19] have achieved up to 46% impedance bandwidth and 70% aperture efficiency. A recent extension of this concept employs 3D-printed dielectric superstrates with variable height profiles to achieve differential transmission delays for phase alignment [20]. Despite their wide bandwidth, these designs tend to be physically large, often exceeding $1.4\lambda_o$ in height, and achieve moderate aperture efficiencies (~46%). In summary, several gain-enhancement techniques, have shown significant potential. Nevertheless, maintaining a balanced trade-off among gain, bandwidth, efficiency, and compactness continues to be a major challenge in mm-wave antenna systems.

1.3 MIMO System

Multiple-Input Multiple-Output (MIMO) technology has become a cornerstone of modern wireless communication, driving advancements from 4G to 5G and beyond [21]-[23]. By employing multiple antennas at both the transmitter and receiver ends, MIMO enables a linear increase in channel capacity without additional bandwidth or transmitted power. It establishes multiple parallel transmission paths that enhance spectral efficiency, mitigate fading, suppress interference, and improve link reliability—particularly in rich-scattering environments. Moreover, by directing radiated energy toward intended users, MIMO enhances energy efficiency and extends coverage, a feature especially vital at mm-wave frequencies where it provides both diversity and array gain to counter high propagation losses.

In real-world conditions, multipath propagation naturally arises due to reflections from obstacles such as buildings, trees, and terrain features. Ironically, the very phenomenon of multipath propagation that once degraded wireless performance has now become indispensable for realizing the full benefits of MIMO technology. When only the LOS propagation exists, such as when the transmitter and receiver are directly aligned within a confined space, all transmitted signals traverse identical paths, experiencing the same channel conditions. In such cases, the key advantages of MIMO, namely multiplexing and diversity gains, vanish, and the system behaves like a conventional antenna array, offering only array gain. Thus, MIMO configurations can achieve spatial diversity or spatial multiplexing benefits only in environments rich in multipath propagation.

The growing demand for ubiquitous, high-quality wireless connectivity—anywhere and anytime—continues to drive innovation in MIMO architecture and deployment strategies [24-25]. Future networks must sustain exponentially increasing data traffic and achieve substantially higher area throughput, which can be realized through a combination of cell densification, spectrum expansion, and improved spectral efficiency (SE) [26]. To meet these requirements, network infrastructures are organized into two tiers: a coverage tier and a hotspot tier. The coverage tier ensures wide-area service continuity and mobility, where increasing SE is the preferred means to enhance throughput, since higher frequency operation or densification may compromise coverage. Conversely, the hotspot tier handles high-capacity, localized traffic—such as in urban and indoor environments—where densification and the utilization of mm-wave spectrum are particularly effective, aided by high-gain antenna arrays that provide significant array and beamforming gains.

In large-scale MIMO systems, the achievable SE of a single user equipment (UE) depends logarithmically on the signal-to-interference-plus-noise ratio (SINR), meaning that significant capacity gains are achieved not through individual link enhancement but by serving multiple UEs simultaneously using spatial division multiple access (SDMA). In this context, massive MIMO configurations, with a large number of base station (BS) antennas (M) serving multiple users (K) such that M/K > 1, enable near-optimal linear precoding and combining strategies that minimize interference [27-28]. As the number of antennas increases, the wireless channel exhibits channel hardening—a phenomenon where random fading effects average out, resulting in nearly deterministic channel behavior and improved reliability. Efficient utilization of such systems depends on accurate channel state information (CSI), which is most effectively acquired in time-division duplexing (TDD) operation using uplink pilots and channel reciprocity, minimizing feedback overhead.

Together, these advancements in MIMO technology—spanning spatial multiplexing, beamforming, and large-scale array processing—form the foundation of next-generation wireless systems. They not only enhance the spectral and energy efficiency of terrestrial networks but also extend seamlessly into NTN architectures, enabling high-capacity, reliable communication links across terrestrial, aerial, and satellite domains [29-30].

The general MIMO topology is shown in Figure 1.3, where *M* and *N* denote the number of transmitting and receiving antennas, respectively. In MIMO, distinct data streams are transmitted simultaneously from each antenna over the same bandwidth, enabling a potential *k*-fold increase in data rate (for *k* antennas at each end) without additional bandwidth or power.

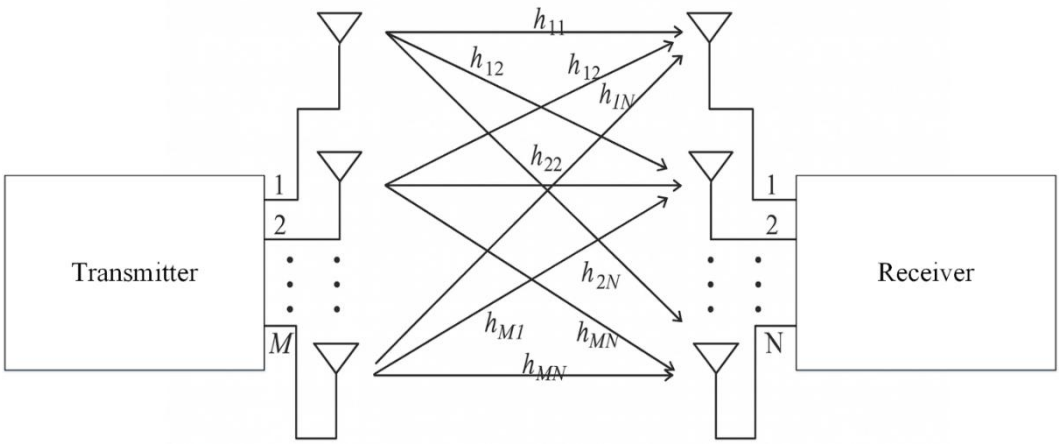

Figure 1.3: The general MIMO topology.

MIMO systems exploit rich multipath environments, where spatial diversity of the received EM fields enables multiple independent channels within the same frequency band. This

architecture maximizes channel capacity, achieving the theoretical Shannon limit, which defines the maximum achievable information rate for a given noise level [31].

A wireless channel can be represented by the following expression:

$$y = hx + n \tag{1.3}$$

where, 'y' corresponds to the vector representing the received signals, and 'x' represents the vector for the transmitted signals. The matrices 'h' and 'n' relate to the characteristics of the channel. The MIMO channel describes the communication pathway of a system comprising M_T transmitters and M_R receivers. This relationship can be concisely represented using a matrix with dimensions $M_T \times M_R$. This matrix encapsulates the interactions between the transmitters and receivers, highlighting the spatial aspects of signal propagation and reception. This representation aids in comprehending the intricate dynamics of MIMO systems.

$$H = \begin{bmatrix} h_{1,1} & h_{1,2} & \cdots & h_{1,M_T} \\ h_{2,1} & h_{2,2} & & h_{2M_T} \\ \vdots & & \ddots & \vdots \\ h_{M_R,1} & h_{M_R,2} & \cdots & h_{M_R,M_T} \end{bmatrix} \tag{1.4}$$

In Equation (1.4), the term h_{M_R,M_T} represents the channel gain that characterizes the communication link between *M*-th transmitting antenna and *N*-th receiving antenna. The configuration of the total number of receiving and transmitting antennas, denoted as *M*, plays a crucial role in defining the unique properties of the signals emitted by the transmitting system.

MIMO technology operates in three principal modes—spatial diversity, spatial multiplexing, and beamforming —each serving distinct performance objectives and operating conditions, as illustrated in Figure 1.4. In the spatial diversity mode, as depicted in Figure 1.4(a), multiple antennas transmit identical copies of the same signal to mitigate multipath fading; when one propagation path is attenuated, another ensures reliable reception, thereby enhancing link robustness in adverse channel conditions. Conversely, the spatial multiplexing mode divides the data stream into several independent sub-streams transmitted simultaneously over multiple antennas, yielding a near-linear increase in data rate without additional bandwidth or power. Figure 1.4(b) shows the spatial multiplexing mode. For instance, employing three transmit antennas can ideally triple throughput relative to a single-antenna system. However, spatial multiplexing performs optimally in high-SNR, bandwidth-limited, and high-rank channels, whereas in power-limited or low-SNR environments, beamforming becomes more advantageous by focusing radiated energy toward the intended user. This

enhances signal strength, extends coverage, and suppresses interference, a capability particularly vital in mm-wave systems where high path loss and noise-limited conditions dominate [32].

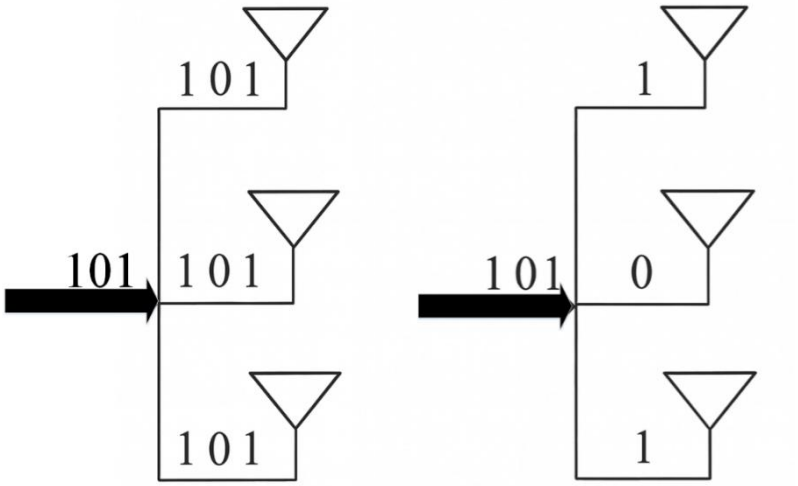

Figure 1.4: Three-port MIMO antenna system operation: (a) spatial diversity mode, and (b) spatial multiplexing mode.

In practice, next-generation mm-wave MIMO systems often operate in a hybrid regime, combining beamforming and spatial multiplexing to balance throughput and reliability. Hybrid beamforming architectures generate multiple high-gain beams to improve SNR while supporting independent data streams when adequate spatial diversity exists [33]. However, realizing such performance within compact wireless devices introduces new design challenges [34]. Modern communication platforms increasingly demand reduced antenna size without compromising efficiency; earlier devices employed large helical antennas, whereas contemporary designs utilize compact configurations such as the Planar Inverted-F Antenna (PIFA) [35]. In MIMO systems, multiple radiating elements are often co-located on a common substrate with a shared ground plane, which gives rise to mutual coupling—the undesired power interaction between adjacent antenna elements. Mutual coupling, essentially the inverse of isolation, is quantified using S-parameters, particularly the transmission coefficient S_{xy}, which measures power transfer between xth antenna and yth antenna. When the inter-element spacing is reduced below half the wavelength ($\lambda/2$), mutual coupling increases significantly, as commonly observed in compact devices such as smartphones, USB dongles, and routers [36-37]. This elevated coupling degrades both overall system efficiency and the independent performance of individual radiators. Consequently, achieving high isolation becomes critical

for maintaining MIMO effectiveness. Various mitigation strategies—targeting both port coupling and field coupling—have been proposed in literature to suppress mutual coupling and preserve the intended diversity, multiplexing, and beamforming gains of advanced MIMO antenna systems [38].

1.4 Diversity Techniques in MIMO

Diversity techniques form a foundational aspect of modern MIMO systems, enabling robust, high-capacity communication even under adverse channel conditions. A wireless communication channel is inherently prone to impairments such as fading, interference, security vulnerabilities, and reduced transmission rates. To overcome these challenges and enhance signal reliability, diversity techniques are employed. The core principle of diversity is to transmit multiple replicas of the same signal through independent propagation paths, ensuring that not all copies experience deep fading simultaneously. For a diversity system to yield significant performance gains, two essential conditions must be met: (a) the individual communication channels should exhibit low cross-correlation, and (b) the average received power from each channel should be approximately equal. Several forms of diversity can be exploited—spatial, frequency, time, polarization, and pattern diversity—each generating uncorrelated signal replicas through distinct physical mechanisms [39-40].

Antenna diversity, in particular, plays a crucial role in MIMO systems by mitigating spatial correlation between antennas and improving link robustness and throughput. In practical designs, multiple diversity techniques are often combined to achieve optimal system performance. Among these, spatial diversity—already discussed in the previous section—is one of the most effective and widely used techniques. It involves placing antennas at different spatial locations to reduce correlation between received signals by exploiting variations in the multipath environment. The required antenna separation depends on factors such as propagation conditions and the angular spread of incoming waves—typically greater than 10λ in urban outdoor environments and about 0.5λ in indoor rich-scattering conditions [41].

Frequency diversity improves reliability by transmitting identical signals across two or more frequencies separated by at least the coherence bandwidth—the frequency range over which channel fading remains correlated [42]. Although this enhances link quality, it requires additional frequency resources. Similarly, time diversity transmits identical information in distinct time slots spaced beyond the channel coherence time, ensuring that successive transmissions experience statistically independent fading.

Polarization diversity [43] provides another effective approach, particularly at mmWave frequencies where large spatial separations between antenna elements are often impractical in compact devices. It employs antennas with orthogonal polarization states—such as vertical and horizontal or left- and right-hand circular polarization—to maintain low signal correlation even when antennas are co-located. Dual-polarized antenna systems have therefore become widely adopted in mm Wave arrays. Further research has also explored utilizing multiple EM field components (three electric and three magnetic) to increase MIMO channel capacity, inspiring innovative antenna designs capable of exciting multiple field components.

At higher frequencies, pattern (or angle) diversity employs multiple antennas with distinct radiation patterns or beam orientations to receive multipath signals arriving from different directions. This technique enhances coverage and reduces correlation by capturing energy from diverse angular regions. Studies have confirmed that pattern diversity performs comparably to spatial diversity, particularly in dense urban and multipath-rich environments [44].

1.5 Performance Metrics for MIMO Antenna Systems

Conventional antenna performance is typically characterized by parameters such as bandwidth, resonance frequency, radiation pattern, gain, and efficiency. However, in the case of MIMO antenna systems, additional performance metrics are essential to fully assess system behaviour [45], [46]. These include the envelope correlation coefficient (ECC) [47], diversity gain (DG), diversity order (DO), diversity measure (DM) [48], total active reflection coefficient (TARC) [49], channel capacity loss (CCL), multiplexing efficiency (ME) [50], and mean effective gain (MEG) [51]. The following subsections describe these parameters in detail.

1.5.1 Envelope Correlation Coefficient

ECC quantifies the degree of correlation or equivalently the degree of isolation between the radiation patterns of antenna elements in a MIMO system. It reflects how much the radiation pattern of one antenna affects the other when both operate simultaneously.

ECC is calculated in Equation (1.16) using the far-field formula with cross-polarization discrimination (XPR) considered as 1 and uniform outdoor propagation environment.

$$ECC = \frac{|\oiint E_1(\theta,\phi).E_2^*(\theta,\phi)d\Omega|^2}{(\oiint|E_1(\theta,\phi)|^2 d\Omega)(\oiint|E_2(\theta,\phi)|^2 d\Omega)} \quad (1.16)$$

Here, $E_1(\theta,\phi), E_2(\theta,\phi)$ are the 3D radiation fields of the MIMO antenna when port 1 and port 2 are excited, respectively, and Ω is the solid angle.

Although accurate, this method requires complete 3D radiation data, which can be cumbersome to obtain. Therefore, ECC is more commonly calculated using S-parameters. This approach requires only measured or simulated S-parameters. For practical applications, an ECC value below 0.1 is considered acceptable for wireless systems.

1.5.2 Diversity Gain, Diversity Order, and Diversity Measure

The diversity gain (DG) is calculated in Equation (1.17). For the highest ECC across both bands of operation, the calculated DG exceeds 9.99 dB.

$$DG = 10\sqrt{1 - |ECC|^2} \tag{1.17}$$

The diversity performance of MIMO antennas, however, cannot be evaluated holistically using the terms ECC and DG. So, diversity order (DO) and diversity measure (DM), as suggested in Ref. [48], are often separately investigated using the antenna correlation coefficient (*ACC*) matrix. Their equations are depicted below:

$$\mathrm{DO} \leq DO_{T_X} \times DO_{R_X} = \mathrm{rank}(ACC_{T_X}) \times \mathrm{rank}(ACC_{R_X}) \tag{1.18}$$

$$\mathrm{DM} = \frac{Q^2}{\sum_{j=0}^{Q}\sum_{i=0}^{Q}\left|ACC_{R_X}(i,j)\right|^2} \times \frac{P^2}{\sum_{j=0}^{P}\sum_{i=0}^{P}\left|ACC_{T_X}(i,j)\right|^2} \tag{1.19}$$

where, $\mathrm{rank}(ACC_{T_X})$ and $\mathrm{rank}(ACC_{R_X})$ are the ranks of the respective transmitter and receiver ACC matrices. In case of single user (SU) MIMO implementation, ACC_{T_X}=ACC_{R_X}. The rank of ACC matrix (a hermitian matrix of full rank) is two and thus, the diversity order is bounded by 4. In any single user (*P*×*Q)* MIMO system with channels considered to be independent and identically Rayleigh distributed, the diversity measure can be derived through ACC matrices at transmitter and receiver, using Equation (1.19). The ACC matrix for 2×2 MIMO antenna system is given by

$$\overline{ACC} \equiv \begin{bmatrix} 1 & ACC_{12} \\ ACC_{12}^{*} & 1 \end{bmatrix}. \tag{1.20}$$

The magnitude of the *ACC*, in case of a two port MIMO antenna, is approximately equal to ECC, i.e. $ACC_{(i,j)} = ECC_{(i,j)}$. Further, the percentage diversity gain reduction (PDGR) is calculated as:

$$PGDR = \frac{(DM - DO)}{DO} * 100 \tag{1.21}$$

1.5.3 Total Active Reflection Coefficient

Mutual coupling between neighboring antenna elements is a common concern in MIMO antenna systems, as it can impact both the operating efficiency and bandwidth when transmitting simultaneously. While S-parameters are often employed to predict system behavior, they may not provide entirely accurate results. To overcome this, TARC is often used as a performance metric. The perceived return loss of the MIMO antenna system is represented by TARC, which is the square root of the ratio of the entire reflected power to the entire incident power. $TARC_{1,2,3}$ for a three port MIMO system can be calculated in Equation (1.22):

$$TARC_{1,2,3} = \frac{\sqrt{\left|S_{11}+S_{12}e^{j\theta^1}+S_{13}e^{j\theta^2}\right|^2+\left|S_{21}+S_{22}e^{j\theta^1}+S_{23}e^{j\theta^2}\right|^2+\left|S_{31}+S_{32}e^{j\theta^1}+S_{33}e^{j\theta^2}\right|^2}}{\sqrt{2}} \quad (1.22)$$

Typically, a TARC value of less than -10 dB is necessary to achieve the desired accuracy.

1.5.4 Channel Capacity Loss

The correlation between the antennas in a MIMO configuration occurring due to their physical placement, mutual coupling, and polarization effect, leads to an ill-conditioned channel matrix (i.e. reduction in the rank of the matrix). This results in a decrease in the number of independent spatial streams that can be transmitted, which in turn reduces the channel capacity. The effect is known as correlation-induced channel capacity loss (CCL). An acceptable value for CCL is below 0.5 bits/s/Hz. For high SNR, it can be calculated as,

$$CCL_{\mathrm{ij}} = -log_2\, det[\Psi_{\mathrm{r}}] = -log_2\, det([\,\Psi_{\mathrm{ii}}\ \ \Psi_{\mathrm{ij}}\,;\ \Psi_{\mathrm{ji}}\ \ \Psi_{\mathrm{jj}}\,]) \quad (1.23)$$

where Ψ_{r} is called the correlation matrix between a pair of antennas in a MIMO system. The elements of the correlation matrix are calculated using *S*-Parameter values, where:

$$\Psi_{\mathrm{ii}} = 1 - \left(|S_{\mathrm{ii}}|^2 + \left|S_{\mathrm{ij}}\right|^2\right), \quad \Psi_{\mathrm{ij}} = -(S_{\mathrm{ii}} * S_{\mathrm{ji}} + S_{\mathrm{ji}} * S_{\mathrm{jj}}) \quad (1.24)$$

1.5.5 Multiplexing Efficiency

Equation (1.25) can be used to compute the multiplexing efficiency (ME), a power-related parameter for high SNR scenario spatial multiplexing mode in 2×2 MIMO systems,

$$ME = \sqrt{\left(1-|r|^2\right)\eta_1\eta_2} \quad (1.25)$$

where, η_1 and η_2 are the efficiencies of port 1 and port 2, which are same in the present case and *r* is complex ECC. The desired value of ME should be close to 0 dB.

1.5.6 Mean Effective Gain

Mean effective gain (MEG) is another significant parameter for diversity power analysis as it measures the relative mean power levels among the signals received from each antenna. For the *i*th Port of a 2 Port MIMO Antenna, MEG can be determined using Equation (1.26). For a good diversity performance, the ratio of MEG of the two ports (1 and 2) should fulfill the criteria as mentioned in Equation (1.27).

$$MEG_i = 0.5 * \left[1 - \sum_{j=1}^{2} \left\|S_{ij}\right\|^2\right] \tag{1.26}$$

$$\left|\frac{MEG_1}{MEG_2}\right| < \pm 3\ dB \tag{1.27}$$

1.6 Literature Survey

This thesis is dedicated to the systematic study and development of various mm-wave antenna configurations designed for both terrestrial networks (TN) and non-terrestrial networks (NTN). The initial sections focus on compact printed MIMO antennas for terrestrial 5G applications, encompassing several design approaches such as split ring resonator (SRR) and complementary split ring resonator (CSRR) loading, artificial magnetic conductor (AMC) integration, Fabry–Perot cavity-based structures, and antennas exhibiting pattern and polarization diversity. Subsequently, the research extends toward the design of high-gain reflectarray antenna for NTN scenarios, targeting satellite and aerial communication platforms operating in the mm-wave spectrum. A comprehensive literature review has been conducted across these domains to establish the current state of the art and identify the research gaps addressed in this work.

1.6.1 Antennas for Millimeter-wave Terrestrial Network

The rapid evolution of mm-wave communication technologies for 5G and beyond systems has driven significant research interest in the design of compact, high-performance MIMO antennas. Antennas operating in the mm-wave spectrum must satisfy stringent design constraints, including compact size, wide bandwidth, high gain, strong isolation, and low mutual coupling. However, as antenna elements in a MIMO are placed in close proximity to achieve compactness, mutual coupling tends to increase, thereby adversely affecting isolation and spatial correlation, which are critical to maintaining MIMO performance. Consequently,

numerous studies have explored diverse strategies to enhance gain, reduce coupling, and ensure reliable operation in both on-body and off-body communication scenarios.

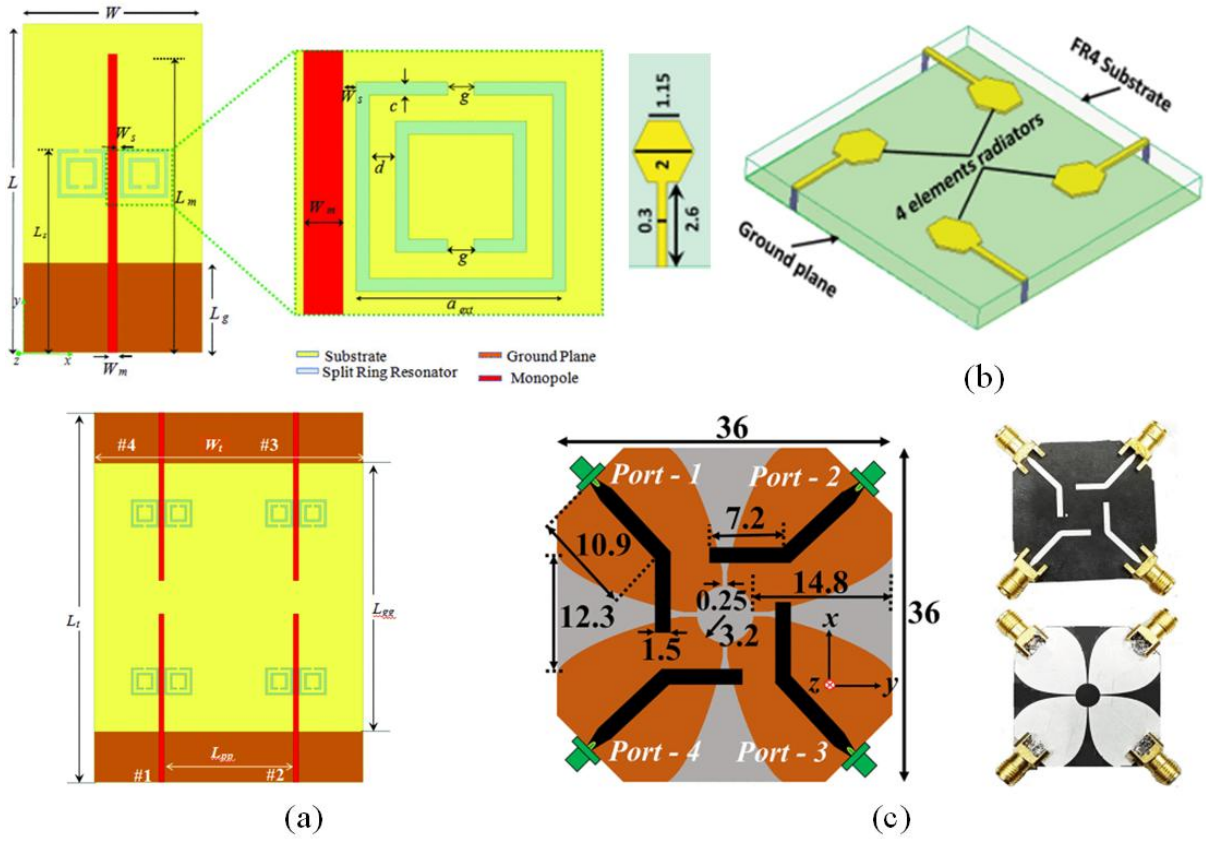

Figure 1.5: Millimeter-wave MIMO antennas using: (a) SRR-loaded printed monopoles for dual-band operation at 28 GHz and 38 GHz [53], (b) four-element MIMO antenna operating at 35 GHz with high isolation and efficiency [54], and (c) Vivaldi MIMO antenna employing bi-axial anisotropic metasurface loading for enhanced end-fire gain and pattern diversity [55].

Early work in mm-wave MIMO antenna design primarily focuses on compact planar geometries aimed at achieving miniaturization and enhanced isolation for 5G applications. In [52], a compact ultra-wideband (UWB) microstrip patch MIMO antenna operating between 24.5–32.2 GHz is introduced; while the structure offers a reduced footprint, it exhibits a gradual decline in gain with increasing frequency, limiting its high-band performance. As shown in Figure 1.5(a) and described in [53], a four-element MIMO configuration employing SRR-loaded printed monopoles is proposed to realize dual-band operation at 28 GHz and 38 GHz. The SRR loading effectively enables multiple resonances and improves impedance matching; however, the side-by-side element placement results in high mutual coupling, which degrades isolation and overall MIMO performance. As shown in Figure 1.5(b) and reported in [54], a compact hexagonal patch-based four-element MIMO antenna operating at 35 GHz is presented,

achieving excellent isolation (> 25 dB), low envelope correlation coefficient (ECC < 0.02), and high radiation efficiency (87%) within a very compact footprint of 12.5 mm × 12.5 mm × 0.8 mm. Despite these merits, the design remains limited to single-band operation, lacking coverage of the widely adopted 28 GHz and 38 GHz 5G bands. Subsequently, as shown in Figure 1.5(c) and detailed in [55], a Vivaldi-based MIMO antenna incorporating a bi-axial anisotropic metasurface is presented to correct nonuniform aperture phase errors and enhance end-fire radiation. The proposed structure achieves 73% gain improvement at 28 GHz, maintains isolation above 15 dB, and exhibits ECC below 0.2, thereby demonstrating strong potential for mm-wave applications requiring both gain enhancement and pattern stability.

For wearable and wireless body area network (WBAN) applications, antenna designs require not only high gain and wide bandwidth but also safety compliance to minimize EM exposure to human tissues. Microstrip antennas with partial or defected ground planes are widely used to enhance impedance bandwidth while maintaining a low profile and lightweight structure. However, such configurations often suffer from back radiation, which reduces gain and poses potential safety risks. Traditionally, metallic reflectors (PEC surfaces) placed at approximately $0.25\lambda_0$ from the antenna are used to suppress this back-lobe radiation, but they significantly increase the overall profile without offering additional performance benefits.

To overcome these limitations, AMC surfaces have emerged as an effective alternative, offering unidirectional radiation, gain enhancement, and compact integration. In [56], as shown in Figure 1.6(a), a V-shaped patch MIMO antenna backed by an AMC reflector achieves substantial gain improvement and a unidirectional beam, while a printed dipole antenna backed with a rhomboid AMC is proposed in [57] and depicted in Figure 1.6(b) for vehicular wireless communication. The geometry is analyzed both with and without the AMC structure, and a performance enhancement is observed in terms of a 42.3% reduction in size, an 8.4 dB gain improvement, and the realization of a unidirectional radiation pattern. Although these studies demonstrate effective back radiation suppression and improved safety performance, they primarily operate at sub-6 GHz frequencies with relatively narrow bandwidths and large geometries, leaving considerable scope for improvement in the mm-wave range.

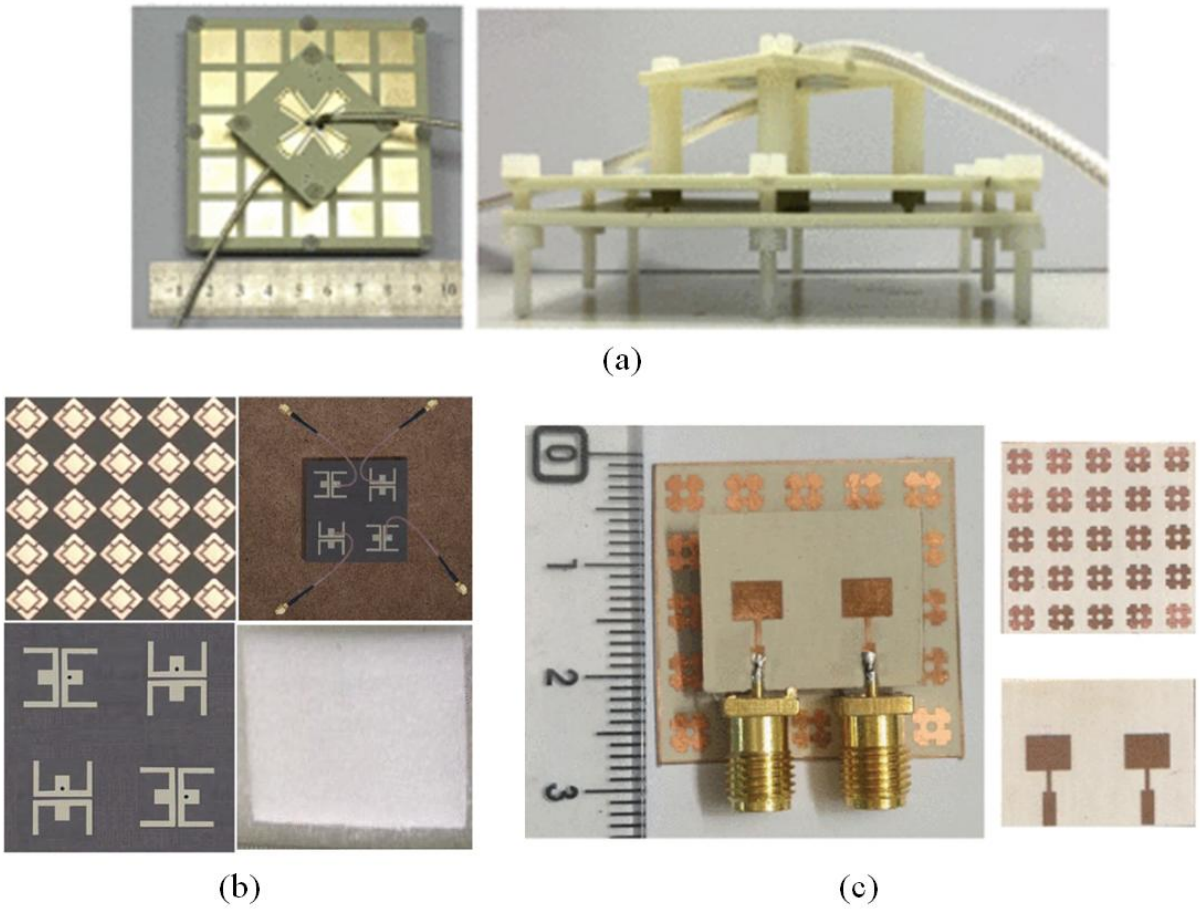

Figure 1.6: Millimeter-wave MIMO antennas using: (a) split-ring resonator (SRR)-loaded printed monopoles for dual-band operation at 28 GHz and 38 GHz [56], (b) four-element MIMO antenna operating at 35 GHz with high isolation and efficiency [57], and (c) Vivaldi MIMO antenna employing bi-axial anisotropic metasurface loading for enhanced end-fire gain and pattern diversity [58].

Recent efforts extend AMC-backed and electromagnetic bandgap (EBG)-based antenna concepts to mm-wave frequencies. Notably, the inclusion of an AMC layer improves the gain by 1.9 dB and reduces backside radiation by 8 dB, while lowering the power density from 200 W/m² to 10 W/m² in [58], as shown in Figure 1.6(c). However, the operational band remains comparatively narrow and centered around 24 GHz. Despite these advances, most designs lack MIMO configurations and omit on-body safety evaluations—an essential requirement for wearable applications. Consequently, the literature highlights a clear gap in compact mm-wave MIMO antenna designs that simultaneously achieve high gain, wideband performance, and safety compliance suitable for 5G WBAN systems.

To enhance inter-element isolation in mm-wave MIMO systems, several decoupling strategies have been reported, including the use of sine corrugations [59], SRR-based

metasurfaces [60], parasitic elements [61], slow-wave structures [62], EBG geometries [63], and neutralization lines [64]. Although these methods effectively suppress surface-wave coupling and improve isolation, they typically increase structural complexity, fabrication difficulty, and overall footprint. Consequently, diversity-based approaches—encompassing spatial, frequency, polarization, and pattern diversity—have emerged as practical alternatives for achieving decorrelated radiation characteristics in compact multi-antenna systems.

Antennas employing pattern diversity can efficiently capture signals from multiple directions, improving link reliability in multipath-rich environments. For instance, [65] demonstrates the use of in-phase and out-of-phase excitations to achieve pattern diversity in closely spaced elements, while [66], as shown in Figure 1.7(b), introduces a pattern-diversity-based decoupling technique that manipulates the electrical lengths of radiators to tailor their radiation patterns and enhance isolation without additional decoupling networks.

Similarly, the polarization diversity that utilizes orthogonal linear and circular polarizations (LP/CP) has been widely explored to overcome polarization mismatch, reduce correlation, and improve channel capacity. In [67], a dual-band MIMO antenna achieves complementary LP responses, while [68], as shown in Figure 1.7(a), presents a dielectric resonator-based circularly polarized MIMO antenna exhibiting polarization diversity and improved isolation through orthogonal feed excitation.

Recent developments have extended these concepts into the mm-wave domain. For example, [69] and [70] explore polarization-agile configurations, whereas [71], as shown in Figure 1.7(c), demonstrates a series-slot-fed circularly polarized MIMO array providing CP diversity at 28 GHz for 5G indoor applications. Likewise, [72], as shown in Figure 1.7(d), reports a high-gain, highly isolated mm-wave diversity MIMO array that employs orthogonal element placement and a decoupling metallic strip to achieve strong isolation (> 40 dB).

Despite these advancements, most designs emphasize either pattern diversity or polarization diversity independently. To date, no reported mm-wave MIMO antenna simultaneously integrates both pattern and polarization diversity within a single architecture—highlighting a key research gap addressed in this thesis.

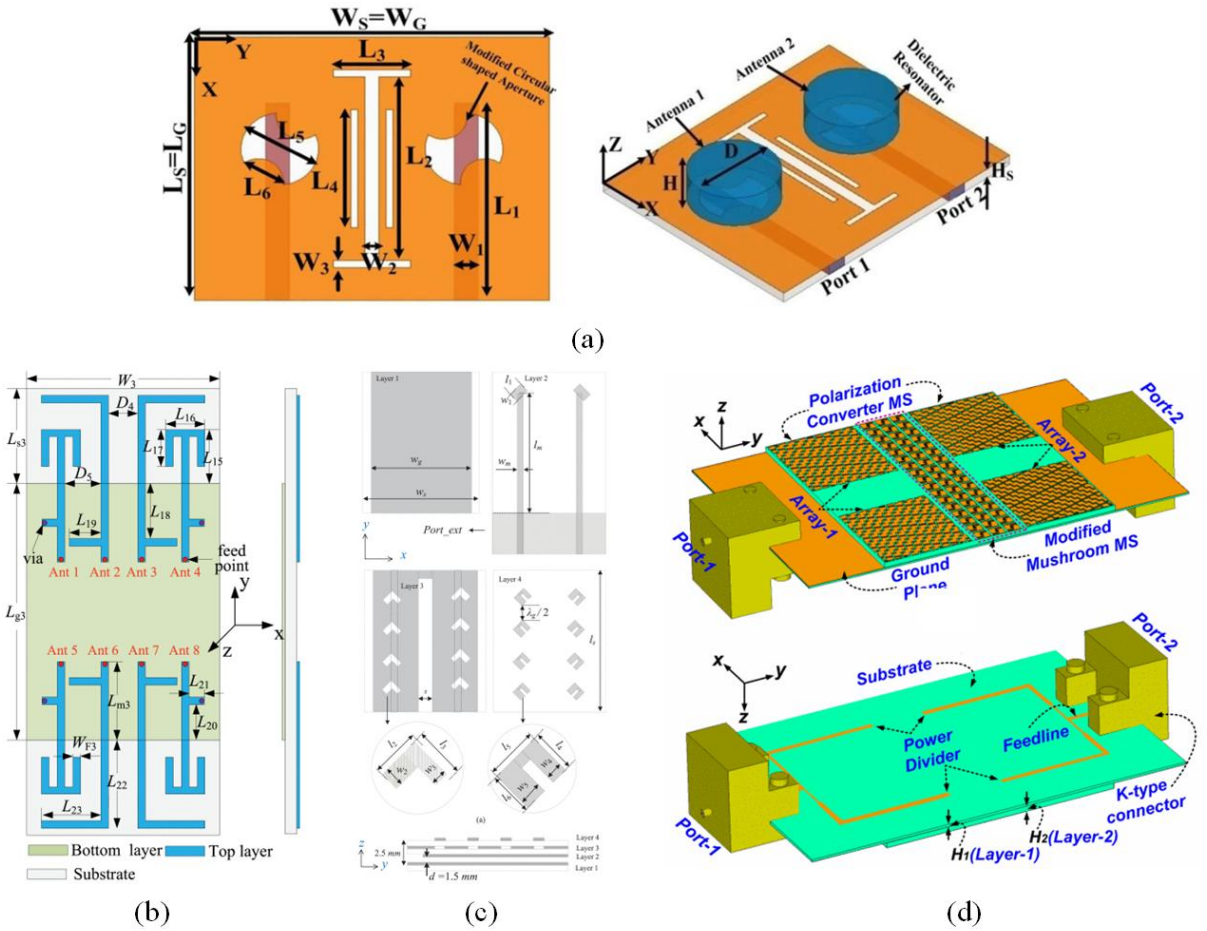

Figure 1.7: Inter-element isolation and diversity enhancement in MIMO antennas using: (a) dielectric resonator-based circularly polarized MIMO antenna employing a defected ground structure (DGS) for polarization diversity and improved isolation [68], (b) Pattern-diversity-based MIMO antenna employing electrical length modification of radiators to manipulate radiation patterns for improved isolation [66], (c) series-slot-fed circularly polarized MIMO array providing circular polarization diversity for 28 GHz 5G indoor applications [71], and (d) Millimetre-wave diversity MIMO array employing orthogonal element placement and decoupling techniques for 5G systems [72].

Fabry–Perot (FP) cavity-based designs have gained significant attention for achieving high gain and directivity enhancement in mm-wave antennas. The idea, originally derived from the optical Fabry–Perot resonator introduced in the late 19th century, was first adapted to the microwave domain by Trentini in 1956 [73]. In his seminal work, Trentini demonstrated that placing a partially reflecting surface (PRS) above a radiating source, with a ground plane beneath, could form a resonant cavity that enhanced radiation directivity through multiple reflections and constructive interference. This early architecture—often referred to as a

resonant cavity antenna (RCA) or reflection (reflex) cavity antenna—featured a planar cavity bounded by a metallic ground plane and a PRS, excited by simple sources such as coaxial probes, microstrip patches, or ground slots. The vertical axis defined the broadside radiation direction, while the corresponding plane represented the antenna aperture at air–PRS interface.

FPCAs offered a versatile and elegant solution to the long-standing challenge of realizing highly directive radiation with a low-profile structure. Their capacity to produce narrow pencil beams or conical scanned beams has led to widespread application in both terrestrial and satellite communication systems [74]. The high directivity of FPCA radiation can be explained using ray optics, as originally formulated by Trentini and later expanded in subsequent analytical studies [75, 76]. Alternative EM models were developed in the 1980s, such as the equivalent circuit approach proposed by Alexopoulos and Jackson [77, 78], which used network representations and the reciprocity theorem to relate cavity resonance to impedance and radiation behavior. A further refinement involved interpreting FPCAs as open waveguides supporting leaky modes, providing deeper insight into the mechanism of directive radiation and its frequency-dependent characteristics.

With advances in printed-circuit technologies, FP cavity antennas evolved rapidly from bulky metallic reflectors to planar printed configurations in the late 20th and early 21st centuries. These printed FPCAs employed frequency-selective surfaces (FSS) and partially reflective surfaces (PRS) as controllable superstrates, enabling designers to tailor reflection phase and amplitude for bandwidth enhancement, beam shaping, and polarization control. The introduction of metasurface- and metamaterial-based PRS layers further expanded their design flexibility, allowing ultrathin, conformal, and broadband realizations compatible with modern high-frequency systems.

At mm-wave frequencies, Fabry–Perot cavity antennas (FPCAs) have emerged as a promising class of high-gain, wideband, and low-profile radiators, offering an attractive solution for modern 5G and beyond wireless systems. The FPCA principle relies on forming a resonant cavity by positioning a PRS or metasurface at approximately half a wavelength above a primary radiator, allowing constructive interference between the direct and reflected waves to enhance directivity. A variety of PRS-based and metamaterial-assisted configurations have been reported in literature to improve gain, bandwidth, or/and polarization performance. In [79], as illustrated in Figure 1.8(a), a dual-layer FSS–based PRS integrated with a ridge-gap waveguide-fed slot antenna operating at 60 GHz achieved a 16.8 dBi gain and 12.5% 3-dB gain bandwidth through effective surface-wave suppression and controlled phase gradient. In [80],

as shown in Figure 1.8(b), a polarization-conversion metasurface (MS) superstrate was designed to realize dual circular polarizations, converting orthogonal linear polarizations into RHCP and LHCP waves using a compact single-layer structure with high reflectivity and a low profile. Similarly, Figure 1.8(c) presented a chessboard-arranged metamaterial superstrate (CAMS) that simultaneously enhanced gain and reduced radar cross section (RCS), achieving a 4.9 dB gain improvement at 10.8 GHz and up to 39.4 dB RCS reduction across 9.6–16.9 GHz [81]. Furthermore, [82] proposed a high-isolation Ku-band FP antenna array employing tandem circular parasitic patches (TCPPs) with a radial-gradient PRS and a double-dumbbell-shaped slot radiator, as presented in Figure 1.8(d), attaining a 21.6 dBi gain, 22.8% fractional bandwidth, and isolation greater than 40 dB.

Beyond these, [83] reported a four-port FP-based antenna spanning 12.87–45.02 GHz, achieving ultra-wide bandwidth at the expense of higher RF front-end complexity and filtering requirements, while [84] employed a transmission-type FSS-printed superstrate to improve the MIMO isolation by 6–12 dB, though the gain improvement was limited to 1.5 dB with a 10° beam tilt. Despite the significant progress in FPCA development, most existing structures rely on thick, high-permittivity substrates and multilayer superstrates, increasing fabrication complexity, cost, and overall profile. Consequently, ongoing research continues to explore compact, and lightweight FP-based antenna architectures capable of maintaining high gain, wide bandwidth, and polarization agility for emerging mm-wave terrestrial and non-terrestrial network applications.

Overall, the literature reveals a steady evolution of mm-wave antenna design from compact SRR/CSRR-loaded monopoles and AMC-backed structures to high-gain FP cavity-based and diversity-enabled MIMO configurations. Despite significant progress, major challenges persist—particularly in achieving wideband dual-frequency operation, compactness, low correlation, and polarization-pattern diversity simultaneously in the mm-wave range. These gaps form the central motivation for the terrestrial antenna developments presented in this thesis, which progressively advance from compact dual-band SRR/CSRR-based MIMO antennas to high-gain AMC/Fabry–Perot cavity and polarization-diverse architectures optimized for 5G mm-wave terrestrial networks.

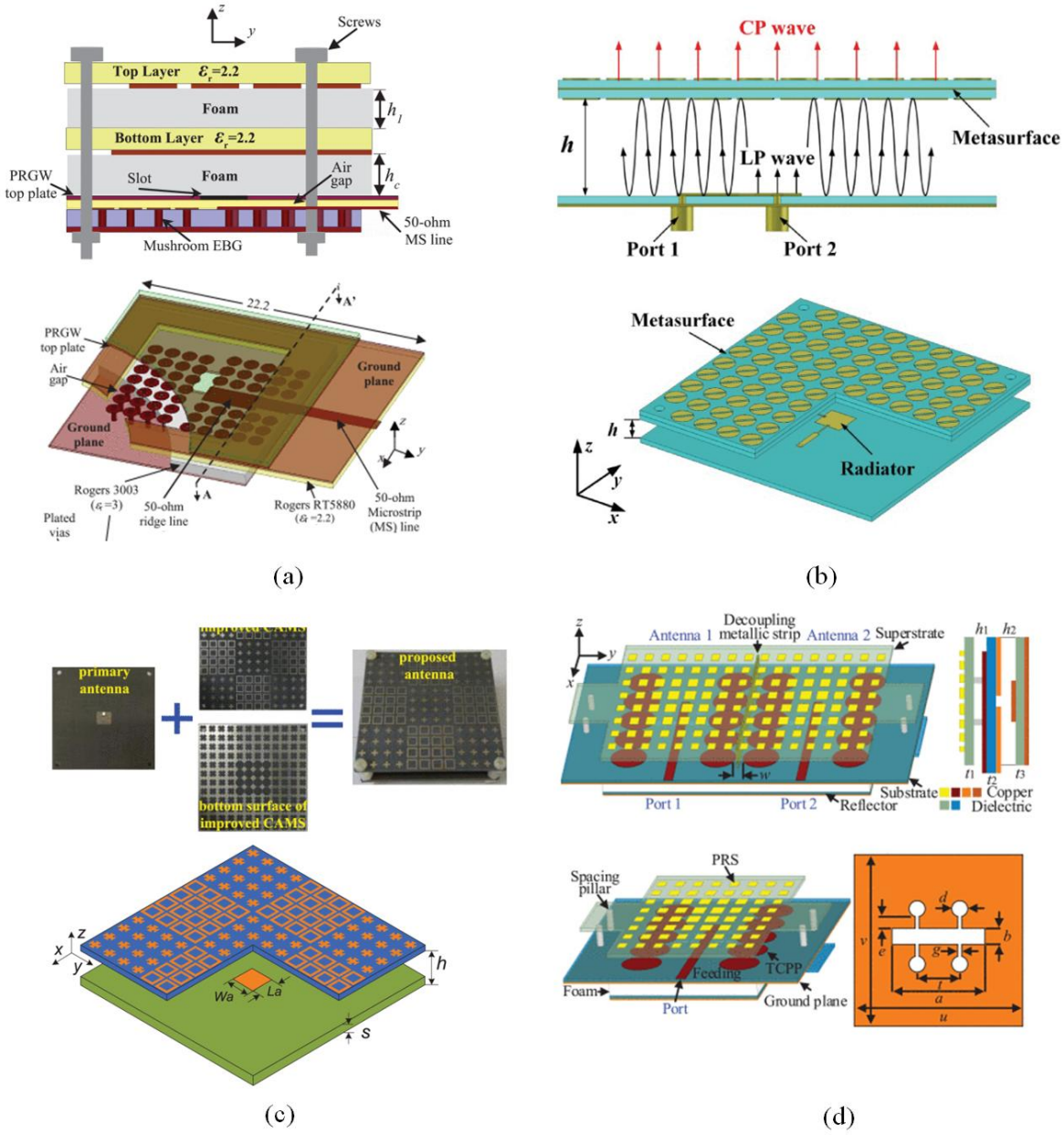

Figure 1.8: Fabry–Perot cavity antennas using: (a) dual-layer printed FSS-based superstrate integrated with a ridge-gap waveguide-fed slot radiator [79], (b) polarization-conversion metasurface (MS) superstrate enabling dual circular polarization [80], (c) chessboard-arranged metamaterial superstrate (CAMS) for simultaneous gain enhancement and RCS reduction [81], and (d) high-isolation Ku-band antenna array employing tandem circular parasitic patches (TCPPs) with a radial-gradient partially reflective surface (PRS) [82].

1.6.2 Antennas for Millimeter Wave Non-Terrestrial Network

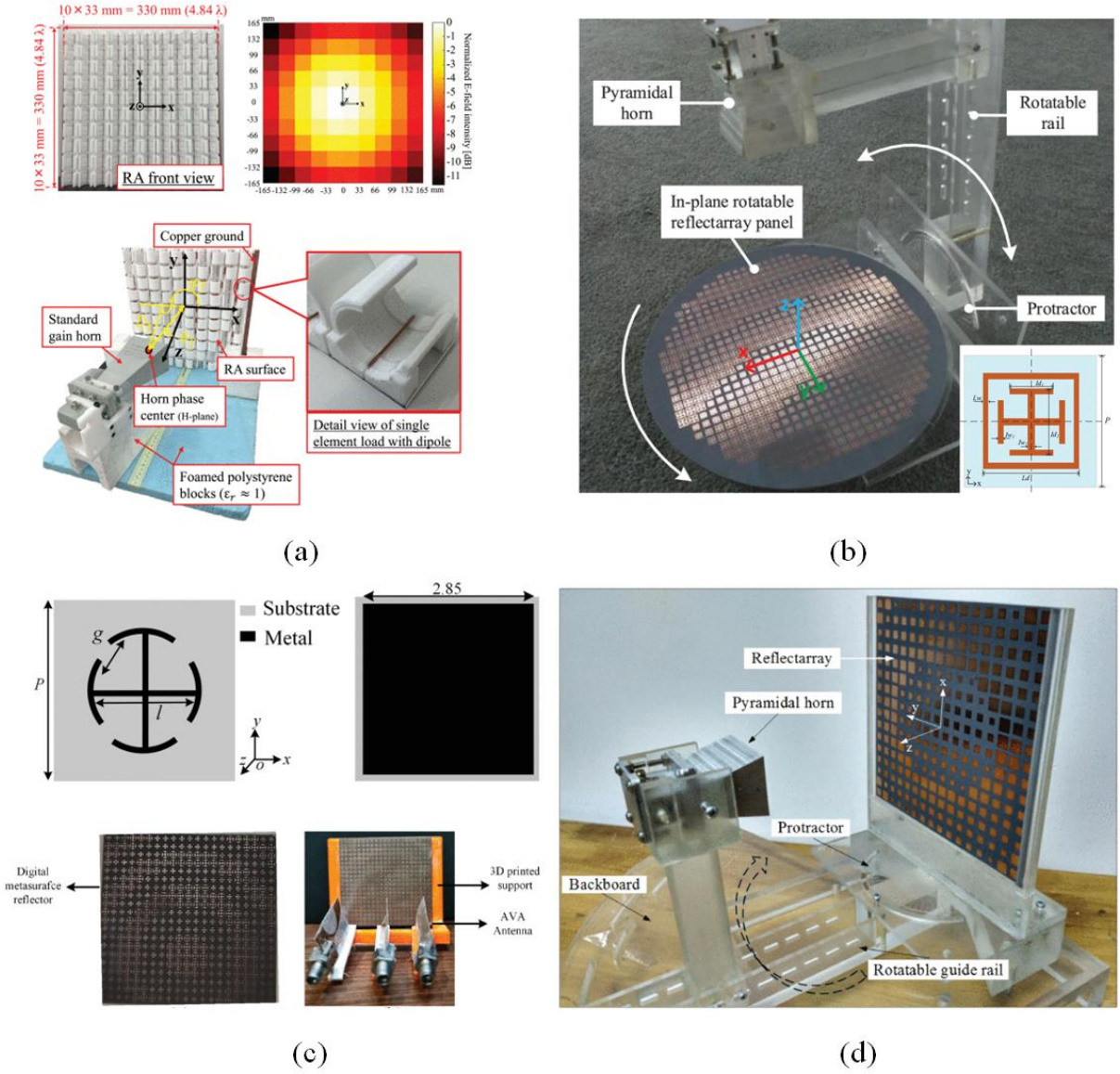

Figure 1.9: Beam-steerable reflectarray antennas using: (a) 2-bit 3D-printed reflectarray employing cylindrical rotation-based phase-tunable elements for mechanical beam scanning [86], (b) one-dimensional mechanically steerable reflectarray achieving ±70° scan coverage [87], (c) digital metasurface reflectarray with extreme offset illumination enabling rapid beam switching for satellite communication [88], and (d) wide-angle mechanically beam-scanning reflectarray utilizing multi-beam phase matching for enhanced scan performance [89].

Reflectarray (RA) antennas have emerged as one of the most promising solutions for Non-Terrestrial Network (NTN) platforms, owing to their unique ability to combine the high-gain characteristics of traditional parabolic reflectors with the compactness and integrability of planar arrays. In contrast to conventional dish antennas, which rely on mechanically curved

surfaces, a reflectarray employs a planar or quasi-planar surface populated with sub-wavelength resonant elements, each introducing a controlled phase shift to the reflected EM wave. By tailoring the reflection phase across the array aperture, the reflected beam can be precisely directed toward a desired direction or focal point. This configuration provides several advantages, including lightweight construction, low profile, ease of fabrication, and conformability to curved or compact platforms, making it highly attractive for spaceborne, airborne, and high-altitude communication systems such as LEO and GEO satellites, high-altitude platforms (HAPs), and unmanned aerial vehicles (UAVs) [85]. Reflectarrays can be broadly classified into two categories based on their beam-control mechanism: electronically reconfigurable reflectarrays (ERRAs) and mechanically steerable reflectarrays (MSRAs).

Electronically reconfigurable designs employ active phase-tuning components such as p–i–n diodes, varactor diodes, MEMS switches, or liquid crystals embedded within each unit cell to dynamically control the reflection phase. These configurations enable real-time beam steering without physically altering the antenna orientation, making them ideal for adaptive satellite communication and beam-tracking applications. However, at mm-wave frequencies, these components introduce significant insertion losses, nonlinear behavior, and thermal instability, all of which degrade overall aperture efficiency and reliability [90]. Moreover, such electronically controlled reflectarrays demand multilayer substrates to accommodate DC bias networks, shorting vias, and RF isolation layers, thereby increasing fabrication complexity and cost. This limits their scalability and practical use in large-aperture arrays intended for high-power NTN missions.

Despite these advancements, most mechanically reconfigurable reflectarrays still face several performance limitations. The achievable scan range is typically constrained by feed geometry and array aperture size; excessive feed displacement leads to gain degradation and increased phase errors across the aperture. Moreover, quantization loss—arising from the finite number of discrete phase states (often 1-, 2-, or 3-bit unit cells)—reduces aperture efficiency and elevates sidelobe levels, particularly in large-aperture or wide-scan systems. Furthermore, designs employing dielectric-based unit cells often suffer from narrow operational bandwidths, increased mutual coupling, and manufacturing tolerances that become critical at mm-wave frequencies. Collectively, these challenges limit their adaptability for next-generation NTN communication systems, which demand high gain, wide bandwidth, beam agility, and low-profile integration.

Recent research has therefore shifted toward hybrid or intelligent reflectarray architectures that merge the advantages of mechanical robustness and electronic reconfigurability. Phase-gradient metasurface reflectarrays and liquid-crystal-based tunable elements have shown potential for achieving wider scanning ranges with reduced loss and improved linearity [90]-[91]. Additionally, 3-bit or higher quantized reflectarrays, as well as designs based on dielectric resonator and metallic ring elements, have been explored to enhance phase resolution and aperture efficiency without compromising manufacturability. Nevertheless, mechanical beam steering remains highly attractive for NTN deployment, especially in cost-sensitive, high-frequency scenarios where low power consumption, structural simplicity, and environmental robustness are prioritized over ultra-fast beam agility.

Thus, reflectarray antennas provide an efficient, compact, and scalable solution for non-terrestrial 5G and beyond communication systems. Their inherent capability to deliver high gain, beam steering, and lightweight integration makes them ideal candidates for satellite and aerial communication payloads. However, achieving wideband, high-efficiency, and low-loss beam control at mm-wave frequencies continues to pose significant challenges—particularly due to quantization losses, fabrication tolerances, and limited scan dynamics. Addressing these issues through 3-bit or above phase quantization, low-loss unit cell design, and mechanically reconfigurable architectures represents a key research direction, forming the foundation of the present work on Ka-band beam-switchable reflectarray antennas for NTN applications.

1.7 Motivation

The current research landscape thus reveals several unresolved challenges:

1. Achieving wideband, dual-band, or multiband operation in compact mm-wave MIMO antennas without sacrificing gain or isolation.
2. Realizing simultaneous polarization and pattern diversity to ensure robust performance in multipath and dynamic propagation environments.
3. Developing high-gain, beam-steerable antennas that can bridge terrestrial and non-terrestrial domains, enabling seamless integration within emerging 5G frameworks.

Motivated by these critical gaps, this thesis seeks to develop a progressive antenna design framework that evolves from compact dual-band MIMO systems for terrestrial 5G communication to wideband high-gain reflectarray antennas suitable for NTN deployment. Each successive design builds upon the limitations of the preceding work—progressing from SRR/CSRR-loaded compact antennas to AMC-backed and FP-cavity high-gain configurations,

and culminating in a 3-bit quantized beam-steerable reflectarray optimized for Ka-band NTN applications. This systematic progression not only demonstrates technological innovation but also aligns with the overarching goal of creating a unified antenna architecture capable of addressing the connectivity demands of both terrestrial and non-terrestrial communication networks in the forthcoming B5G and 6G eras.

1.8 Objective of Thesis

This thesis aims to address the limitations identified in the existing literature by systematically developing a sequence of mm-wave antenna architectures that evolve from compact terrestrial MIMO systems to high-gain reflectarray antenna for NTN applications. The emphasis is placed on achieving compactness, high isolation, wide bandwidth, dual/polarization diversity, and beam-steering capability across successive antenna designs.

Accordingly, the detailed objectives of this thesis are as follows:

1. To design and analyze dual band mm wave MIMO antennas employing SRR and CSRR geometries to achieve compactness, dual-band operation (28 GHz and 38 GHz), and low envelope correlation coefficient (ECC). The focus is on enhancing inter-element isolation and radiation characteristics suitable for 5G terrestrial communication.
2. To design and investigate AMC backed MIMO antennas for WBAN operating in the mm-wave band. The objective is to improve antenna gain and front-to-back ratio while ensuring radiation safety and compact form factor without compromising efficiency.
3. To develop a high-gain dual-band CSRR-loaded MIMO antenna array optimized for 28 GHz and 38 GHz applications, emphasizing improved aperture efficiency and reduced mutual coupling. The goal is to enhance broadside radiation and minimize performance degradation due to mutual coupling.
4. To design and realize Fabry Perot cavity backed MIMO antennas that leverage the PRS for directivity and aperture efficiency enhancement. The focus is on achieving wide impedance bandwidth, high gain, and low-profile configurations suitable for compact mm-wave 5G front-ends.
5. To propose and demonstrate a five-port MIMO antenna system integrating polarization and pattern diversity, enabling simultaneous transmission of Right-Hand Circularly Polarized (RHCP), Left-Hand Circularly Polarized (LHCP), and Linearly Polarized (LP) waves. This design aims to enhance link reliability and multipath resilience in dynamic 5G terrestrial environments.

6. To design and implement a 3-bit quantized beam-steerable reflectarray antenna operating in the Ka-band (26.5–40 GHz) for NTN such as LEO/GEO satellites, HAPs, and UAVs. The objective is to achieve high gain, wideband performance, and low-profile beam steering using a mechanically reconfigurable architecture, offering a low-cost and energy-efficient alternative to active phased arrays.

Collectively, these objectives aim to establish a unified antenna design framework that bridges terrestrial and non-terrestrial communication domains, contributing to the realization of 5G/6G wireless ecosystems with compact, high-performance, and scalable antenna technologies.

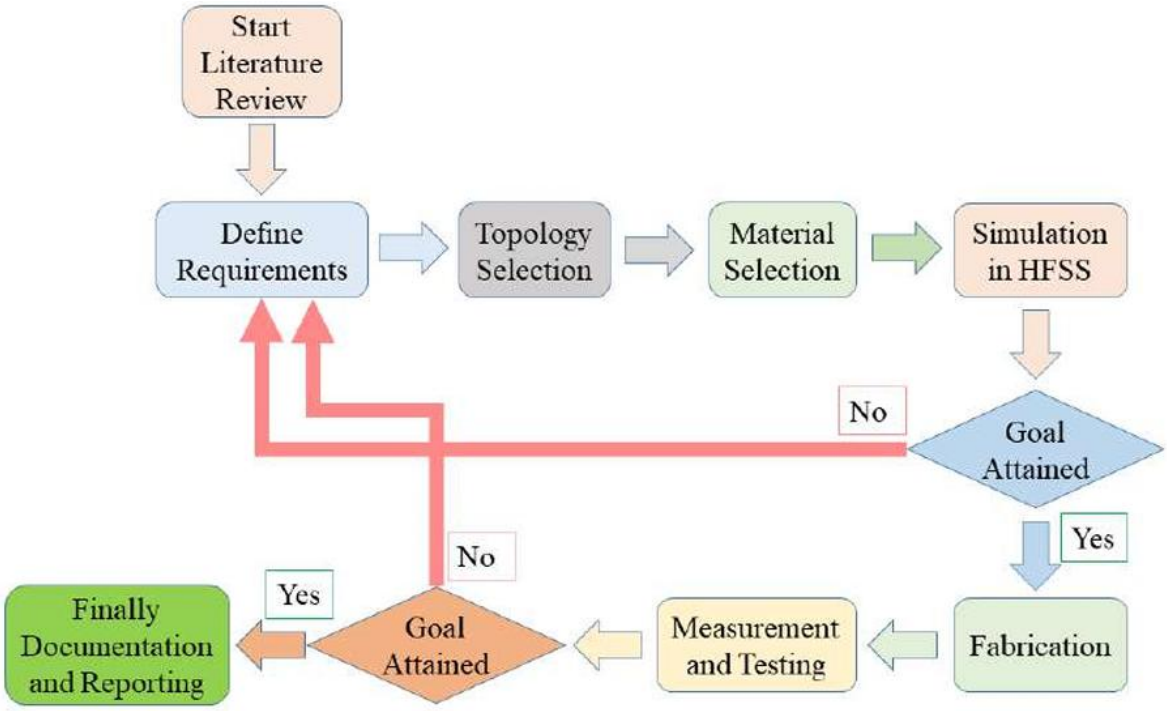

Figure 1.10: Research methodology flow diagram.

1.9 Methodology

The overall methodology adopted in this thesis for the systematic design, simulation, fabrication, and validation of various mm-wave antennas is illustrated in Figure 1.10. Each stage is designed to ensure a rigorous and iterative workflow that bridges theoretical design concepts with practical implementation for both terrestrial and non-terrestrial 5G communication applications. The steps are outlined below:

1. Comprehensive Literature Review: A detailed review of existing works was undertaken to establish a strong foundation for the research. The review focused on mm-wave

antennas—including MIMO, Fabry–Perot cavity, AMC-backed, and Reflectarray architectures—to understand their evolution, identify design trends, and recognize performance limitations related to gain, bandwidth, isolation, and reconfigurability. This step helped formulate the research problem and define the thesis objectives.

2. Definition of Design Requirements: Based on the research objectives, the key design specifications such as operating frequency bands (28 GHz and 38 GHz), polarization characteristics (linear and circular), gain, radiation pattern, and bandwidth requirements were clearly outlined. The performance targets were set in alignment with the demands of 5G terrestrial and NTN satellite communication systems.
3. Antenna Topology Selection: Various antenna configurations were studied to determine suitable geometries for achieving the desired performance metrics. Designs such as SRR/CSRR-loaded MIMO antennas, AMC-backed structures, FP cavity antennas, and 3-bit quantized Reflectarray geometries were evaluated. Each topology was selected based on factors including compactness, isolation, gain enhancement, and fabrication simplicity, ensuring progressive development through each work.
4. Material Selection: Appropriate substrate materials such as Rogers RT/Duroid, FR4, Polylactic acid (PLA), etc. were chosen depending on the targeted frequency band, dielectric constant, loss tangent, and fabrication feasibility. Material properties and mechanical stability were carefully analyzed to ensure optimal performance across mm-wave frequencies.
5. Simulation and Optimization: The antenna structures were designed and analyzed using a full-wave EM simulator ANSYS HFSS 2020/2025. Parametric sweeps were conducted to optimize impedance matching, S-parameters, gain, efficiency, and radiation patterns. The performance characteristics were also evaluated for MIMO configurations. In the case of the Reflectarray design, unit-cell phase response, quantization characteristics, and beam-steering behaviour were optimized using full-wave simulations.
6. Prototyping and Fabrication: Optimized antenna prototypes were fabricated using the LPKF ProtoMat S104 PCB prototyping system. The fabrication process involved copper etching, substrate drilling, and via metallization using the plated-through-hole (PTH) technique to realize vertical interconnections and ensure structural stability at mm-wave frequencies. The horn antenna of Reflectarray prototype was fabricated using a precision 3D printing process.

7. Measurement and Testing: Fabricated prototypes were experimentally characterized in a standard anechoic chamber. The key antenna parameters—including S-parameters, gain, efficiency, radiation pattern, and axial ratio (for CP antennas) — were measured using a vector network analyzer (VNA) and standard gain horn antennas.
8. Design Validation and Iterative Optimization: The experimental results were compared with simulated data to ensure consistency and validate design accuracy. Discrepancies arising from fabrication tolerances or substrate losses were iteratively compensated through fine-tuning of design parameters, followed by re-simulation and, where necessary, prototype re-fabrication.
9. Documentation and Reporting: The entire research process—from conceptualization and simulation through fabrication, testing, and optimization—was comprehensively documented. Results from each stage, along with performance comparisons, were analyzed to derive insights for subsequent designs. The validated findings are presented in the subsequent chapters of this thesis, highlighting the progressive improvement achieved in performance metrics across successive antenna generations.

1.10 Thesis Overview

This thesis consists of eight chapters. A brief overview of each chapter is presented below:

In **Chapter 1**, an introduction to the fundamentals of antennas, mm-wave communication, and the evolution toward integrated terrestrial and non-terrestrial networks is presented. The chapter begins with the importance of MIMO technology, followed by an overview of key antenna design challenges such as compactness, gain, bandwidth, and isolation at mm-wave frequencies. A comprehensive literature review of state-of-the-art mm-wave MIMO, AMC-backed, Fabry–Perot cavity, and reflectarray antennas is provided to highlight existing research gaps. The chapter concludes with the motivation, objectives, methodology, and overall framework of the research.

In **Chapter 2**, a compact dual-band SRR-loaded printed monopole MIMO antenna is designed for 28 GHz and 38 GHz 5G applications. The design is developed in two stages—first, a single SRR-loaded monopole achieving dual-band operation with broadside radiation, and second, its extension to a two-port MIMO configuration with improved isolation and low envelope correlation. Simulated and measured results are compared to validate performance, demonstrating suitability for mm-wave terrestrial communication systems.

In **Chapter 3**, an AMC-backed four-port MIMO antenna is designed for wearable WBAN applications operating at 28 GHz. The work builds on the SRR-loaded design to address on-body radiation safety by integrating an AMC layer beneath the antenna. The AMC suppresses back radiation, enhances gain, and improves inter-element isolation. Simulated and measured results confirm enhanced performance and reduced power density, validating its suitability for safe, high-performance body-centric communication.

In **Chapter 4**, a dual-band CSRR-loaded high-gain two-port MIMO antenna array is presented for 28 GHz and 38 GHz operation. The design employs multiple CSRRs and a T-junction feed network to achieve compactness and dual-band operation while maintaining broadside radiation and high isolation. The antenna achieves over 10 dBi gain and high efficiency across both bands, offering improved bandwidth and radiation performance compared to AMC-backed systems.

In **Chapter 5**, a Fabry–Perot cavity-backed MIMO antenna is proposed to achieve high gain, broad bandwidth, and improved aperture efficiency at 28 GHz. The antenna utilizes three types of superstrate layers—unprinted dielectric, single-side printed PRS, and double-side printed PRS—placed at approximately half-wavelength height above the feed antenna. Constructive interference within the FP cavity results in a significant gain enhancement (up to 12.74 dBi) and over 90% aperture efficiency. The design demonstrates the effectiveness of FP cavities in achieving high-gain mm-wave MIMO antenna with low profile and high radiation stability.

In **Chapter 6**, a five-port hybrid MIMO antenna is introduced, incorporating polarization and pattern diversity for enhanced link reliability under multipath fading. The design combines three circularly polarized (RHCP/LHCP) and two linearly polarized (LP) ports arranged orthogonally to provide both broadside and end-fire radiation. The antenna achieves high isolation (22–61 dB), excellent efficiency (up to 97%), and gain exceeding 9 dBi, providing robust spatial and polarization diversity. This design marks a significant step toward practical high-capacity mm-wave MIMO systems.

In **Chapter 7**, a wideband, high-gain 3-bit quantized reflectarray antenna is designed for Ka-band NTN applications, including LEO/GEO satellites, HAPs, and UAVs. The planar reflectarray consists of 31 × 31 metallic square-ring unit cells providing a 360° reflection phase range with low loss (< 0.8 dB). The antenna achieves mechanical beam steering up to ±20°, a peak gain of 27.8 dBi, and 56.1% aperture efficiency. This work bridges terrestrial and non-

terrestrial communication domains, offering a low-cost, high-efficiency alternative to active phased arrays for future 5G/6G NTN systems.

Finally, **Chapter 8** presents the conclusions and future scope derived from the entire research work. The major findings from each chapter are summarized, emphasizing the progressive enhancement achieved across the six antenna designs—from compact MIMO architectures to beam-steerable reflectarrays. The chapter concludes by outlining possible future directions, including the development of electronically reconfigurable reflectarrays, integration with intelligent metasurfaces, hybrid beamforming arrays, and adaptive antenna front-ends tailored for next-generation 6G and non-terrestrial network communication platforms.

***

Chapter 2

Dual-Band SRR-Loaded Printed Monopole MIMO Antenna

In recent years, the growing demand for compact, high-performance antennas tailored for mm-wave 5G and beyond communication systems has intensified research on wideband and multiband printed antenna designs. Among these, printed monopole configurations have emerged as a preferred choice owing to their inherently low profile, lightweight structure, ease of fabrication, and straightforward impedance matching. Their high radiation efficiency and mechanical robustness make them suitable for integration into handheld and portable devices, where space constraints and form-factor compatibility are critical design considerations.

Achieving dual-band operation within a compact structure typically requires the incorporation of resonant elements or defected ground modifications to generate multiple resonances without enlarging the primary radiator. Techniques such as slot etching, metamaterial loading, and split-ring resonator (SRR) inclusion have proven effective in controlling surface current distribution and achieving miniaturization [91–92].

This chapter presents the design, analysis, fabrication, and experimental demonstration of a dual-band SRR-loaded printed monopole MIMO antenna operating at 28 GHz and 38 GHz, optimized for 5G communication systems. The proposed configuration combines the benefits of SRR loading and an annular slot defected ground structure to achieve dual-band resonance, high isolation, and stable broadside radiation patterns within a compact form factor. Simulation and measurement results validate the design, confirming its potential for next-generation mm-wave MIMO communication systems.

2.1 Antenna Design Methodology

2.1.1 Single Antenna Design

The schematic of the proposed single antenna design is illustrated in Figure 2.1. It consists of a printed monopole element along with one SRR geometry patterned on the top side of a dielectric substrate, whereas the bottom side contains a defected ground plane along with an annular slot. Rogers RO 4003(TM) substrate has been used as the constituent dielectric, which has the following properties: relative permittivity of 3.55 and loss tangent of 0.0027. The

thickness of the substrate is taken as 0.3 mm. The overall dimensions of the proposed geometry are 15 mm × 15 mm. Other physical dimensions are mentioned in Figure 2.1.

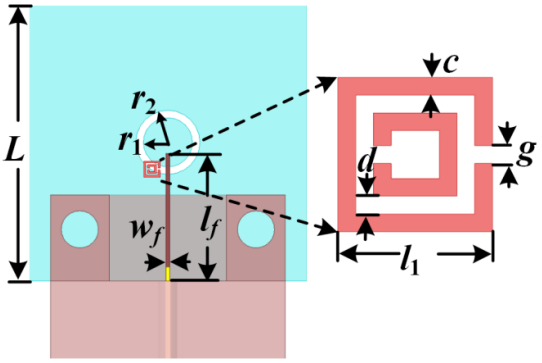

Figure 2.1: Schematic diagram of the proposed dual-band single antenna. The dimensions are: L= 15, l_f = 6.8, w_f = 0.7, r_1= 1.0, r_2= 1.3, l_1 = 1.74, d = 0.2, c = 0.2, and g = 0.2 (units: mm).

The proposed antenna geometry is numerically designed and analyzed using ANSYS HFSS 2020, with a detailed step-by-step optimization process to achieve dual-band operation and compact integration. To realize independent control of two distinct resonant bands within a single structure, the antenna configuration employs two radiating elements excited through a single feed line. As illustrated in Figure 2.2, a printed monopole radiator is placed on the top surface to function as the primary feed element, while an annular slot is etched on the bottom surface of the substrate to enhance the radiation performance.

In the initial design stage, the monopole and annular slot combination produces a –10 dB impedance bandwidth of 3.0 GHz (28.20–31.20 GHz), with a minimum reflection coefficient (S_{11}) of –24.94 dB at 29.70 GHz, indicating excellent impedance matching. The monopole primarily excites the fundamental resonance around 28 GHz, while the annular slot contributes to resonance stabilization and minor frequency tuning through its capacitive coupling effect.

To introduce an additional resonance without disturbing the primary mode, an SRR is integrated adjacent to the monopole radiator on the top layer of the substrate. The SRR operates as an inductive–capacitive (LC) resonator, where the circulating currents along the metallic rings and capacitive gap collectively generate a second resonant mode. The dimensions and placement of the SRR are optimized to achieve strong EM coupling with the monopole while maintaining adequate spatial separation to minimize interference between the two resonant modes. Through careful tuning of the SRR parameters, the final geometry achieves dual-band operation, exhibiting two well-defined resonances at 29.20 GHz (S_{11} = –21.21 dB) and 37.90

GHz (S_{11}= –13.70 dB). The lower band corresponds to the monopole–slot resonance, while the upper band originates from the SRR excitation.

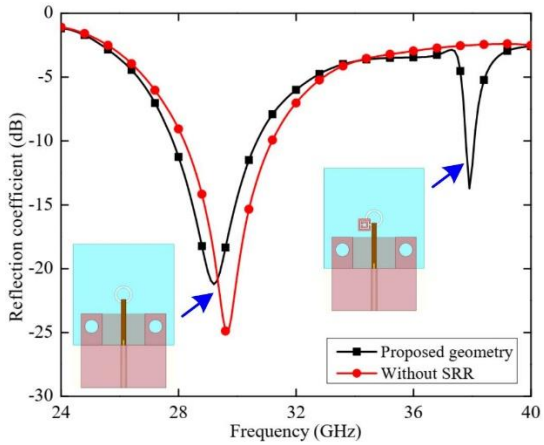

Figure 2.2: Comparison of simulated reflection coefficient (S_{11}) of the proposed single-band antenna design with and without the SRR geometry.

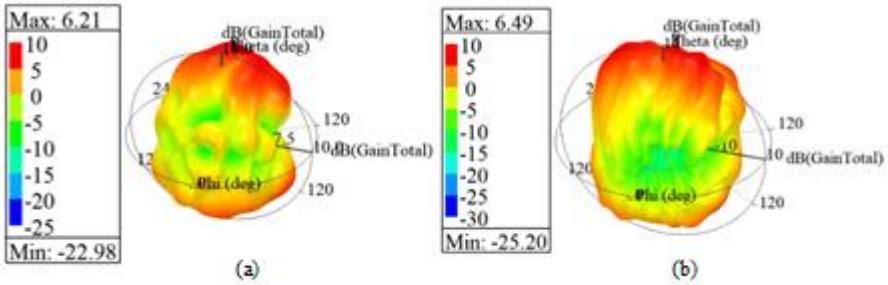

Figure 2.3: Simulated 3D far field gain pattern of the proposed single-band antenna at (a) 29.20 GHz, and (b) 37.90 GHz.

The simulated 3D far-field gain patterns for the proposed single antenna are shown in Figures 2.3(a) and 2.3(b) for 29.20 GHz and 37.90 GHz, respectively. It can be observed that the peak gains of 6.21 dBi and 6.49 dBi are obtained at these two frequencies, respectively. It is also evident that the antenna is radiating in broadside direction at both the frequencies.

2.1.2 Two-Port MIMO Antenna Design

After presenting the single-band antenna design, the two-port MIMO antenna geometry is depicted in Figure 2.4, where the elements are placed side by side. The geometric dimensions and the substrate properties remain same, whereas the separation between the elements (d) is considered as 15 mm, based on the optimized responses.

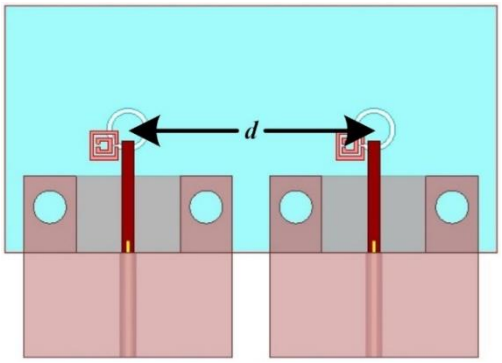

Figure 2.4: Geometry of the proposed 1 × 2 MIMO antenna with d = 15 mm.

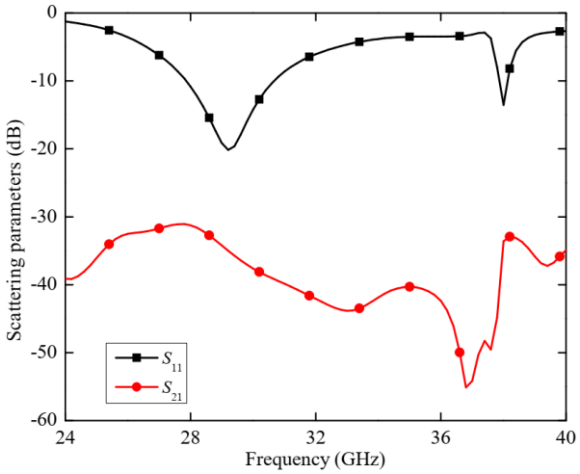

Figure 2.5: S-parameter plot for the proposed 2-port MIMO antenna.

The simulated scattering parameters for the proposed 2-element (1 × 2) MIMO antenna is depicted in Figure 2.5. It is observed that the reflection coefficient of the individual antennas remain constant as that of the single antenna, whereas the isolation between the antennas are below -30 dB throughout the operating range. Owing to the symmetry between the antennas, scattering parameters from one set of antennas (antenna # 1) are presented. If the separation is increased further, the isolation will further be improved, but at the expense of a larger antenna footprint. Thus, the separation is maintained at an optimum value of 15 mm.

2.2 Fabrication and Measurement

To validate the proposed antennas, sample prototypes of both single element and MIMO have been fabricated on a 0.3 mm thick RO4003(TM) substrate using LPKF Protomat S104 equipment. Figure 2.6 depicts the photograph of the fabricated single element. The reflection coefficient of the geometry has been measured and it is observed in Figure 2.7 that the lower band (around 28 GHz) operates from 26.2 GHz to 28.3 GHz with S_{11} below -10 dB, whereas the upper band (around 38 GHz) has a -10 dB bandwidth from 35.6 GHz to 39.37 GHz.

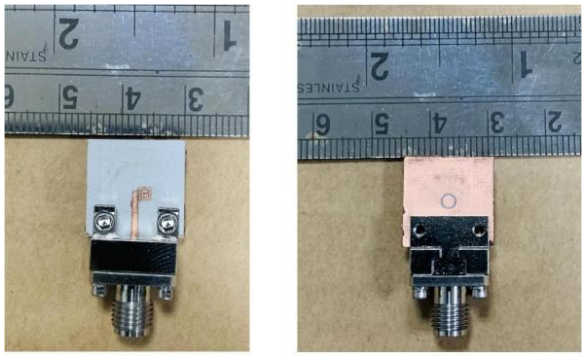

(a) (b)

Figure 2.6: Photograph of the fabricated single antenna: (a) top layer, and (b) bottom layer.

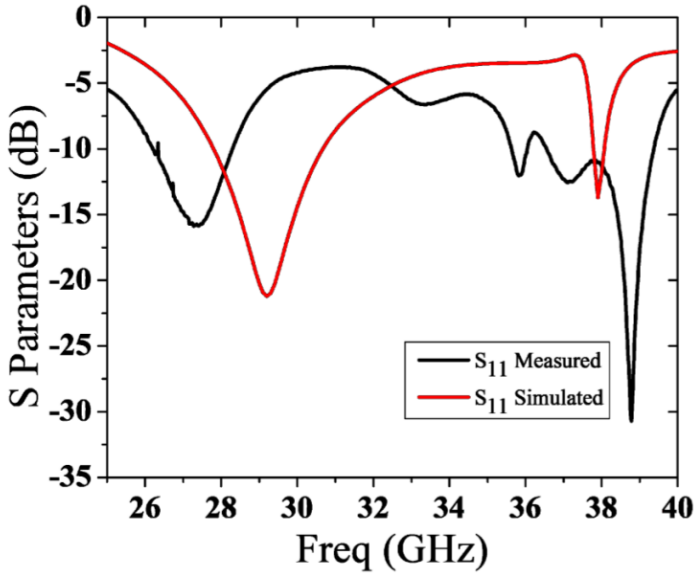

Figure 2.7: Simulated and measured S_{11} response of the proposed single antenna.

After fabricating the single antenna element, the proposed 1 × 2 MIMO antenna has also been fabricated using LPKF Protomat S104 equipment and the photograph is depicted in Figure 2.8. The reflection and transmission characteristics of the antenna are experimentally measured using a Vector Network Analyzer (VNA) to validate the simulated performance.

As illustrated in Figure 2.9, the measured S_{11} demonstrates two well-defined impedance bands. The first band spans from 27.46 GHz to 30.33 GHz, corresponding to the lower 28 GHz 5G band, while the second band extends from 37.10 GHz to 38.10 GHz, corresponding to the upper 38 GHz band. In both cases, the S_{11} values remain below –10 dB, confirming satisfactory impedance matching across the operating frequencies. The transmission coefficient (S_{21}) between the two antenna elements remains consistently below –28 dB throughout the entire frequency range, indicating excellent inter-element isolation and minimal mutual coupling.

Such high isolation ensures independent operation of the antenna elements, which is critical for maintaining low envelope correlation and reliable MIMO performance.

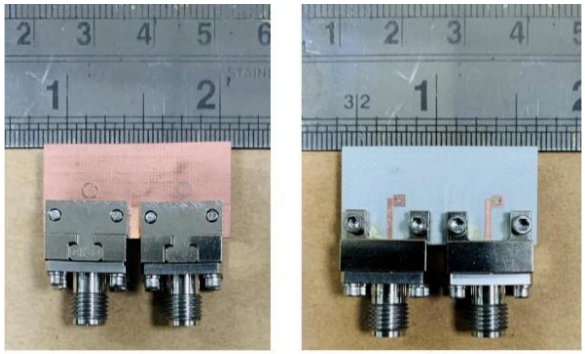

Figure 2.8: Photograph of the fabricated 1 × 2 MIMO antenna: (a) top layer, and (b) bottom layer.

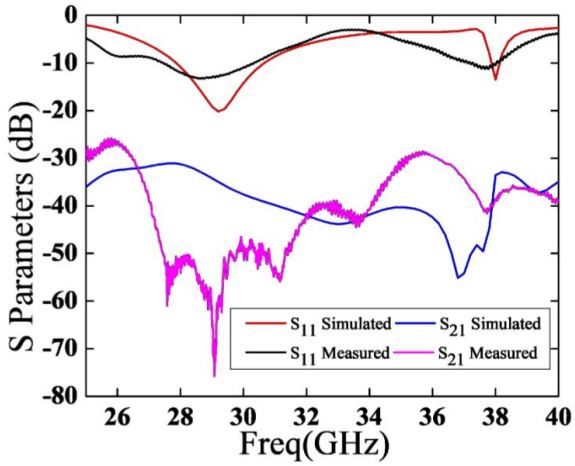

Figure 2.9: Simulated and measured scattering parameter responses (S_{11}, S_{21}) of the proposed 1 × 2 MIMO antenna.

2.3 Evaluation of MIMO Performance Metrics

Once the scattering coefficients are determined, several important parameters for validating the MIMO antenna performance have been investigated. The parameters are determined from conventional equations. The ECC, which is a measure of correlation or isolation between the radiation patterns of the proposed MIMO antenna, has been achieved well below the desired limit at both the operating frequencies (around 28 GHz and 38 GHz), as shown in Figure 2.10(a). The TARC, which is the ratio of total reflected power to the total incident power, is obtained within the desired value, as depicted in Figure 2.10(b). The CCL is related to the rate of information that can be reliably transmitted over the communication channel and its desired

value (which should be less than 0.5 bits/seconds/Hertz) is obtained in the proposed MIMO antenna. The response is depicted in Figure 2.10(c). All the parameters are determined from simulated as well as measured S-parameters, and they have a close similarity around the operating frequencies (28 GHz and 38 GHz).

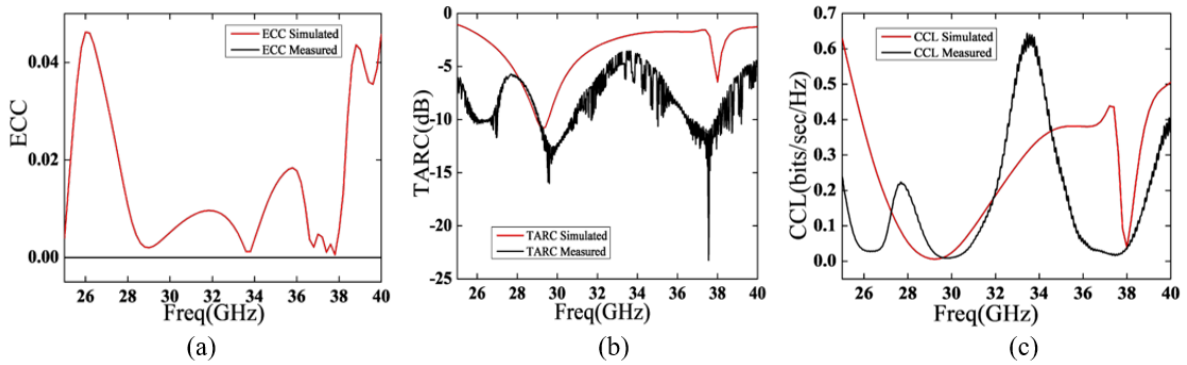

Figure 2.10: Simulated and measured parameters of the proposed 1 × 2 MIMO antenna: (a) ECC, (b) TARC, and (c) CCL.

2.4 Conclusion

Table 2.1: Comparison with earlier reported single-layer dual band 28/38 GHz antennas

References	No. of element	Antenna dimension (mm × mm × mm)	Frequency band (GHz)	Gain (dBi)
[54]	4	12.5 × 12.5 × 0.8	35	6.00
[93]	4	11 × 8 × 0.787	28, 38	4.85, 6.00
[94]	1	1.3 × 1.3 × 1.1	28, 38	3.75, 5.06
[95]	4	19.25 × 26 × 0.79	28, 38	7.58, 5.72
[96]	2	55 ×110 × 0.508	28, 38	7.88, 9.49
Proposed MIMO	**2**	**30 × 15 × 0.3**	**28, 38**	**6.21, 6.49**

In this chapter, a dual-band single antenna as well as its MIMO configuration have been presented for mm-wave 5G applications. The proposed topology exploits planar monopole element along with a simple SRR and a defected ground plane for realizing two discrete resonances at around 28 GHz and 38 GHz. A broadside radiation response is observed with a

gain value of 6.21 dBi and 6.49 dBi at these two frequencies, respectively. Both single element and MIMO configurations have small profiles, thereby resulting compact geometries. Several MIMO antenna characteristics, such as ECC, TARC, and CCL are examined and all of their values are found within the acceptable range. Further, the geometries are fabricated and the measured responses are in reasonable agreement with those of the simulated results. A comparative performance analysis between the proposed antenna and existing mm-wave antennas is summarized in Table 2.1, and the proposed geometry exhibits higher gain and smaller size compared to reported works, while maintaining dual-band operation and strong isolation. In future, the proposed concept will be expanded for higher order MIMO antennas along with its possible deployment in 5G and future wireless communication systems.

***

Chapter 3

AMC-Backed MIMO Antenna for Wearable WBAN Applications

With the rapid advancement of wearable and body-centric communication technologies, wireless body area networks (WBANs) have emerged as a key enabler of next-generation 5G and beyond systems. These networks support diverse applications ranging from remote healthcare monitoring and rehabilitation to military tracking and sports analytics, requiring antennas that are compact, efficient, and electromagnetically safe when integrated onto or near the human body.

At mm-wave frequencies, particularly around 28 GHz, antennas experience significant free-space path loss and tissue absorption, which can degrade signal strength and pose potential safety concerns. In addition, the close proximity between radiating elements in compact MIMO systems leads to mutual coupling, thereby reducing isolation, altering radiation characteristics, and impacting overall system capacity. These challenges necessitate antenna architectures that can simultaneously achieve high gain, low mutual coupling, and suppressed backward radiation toward the body.

Building upon the dual-band SRR-loaded antenna presented in Chapter 2, this work introduces a four-port MIMO antenna integrated with a broadband artificial magnetic conductor (AMC) layer designed specifically for wearable mm-wave WBAN applications. The AMC surface is engineered to exhibit an in-phase reflection response around 28 GHz, resulting in enhanced forward gain, reduced power density toward the body, and improved isolation among antenna elements.

The proposed AMC-backed four-port MIMO antenna offers multiple performance advantages for wearable mm-wave WBAN applications. It achieves high-gain unidirectional radiation while maintaining a compact and low-profile structure suitable for on-body integration. The incorporated AMC layer effectively suppresses surface currents and backward radiation, thereby reducing EM exposure to human tissues and enhancing radiation safety. Moreover, due to orthogonal arrangement the four-port MIMO configuration ensures strong spatial diversity and excellent isolation, with inter-element coupling levels better than –28 dB, enabling robust and reliable performance in multipath-rich communication environments.

3.1 AMC-Backed MIMO Antenna Design

3.1.1 Design of Single Antenna and Four-port MIMO

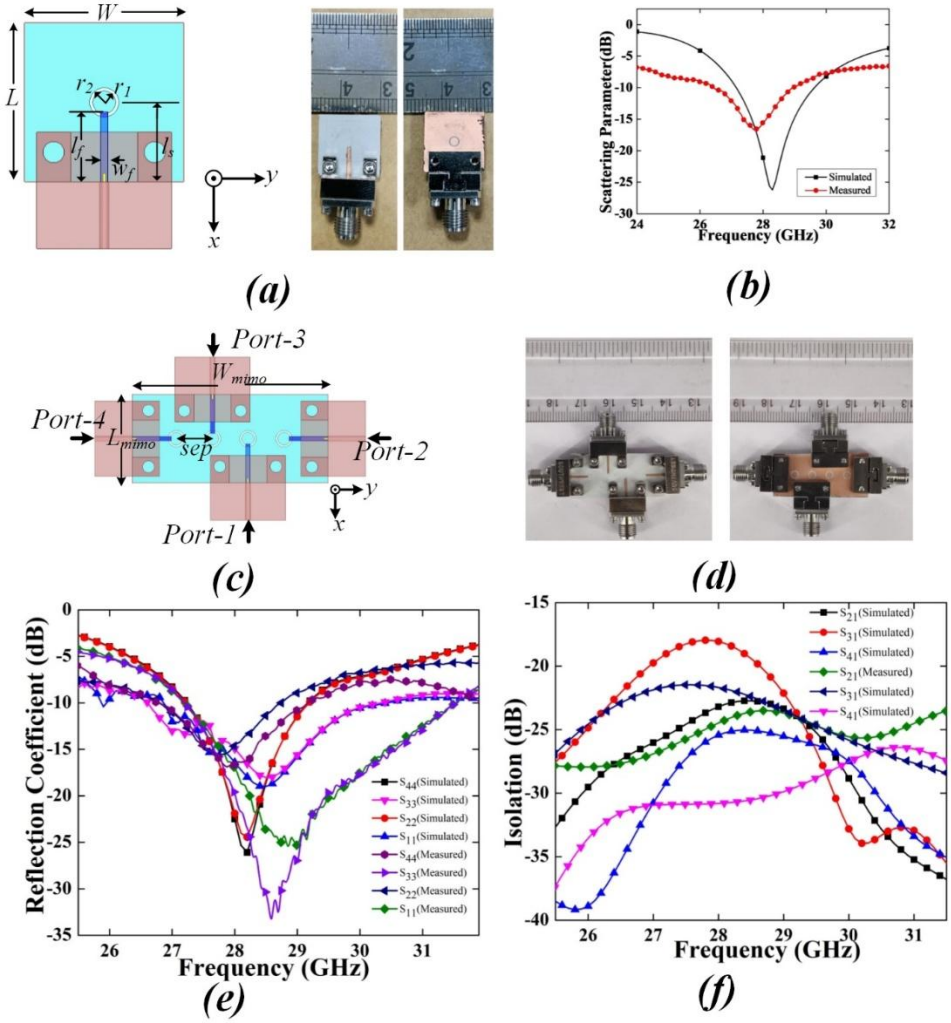

Figure 3.1: (a) Geometry and fabricated prototype (top and bottom layer) of the proposed single antenna. The optimized dimensions are: L=W= 15, r_1 = 1.08, r_2 = 1.38, w_f = 0.7, l_f = 6.6, l_s = 7.5 (units: mm). (b) Simulated and measured reflection coefficient (S_{11}) response of the proposed single antenna. (c) Geometry of the proposed four-port MIMO antenna with dimension: sep = 6.1, L_{mimo} = 15, W_{mimo} = 33.2 (units: mm). (d) Fabricated prototype (top and bottom layer) of the proposed MIMO antenna. (e) Simulated and measured reflection coefficient of the proposed MIMO antenna without AMC. (f) Simulated and measured isolation of the proposed MIMO antenna without AMC.

The schematic of the proposed single antenna design is illustrated in Figure. 3.1(a). The geometry is based on a single-layer dielectric substrate, where a printed monopole is patterned on the top side of the substrate and an annular slot is engraved on the ground plane. Rogers RO

4003(TM) is used as the constituent substrate with a thickness of 0.3 mm and a relative permittivity (ε_r) of 3.55 and loss tangent (tan δ) of 0.0027. The dimensions are provided in the caption of Figure 3.1. The monopole length is optimized to resonate the antenna at 28 GHz band, whereas the annular slot improves the overall impedance bandwidth. The simulated result shows a -10 dB impedance bandwidth from 27.2 to 29.6 GHz with a maximum peak gain of 4.5 dBi at 28 GHz. The fabricated antenna prototype is also depicted in Figure 3.1(a). The simulated and measured reflection coefficient (S_{11}) responses of the proposed antenna are presented in Figure 3.1(b), indicating a good resemblance between them.

Next, a four-port MIMO antenna is designed, as shown in Figure 3.1(c), where the radiating elements are arranged orthogonally with a slight offset to minimize the overall footprint. The geometric parameters and substrate characteristics remain identical to those used in the single-element antenna, while the inter-element spacing (sep) is optimized to 6.1 mm for achieving the best MIMO performance. The top and bottom views of the fabricated MIMO antenna prototype are presented in Figure 3.1(d).

The simulated and measured reflection coefficient of four port MIMO antenna are shown in Figures 3.1(e). It can be observed that for ports 1 and 3, the reflection coefficient responses are slightly shifted away from 28 GHz, probably due to high coupling between those two ports. The measured -10 dB impedance bandwidth for both ports 1 and 3 is found to be 3.10 GHz (26.82-29.92 GHz), whereas the bandwidth is recorded slightly larger 4.70 GHz for ports 2 and 4. Figure 3.1(f) depicts the isolation response between the ports, and it is found above 15 dB for all cases. The measured responses overall match the simulated results, however, minor non-conformity is observed which can be accounted to fabrication tolerance, as a slight variation of 0.1 mm during fabrication can result in shift of resonance and impedance bandwidth.

3.1.2 MIMO Antenna Backed with Wideband AMC

An artificial magnetic conductor (AMC) is a periodic structure made from unit cell patterns providing a high impedance surface (HIS) along with a 0^o reflection phase at the resonance frequency [97], [98]. The unit cell geometry is generally made from a combination of inductive and capacitive elements to exhibit resonance. The incoming EM wave gets reflected from the AMC surface at the resonance, without any phase addition, unlike in the PEC case. This reflected wave, while properly transmitted in the desired direction, can constructively interfere with the radiating beam and can contribute in increasing the gain of the antenna along with a

unidirectional radiation pattern. The AMC used in this work has been designed to exhibit a wideband operation in line with the proposed mm-wave antenna.

The unit cell of the proposed AMC is made of a single layer dielectric of Rogers RO 4003 (TM) substrate of thickness 0.3 mm, whose top side has a metallic square patch and the bottom side has a full ground. The unit cell geometry, its periodic boundary set up, its equivalent circuit, and the overall AMC surface (comprising 10×7 unit cells) are presented in Figure. 3.2(a). In the equivalent circuit diagram, L_{se} represents the inductance due to the square patch, C_{se} represents the capacitance due to the spacing between the adjacent patches, L_{sh} and C_{sh} are the shunt inductance and shunt capacitance between the square-shaped patch and the ground plane, respectively. These distributed reactive parameters overall regulate the resonance frequency as well as reflection phase of the AMC array. It can be observed from Figure 3.2(b) that the reflection phase of the AMC unit cell crosses the 0^o level at 28 GHz. While considering the phase range from -90^o to $+90^o$, a wide bandwidth is thus obtained around 28 GHz which will be used in improving the antenna performance.

The designed four-port MIMO antenna is placed above the AMC array as shown in Figure 3.2(c) with a 3.4 mm separation (which corresponds to $0.31\lambda_o$, λ_o being the wavelength at the operating frequency) between them. The separation is selected such that the mm-wave connector of the antenna can be accommodated in the space between the antenna and the AMC. The array size (10×7 unit cells) is chosen in such away so as to completely cover the four-port MIMO antenna geometry. The simulated and measured reflection coefficients of MIMO antenna with AMC are presented in Figure 3.2(d). It is observed that the port 2 and port 4 of the MIMO antenna with AMC exhibit a measured -10 dB impedance bandwidth of 5.35 GHz (25.6–30.95 GHz), which is an improvement of 0.65 GHz with respect to that of the antenna without AMC. For port 1 and port 3, an improvement in the measured impedance bandwidth is also observed. The return losses obtained for port 1 and port 3 are around 50 dB at 28.8 GHz, which is a major improvement of around 18 dB while compared with the antenna without AMC. Further, as shown in Figure 3.2(e), the use of AMC improves the isolation at all four ports at 28 GHz as compared to their counterparts without the AMC case. The plots demonstrate good conformity between the measured and simulated results.

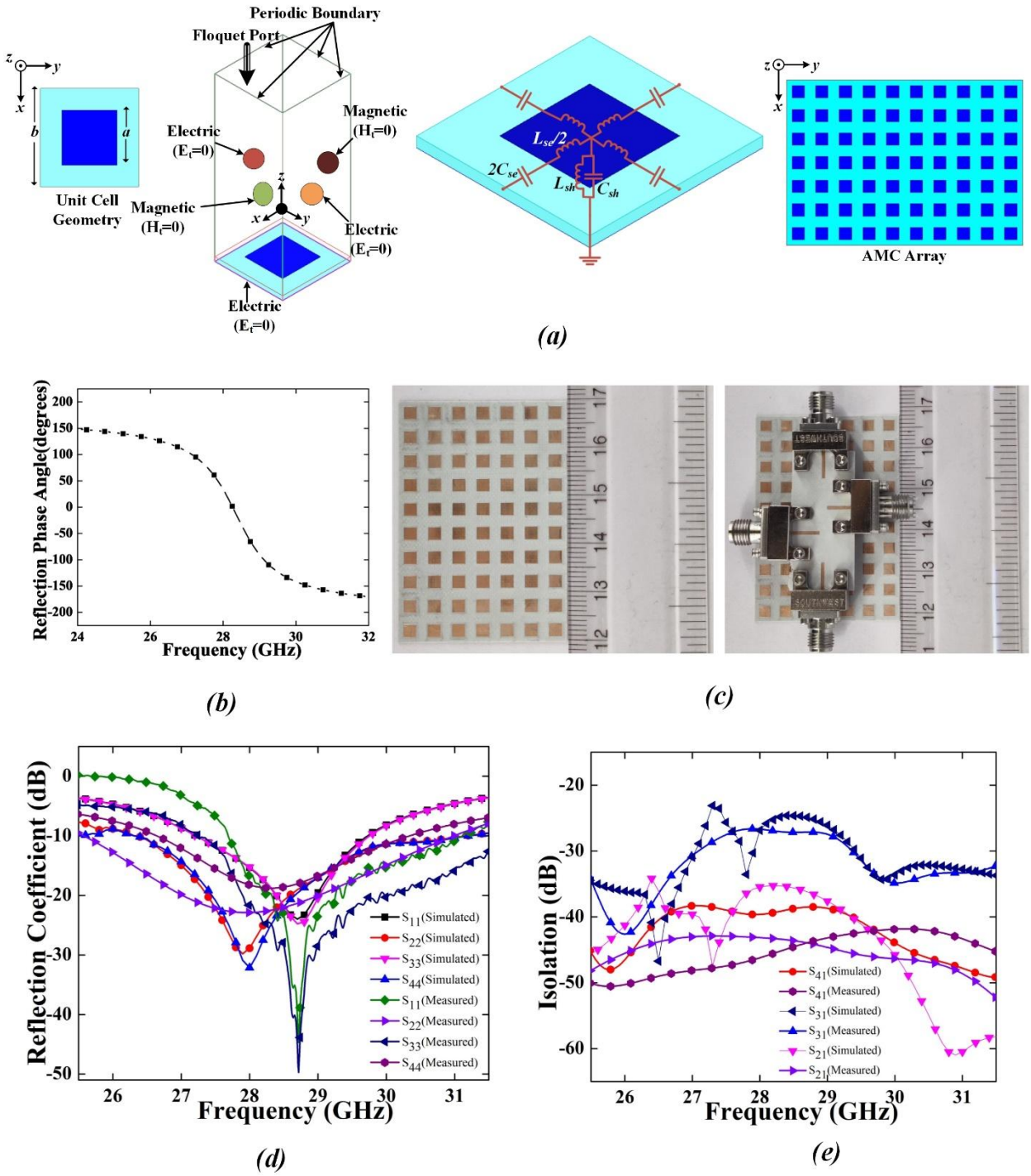

Figure 3.2: (a) The unit cell geometry of the proposed AMC with the dimensions: a = 2.6, b=5 (units: mm), periodic boundary set up for simulation, equivalent circuit and geometry of the AMC array (10×7 unit cells). (b) Simulated reflection phase characteristics of the AMC unit cell. (c) Fabricated prototype of the proposed AMC array (10 × 7) and 4 port MIMO antenna placed on top of AMC at the separation of 3.4 mm. (d) Simulated and measured reflection coefficient of the proposed MIMO antenna with AMC. (e) Simulated and measured Isolation of the proposed MIMO antenna with AMC.

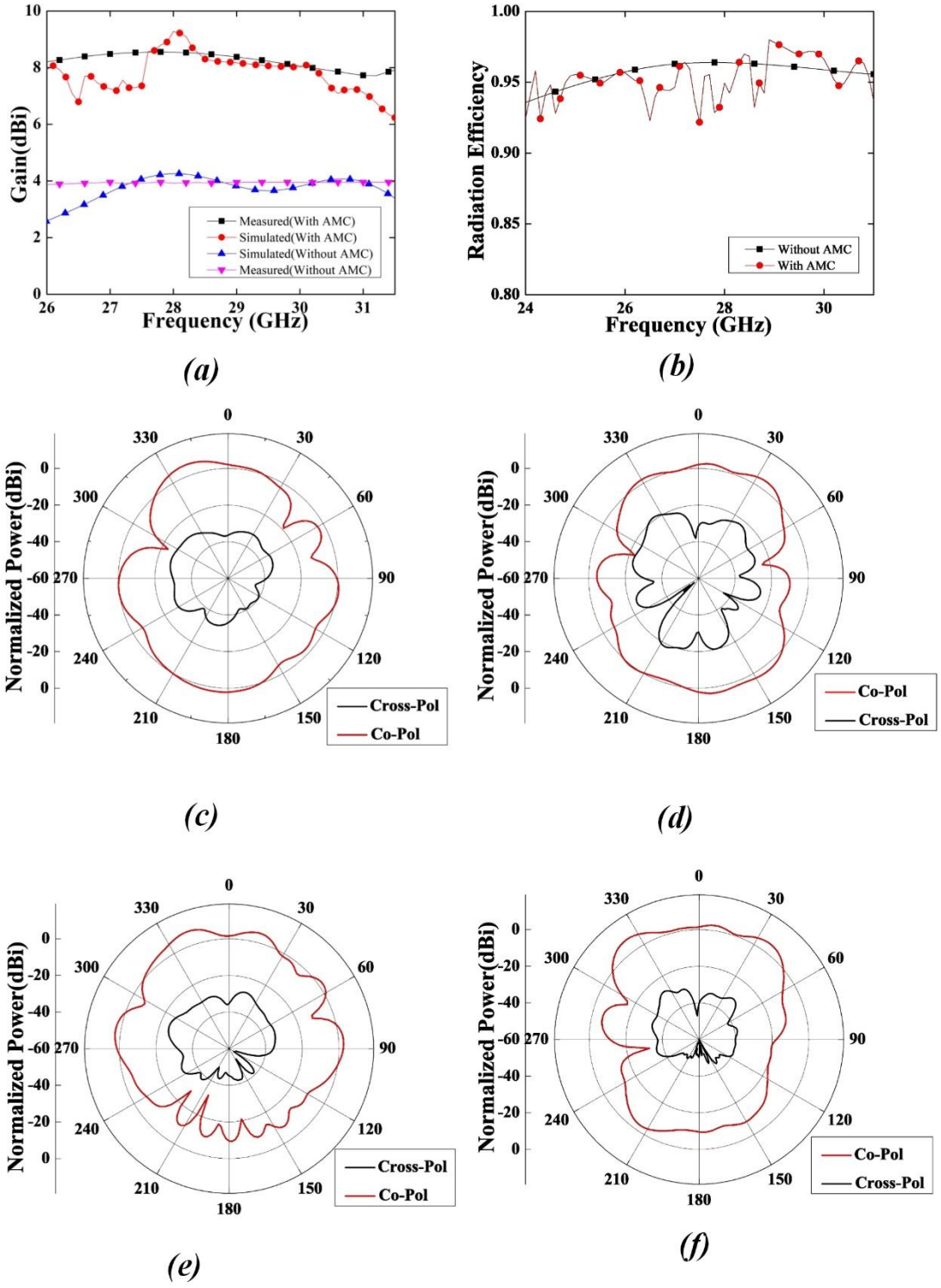

Figure 3.3. (a) Simulated and measured gain for MIMO antenna (without and with AMC), (b) simulated radiation efficiency for MIMO antenna (without and with AMC). Simulated 2D radiation pattern of MIMO antenna at 28 GHz: (c) E-Plane (without AMC), (d) H-Plane (without AMC), (e) E-Plane (with AMC), (f) H-Plane (with AMC).

3.2 Results and Discussion

3.2.1 Gain and Radiation Pattern

The simulated as well as measured gain plot for the proposed antenna (with and without AMC) are shown in Figure 3.3(a). It is observed that the simulated gain of the antenna with AMC is 9.25 dBi at 28 GHz, which is a significant improvement of 4.25 dBi with respect to the antenna without AMC. The measured gain is shown to follow the simulated gain curve at the operating bandwidth, however, it reduces away from the frequency. Figure 3.3(b) presents the simulated radiation efficiency of the proposed antenna, with and without AMC. It is shown that radiation efficiency of the antenna marginally reduces after introduction of the AMC in the operating frequency band.

The simulated 2D radiation patterns of the proposed MIMO antenna (without and with AMC) in two orthogonal planes (*E* and *H* planes) are depicted in Figures 3.3(c)-3.3(f), showing the radiation taking place in the broadside direction. With the introduction of the AMC structure, the radiation pattern of the designed antenna becomes unidirectional as it acts as a reflector to the main radiator.

3.2.2 MIMO Parameters

Several important parameters, like envelope correlation constant (ECC), total active reflection constant (TARC), channel capacity loss (CCL), and diversity gain (DG) have been examined for confirming the MIMO antenna (with and without AMC) performance. The ECC has been achieved well below the desired limit of less than 0.1 at the operating frequency (i.e. around 28 GHz), as shown in Figure 3.4(a). The TARC is also obtained within the desired value less than -10 dB, as depicted in Figure 3.4(b). The desired value of CCL is less than 0.5 bits/seconds/Hertz. Figure 3.4(c) shows the CCL response for the proposed MIMO antenna, displaying its compliance. The DG curve, as shown in Figure 3.4(d), is obtained within the desired value of less than 10 dB in the proposed MIMO antenna. All the plots are presented with and without the AMC, and it is observed that the MIMO performance parameters remain within acceptable values. The characteristics are also determined from the measured S-parameters (magnitude and phase), and they have conformity around the operating frequency.

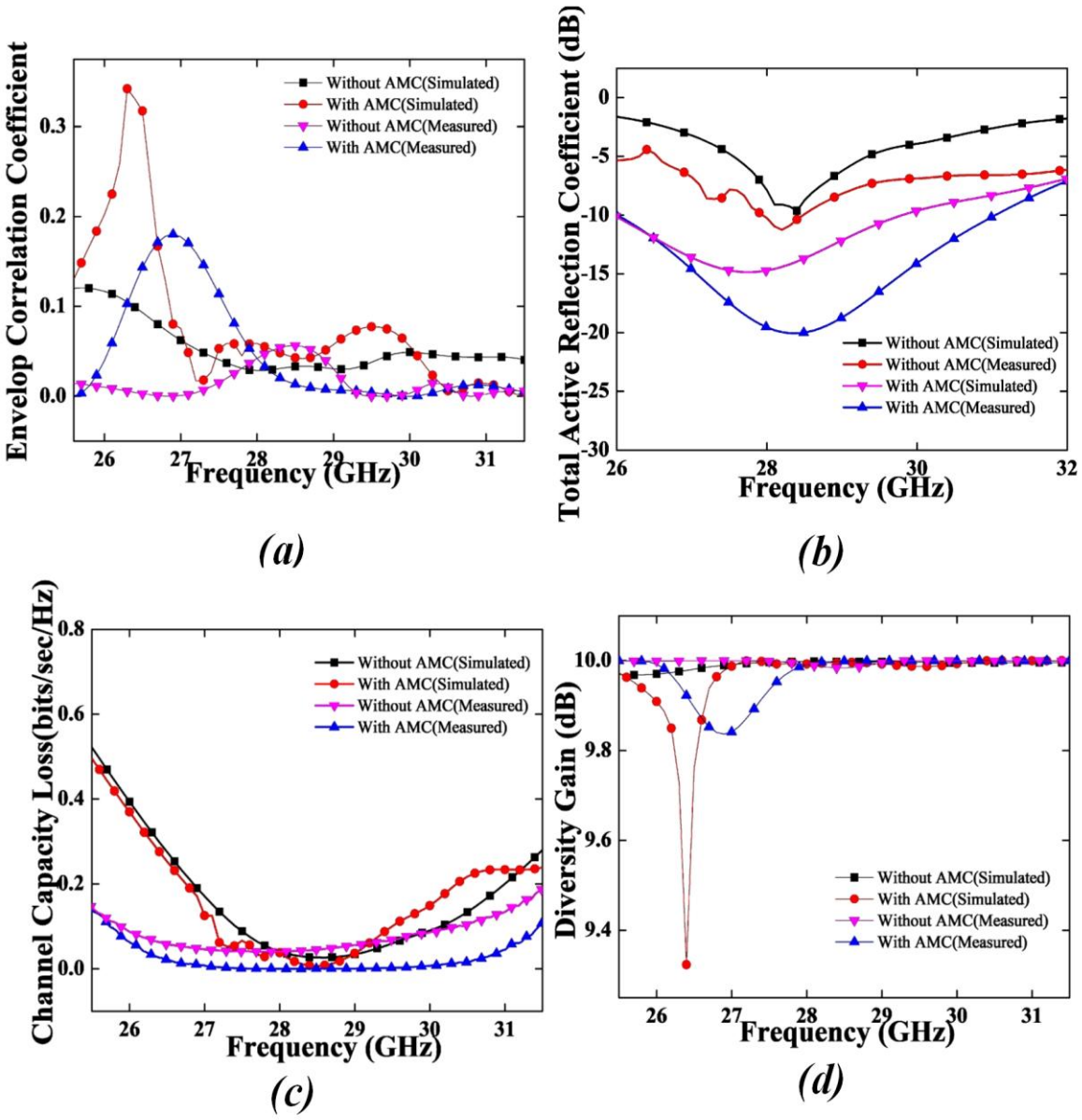

Figure 3.4. Simulated and measured MIMO performance parameters of the proposed four-port MIMO antenna: (a) ECC, (b) TARC, (c) CCL and (d) DG.

3.3 Safety Analysis

Analysis of the health risk of an antenna for wearable networks is of paramount importance. For assessing the absorbed energy in human tissue, specific absorption rate (SAR) is a quantitative Figure of merit [99]. The American standard for accepted value of SAR is 1.6 W/kg for 1 g of tissue while the European standard is of 2 W/kg for 10 g of tissue [100]–[101]. To conduct the SAR analysis, two different human body models, viz. one three-layer and other four-layer models are considered in this work. The length and breadth of both models are assumed as 25 mm and 10 mm, respectively, while thickness values of constituents (i.e. skin,

fat, muscles, and bone) are given in Table 3.1 [102]. The models are frequency dependent. For three-layer human body model, layers of skin, fat, and muscles are considered for analysis, while for the four-layer human body model, the bone layer is also included along with skin, fat, and muscles. The values of conductivity, permittivity, loss tangent, and density for constituents of human model are calculated at 28 GHz and are given in Table 3.2 [103].

Table 3.1: Human tissue models with layer thicknesses (units: mm)

Model/ Tissue (Layers)	Skin (Top Most layer)	Fat (Second Layer)	Muscle (Third Layer)	Bone (Fourth Layer)
Three Layer Model (units: mm)	3	7	50	-
Four Layer Model (units: mm)	2	5	20	13

Table 3.2: Dielectric properties of the human tissues at 28 GHz

Sl. No.	Tissue (layers)	Bulk Conductivity (S/m)	Relative Permittivity	Loss tangent	Mass Density (Kg/m3)
1	Skin	25.82	16.55	0.33	1114
2	Fat	5.04	6.09	0.18	909
3	Muscle	33.61	24.41	0.3	1103
4	Bone	4.94	5.17	0.37	1821

Two different simulation set ups (one without AMC and other with AMC) have been made for the proposed MIMO antenna for both human tissue models at 28 GHz, by considering 1 g of tissue average as per IEEE standards. The human model is kept at a separation of 6 mm from the antenna. At the operating frequency, the SAR value has been calculated for an input power

of 24 dBm, which is the standard value used for LTE smartphone as well [104]. Figure 3.5 shows the simulation setup for the calculation of SAR distribution of the proposed MIMO antenna (with and without AMC) on three layer and four-layer human body models.

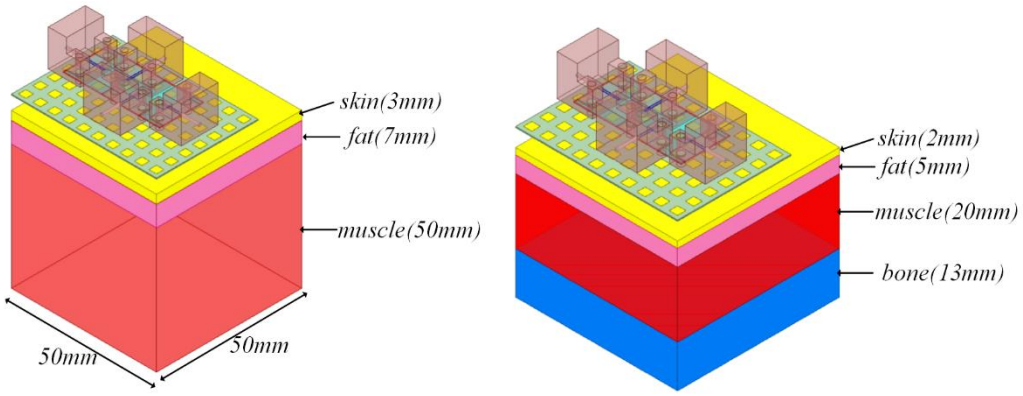

Figure 3.5. Three-layer and four-layer human tissue models at 28 GHz.

Table 3.3: SAR level (W/Kg) and SPD level (W/m^2) of the proposed antenna at 28 GHz (Input Power = 24 dBm)

Antenna	3 Layer Model		4 Layer Model	
	SAR	PD	SAR	PD
Without AMC	37.02	453.92	34.09	534.44
With AMC	0.112	2.38	0.755	7.07

Table 3.3 shows the average SAR values calculated over 1 g of tissue for the three-layer and four-layer human models with 24 dBm input power. It is observed that the introduction of AMC significantly decreases SAR values of the antenna at 28 GHz, thereby reducing it below the specified maximum value of 1.6 W/Kg for the input power of 24 dBm.

However, at mm-wave frequencies, EM waves exhibit negligible penetration into human skin, and therefore, the safety evaluation of antennas at these frequencies cannot rely solely on SAR analysis [105]. Instead, spatial power density (SPD) estimation is the recommended and widely accepted metric for assessing human exposure and ensuring compliance with safety guidelines for mm-wave antennas. The SPD exposure limits as per IEEE specifications is 10W/m^2 for 3-30 GHz frequency range [106]-[107]. Table 3.3 also presents the power density exposure distributions at 28 GHz for the three layer and four-layer model at 24 dBm input

power. It can be observed that the introduction of AMC reduces PD values for the antenna and makes it lower than the limit of 10 W/m^2.

Table 3.4: Comparison of Antennas for mm-wave WBAN applications

Ref	Single /MIMO Antenna	Board Size (mm^3)	Freq. Band (GHz)	Gain (dBi)	Reflector	Input Power (dBm)	SAR (1-g average - W/Kg)	SPD (W/m^2)
[108]	Single	72 × 72 × 11	2.2-2.6 4.9–5.5	5.1, 6.2	AMC	-	-	-
[109]	Single	62.5 × 37.5 × 3.5	2.36-2.4	6.2	Metasurface	20	0.66	-
[110]	Single	38 × 38 × 3	2.40–2.48	-	HIS	20	0.29	-
[111]	Single	46 × 46 × 2.4	2.4	7.8	EBG	20	0.0368	-
[112]	Single	89 × 83 × 6.25	2.4–2.5, 3.28–3.38	6.4, 3	AMC	20	0.29	-
[113]	Single	102 × 68 × 3.6	4.30–5.90	6.12	AMC	30	47.26	-
[56]	2 Port MIMO	40 × 40 × 12.024	3-4.1	7.1	AMC	-	-	-
[58]	2 Port MIMO	19.04 × 15.06 × 5.14	24	5.9	EBG	30	-	2428.3
Proposed Antenna	**Single antenna, 4 port MIMO**	**50 × 35 × 3.7**	**28**	**9.25**	**AMC**	**20**	**0.112**	**2.38**

3.4 Conclusion

In this chapter, a compact four-port AMC-backed MIMO antenna has been designed, analyzed, fabricated, and experimentally demonstrated for mm-wave 5G WBAN applications operating at 28 GHz. The integration of an AMC surface beneath the antenna significantly enhances its gain, impedance bandwidth, return loss, and inter-element isolation, while

effectively suppressing backward radiation. As a result, the proposed design achieves superior radiation performance and improved EM safety, as evidenced by the substantial reduction in SAR and PD values. The proposed geometry is compared with earlier reported AMC based antenna structures in Table 3.4 and it is observed that the designed MIMO antenna shows significantly high gain, compact size, simpler topology, wideband characteristics, and good safety performance. The fabricated prototype demonstrates close agreement between measured and simulated results, validating the proposed concept. Owing to its high gain, compact form factor, and excellent on-body safety characteristics, the proposed MIMO antenna serves as a strong candidate for next-generation wearable and body-centric communication systems in the mm-wave 5G spectrum.

***

Chapter 4

Dual-Band CSRR-Loaded Two-Port MIMO Antenna Array

Building upon the AMC-backed MIMO antenna developed in Chapter 3 for wearable WBAN applications, this chapter advances the design framework by introducing a dual-band, high-gain MIMO antenna array operating in the mm-wave range. In the previous chapter, an annular slot was etched in the ground plane to enhance the impedance bandwidth, however this resulted in an undesired backside radiation, which was mitigated by deploying an artificial magnetic conductor (AMC) layer. The AMC not only suppressed backward radiation but also enhanced the antenna's forward gain, making it suitable for on-body WBAN environments.

In contrast, the antenna presented in this chapter incorporates a complete ground plane, effectively eliminating backside radiation without requiring an external AMC surface. This modification leads to a more compact and mechanically robust structure, making it inherently safer for on-body operation. Furthermore, by employing a two-element array configuration, the proposed design achieves enhanced gain through constructive array radiation, while maintaining excellent impedance matching and broadside directivity.

In addition, complementary split ring resonators (CSRRs) are integrated in the antenna deign to achieve dual-band operation within the 28 GHz (n257) and 38 GHz (n260) bands. The CSRRs introduce an additional higher-order resonance and facilitate frequency miniaturization through localized EM coupling. This enables efficient multi-band performance without increasing the antenna's physical footprint.

4.1 Single Antenna and Antenna Array

A rectangular microstrip patch antenna with optimized dimensions of length (L_{patch}) and width (W_{patch}) can be designed using Equations (4.1) and (4.2) [11]:

$$L_{patch} = \frac{c}{2f_r\sqrt{\varepsilon_{eff}}} - 2\Delta L \tag{4.1}$$

$$W_{patch} = \frac{c\sqrt{2}}{2f_r\sqrt{1+\varepsilon_r}} \tag{4.2}$$

where, c is the speed of light, f_r is the resonance frequency, ε_r denotes dielectric constant of the substrate, ε_{eff} denotes effective dielectric constant, and ΔL accounts for the fringing effect [114], [115] occurred in the antenna geometry.

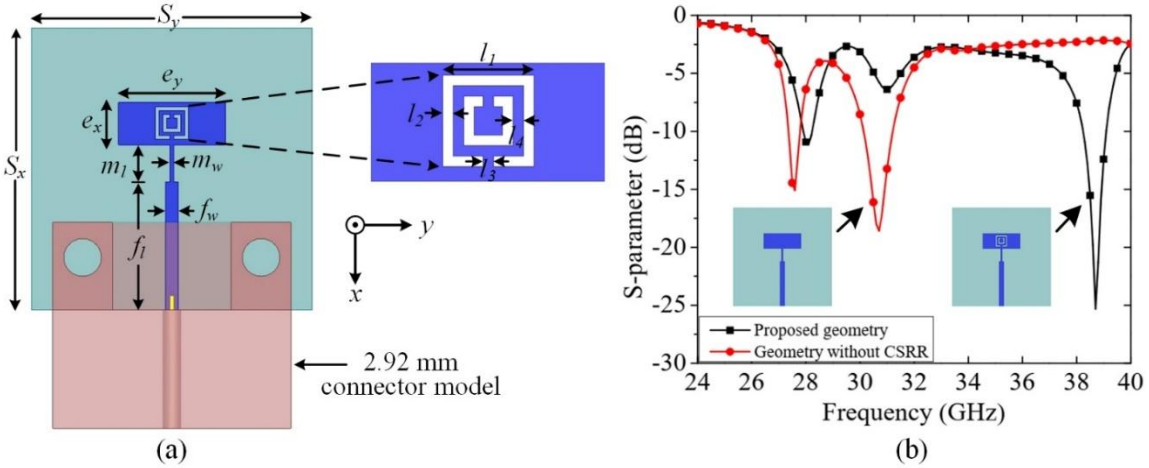

Figure 4.1: (a) Proposed single antenna geometry with the connector model, and (b) simulated reflection coefficient (S_{11}) of the antenna topology with and without CSRR loading. The geometric dimensions are: $S_x = S_y = 15$, $f_l = 15$, $f_w = 0.7$, $m_l = 2$, $m_w = 0.2$, $e_x = 2.25$, $e_y = 5.7$, $l_1 = 1.74$, and $l_2 = l_3 = l_4 = 0.2$ (unit: mm).

The reference rectangular patch antenna, based on the above design equations, is initially realized at 28 GHz, and a CSRR is then etched at the centre of the patch to obtain the second resonance at around 38 GHz [116]. Rogers RO 4003(TM) substrate (having a thickness of 0.3 mm) with relative permittivity of 3.55 and loss tangent of 0.0027 is considered as the dielectric.

Figure 4.1(a) demonstrates a pictorial representation of the suggested antenna along with a 2.92 mm connector model. The comparison of S_{11} response with and without CSRR is presented in Figure 4.1(b). It can be seen that the loading of CSRR causes a reduction in the resonance frequency of the patch antenna by around 2 GHz, along with generating the second resonance at 38 GHz. Thus the CSRR not only introduces another band of operation but also leads to the miniaturization of the antenna topology. The overall antenna dimensions are thus reduced to $0.21\lambda_o \times 0.53\ \lambda_o \times 0.028\ \lambda_o$, where λ_o is the free space wavelength at 28 GHz. Further, it is witnessed that the proposed design demonstrates an impedance bandwidth (S_{11} < -10 dB) of 0.58 GHz in 28 GHz band and 0.76 GHz in 38 GHz band.

Few parametric analyses with respect to the patch width (p_y) and horizontal offset positions of CSRR (d_y) are shown in Figures 4.2(a) and 4.2(b), respectively, for in-depth analysis. The reflection coefficient (S_{11}) has been studied during this parametric variation.

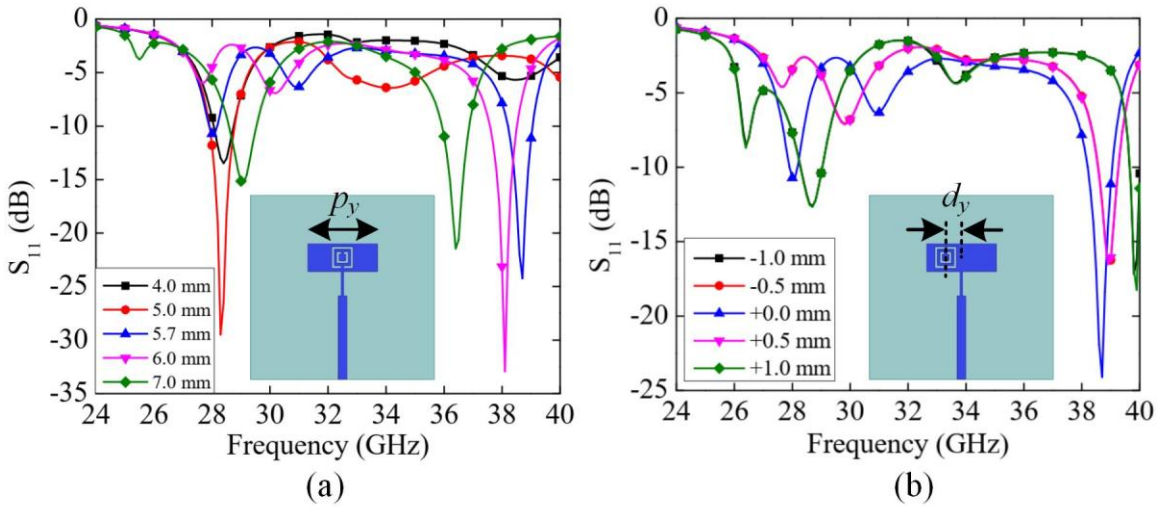

Figure 4.2: Simulated parametric variation of S_{11} with respect to: (a) patch width (p_y), and (b) horizontal offset positions of CSRR (d_y).

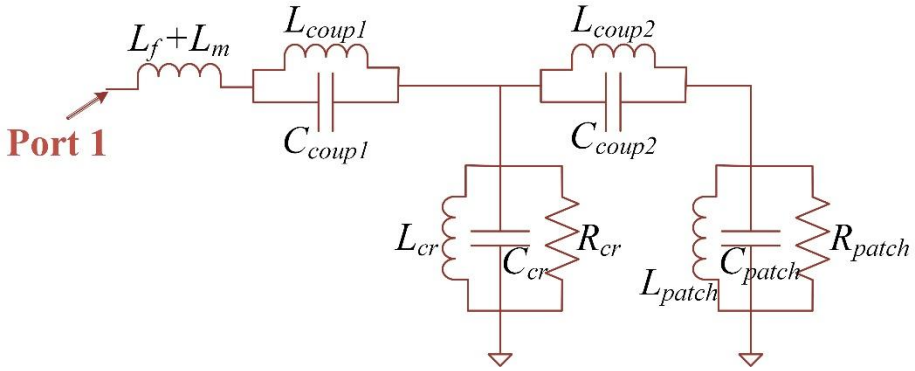

Figure 4.3: Equivalent circuit model of the proposed single antenna geometry. The circuit parameters derived are: L_{cr} = 0.028 nH, C_{cr} = 0.63 pF, L_{patch} = 0.035 nH, C_{patch} = 0.92 pF, L_{coup1} = 0.015 nH, C_{coup1} = 1.23 pF, L_{coup2} = 0.026 nH, and C_{coup2} = 0.98 pF.

An equivalent circuit model is used to describe the behavior of the CSRR loading effect. The CSRR geometry is excited by an orthogonal electric field and exerts a combination of inductance (L_{cr}), capacitance (C_{cr}), and resistance (R_{cr}), accounting for both dielectric loss and conductor loss. The microstrip patch also produces a *RLC* combination (L_{patch}, C_{patch}, and R_{patch}), whereas the couplings between the CSRR and patch are represented by L_{coup1}, C_{coup1}, L_{coup2}, and C_{coup2}. The feed-line is represented by inductance L_f and matching transformer is represented by inductance L_m. The component values are obtained through curve-tracing

method with the help of Advanced Design System (ADS) software and are presented in the caption of Figure 4.3.

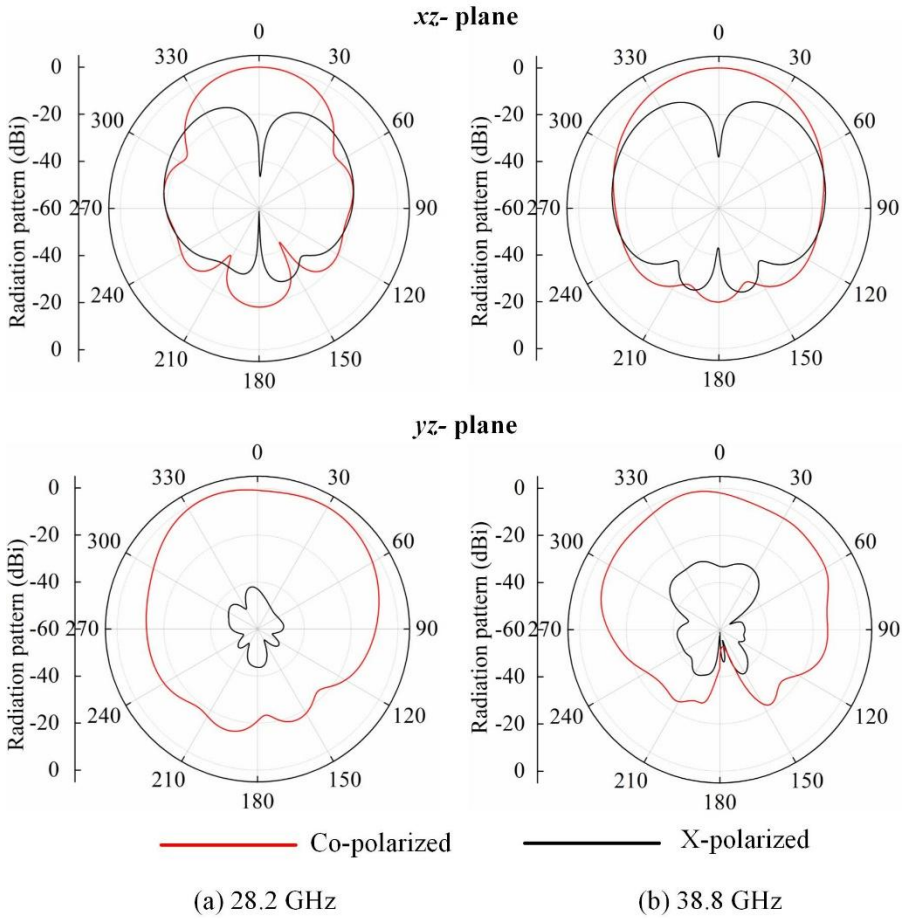

Figure 4.4: Simulated radiation patterns of single antenna in E-plane (Top), H-plane (Bottom) at (a) 28.2 GHz, (b) 38.8 GHz.

The simulated radiation patterns of the single antenna are demonstrated at 28.2 GHz and 38.8 GHz, indicating an overall broadside radiation direction at both resonance frequencies. Figure 4.4. presents the radiation patterns in E-plane and H-plane for both 28 GHz and 38 GHz.

To implement the array geometry, a power divider, as depicted in the Figure 4.5(a), is conceptualized. Its corresponding amplitude response and phase characteristics are displayed in Figures 4.5(b) and 4.5(c), respectively. The geometry divides the power evenly among the output ports 2 and 3, as observed from the scattering parameters. Thereafter, two single antenna elements are integrated with the power divider and the complete antenna array is demonstrated in Figure 4.6(a). The simulated S_{11} response is depicted in In Figure 4.6(b) showing -10 dB impedance bandwidth of 0.91 GHz in 28 GHz band and 0.68 GHz in 38 GHz band. Further, it

is witnessed that with the array structure, the simulated peak gain at 28.2 GHz increases from 7.26 dBi to 10.21 dBi, while at 38.8 GHz, it increases from 10.06 dBi to 12.30 dBi.

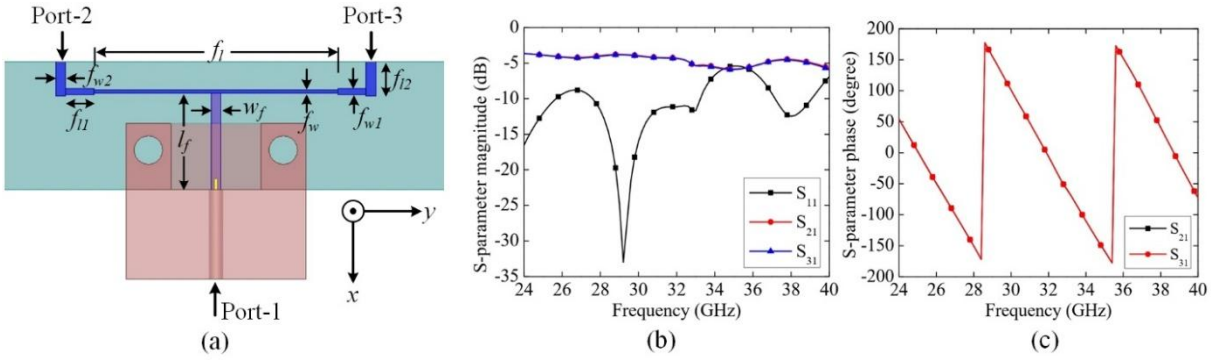

Figure 4.5: (a) Proposed 1× 2 power divider design. Simulated S-parameters of the power divider: (b) amplitude response, and (c) phase response. The geometric dimensions are as follows: $l_f = 6.8$, $w_f = 0.7$, $f_l = 17.2$, $f_w = 0.23$, $f_{l1} = 2$, $f_{w1} = 0.46$, $f_{l2} = 2.4$, $f_{w2} = 0.7$ (units: mm).

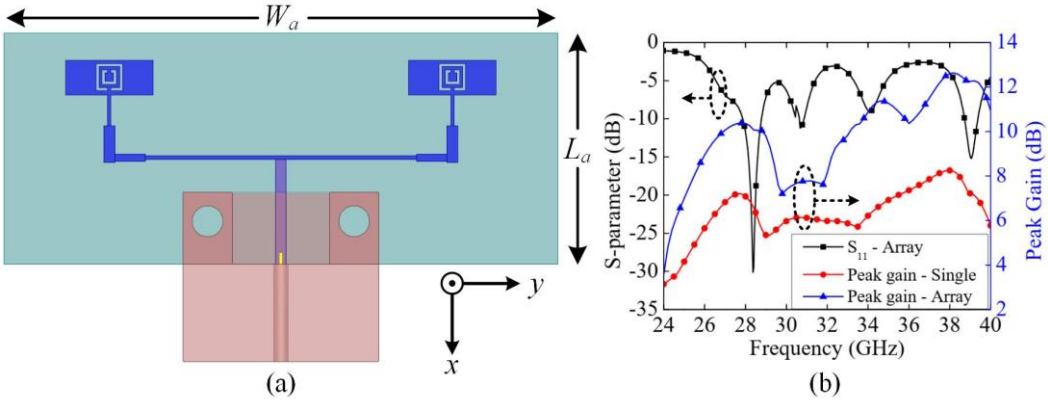

Figure 4.6: (a) Schematic diagram of proposed antenna array, (b) Simulated scattering parameter and comparison between simulated gains of single antenna and array structure. The overall array size is: 15 mm x 08 mm ($W_a \times L_a$).

4.2 MIMO Antenna Array

A MIMO antenna array offers significant advantages over a conventional antenna array by combining array gain with spatial diversity and multiplexing capabilities. While a traditional array primarily enhances directivity and beamforming, a MIMO array additionally improves channel capacity, mitigates fading through diversity, and supports multiple parallel data streams. Unlike the previous chapter, which focused solely on a MIMO antenna, this chapter extends the work by developing a MIMO antenna array to harness the combined advantages of

MIMO diversity and array gain. This hybrid configuration results in superior throughput, reliability, and system performance, making it suitable for advanced wireless applications.

4.2.1 Design and Fabrication

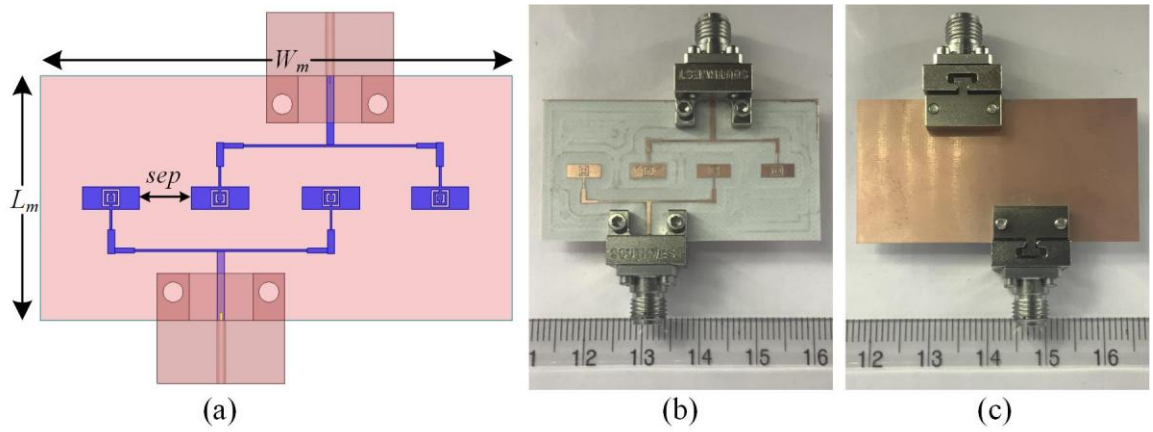

Figure 4.7: (a) Schematic representation of the proposed two-port MIMO antenna array. Fabricated prototypes of the two-port MIMO antenna array: (b) top view and (c) bottom view.

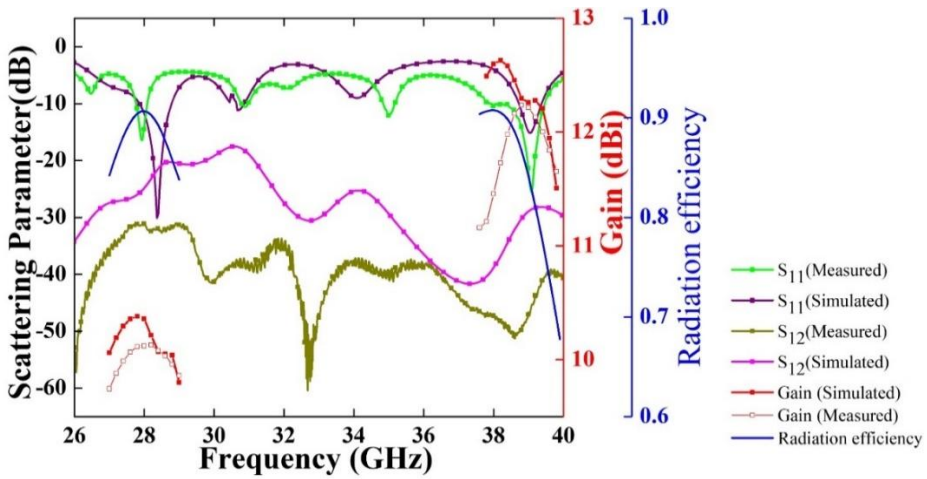

Figure 4.8: Simulated and measured scattering parameter responses (S_{11}, S_{12}), gain, and radiation efficiency for the proposed two-port MIMO antenna array.

A two-port 1 × 2 MIMO antenna array geometry is realized by smartly placing the individual array antennas in an interdigital configuration, as shown in Figure 4.7(a). Each of the two-port MIMO antenna is further made of a 1 × 2 array configuration, where the antenna elements are fed through a corporate power divider. The physical extents of the antenna geometry and the substrate properties are unchanged, however, the separation (*sep*) among the CSRR loaded patches is taken as 5.15 mm, based on the iterative optimization procedure. Figures 4.7(b) and

4.7(c) illustrate the top and bottom sides of the fabricated prototype, respectively, which has been manufactured using the LPKF S104 Protomat milling machine.

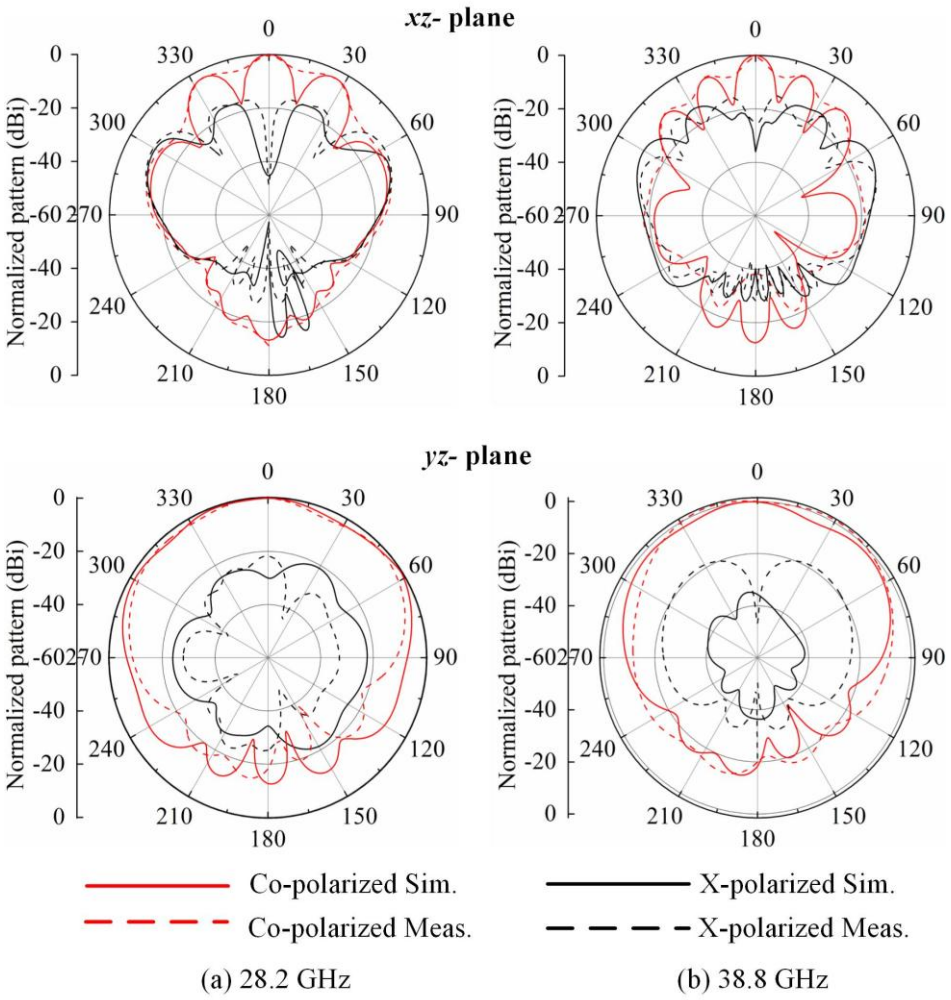

Figure 4.9: Simulated and measured radiation patterns of the proposed MIMO array antenna in E-plane (Top), H-plane (Bottom) at (a) 28.2 GHz, (b) 38.8 GHz.

Figure 4.8 shows the scattering parameters, both simulated and measured, for the proposed two-port MIMO antenna array. The reflection coefficients of each of the antenna elements are similar to those of a single antenna, and the isolation between the two ports is consistently less than 20 dB throughout the functional range. The operating bands, defined as S_{11} less than -10 dB, are in the range of 27.87 GHz - 28.78 GHz and 38.72 GHz - 39.4 GHz. As the two ports are symmetrical, only Port 1's scattering parameters are displayed. The simulated gains of the proposed geometry are 11.35 dBi at 28.2 GHz and 12.35 dBi at 38.8 GHz, while the simulated radiation efficiencies are 83.4% at 28.2 GHz and 77.8% at 38.8 GHz. The measurements were carried out with an Anritsu S820E Vector Network Analyzer (VNA) between 26 and 40 GHz [117], [118]. The measured gain for the fabricated MIMO antenna array at 28.2 GHz is 10.13

dBi, while at 38.8 GHz it is 12.23 dBi. In Figure 4.9, the simulated and measured radiation patterns of the array configuration of Antenna are demonstrated at 28.2 GHz and 38.8 GHz, indicating an overall broadside radiation direction at both resonance frequencies.

4.2.2 MIMO Parameters

For the suggested design, several important MIMO specifications have been examined. The simulated value of *ECC* is well below 0.1 (which is the desired value) at both operational frequencies (28 GHz and 38.8 GHz), as presented in Table I. For the highest *ECC* across both bands of operation, the calculated *DG* exceeds 9.99 dB.

Table 4.1: ECC / ACC, DM, PDGR, and ME for MIMO Antenna Array

Frequency (GHz)	$\lvert ACC_{12} \rvert = ECC$	*DM*	*PDGR*	*ME (dB)*
28.2	7.52×10^{-4}	3.99999544	1.14×10^{-4}	-0.78
38.8	2.415×10^{-3}	3.99995334	1.1665×10^{-3}	-1.09

The diversity performance of MIMO antennas, however, cannot be evaluated holistically using the terms *ECC* and *DG*. So diversity order (*DO*) and diversity measure (*DM*), as suggested in Ref. [48], are also investigated in this work using the antenna correlation coefficient (*ACC*) matrix. Table I shows that percentage diversity gain reduction (PDGR) is 0.000114% at 28 GHz and 0.0011665% at 38 GHz, indicating excellent diversity performance of the designed MIMO array antenna, primarily owing to the orthogonal arrangement of the two ports. From Table 4.1, it can be seen that the proposed MIMO antenna provides a very good multiplexing efficiency (ME) value.

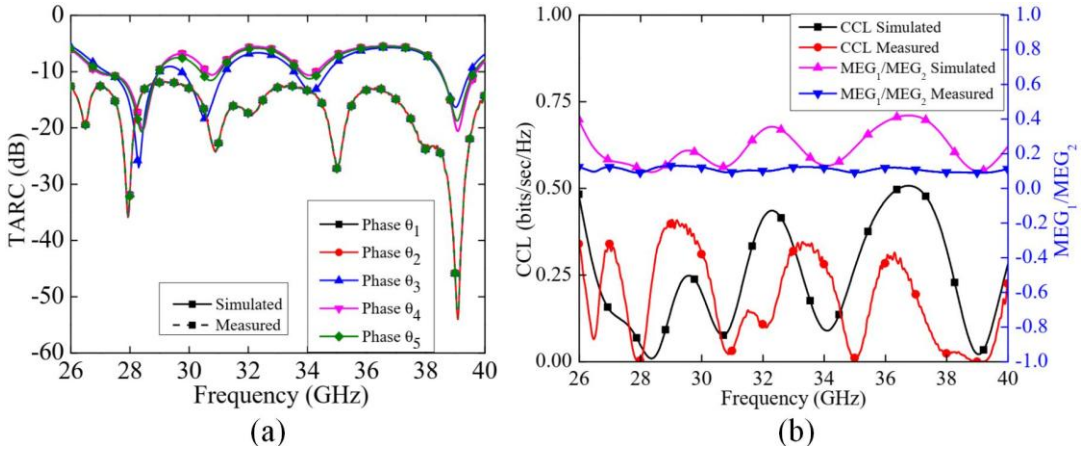

Figure 4.10. Simulated and measured MIMO performance specifications of the proposed two-port MIMO antenna array: (a) TARC, and (b) CCL and MEG.

Figure 4.10(a) illustrates TARC plots for the proposed 2-port MIMO antenna array. TARC is obtained for five values of random phases (θ_1, θ_2, θ_3, θ_4, θ_5), and all cases exhibit strong convergence. This suggests that the proposed antenna is insensitive to phase changes. The measured TARC curves for five values of random phases are also in close conformity with the simulated curves, indicating a good performance of the MIMO system. From Figure 4.10(b), it is observed that the ratio of MEG for both simulated and measured responses of the designed MIMO antenna array is within the mentioned limits for the entire operating band. The simulated and measured correlation-induced CCL are also shown in Figure 4.10(b), and both are found within the anticipated value (< 0.5 bits/seconds/Hz).

4.3 Safety Analysis and Human Body Loading Analysis

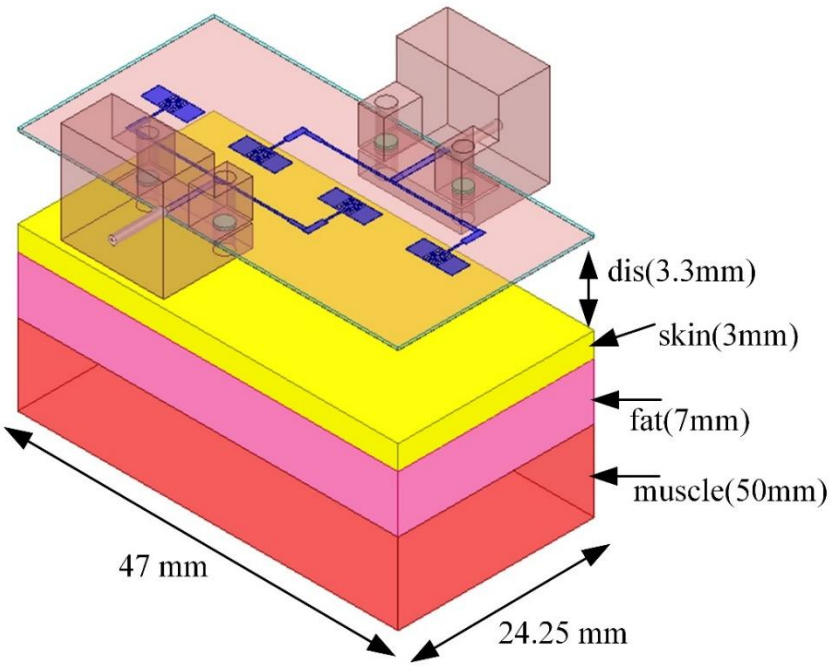

Figure 4.11: Frequency dependent three-layer human body model.

To assess the energy absorption at mm-wave frequency range in the human body, spatial power density (SPD) of the proposed MIMO antenna array is evaluated on a three-layer (i.e. skin, fat, and muscle) human body model, similar to the one considered in the previous chapter. The length, breadth, and thickness values of different constituent materials of the human model are provided in Figure 4.11 [113]. The separation between the MIMO antenna array and the

human body model is kept as 3 mm. The characteristic parameters of human tissues such as conductivity, permittivity, loss tangent, mass density, and penetration depth at 28.2 GHz and 38.8 GHz are obtained from Ref. [103] and are mentioned in Table II. The peak SPD exposure values at 28.2 GHz and 38.8 GHz for the three-layer model corresponding to 20 dBm input power are obtained as 3.79 W/m^2 and 9.52 W/m^2, respectively. It is observed that SPD values are well below the limit of 10 W/m^2 at both bands, thereby confirming the safety of the proposed MIMO antenna array geometry for WBAN networks.

Table 4.2: 28/38 GHz constituent properties of human tissue [113]

Human Tissue	Conductivity		Relative permittivity (ε)		Loss tangent (δ)		Mass density	Penetration depth	
	28.2 GHz	38.8 GHz	28.2 GHz	38.8 GHz	28.2 GHz	38.8 GHz	28.2/38.8 GHz	28.2 GHz	38.8 GHz
skin	25.82	31.35	16.55	12.04	1.001	1.206	1114	0.919	0.665
fat	1.69	2.16	3.69	3.42	0.29	0.292	909	6.07	4.584
muscle	33.61	42.4	24.41	18.71	0.3	1.048	1103	0.84	0.599

Table 4.3 Performance Comparison of Proposed MIMO Antenna Array in Free Space and Body Worn Scenario

Parameter	**Free space (simulated)**		**On body (simulated)**	
Frequency (GHz)	28.2	38.8	28.2	38.8
B.W.(GHz)/FBW	0.91/3.25%	0.68/1.75%	0.87/3.10%	0.66/1.70%
Isolation (dB)	-18.4	-26.3	-20.51	-27.88
Peak Gain (dBi)	10.48	11.21	10.4	11.1
Radiation efficiency	84.05%	78.6%	79.58%	72.21%
ECC	0.000752	0.002415	0.001094	0.004740
TARC (dB)	-12.02	-6.6	-8.92	-5.1
CCL (bits/sec/Hz)	0.0092	0.0227	0.039	0.045

In Table 4.3, the antenna performance vis-à-vis several parameters is compared between the free space scenario and on the human body (separation 3 mm) case. It can be observed that due

to the use of the complete ground, there is high isolation between the antenna and the human body. Thus key antenna performance parameters show excellent stability in the vicinity of the human body.

4.4 Conclusion

Table 4.4 Comparative Assessment of Designed MIMO Antenna Array

Ref.	**Ports**	**Board Size (mm^3)**	**Freq (GHz)**	**B.W. (GHz)**	**Gain (dBi)**
[95]	4	26 × 19.25 × 0.79	28, 38	4, 0.37	7.58, 5.72
[119]	2	20 × 20 × 0.254	28	0.85	8
[120]	2	40 × 25 × 0.254	5.2, 24	0.1, 0.77	5,7.37
[121]	4	41.3 × 46 × 0.508	28	3.35	13.1
[122]	2	48 × 21 × 0.13	30	1	7
[58]	2	19.04 × 15.06 × 5.14	24	0.8	5.9
[123]	1	29.06 × 11.42 × 0.508	28	2	11.7
[124]	1	15 × 18.4 × 0.508	35.5	8.2	4.5
This work	**2**	**47 × 24.25 × 0.3**	**28.2, 38.8**	**0.91, 0.68**	**10.48, 11.21**

In this chapter, a dual-band two-port 1 × 2 MIMO antenna array is presented for mm-wave WBAN applications. Each of the antenna elements is made of a rectangular microstrip patch, and a CSRR is etched at the centre of the patch. The loading of CSRR leads to the miniaturization of the patch frequency as well as the introduction of a higher operating band. Subsequently, a 1 × 2 antenna array is designed, which is further extended to a two-port 1 × 2 MIMO antenna array. The performances of several key MIMO parameters are scrutinized and their values are found satisfactory for executing reliable operations. Further, detailed safety analysis and human body model analysis of the proposed MIMO antenna array are carried out and results support the fact that the proposed design is suitable in mm-wave bands (n257 and n260) for 5G WBAN applications. The final antenna array structure has also been fabricated as well as measured, whose results conform well to those of the simulated responses. The proposed geometry has been compared with the existing mm-wave MIMO antennas in Table

4.4 with respect to several matrices, such as size, frequency bands, bandwidth, and gain, and it is evident that the proposed design is significantly compact, has considerably higher gain, and has superior safety performance.

***

Chapter 5

Fabry–Perot Cavity-Backed High-Gain MIMO Antenna

Building upon the CSRR-loaded MIMO antenna array presented in Chapter 4, which demonstrated a compact dual-band operation with high isolation, this chapter focuses on further improving the gain, bandwidth, and aperture efficiency of the antenna system through the incorporation of a Fabry–Perot cavity (FPC) configuration. Although the previous design offered excellent radiation stability and compactness, the effective aperture and directivity were inherently limited by the planar patch geometry. To address these limitations, the present work introduces a Fabry–Perot cavity-backed MIMO antenna that utilizes a partially reflective superstrate placed above the radiating elements to form a resonant cavity. The constructive interference between direct and reflected waves inside the cavity enhances forward radiation, improving both gain and aperture efficiency without substantially increasing the overall profile.

Unlike AMC or array based gain enhancement techniques discussed in earlier chapters, which relied on localized surface current manipulation, the FPC approach leverages cavity resonance and controlled phase reflection to achieve broadside gain enhancement and field uniformity across the radiating aperture. The design is specifically optimized for 28 GHz operation, where achieving high directivity within a compact footprint remains a key challenge. The inclusion of the FPC effectively transforms the antenna system into a directive radiator with improved power concentration in the desired direction, making it particularly suitable for high-data-rate, line-of-sight mm-wave communication links.

To realize the cavity, three types of superstrate configurations are examined—an unprinted dielectric layer, a single-side printed partially reflective surface (PRS), and a double-side printed PRS—each positioned at an optimized distance of approximately half a wavelength above the feed antenna. The unprinted dielectric version serves as a reference model, while the printed PRS configurations introduce tunable reflection properties that enhance the constructive interference within the cavity. Through systematic simulation and optimization, the double-side PRS configuration is found to deliver the best performance, achieving a peak gain of 12.74 dBi, an aperture efficiency exceeding 90%, and stable impedance matching over

a broad frequency range. In addition, the complete ground plane effectively suppresses backside radiation and minimizes coupling between MIMO ports, ensuring reliable performance and high radiation purity.

The proposed Fabry–Perot cavity-backed MIMO antenna thus provides a compact, low-profile, and high-efficiency solution for 28 GHz mm-wave front-end modules, access points, and short-range fixed wireless links. The subsequent sections of this chapter present the antenna geometry and design methodology, the characterization of the superstrate configurations, the simulation and measurement analyses, a comparative evaluation with existing designs, and a summary highlighting the key findings and performance improvements of the proposed configuration.

5.1 Design of Proposed MIMO Antenna

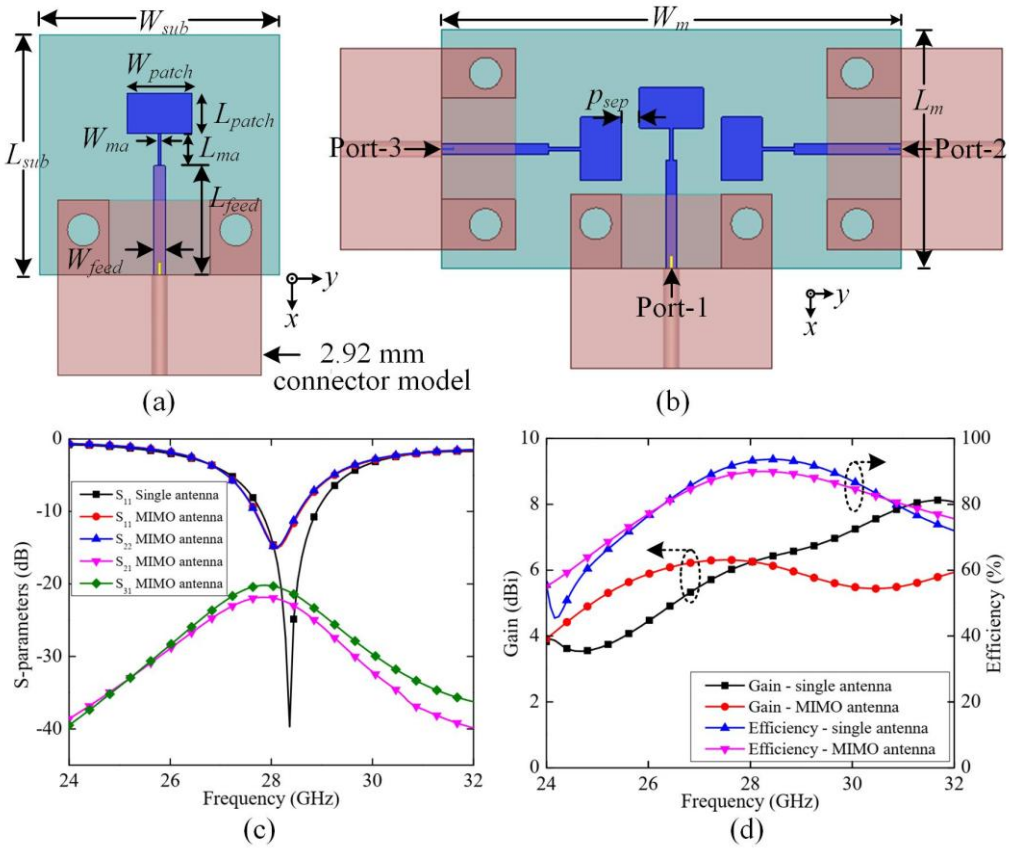

Figure 5.1: Schematic diagrams of the proposed (a) antenna element along with the connector model, and (b) its 3-port MIMO antenna configuration. Simulated responses of both antenna element and MIMO antenna: (c) scattering parameters, (d) gain and efficiencies. The geometric dimensions are: L_{sub} = W_{sub} = 15, L_{patch} = 2.54, W_{patch} = 4, L_{ma} = 2, W_{ma} = 0.2, and L_{feed} = 6.8, W_{feed} = 0.7 W_m = 29, L_{m} = 15, p_{sep} = 1.16 (unit: mm).

A rectangular patch geometry is considered as the radiating element in the proposed mm-wave antenna. The patch is fed through a microstrip line, and the overall structure is printed on Rogers RO 4003(TM) substrate with a relative permittivity of 3.55, a loss tangent of 0.0027, and a thickness of 0.3 mm. The dimensions of the patch are calculated based on the design equations [114], [115] to achieve the radiation at 28 GHz.

Once the single antenna is constructed, three elements are positioned in an orthogonal configuration to realize the three-port MIMO antenna. The individual dimensions and the substrate property are kept unchanged, and the separation between the patches (p_{sep}) is optimized to a minimum value. This straightforward yet innovative layout not only simplifies fabrication and integration, but also achieves a broadside radiation pattern with negligible back lobe, along with high aperture efficiency and excellent inter-port isolation.

Figures 5.1(a) and 5.1(b) depict the schematic geometries of the antenna element and its MIMO structure, respectively. Both geometries are simulated using Ansys HFSS 2020. The single antenna has a resonance peak around 28 GHz, with the minimum reflection coefficient (S_{11}) reaching to -40 dB at 28.26 GHz, while the antenna array shows a maximum reflection loss of 15.07 dB at 28.12 GHz. The transmission coefficients (S_{21}, S_{31}, and S_{32}) between the elements are also studied and found below -20 dB at the operating frequency, as depicted in Figure 5.1(c). The peak realized gain are observed above 6.21 dBi at 28 GHz for both single antenna and MIMO configurations, while the radiation efficiency is found around 92% for both cases, as shown in Figure 5.1(d).

5.2 Design of PRS Layers

To further improve the antenna performance, the Fabry-Perot cavity concept is utilized in the proposed design. The cavity is generally constituted by loading a superstrate above the antenna and behaving as a PRS, such that the signal undergoes multiple reflections and finally radiates with improved performance. An unprinted PRS is often replaced with a printed PRS, with patterns on either single or both sides of the superstrate, to further enhance the properties.

5.2.1 Design I: Unprinted PRS

Initially, an unprinted PRS is considered for the proposed antenna, and its operating mechanism is described using the Fabry-Perot resonance condition derived from ray tracking analysis, as illustrated in Figure 5.2(a). The antenna used in this chapter has a radiating element (rectangular patch) printed on a substrate, with the back side having a complete ground plane.

In case of unprinted PRS, a dielectric substrate is used as a superstrate at a height of H_{ca} above the ground plane of the antenna, such that the wave directly radiated through the PRS (having a phase of ϕ_d) and the waves radiated after multiple reflections between the ground plane of the antenna and the PRS (having a phase of ϕ_{gnd}) have similar phases and therefore results in a constructive interference. This interference significantly improves the directivity and other parameters of the antenna geometry. The overall reflection phase can be expressed as [73]:

$$\phi_{PRS} = \frac{4\pi H_{Ca}}{c} f_{res} + (2n-1)\pi, n = 0,1,2,3.. \quad (5.1)$$

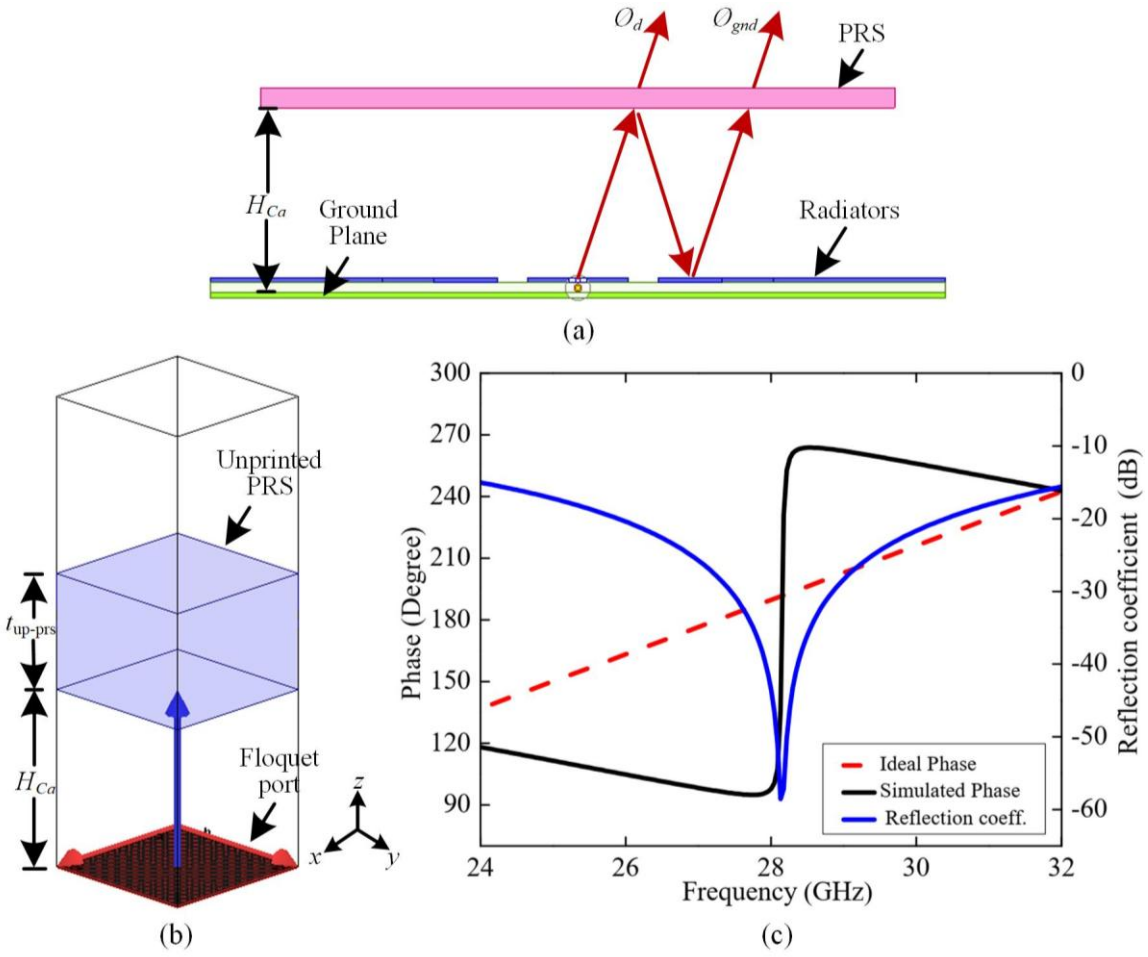

Figure 5.2: (a) Radiation mechanism in an FP cavity, (b) simulation setup using a superstrate reflection model (SRM) to characterize reflection profile, (c) simulated reflection phase and reflection coefficient of the proposed Rogers RO5880 based unprinted PRS.

Rogers RO5880 substrate (ε_r = 2.2, $tan\ \delta$ = 0.0009) with a thickness of $t_{up\text{-}prs}$ = 3.6 mm is considered as the unprinted PRS in the proposed design. The gap between the PRS and ground plane of the antenna (H_{ca}) is adjusted to approximately half-wavelength (= 5.5 mm) at the resonance frequency 28 GHz. In the simulation set up, as illustrated in Figure 5.2(b), periodic

boundary conditions (PBC) are applied along x and y directions, while a Floquet port excitation is provided along z-direction. The EM wave impinges on the PRS from z-direction.

The ideal phase characteristics of PRS, while taking n = 0 in Equation (5.1) is presented in Figure 5.2(c), where it is seen monotonically increasing with frequency. Next, the reflection coefficient (S_{11}) phase and amplitude of the unprinted PRS, calculated using a superstrate reflection model (SRM), are illustrated in the same figure, where a 180° phase reversal is observed at 28 GHz, indicating the potential of utilizing the PRS as a Fabry-Perot cavity at this frequency. The waves undergoing through multiple reflections between the ground plane (which also produces a 180° phase change) and the PRS receive a total of 360° phase difference with respect to the direct waves and therefore constructively enhance the radiation performance of the geometry.

5.2.2 Design II: Single-Side Printed PRS

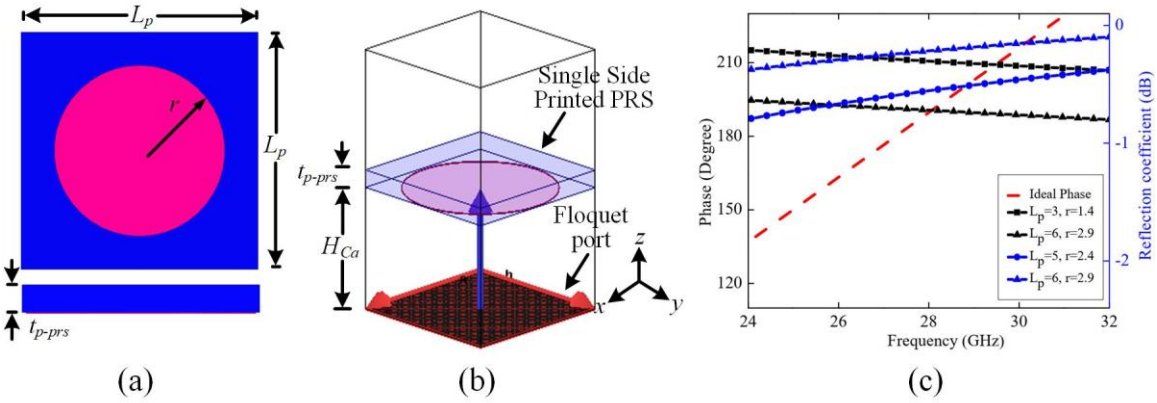

Figure 5.3: (a) Proposed single-side printed unit cell geometry, and (b) its simulation setup using SRM model. (c) Simulated S_{11} amplitude and phase responses of the geometry for different parameters (L_p and r). The final dimensions are as follows: $L_p = 6$, $r = 2.9$, and $t_{p\text{-}prs} = 0.787$ (unit: mm).

While an unprinted PRS is easy to design and deploy, a printed PRS offers a compact solution. To satisfy the Fabry-Perot cavity condition, the unprinted PRS needs to be half a wavelength thick. In contrast, the antenna profile can be reduced by employing a pattern on the superstrate that offers a bandstop solution at the resonance [125]. In this section, a single-side printed dielectric is used to construct the PRS at 28 GHz. The unit cell is based on a circular metallic patch of copper material (conductivity of 5.8×10^7 S/m) printed on the bottom side of the same substrate Rogers RO5880 having a thickness of $t_{p\text{-}prs} = 0.787$ mm. The unit cell design and its simulated setup using periodic boundary conditions are illustrated in Figures 5.3(a) and

5.3(b), respectively. Figure 5.3(c) shows simulated S_{11} amplitude and phase responses for different parameters (L_p and r), and finally the antenna geometry with L_p = 6 mm and r = 2.9 mm is chosen as its corresponding response intersects the ideal reflection phase at 28 GHz.

5.2.3 Design III: Double-Side Printed PRS

As observed in Figure 5.3(c),the S_{11} phase of the single-side printed PRS intersects the ideal phase curve at only one frequency. Further, the reflection magnitude is around 0.4 at this frequency, thereby leading to intense reflections within the cavity. This often causes radiation spillage from the sides of the cavity, and subsequently results in several grating lobes and back lobes. The problem can be alleviated by increasing the lateral dimensions of the cavity, but at the expense of compromising with the antenna aperture efficiency. A plausible solution to overcome the limitation is to introduce multiple coherent wavefront radiations on the surface of the PRS, by employing printed patterns on both sides of the superstrate [126]. The patterns will efficiently regulate the reflection phase, without increasing the antenna profile.

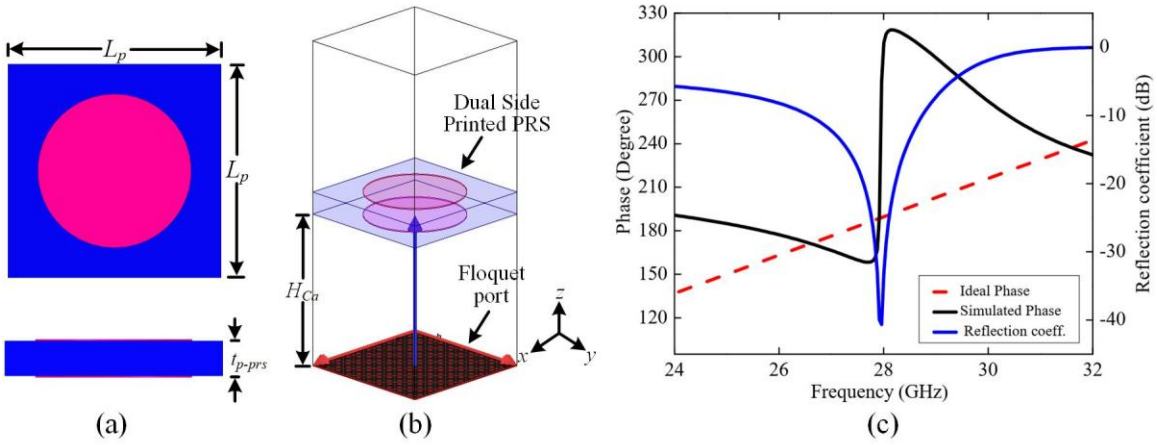

Figure 5.4: (a) Proposed double-side printed unit cell, and (b) its simulation setup using SRM model. (c) Simulated reflection amplitude and phase of the proposed double-side printed PRS. The final dimensions are as follows: L_p= 5, r=1.8, and t_{prs}=0.787 (unit: mm).

The previously designed circular metallic patch is now printed on both top and bottom sides of the dielectric. The dimensions are accordingly optimized as L_p = 5 mm and r =1.8 mm, while the thickness is kept same as before ($t_{p\text{-}prs}$ = 0.787 mm). Figures 5.4(a) and 5.4(b) depict the unit cell and its simulated setup, respectively. The simulated S_{11} phase and amplitudes are presented in Figure 5.4(c) and compared with that of the ideal reflection phase. An intersection between the ideal and simulated phase at around 28 GHz, as similar as that of the unprinted PRS, confirms the operation of the double-sided printed PRS as the Fabry-Perot cavity for the

proposed antenna. Additionally, the S_{11} magnitude is much lower compared to the single-sided printed PRS, resulting in minimal radiation spillage outside the cavity and virtually no radiation on the backside of the antenna.

To further elucidate the working mechanism of the structure, an equivalent circuit model for the double-side printed PRS based antenna geometry is depicted in Figure 5.5. Each of the metallic pattern printed on the superstrate is represented by a series *R*-*L*-*C* circuit (R_1-L_1-C_1 for the top pattern and R_2-L_2-C_2 for the bottom pattern). The capacitance is resulted from the gap between the successive unit cells, while the inductance and resistance are generated due to the metallic pattern. The microstrip patch antenna printed on the grounded substrate is modeled by a parallel combination of resistance (R_p), inductance (L_p), and capacitance (C_p), in series with another inductance (L_m) [20]. The superstrate ($t_{p\text{-}prs}$) and intermediate air spacer (H_{ca}) are represented as equivalent transmission line sections. The antenna circuit parameters are primarily responsible for the resonance at 28 GHz, while the Fabry-Perot cavity condition is generated by the superstrate assembly. With the variation in the dielectric properties and metallic pattern dimensions, the Fabry-Perot condition can efficiently be tuned to the resonance frequency, and the antenna parameters are significantly enhanced.

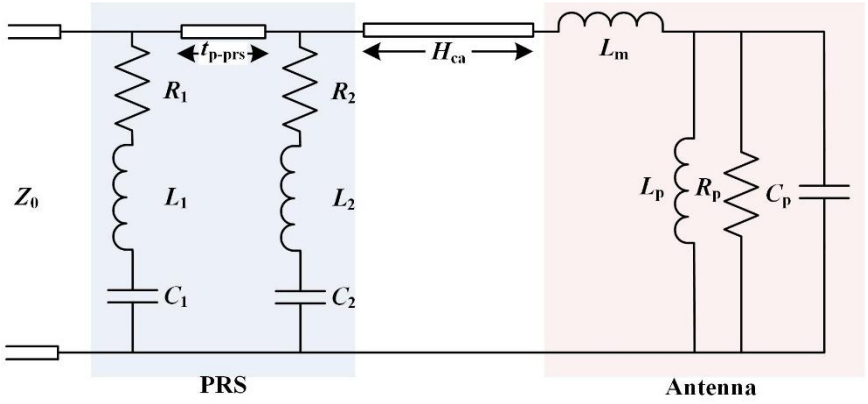

Figure 5.5. Equivalent circuit model for the proposed PRS-integrated microstrip patch antenna.

5.3 Analysis of PRS and Antenna Assembly

To observe the effects of the distance (H_{ca}) between the antenna ground plane and superstrate, parametric variations are conducted by placing different types of PRS geometries above a single antenna element and the corresponding S_{11} amplitude responses are presented in Figure 5.6. To cover the antenna size (15 mm × 15 mm), 3 × 3 unit cells of PRS arrays are considered in each case. It is observed that for the unprinted PRS design, the reflection amplitude is insensitive to the cavity height (although the phase changes are occurred as

described before), while it is most sensitive for the single-side printed PRS. In case of the double-side printed PRS, the S_{11} response is relatively constant, thereby showing its robustness over the single-side PRS structure.

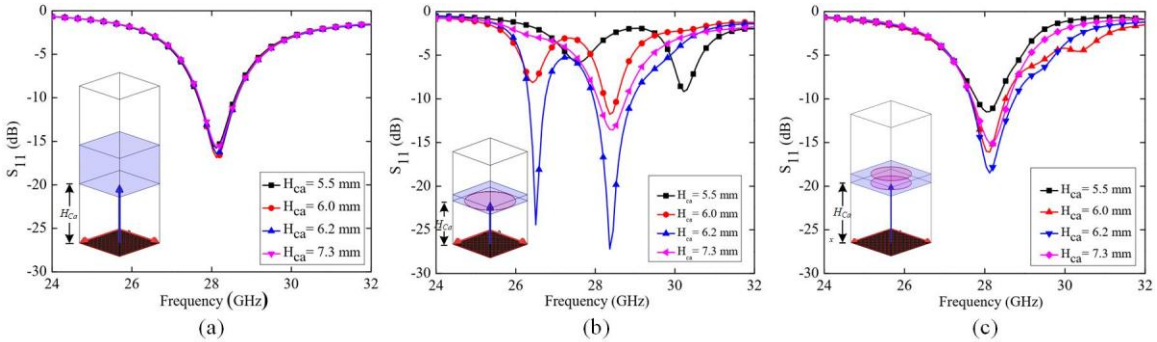

Figure 5.6: Simulated parametric variation of reflection coefficients (S_{11}) with respect to height of the cavity (H_{ca}), when a single antenna element is loaded with (a) an unprinted PRS, (b) a 3×3 single-side printed PRS array, and (c) a 3×3 double-side printed PRS array.

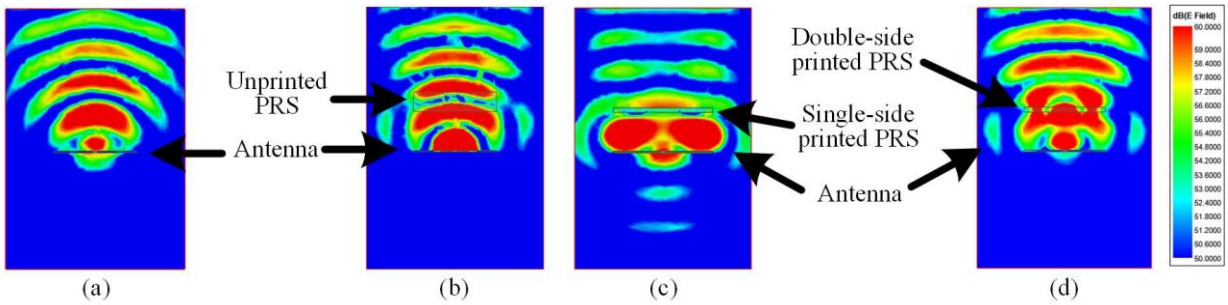

Figure 5.7: Simulated E-field distributions of the single antenna for different conditions: (a) without loading of any PRS geometry, (b) loaded with an unprinted PRS made of RO5880 (H_{ca} = 5.5 mm), (c) loaded with a 3×3 single-side printed PRS array (H_{ca} = 6.3 mm), and (d) loaded with a 3×3 double-side printed PRS array (H_{ca} = 6.2 mm).

The electric-field (E-field) distributions of the antenna structure for different loading conditions are also illustrated in Figure 5.7. It is observed that the single antenna, without the loading of any PRS structure, radiates the signal in the broadside direction (*z*-direction). With the unprinted PRS, the concentration of the E-field is further increased, consequently leading to significant gain enhancement. The improvement is diminished for the single-side printed PRS structure due to the radiation spillage, which is again restored in the case of the double-side printed configuration.

5.4 Fabrication and Measurement

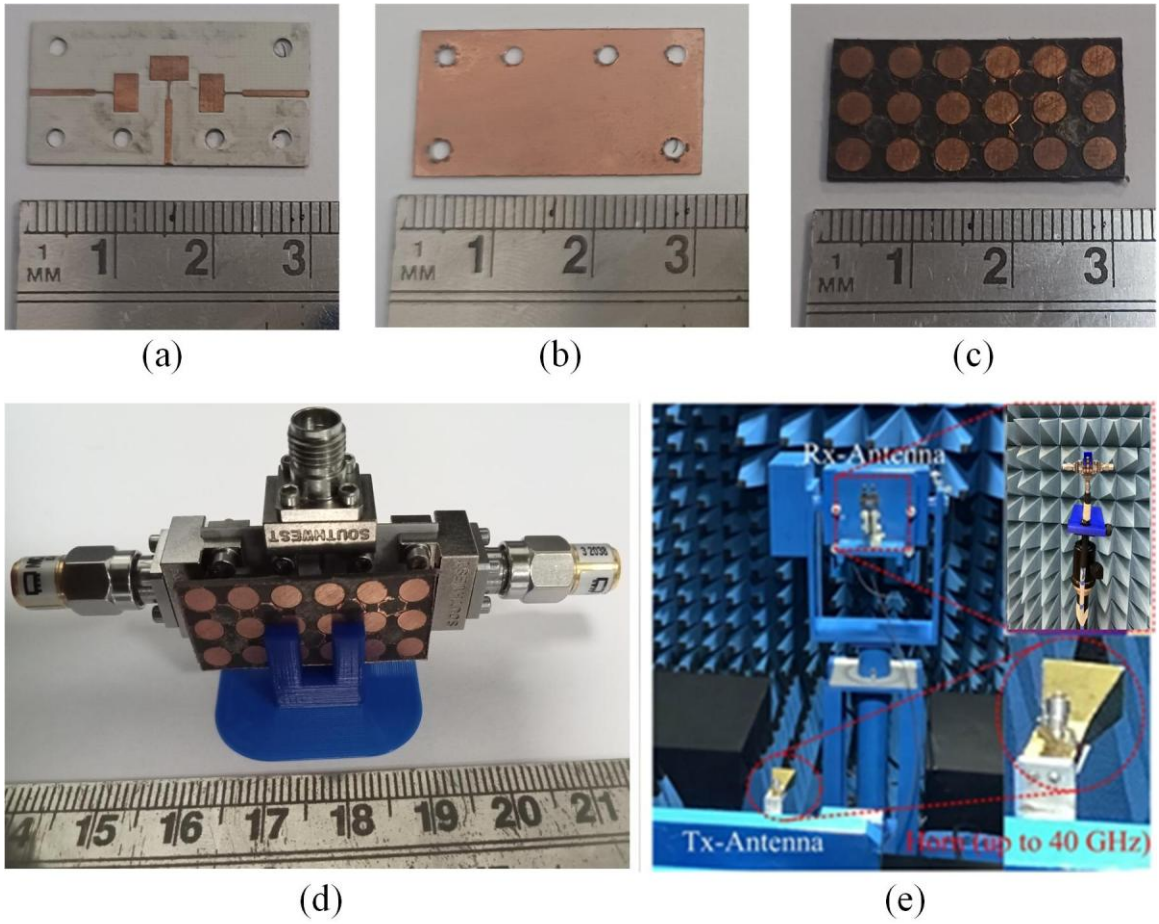

Figure 5.8: Photographs of the fabricated prototype: (a) top side and (b) bottom side of the designed three-port MIMO antenna, (c) 3×6 double-side printed PRS array, and (d) overall antenna and PRS assembly. (e) Experimental setup of the antenna inside an anechoic chamber.

To demonstrate the proposed concept, the three-port antenna array and different PRS structures are fabricated using the printed circuit board etching method. Figures 5.8(a) and 5.8(b) depict the top and bottom sides, respectively, of the MIMO antenna prototype, and the double-side printed PRS surface is shown in Figure 5.8(c). The MIMO dimension is 29 mm × 15 mm, and therefore, the PRS arrays are made of 6 × 3 unit cells (= 30 mm × 15 mm) to cover the entire antenna. A 3-D printed support made of polylactic acid (PLA) filament is used to maintain the necessary gap between the antenna and PRS, and the overall assembly is presented in Figure 5.8(d). Millimeter-wave connectors from Southwest are used at each port of the MIMO antenna, and the same connector model is used in the simulation setup as well. Initially, the S-parameters of the antenna are measured for different PRS loading conditions, followed

by characterizing the gain and radiation patterns. The experimental setup inside the anechoic chamber is illustrated in Figure 5.8(e).

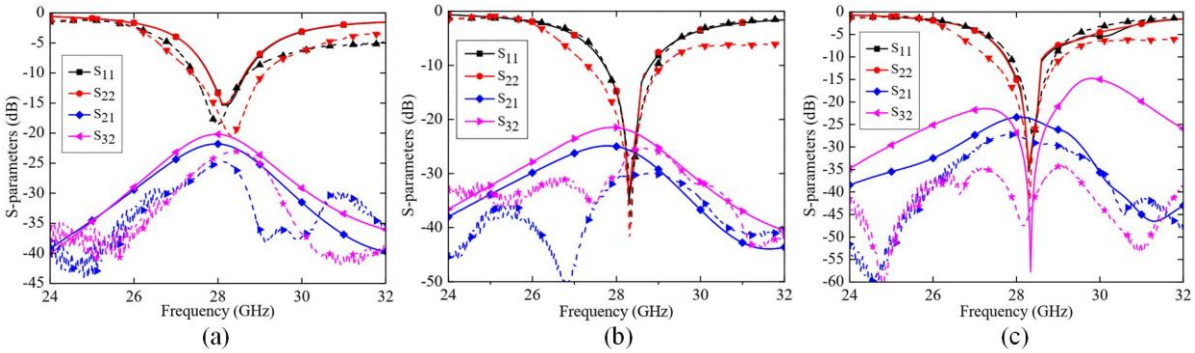

Figure 5.9: Simulated and measured S-parameters of the proposed MIMO antenna for different cases: (a) without loading any PRS (i.e. only antenna geometry), (b) loaded with unprinted PRS, and (c) loaded with double-side printed PRS. The solid and dashed lines represent simulated and measured responses, respectively.

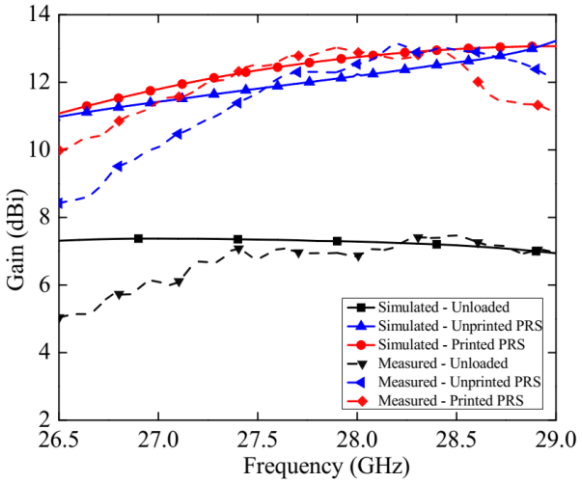

Figure 5.10: Simulated and measured broadside gain of the proposed MIMO antenna (Port 1) for all cases (i.e., without loading any PRS, loaded with unprinted PRS, and loaded with double-side printed PRS).

The simulated and measured S-parameter responses of the MIMO antenna are presented for three cases, viz. without loading any PRS (i.e. only antenna geometry), loaded with an unprinted PRS, and loaded with a double-side printed PRS. Since Ports 2 and 3 are identical and symmetrically placed, responses from only Port 2 are presented along with Port 1 for the above three cases in Figure 5.9. It is observed that both ports exhibit nearly identical reflection responses across all three cases (without loading, unprinted PRS, and double-side printed PRS). The resonance frequency is nearly maintained at 28 GHz, even after the geometry loaded with

the unprinted or printed PRS. The transmission coefficients between the ports (S_{21} and S_{32}) are also plotted. It is observed that the isolation remains below 20 dB throughout the operating range and there is no significant degradation after the PRS loading. In fact, the isolation between Ports 2 and 3 (i.e. S_{32}) is further improved to around 30 dB for the double-side printed PRS. The measured responses also align well with the simulated ones for all the cases.

Figure 5.10 depicts the simulated and measured broadside gain of the antenna, both before and after incorporating the PRS superstrates. The antenna without the PRS achieves a typical low gain of 7.2 dBi. In contrast, the antenna loaded with the unprinted PRS demonstrates a simulated gain of 12.24 dBi, while the double-side printed PRS configuration shows a simulated gain of 12.74 dBi at 28 GHz. The measured gain values closely match with the simulated ones in all cases.

Additionally, there is a significant improvement in the aperture efficiency with the inclusion of the PRS geometry. The maximum gain (G_{max}) achievable by an antenna having an aperture area of A_{eff} can be calculated using Equation (1.2). Assuming 100% radiation efficiency, G_{max} can be computed as 13.92 dBi for an aperture area of 15 mm × 15 mm at 28 GHz. Thus, the antenna without any PRS loading and a gain of 7.2 dBi has an 51.7% aperture efficiency, while the inclusion of the unprinted PRS and double-side printed PRS increases the efficiency value to 87.9% and 91.5%, respectively. This confirms that the proposed PRS-based antenna structures are highly aperture efficient.

Table 5.1. Simulated and Measured gains of the Proposed MIMO antenna

Gain (dBi)	**Unloaded**			**Unprinted PRS**			**3×3 Double-Side Printed PRS Array**			**3×6 Double-Side Printed PRS Array**		
Ports	1	2	3	1	2	3	1	2	3	1	2	3
Simulated	7.9	7.1	7.1	12.2	12.1	12.1	12.8	12.7	12.7	12.7	12.7	12.7
Measured	7.2	7.2	7.2	12.2	12.1	12.1	12.8	12.7	12.7	12.7	12.7	12.7

Table 5.1 compares the simulated and measured gains of all ports in the proposed MIMO system under various loading conditions. The gain values for all antennas are almost the same

under analogous loading conditions. Additionally, increasing the aperture size of the double-side printed PRS array from 3×3 to 3×6 unit cells does not enhance the antenna's gain further.

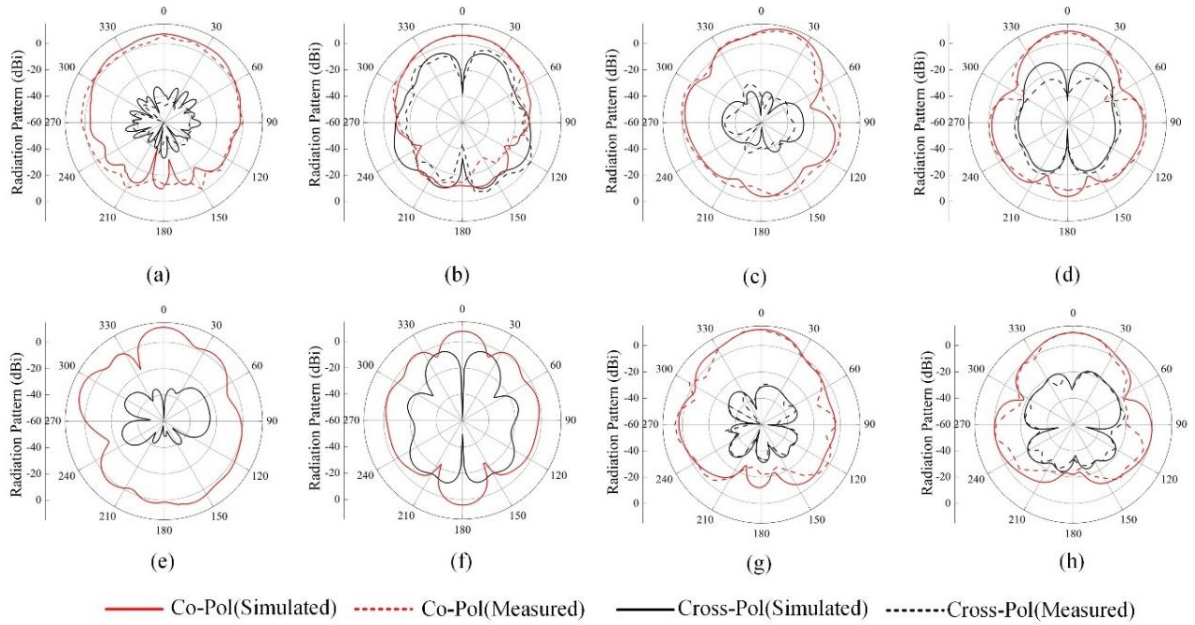

Figure 5.11: Simulated and measured radiation patterns at 28 GHz of the proposed MIMO antenna (Port 1): (a) E Plane (unloaded), (b) H Plane (unloaded); (c) E Plane (loaded with unprinted PRS), (d) H Plane (loaded with unprinted PRS); (e) E Plane (loaded with single side printed PRS), (f) H Plane (loaded with single side printed PRS); (g) E Plane (loaded with double-side printed PRS), (h) H Plane (loaded with double-side printed PRS).

The radiation characteristics of the 3-port MIMO antenna under different loading conditions are measured in the anechoic chamber. Only Port 1 is considered, and the patterns for different scenarios, such as unloaded PRS (i.e. only MIMO antenna), unprinted PRS, single-side printed PRS, and double-side printed PRS are presented in Figure 5.11. The figures clearly indicate the superiority of the double-side printed PRS vis a vis single-side printed PRS due to less cross polarization level and side lobes. Further, the simulated and measured results are in good agreement in all cases.

5.5 MIMO Characterization

To demonstrate the novelty of the proposed MIMO antenna, several important parameters, such as ECC, TARC, CCL, and MEG are computed for different PRS loading conditions (unloaded, loaded with unprinted PRS, and loaded with double-side printed PRS). The simulated value of *ECC* is found well below 0.1 (which is the desired value) at the operational frequencies, as presented in Table 5.2. This indicates that ports 1, 2, and 3 can operate

independently in all three cases. Further, it can be observed that the ECC between the port 1 and port 2 is similar to that of between port 1 and port 3.

Table 5.2. ECC between Various Ports of MIMO Antenna

Freq. (GHz)/ ECC	**ECC_{12}**			**ECC_{13}**			**ECC_{23}**		
	Case I	**Case II**	**Case III**	**Case I**	**Case II**	**Case III**	**Case I**	**Case II**	**Case III**
27.8	0.0062	0.0033	0.0076	0.0062	0.0031	0.0081	0.0052	0.0037	0.0019
28	0.0046	0.0021	0.0016	0.0045	0.0021	0.0014	0.0036	0.0026	0.0011
28.2	0.0059	0.0011	0.0050	0.0056	0.0011	0.0049	0.0034	0.0021	0.0014

Case I: Unloaded, Case II: Loaded with unprinted PRS, Case III: Loaded with double-side printed PRS.

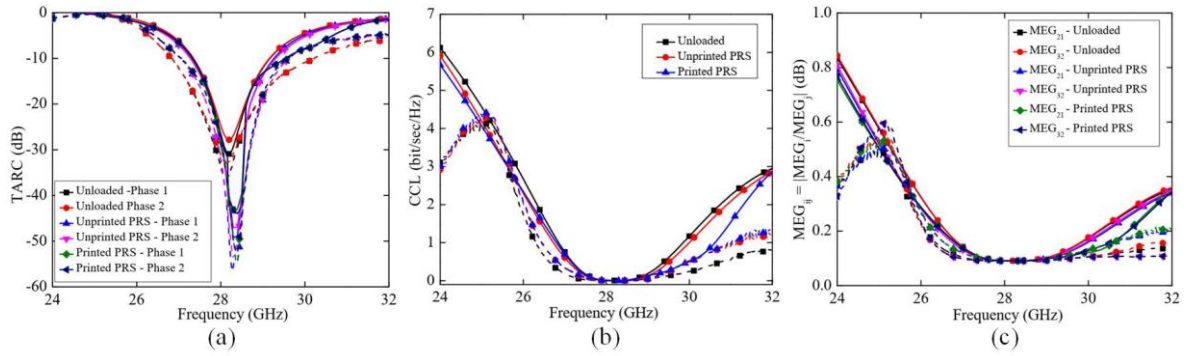

Figure 5.12: Performance specifications of the proposed MIMO antenna: (a) TARC, and (b) CCL, and (c) MEG. The solid and dashed lines represent simulated and measured responses, respectively.

Figure 5.12(a) presents the TARC plots for two random phase values (θ_1, θ_2) across all cases, and their responses are observed below -10 dB at 28 GHz. The measured curves are also in close conformity with the simulated curves, indicating a good performance of the MIMO system. Both the simulated and measured CCL values are presented in Figure 5.12(b), and are found within the anticipated value (< 0.5 bits/seconds/Hz). As observed from Figure 5.12(c), both the simulated and measured MEG ratios for different ports of the proposed MIMO antenna lie well within this acceptable range across the entire operating frequency band.

Table 5.3. Comparison with reported 28 GHz Superstrate based MIMO Antennas

Ref.	No. of Port	Overall size (λ^3)	Freq. range (GHz)	Max. Isolation (dB)	Number of types of superstrate(s)	PRG (dBi)	AE (%)
[82]	2	3.04 × 4.92 × 0.6	13.48-16.95	-40.8	1 layer; PPRS and reflector	21.59	N.R.
[83]	4	2.89 × 2.89 × 0.5	12.87-45.02	-52.53	1 layer; PPRS	11.93	84
[84]	4	2.52 × 2.52 × 0.47	28-33	N.R.	2 layers; PPRS	8	61.5
[127]	4	1.58 × 1.58 × 0.7	25-33	-30	1 layer; UPRS	14.1	N.R.
[128]	1	1.89 × 1.89 × 0.55	27.1-29.5	NA	1 layer; UPRS	16	97.4
[129]	4	2.89 × 2.89 × 0.39	23.5-29.4	-32.5	1 layer; Metasurface	10.44	59.2
[130]	4	2.80 × 4.01 × 0.64	24.55 - 26.5	-45	1 layer; PPRS	10.27	66.6
[131]	1	1.92 × 1.91 × 0.62	27.38-33.34	NA	1 layer; PPRS	12.7	76.5
[132]	4	2.24 × 2.24 × 0.26	23.6-28.8	-55	1 layer; PPRS	11.4	95.2
This work	**3**	**1.4 × 2.71 × 0.85**	**27.8-28.8**	**-24.8**	**1 layer; UPRS**	**12.24**	**87.9**
		1.4 × 2.71 × 0.65	**27.8-28.8**	**-57.6**	**1 layer; PPRS**	**12.74**	**91.5**

PRG: Peak realized gain; AE: Aperture efficiency, PPRS: Printed PRS, UPRS: Unprinted PRS, NR: Not Reported

5.6 Conclusion

In this chapter, a Fabry–Perot cavity-backed high-gain three-port MIMO antenna is designed and demonstrated for 5G wireless communication applications. The proposed single-element antenna is made on a microstrip fed rectangular patch geometry, with three such elements arranged orthogonally in a compact configuration to form the MIMO system. To enhance the antenna performance, three different variants of PRS arrays are employed above the antenna at an optimized height; initially, an unprinted PRS is used, followed by a single-side printed PRS array and then a double-side printed PRS array. This progressive modification increases the antenna gain from 7.21 dBi (without PRS) to 12.24 dBi (with unprinted PRS), and further to 12.74 dBi (with double-sided printed PRS). The printed PRS structures also improve the aperture efficiency (from 51.7% during unprinted PRS to 91.5% during double-side printed PRS) and significantly enhance inter-port isolation. The proposed design is benchmarked against several reported mm-wave superstrate-based MIMO antennas operating around 28 GHz, as summarized in Table 5.3. The results indicate that the proposed antenna achieves a more compact footprint, higher gain, improved port isolation, and significantly lower correlation coefficient compared to most existing designs. Owing to these advantages, the PRS-loaded MIMO antenna system demonstrates strong potential for consideration into advanced 5G communication platforms.

***

Chapter 6

Five-Port MIMO Antenna with Polarization and Pattern Diversity

Building upon the high-gain Fabry–Perot cavity-backed MIMO antenna discussed in Chapter 5, which focused on gain enhancement and aperture efficiency, this chapter extends the design framework toward improving link reliability under multipath fading conditions through the incorporation of polarization and pattern diversity mechanisms. While the earlier designs primarily addressed gain, isolation, and safety performance, their operations were based on uniform polarization, which limited robustness in dynamic propagation environments typical of body-centric and mobile 5G systems. To overcome this limitation, the present work introduces a compact five-port mm-wave MIMO antenna system that simultaneously supports circular and linear polarizations, achieving hybrid diversity behavior within a single structure.

The proposed configuration integrates multiple radiating elements arranged orthogonally on a common substrate to generate broadside circularly polarized and end-fire linearly polarized radiation patterns. This arrangement provides both polarization and spatial diversity, enhancing signal decorrelation and minimizing polarization mismatch between the transmitting and receiving channels without requiring external decoupling structures.

The combination of broadside circularly polarized (CP) and end-fire linearly polarized (LP) radiation patterns is particularly useful in practical 5G mm-wave scenarios where devices operate in dynamic multipath environments and varying user orientations. Broadside CP radiation helps maintain stable links under polarization mismatch and device rotation, which is beneficial for handheld and wearable terminals as well as access-point connectivity. In contrast, end-fire LP radiation supports directional links along the device plane, enabling pattern diversity and improved spatial coverage in dense urban or indoor deployments. Such hybrid radiation characteristics can also be advantageous in multi-functional platforms requiring simultaneous coverage toward infrastructure (broadside CP) and peer devices or edge nodes (end-fire LP).

6.1 Antenna Design and Analysis

Figures 6.1(a) and 6.1(b) depict the top view and bottom view, respectively, of the proposed five-port MIMO antenna. The geometry consists of three rectangular patch antennas, all of which are excited using microstrip feeds. Among them, two patches (Port 4 and Port 5) are chamfered on two diagonally opposite edges to achieve the RHCP behavior in the broadside direction, whereas Port 2 patch geometry is chamfered at opposite edges to obtain the LHCP response. On the extreme ends, two dipole antennas are printed on the top and bottom sides of the substrate such that they can exhibit LP radiation in the end-fire direction. These chamfered patch and dipole elements are innovatively arranged and integrated in a compact manner in the design to achieve enhanced performance metrics. A common ground is used for all five MIMO antennas. Rogers RO5880 dielectric (ε_r = 2.2, and *tan* δ = 0.0009) with a thickness of 0.254 mm is used as the constituent dielectric substrate for the antenna. The dimensions of the patch and dipole are chosen such that each element radiates at 28 GHz. The overall structure size is 15 mm × 45.7 mm, which corresponds to 1.4λ × 4.26λ, λ being the operating wavelength at 28 GHz. A high frequency connector model (which has been used during the measurement) has been used in the simulation for accuracy.

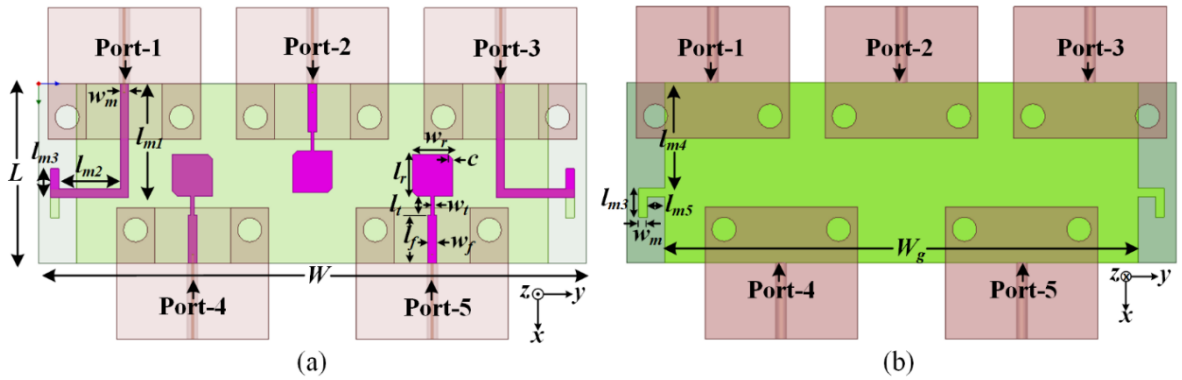

Figure 6.1: Illustration of the proposed five-port MIMO antenna design: (a) top view, and (b) bottom view. The optimized dimensions are as follows: l_f = 4, w_f = 0.77, l_t = 1.6, w_t = 0.2, l_r = 3.5, w_r = 3.35, c = 0.55, l_{m1} = 9.5, w_m = 0.7, l_{m2} = 5.1, l_{m3} = 2.4, l_{m4} = 8.8, l_{m5} = 1.45, and W_g = 23 (units: mm).

The simulated S-parameters for each port of the proposed MIMO antenna system are shown in Figures 6.2(a)-(e). The simulated -10 dB fractional impedance bandwidths (FIBWs) of the LP antennas at Ports 1 and 3 are obtained 21.05 and 25.00%, respectively, while the FIBWs of 4.28, 3.58, and 3.54% are attained for CP antennas at Ports 2, 4, and 5, respectively, each of which is computed at 28 GHz. The isolation parameters between various ports are found lower than 24 dB at the operating frequency, without any additional isolation enhancement method. This is primarily because of the intrinsic benefit of pattern diversity among five antennas. The

LP/CP pattern diversity is achieved between the adjacent ports 1 and 4, 3 and 5, whereas the RHCP/LHCP diversity is realized between the other sets of neighboring ports 2 and 4, 2 and 5. Ports 1 and 3 exhibit nearly identical resonance characteristics and fractional bandwidths due to their symmetric placement at the ends of the substrate. Similarly, Ports 4 and 5 show consistent characteristics owing to their symmetrical positioning. However, variations between Port 2 and Ports 4/5 arise from differences in polarization (LHCP vs. RHCP), mutual coupling conditions, and differences in feed orientation. The axial ratios of the CP antennas (Ports 2, 4, and 5) are depicted in Figure 6.2(f).

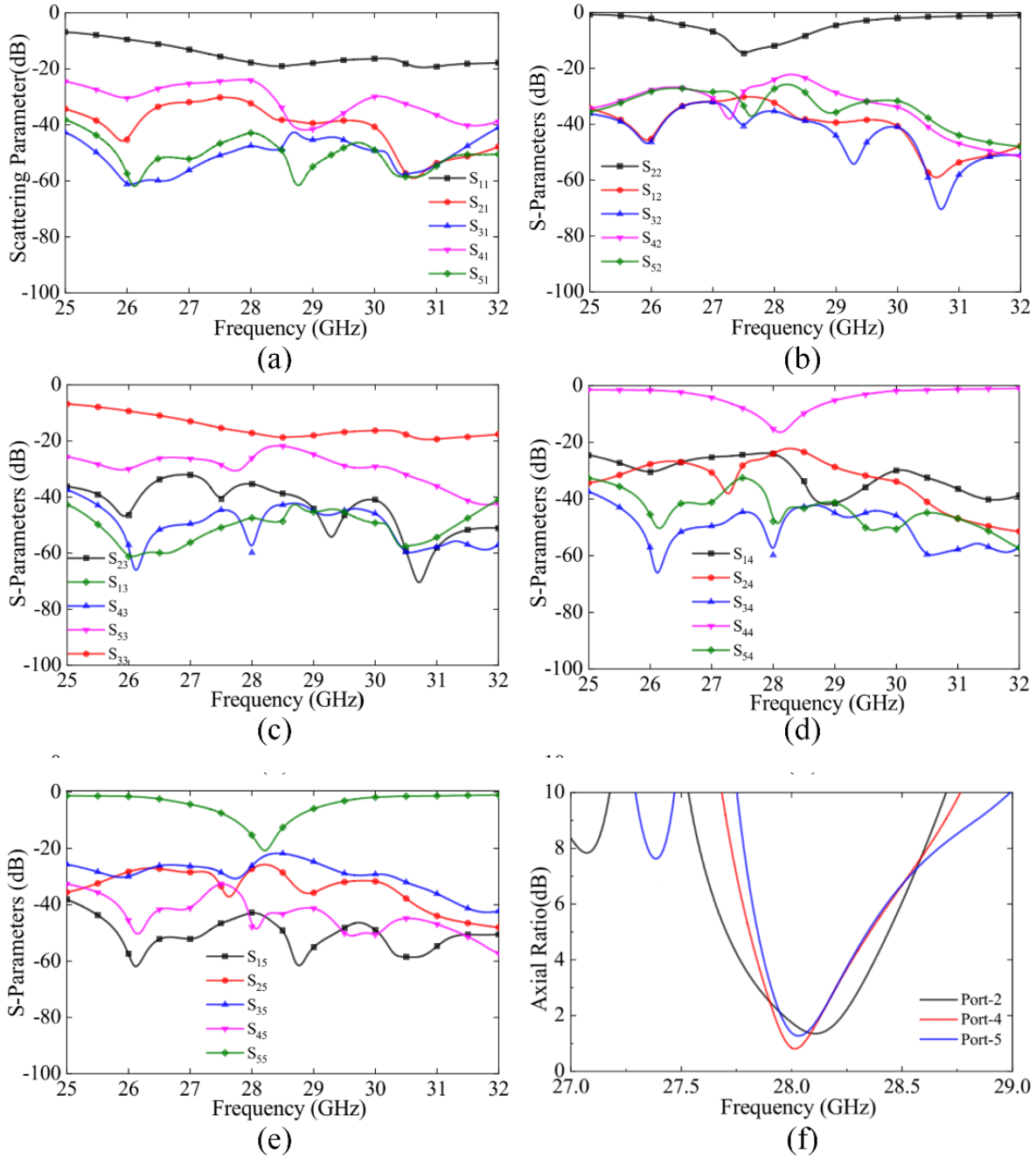

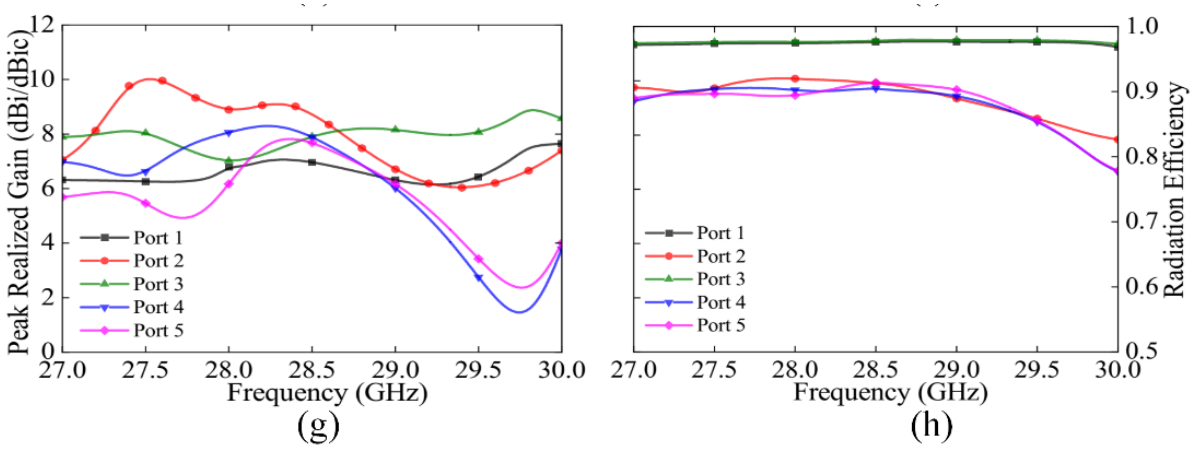

Figure 6.2: The simulated S-parameters of the proposed MIMO antenna system when: (a) Port-1, (b) Port-2, (c) Port-3, (d) Port 4, and (e) Port 5 are individually excited. (When one port is excited, others are terminated with matched loads). (f) Simulated axial ratio, when Ports 2, 4, and 5 are individually excited. (g) Simulated peak realized gain and (h) radiation efficiency, when all ports are individually excited.

The peak realized gain and radiation efficiency of individual ports are also plotted in Figures 6.2(g) and 6.2(h), respectively. It is observed that the operating gain varies between 6.8 to 7.01 dBi for LP antennas (Ports 1 and 3), whereas the gains of the CP antennas (Ports 2, 4, and 5) range from 6.2 to 9.05 dBic at 28 GHz. The radiation efficiency in each port also varies from 89% to 97% at the resonance frequencies.

Table 6.1: Impedance BW, Axial Ratio BW, and Isolation between Various Ports

Port Number	**IBW (GHz)**	**FIBW (%)**	**ARBW (GHz/%)**	**Isolation: Better than/Max (dB)**
1	26.0-32.0	21.05	NA	25.00/61.00
2	27.2-28.4	4.28	0.45/1.60	27.70/36.45
3	26.1-32.0	21.05	NA	35.00/59.80
4	27.5-28.5	3.58	0.35/1.25	24.43/59.80
5	27.7-28.7	3.54	0.30/1.07	22.00/43.67

FIBW: Fractional impedance bandwidth; NA: Not applicable (for LP antennas, ARBW is NA)

The 3-dB LHCP axial ratio bandwidths (ARBWs) range from 27.85-28.25 GHz (0.4 GHz) for Port 2. Similarly, the 3-dB RHCP ARBW of Ports 4 and 5 are 27.9 - 28.2 GHz and 27.85-28.25 GHz. All the responses are summarized in Table 6.1.

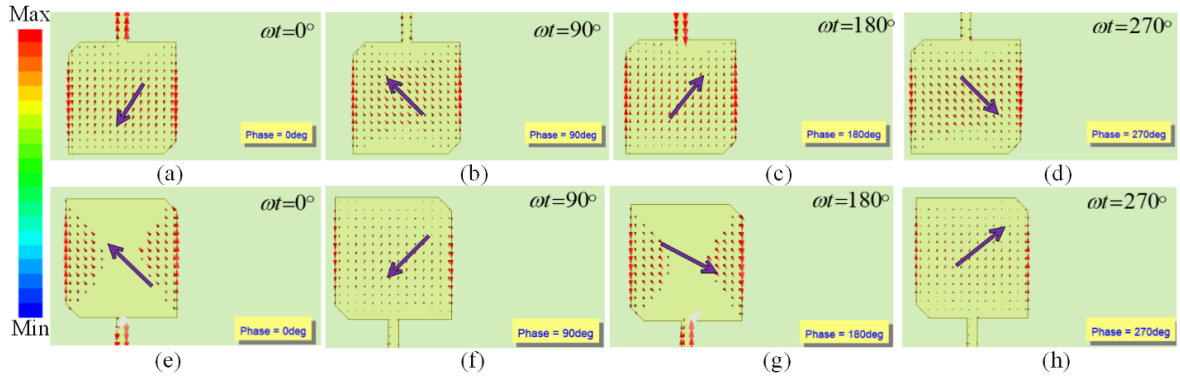

Figure 6.3: Phase variation of surface current distributions at 28 GHz, when Port-2 is fed: (a) ωt=0°, (b) ωt =90°, (c) ωt =180°, and (d) ωt =270°. Phase variation of surface current distribution at 28 GHz, when Port 4 and 5 are fed: (e) ωt=0°, (f) ωt =90°, (g) ωt =180°, and (h) ωt =270°.

The current distributions at different ports are illustrated in Figure 6.3 to analyze the antenna's polarization characteristics. The surface currents are observed in Figures 6.3(a)-(d) on Port 2 patch antenna at 28 GHz. The current direction undergoes clockwise rotation while varying the phase from 0° to 90°, and therefore emits an LHCP radiation in the direction perpendicular to the antenna. Similarly, the current distribution on Port 4 antenna is checked at 28 GHz, as depicted in Figures 6.3(e)-(h). As the phase is altered from 0° to 90°, the current vector rotates anticlockwise; hence, Port 4 antenna radiates RHCP in the broadside direction. Port 5 has a likewise RHCP behavior owing to its similarity to Port 4 antenna topology.

6.2. Fabrication and Measurement

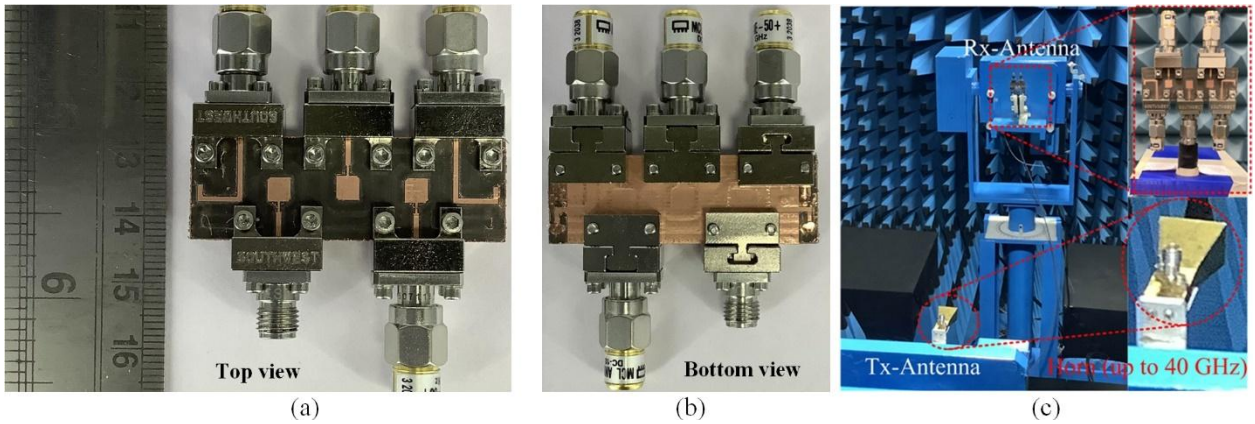

Figure 6.4: Photograph of the fabricated prototype: (a) top view, (b) bottom view. (c) Measurement setup of the proposed MIMO antenna in an anechoic chamber. Inset shows the

reference antenna and test antenna. During measurement of each port, all other ports are terminated with 50 Ω matched loads.

The proposed MIMO antenna geometry has been fabricated using standard milling technology in LPKF Protomat S104 equipment. The top and bottom views of the prototype are shown in Figures 6.4(a) and 6.4(b), respectively. SMA connectors (model no. 1092-01A-11 from Southwest) with operating frequencies up to 40 GHz are used in the design. A vector network analyzer (S820E from Anritsu) has been used to measure various antenna parameters and compare them with those of the simulated results.

The measured S-parameters for each port of the proposed MIMO antenna system are shown in Figures 6.5(a)-(e). The -10 dB fractional impedance bandwidths (FIBWs) of the LP antennas at Ports 1 and 3 are measured 21.05% and 25.00%, respectively, while the FIBWs of 3.07%, 5.85%, and 4.81% are attained for CP antennas at Ports 2, 4, and 5, respectively, each of which measured at 28 GHz. Although the measured and simulated responses are not overlaid in Figure 6.5 to avoid visual congestion, an agreement is observed across all ports. Some discrepancies in return loss depth and isolation, when compared with the simulated plots in Figure 6.2, are evident; however, such variations can be attributed to fabrication tolerances, connector parasitic effects, and measurement setup influences. Despite these differences, the measured results successfully validate the antenna's key performance parameters, including impedance bandwidth, and inter-port isolation.

The axial ratio, as well as, radiation patterns of the fabricated MIMO antenna have been measured inside an anechoic chamber and the setup is illustrated in Figure 6.4(c). One standard gain LP horn antenna (18-40 GHz) has been used as the reference antenna for computing those experiment data. The measured 3-dB axial ratio bandwidths (ARBWs) range from 27.59-28.15 GHz (0.56 GHz) for Port 2. Similarly, the measured 3-dB ARBW of Ports 4 and 5 are 27.64 - 28.05 GHz and 27.58- 28.14 GHz, respectively. Ports 1 and 5 exhibit LP responses, and hence AR parameters are not applicable for those cases.

Afterward, the radiation patterns have been measured for the fabricated MIMO antenna across different ports. Owing to the absence of any CP antenna, the same reference LP antenna has been used to measure the radiation patterns for all the ports. An innovative procedure has been adapted to use the LP antenna in measuring the antenna parameters for different CP conditions (LHCP and RHCP). The measured radiation patterns in two principal planes (*xz* and *yz* planes) for each port are plotted in Figure 6.6. Both LP dipole antennas (Ports 1 and 3)

radiate in the end-fire directions (θ = 90°, ϕ = 270°) with a prominent difference between the co-and cross-polarizations. In contrast, the LHCP radiation from the Port 2 patch antenna is directed towards the broadside (θ = 0°). The other two antennas (Ports 4 and 5) radiate RHCP

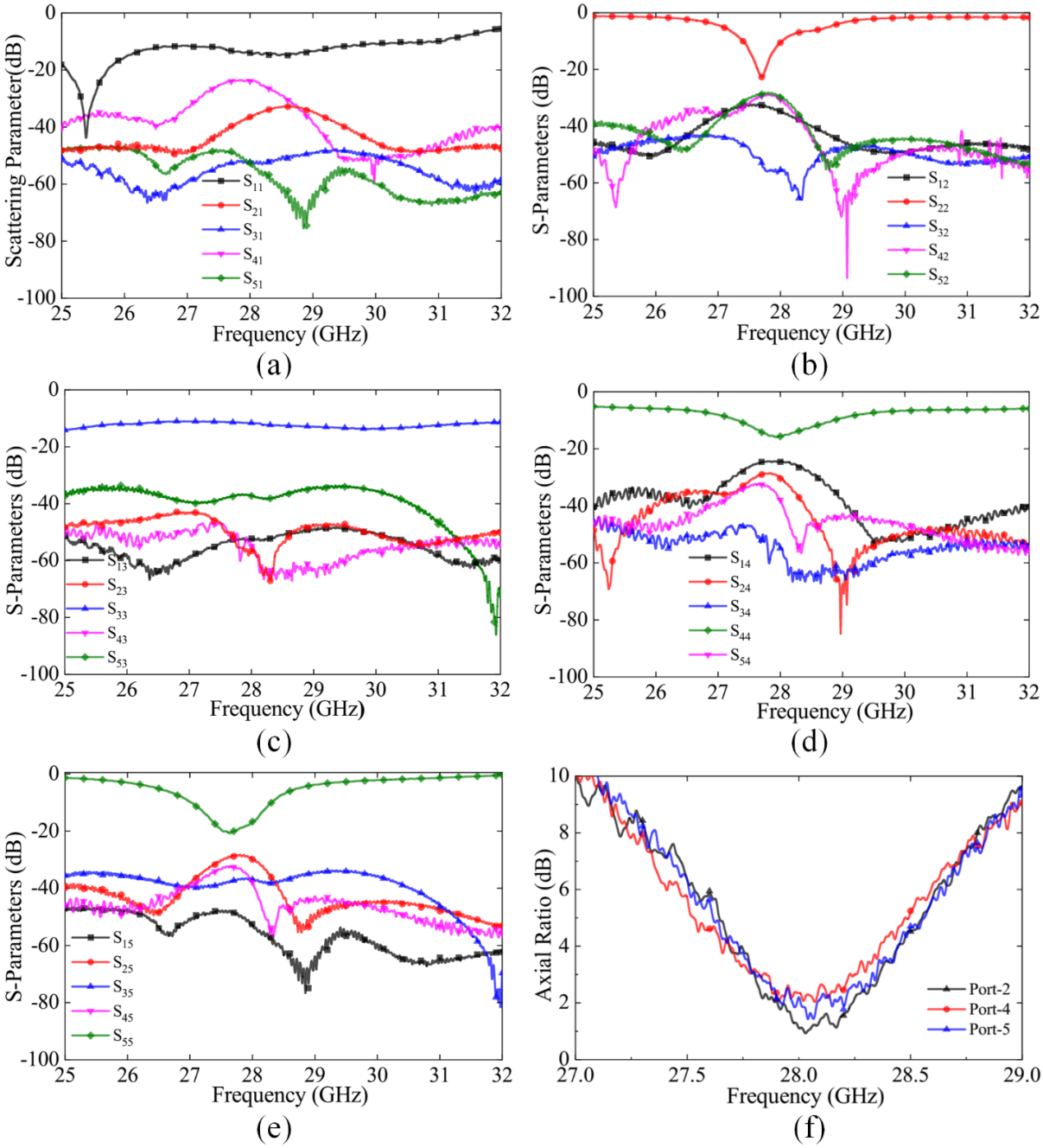

Figure 6.5: The measured S-parameters of the fabricated MIMO antenna system when: (a) Port-1, (b) Port-2, (c) Port-3, (d) Port 4, and (e) Port 5 are individually excited. (When one port is excited, others are terminated with matched loads). (f) Measured axial ratio, when Ports 2, 4, and 5 are individually excited.

behaviors in the perpendicular direction, and owing to their similarity, responses from Port 4 are only presented. The plots indicate that the proposed MIMO antenna exhibits bidirectional (±*y*-axis) end-fire characteristics as well as broadside (+*z*-axis) RHCP/LHCP responses at 28 GHz. It is noteworthy that Ports 4 and 5 bearing similar responses, responses from only one of them has been presented. The simulated radiation patterns are simultaneously presented along with the measured responses and a notable agreement is witnessed. Slight deviations in the results, although lying within tolerable limits, can be attributed to manufacturing imperfections and measurement errors.

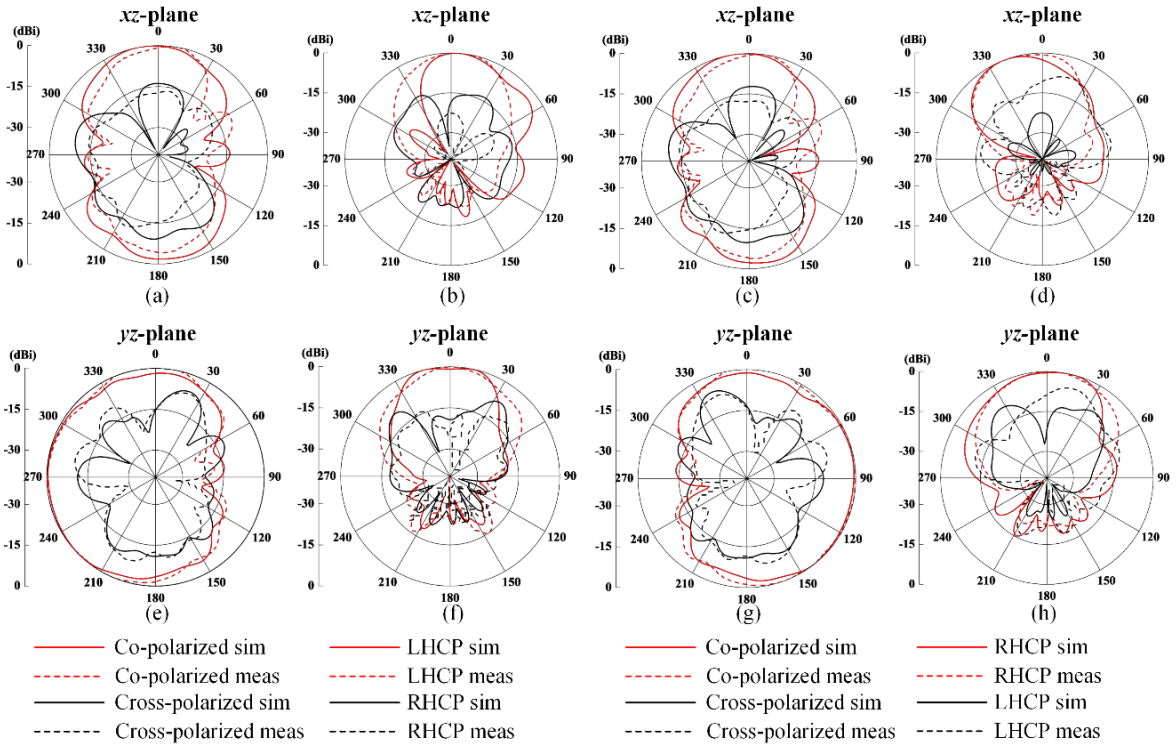

Figure 6.6: Simulated and measured normalized radiation pattern plots at 28 GHz in *xz*-plane: (a) port 1, (b) port 2, (c) port 3; (d) port 4 (= 5), and in *yz*-plane: (e) port 1, (f) port 2, (g) port 3, and (h) port 4 (= 5).

6.3 MIMO System Performance

To better understand the diversity performance of the proposed antenna, different MIMO performance matrices, such as envelope correlation coefficient (ECC), total active reflection coefficient (TARC), mean effective gain (MEG), and channel capacity loss (CCL) have been evaluated and experimentally verified. The simulated values of ECC at 28 GHz between any two ports of the proposed MIMO antenna are well below 0.1, as shown in Table 6.2.

Table 6.2: ECC between Various Ports of MIMO Antenna

Freq. (GHz)	***ECC*12**	***ECC*13**	***ECC*14**	***ECC*15**	***ECC*24**	***ECC*45**
27.8	9.52×10^{-3}	3.67×10^{-3}	6.07×10^{-3}	3.01×10^{-3}	5.97×10^{-3}	1.56×10^{-2}
28	9.75×10^{-3}	3.67×10^{-3}	6.89×10^{-3}	3.43×10^{-3}	1.02×10^{-2}	1.40×10^{-2}
28.2	9.82×10^{-3}	3.36×10^{-3}	7.99×10^{-3}	3.56×10^{-3}	1.50×10^{-2}	1.43×10^{-2}

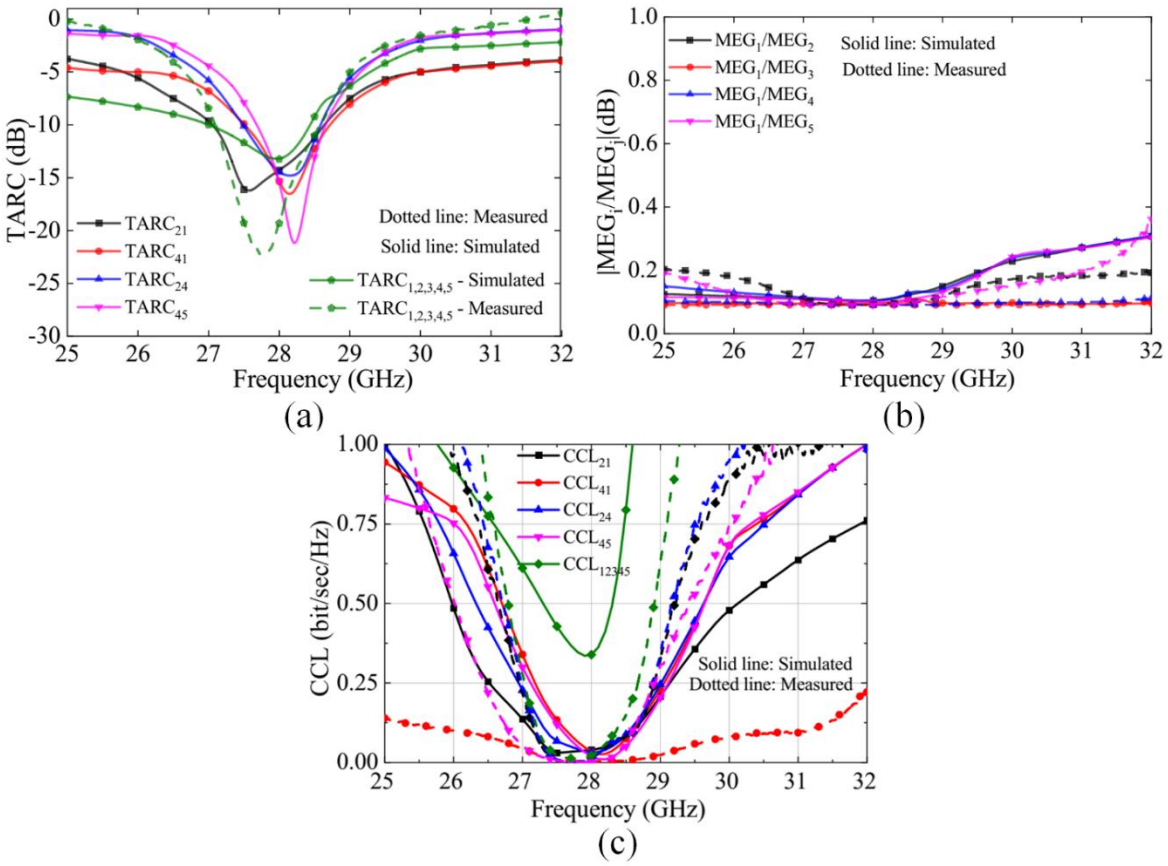

Figure 6.7: Performance specifications of the proposed MIMO antenna: (a) TARC, (b) MEG, and (c) CCL.

In the proposed configuration, the TARC responses between two adjacent ports (between ports *i* and *j*, when other ports are matched; $i \neq j = 1, 2, 3, 4, 5$) as well as among all five ports (when no port is matched and all ports are simultaneously transmitting) are presented in Figure 6.7(a). A close similarity between the two-port response ($TARC_{ij}$) and the overall five-port response ($TARC_{12345}$) indicates a good performance of the MIMO system. While considering the responses for two-port system, only neighboring antennas are considered for proper visualization. The measured responses are also in close conformity with the simulated curves.

For a good diversity performance, the ratio of MEG between two ports (*i* and *j*) should be below 3 dB, i.e. $|MEG_i/MEG_j| < \pm 3$ dB over the entire operating band. It is observed from Figure 6.7(b) that the MEG ratios between different ports lie much below 3 dB, thereby satisfying the MIMO performance.

The simulated and measured CCL responses between different ports are calculated, as shown in Figure 6.7(c), and all of them are obtained within the anticipated value (< 0.5 bits/seconds/Hz). The simulated and measured responses conform to each other over the frequency band.

6.4 Conclusion

This chapter presented a compact five-port mm-wave MIMO antenna operating in the n257 band (26.5–29.5 GHz) that integrates polarization and pattern diversity within a single structure. The antenna combines circularly and linearly polarized elements to enhance link reliability and mitigate multipath fading. It achieves high isolation (>22 dB), radiation efficiency up to 97%, and balanced gain across all ports. The low ECC (<0.02) and minimal channel capacity loss (<0.5 bits/s/Hz) confirm excellent MIMO diversity performance. The work has also been compared with several reported mm-wave MIMO designs operating around 28 GHz in Table 6.3. The distinctive merits of the proposed geometry in terms of its diversity capabilities (both polarization and pattern diversity), compact profile, and key performance parameters (large gain, high isolation, and low correlation coefficient) clearly establish the novelty and practical relevance of this work in the context of 5G and beyond mm-wave wireless communication systems.

Table 6.3: Comparison with Reported LP/CP 28 GHz MIMO Antennas

Ref.	Port	Overall size (λ^2)	Freq range (GHz)	FBW (%)	Isolation (dB)	ARABW (GHz) / ARFBW (%)	Pattern/ Pol. diversity	PRG (dBi/dBic)	Max ECC	LP/CP
[134]	4	1.0 × 1.0	24.50 – 31.00	23.40	> 30	25-29.6/16.8	No/No	$7^{*}/11^{\#}$	0.015	CP
[127]	4	0.93 × 0.93	25.00 – 33.00	27.60	> 25	26-31.3/17	No/Yes	$7.5^{*}/14.1^{\#}$	0.008	CP
[123]	2	2.71 × 1.06	27.00 – 29.00	7.14	NR	NA	No/No	11.7	NR	LP
[134]	4	2.8 × 3.27	25.50 – 29.60	14.64	> 17	NA	No/No	8.3	0.01	LP
[135]	4	1.04 × 1.00	25.9-27.8 47.1-49.9	7.07 5.77	> 27	NA	No/ No	> 6	$< 10^{-6}$	LP
[136]	4	0.39 × 0.39	3.4-3.6 5.15-5.36	5.7 3.8	> 19.2	NA	No/ No	1.3 2.7	0.002	LP
[137]	2	1.87 × 2.59	26.90 – 30.70	13.20	> 37	27.31-29.65 /8.3	No/Yes	11.86	0.00025	CP
[138]	2	5.39 × 3.60	23.61 – 33.30	34.10	> 30	28.35-31/8.93	No/Yes	11	0.001	RHCP/ LHCP
[70]	2	1.91 × 1.12	25.5-29.5	14.55	> 35	25.2-28.3/11.59	No/Yes	8.1	NR	RHCP/ LHCP
[139]	4	4.01 × 4.90	34.4-42.5	21.06	> 16	36.14-38.25/ 5.67	No/Yes	18.5	0.003	RHCP/ LHCP
This work	**5**	**1.4 × 4.26**	**25.00 – 31.00 (Ports 1, 3)**	**21.05 (Ports 1, 3)**	**> 25 (Ports 1, 3)**	**NA**	**Yes/ Yes**	**6.8-7.01 (LP)**	**0.003**	**LP (end-fire)**
			27.34 – 28.20 (Ports 2, 4, 5)	**3.07 (Ports 2, 4, 5)**	**> 22 (Ports 2, 4, 5)**	**27.64 - 28.05 /1.47**		**6.2-9.05 (CP)**	**0.014**	**RHCP / LHCP (broad side)**

PRG: Peak realized gain; *: Gain without PRS or metasurface; #: Gain with PRS or metasurface; NA: Not applicable; NR: Not reported

***

Chapter 7

Reflectarray for Millimeter Wave Non-Terrestrial Networks

As established in Chapter 1, reflectarray antennas provide a practical solution for Non-Terrestrial Network (NTN) platforms, combining high gain and low profile with structural simplicity and design flexibility suitable for satellite, aerial, and high-altitude communication systems. Figure 7.1 illustrates the potential usage of reflectarray antennas in NTN scenarios. Building on this foundation, the present chapter focuses on the development and experimental validation of a wideband reflectarray antenna optimized for Ka-band (28 GHz) NTN applications. This work specifically addresses the critical challenges of quantization loss, aperture efficiency, and beam-steering accuracy encountered in mechanically reconfigurable reflectarrays operating at millimeter wave (mm-wave) frequencies.

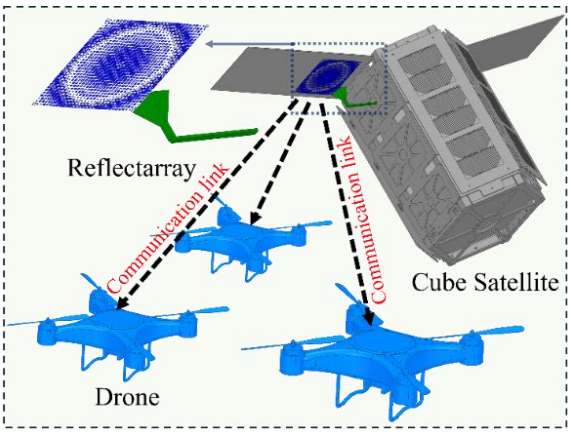

Figure 7.1: Potential applications of reflectarray antennas in NTN platforms.

The proposed design employs a 31 × 31 planar arrays of metallic square-ring unit cells, each engineered to provide eight discrete reflection-phase states covering a full 360° range with low reflection loss (< 0.8 dB). The use of 3-bit phase quantization enhances phase resolution, reduces aperture degradation, and improves beam-forming precision compared with conventional 1- or 2-bit designs. The array is illuminated by an optimized 3D-printed pyramidal horn feed, positioned at a calculated focal distance to achieve uniform amplitude distribution and low spillover loss. Mechanical beam steering of up to ±20° in the elevation plane is accomplished by laterally translating the feed, offering a low-cost and low-loss approach to beam control without active tuning elements or multilayer circuitry. The fabricated

prototype shows close agreement between simulated and measured results, confirming stable beam formation and high-gain performance across the Ka-band.

By achieving high aperture efficiency, minimal scan loss, and mechanical reconfigurability within a compact single-layer structure, the proposed design offers a cost-effective and scalable alternative to active phased-array systems for next-generation 5G/6G NTN payloads. This chapter presents the complete design methodology, simulation results, fabrication process, and measurement outcomes of the developed reflectarray antenna.

7.1 Unit Cell Topology

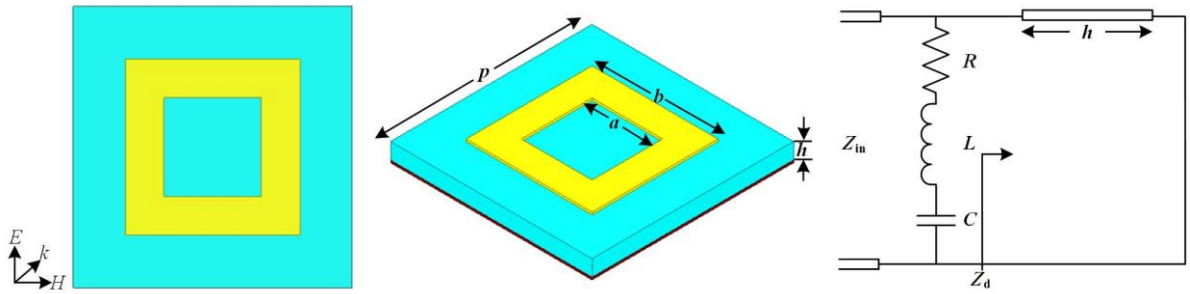

(a) (b) (c)

Fig. 7.2: Geometry of the proposed unit cell: (a) top view, (b) isometric view. (c) Equivalent circuit model of the unit cell. Dimensions: l_1= 3.2 mm, h = 0.797 mm.

Figure 7.2(a) presents the design and equivalent circuit model (ECM) of the proposed unit cell geometry, which consists of a metallic square ring printed on an RT/Duroid 5880 substrate (ε_r = 2.2, tanδ = 0.0009), backed by a full metal ground. During plane wave incidence, surface currents flow through the ring in a closed loop, thereby generating an equivalent inductance (L), while an equivalent capacitance (C) is formed between adjacent unit cells. A small resistance (R) arises due to the finite conductivity of copper. In the equivalent circuit model (ECM), the dielectric substrate is represented as a transmission-line segment, whereas the ground plane is modeled as a short-circuit line, as shown in Fig. 7.2(c). For simplicity, the horizontal coupling effects (perpendicular to the E-field direction) and the effects arising from the right-angle bends in the ring are neglected in this analysis [90]. Thus, the input impedance of the unit cell can be expressed as:

$$Z_{in} = \left[R + j\omega L + \frac{1}{j\omega C}\right] \parallel \left[j\frac{Z_0}{\sqrt{\varepsilon_r}} tan(\beta d)\right] \tag{7.1}$$

where β is the phase constant and βd is the electrical length of the substrate. The equivalent circuit behaves as a resonant network, where the primary resonance originates from the metallic square ring, while the metal-backed dielectric contributes a small reactance component that depends on the substrate material properties and thickness. As the resonance frequency varies, Z_{in} alternates between inductive and capacitive states, thereby modifying the phase response. This mechanism enables the generation of discrete phase values by appropriately varying the geometric dimensions of the proposed unit cell.

The circuit model is designed in ADS software, and the circuit parameters are extracted using a curve-fitting method, yielding L = 0.646 nH, C = 0.1 pF, and R = 0.2 Ω. The close agreement between the numerical results and HFSS simulations validates the accuracy of the proposed ECM. The model is primarily used as a design aid to capture the resonant behavior of the square-ring unit cell and to estimate its initial dimensions. Although the detailed values correspond to a specific unit cell, the same ECM topology applies to other unit cells derived for phase modulation, with only minor variations in parameter values that shift the reflection phase. Once these approximate values are determined, full-wave simulations are employed for the final optimization of all unit cells. This hybrid approach is widely adopted in reflectarray design, as it significantly reduces computational effort while maintaining close agreement between ECM predictions and full-wave results.

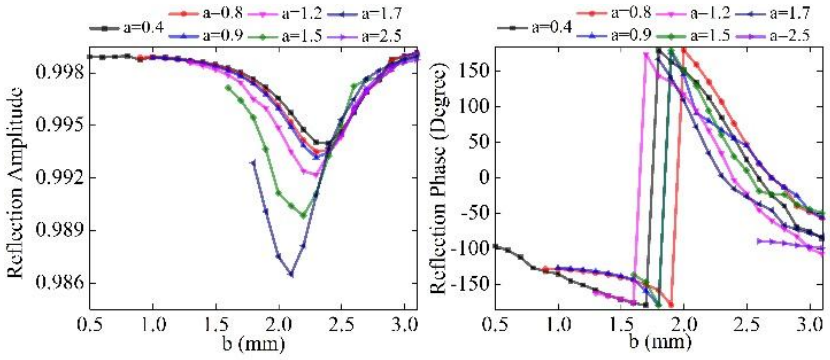

(a) (b)

Figure 7.3. Variation of reflection coefficient: (a) magnitude and (b) phase for different values of a and b of the proposed unit cell at 28 GHz.

In the proposed reflectarray, only the square-ring dimensions (a and b) are parametrically varied to achieve phase modulation, while other parameters, such as the unit-cell period (l_1) and substrate height (h), are kept constant. Figures 7.3(a) and 7.3(b) show the reflection amplitude and phase responses, respectively, at 28 GHz for different values of a and b. By

jointly varying these dimensions, a full 360° phase tuning range is achieved. The reflection amplitude remains high (> 0.98) across the range, confirming the low-loss nature of the unit cell. Furthermore, the phase variation exhibits near-linear behavior over certain intervals, facilitating discrete phase quantization. These results demonstrate the design flexibility of the unit cell and validate its suitability for implementing the quantized phase modulation scheme.

Eight different unit cells with a 45° phase difference are then selected by varying the dimensions of *a* and *b*, thereby realizing the 3-bit quantized phase modulation scheme. This discretization simplifies design and fabrication, reduces sensitivity to manufacturing tolerances, and requires less effort compared to continuously varying unit dimensions, while incurring only negligible quantization loss. Figures 7.4(a) and 7.4(b) show the reflection magnitude and phase responses of the eight unit cells, while Table 7.1 lists their corresponding dimensions. It is observed in Fig. 7.4(b) that the simulated reflection phase responses do not maintain perfectly parallel curves with constant 45° spacing across the entire frequency range. This is inherent to the dispersive nature of passive resonant unit cells, whose reflection phase varies nonlinearly with frequency. In this work, the unit cells were optimized to achieve 45° phase spacing at the design frequency of 28 GHz. As the frequency deviates from this center value, the phase spacing naturally becomes non-uniform due to dispersion effects. Moreover, each unit cell was independently designed to achieve its target phase at 28 GHz rather than being co-optimized as a set across the full band, resulting in slight convergence or divergence of phase curves away from the design frequency. Such non-ideal spacing is typical in quantized reflectarray designs and does not significantly affect the beamforming performance within the operational bandwidth.

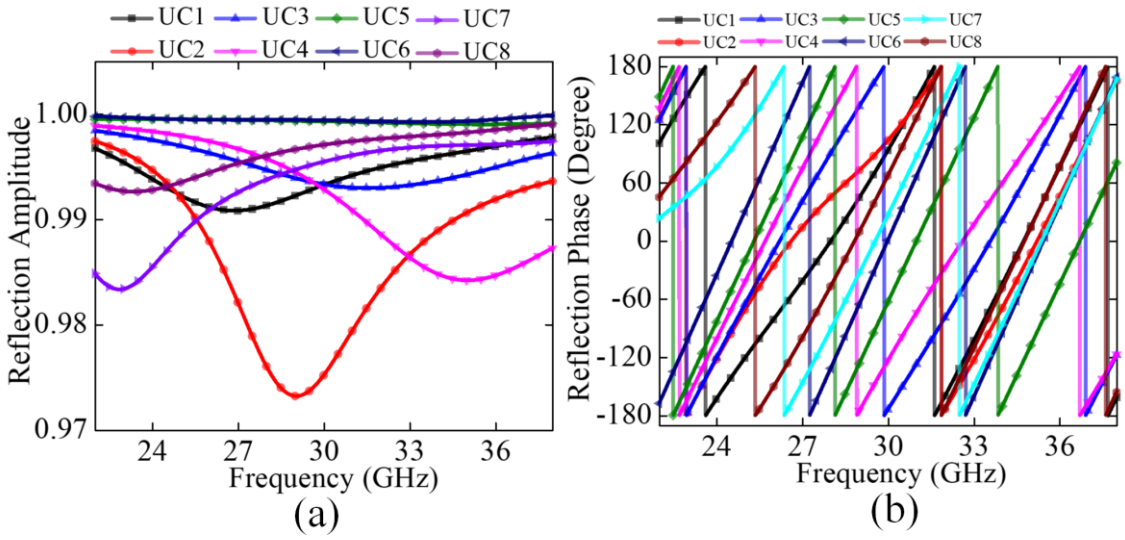

Figure 7.4. (a) Reflection magnitude, and (b) reflection phase of eight different unit cells.

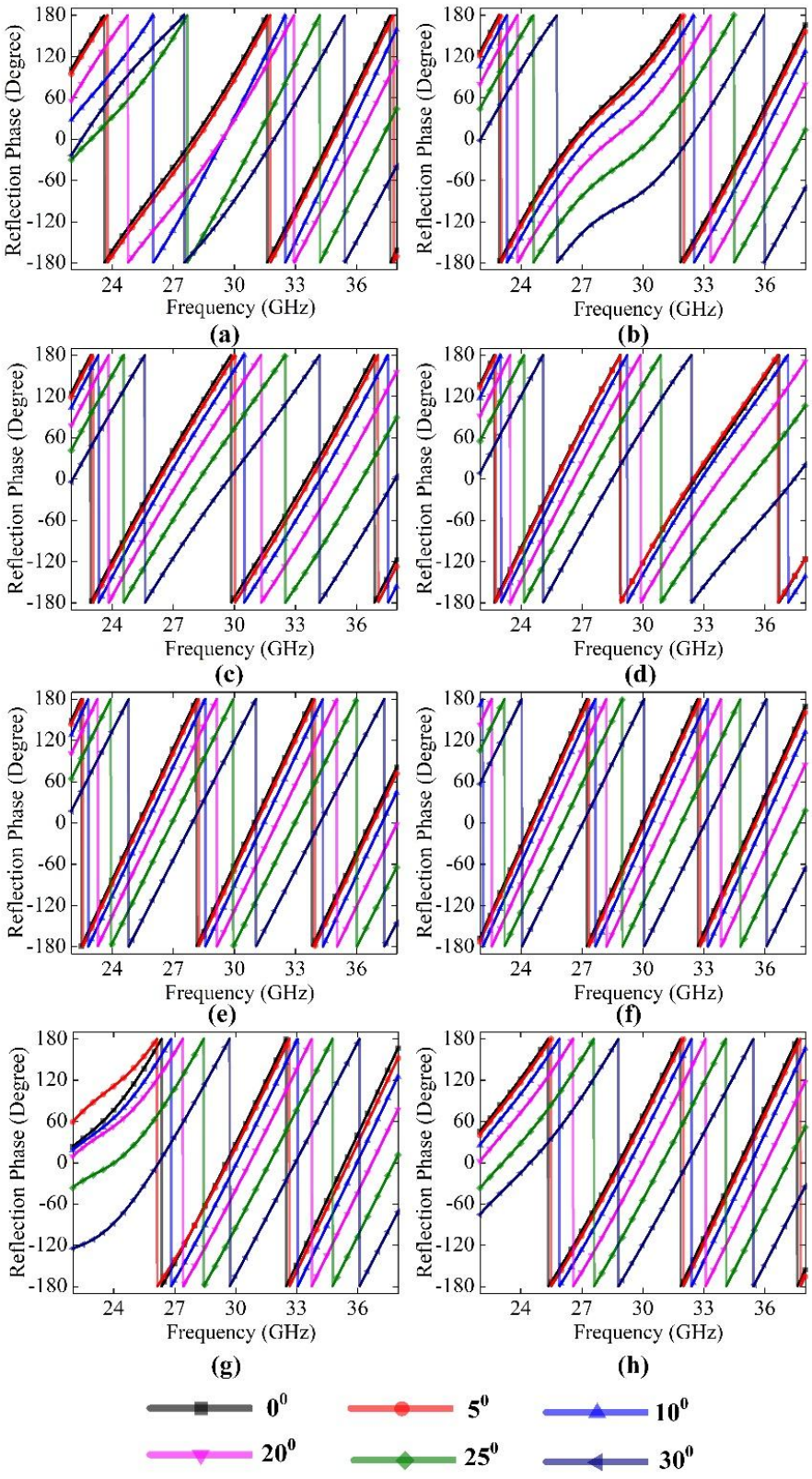

Figure 7.5: Sensitivity of the proposed unit cells at an oblique angle of incidence: (a) Unit Cell-1, (b) Unit Cell-2, (c) Unit Cell-3, (d) Unit Cell-4, (e) Unit Cell-5, (f) Unit Cell-6, (g) Unit Cell-7, (h) Unit Cell-8.

Table 7.1: Dimensions of the corresponding unit cells

Phase (deg)	a (mm)	b (mm)	Unit cell no	Phase (deg)	a (mm)	b (mm)	Unit cell no
0	0.8	2.7	UC1	180	0.4	1.7	UC5
45	0.9	2.5	UC2	-135	0.4	1	UC6
90	0.9	2.1	UC3	-90	2.5	2.8	UC7
135	1.2	1.9	UC4	-45	1.7	2.7	UC8

The angular stability of the designed unit cells is evaluated by varying the incidence angle, with results shown in Figures 7.5(a–h). It can be observed that all unit cells maintain the 45° reflection phase separation up to an incidence angle of 20°. Owing to their axial symmetry, the unit cells also exhibit polarization-independent behavior. For incidence angles beyond ±20°, however, the reflection phase of certain unit cells deviates from the 45° separation, indicating increased angular sensitivity. While this does not significantly affect the performance within the intended beam-steering range (±20°), additional tuning or compensation would be required for larger scan angles.

7.2 Reflectarray Antenna Design

When a planar reflectarray aperture, composed of P × Q sub-wavelength reflecting elements is excited by a feeding source, the reflected electric field $E_{ref}(r)$, magnetic field $H_{ref}(r)$, and power $P_{ref}(r)$ from the reflectarray at an observation point *r* can be expressed as [114].

$$\mathbf{E_{ref}}(\mathbf{r}) = \sum_{p=1}^{P}\sum_{q=1}^{Q}|R(p,q)|\mathbf{E_{inc}}\left(\mathbf{r_{pq}}\right)e^{-j\phi(p,q)}\, e^{jk\mathbf{r}_{pq}.\hat{\mathbf{r}}} \tag{7.2}$$

$$\mathbf{H_{ref}}(\mathbf{r}) = \frac{1}{\eta_0}\,\hat{\boldsymbol{k}} \times \mathbf{E_{ref}}(\mathbf{r}) \tag{7.3}$$

$$\mathbf{P_{ref}}(\mathbf{r}) = \frac{1}{2}\,\Re\left[\mathbf{E_{ref}}(\mathbf{r}) \times \mathbf{H^{*}_{ref}}(\mathbf{r})\right] \tag{7.4}$$

Where, $\mathrm{E_{inc}}\left(r_{pq}\right)$ is incident electric field from the feed at the position of the unit cell r_{pq}, $|R(p,q)|$is reflection amplitude of unit cell and $e^{-j\phi(p,q)}$ is phase shift introduced by unit cell at (p,q) and $e^{jk\mathbf{r}_{pq}.\hat{\mathbf{r}}}$ is phase factor accounting for the radiation from the unit cell to the far field observation point in direction $\hat{r}$.

It is evident from Equations (7.2) - (7.4) that the characteristics of the reflected power can be adjusted by modifying the phase distribution on the reflecting surface. Furthermore, the required reflection phase distribution of each element, $\varphi(p,q)$ must be designed such that the phase of the reflected field from each element maintains a uniform phase delay between the feed source and observation point [91]. This condition is crucial for achieving the desired beam orientation and can be determined using (7.5).

$$\varphi(p,q) = -k\left[\sqrt{(p-x_f)^2+(q-y_f)^2+(z-z_f)^2} - (psin\theta_0 cos\varphi_0 + qsin\theta_0 sin\varphi_0 + zcos\theta_0)\right] \quad (7.5)$$

Here, (p,q,z) and (x_f,y_f,z_f) denote the unit cell position and feed position respectively, while (θ_0,φ_0) define the desired beam direction in the azimuthal and elevation planes, respectively. *k* is the free space wave number.

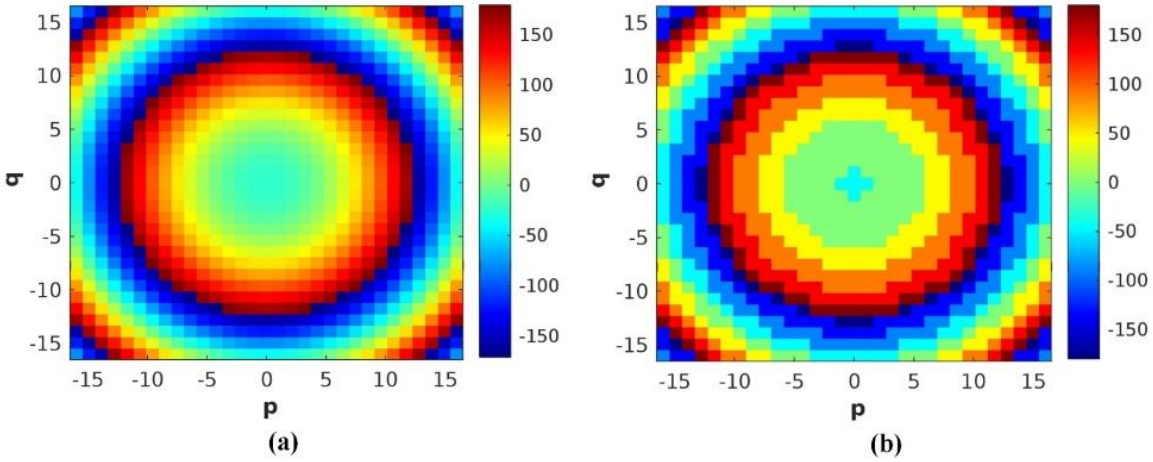

Figure 7.6: (a) Required Continuous reflection phase distribution plot for the radiated beam at θ = 0° and φ = 0° and its (b) 3-bit quantized reflection phase distribution plot.

For the broadside radiation, the required reflection phase profile is obtained directly from Equation (7.5) by substituting the coordinates of the focal feed. When the feed is laterally displaced to realize off-axis beams (±20°), the path length between the new feed position and each unit cell changes accordingly. By substituting these updated feed coordinates into Equation (7.5), a new phase distribution is automatically calculated, ensuring that the reflected wavefronts combine coherently in the desired steered direction. Thus, the same mathematical formulation governs both broadside and tilted beams, and beam steering is realized by repositioning the feed without modifying the unit cell configuration.

To realize the required phase profile for beam-steering operation, different unit cells with appropriate phase compensation values are positioned at designated locations. Figure 7.6(a) illustrates the continuous reflection phase distribution for broadside radiation ($\theta = 0°$, $\phi = 0°$). However, realizing a large number of unit-cell structures to match each small phase variation and subsequently fabricating them is highly challenging. To address this, the continuous phase distribution is discretized into a 3-bit phase profile with eight distinct phase levels (-180°, -135°, -90°, -45°, 0°, 45°, 90°, and 135°), as shown in Figure 7.6(b).

7.2.1 Design of Feed Horn Antenna

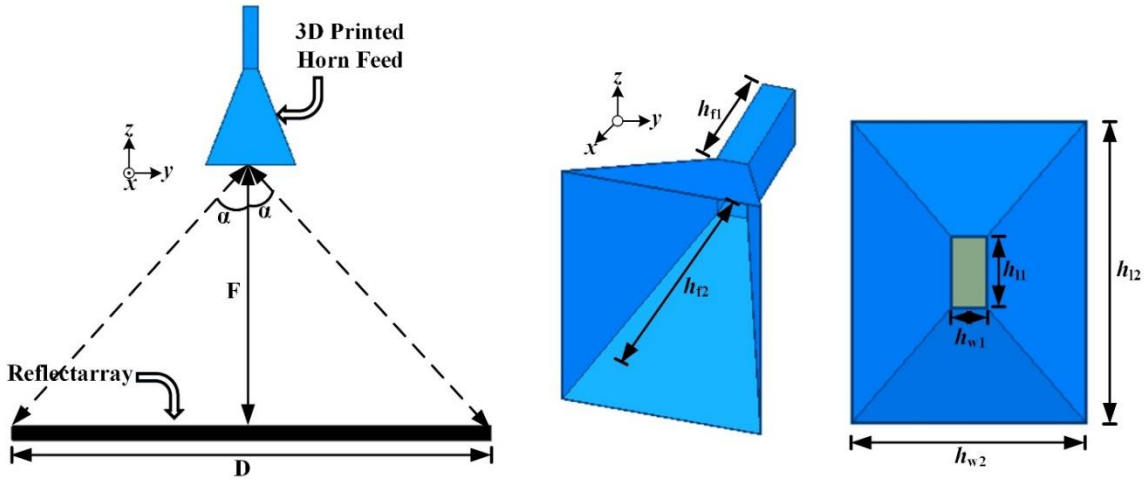

(a) (b)

Figure 7.7: (a) General setup of the proposed reflectarray antenna fed by a horn antenna. (b) Schematics of the designed 3D printed horn antenna, with dimensions h_{f1}= 13.05, h_{f2} = 19.89, h_{l1}= 5.6, h_{l2}= 24, h_{w1} = 3, and h_{w2} = 18.53 (Units: mm).

The planar reflectarray geometry developed using the phase modulation technique requires a feed source positioned appropriately to radiate the reflected beam in the desired direction. A Ku-band pyramidal horn antenna, as depicted in Figure 7.7, is employed as the feed. The antenna is designed using conventional design equations, where D represents the reflectarray aperture dimension and F denotes the distance between the feed source and the reflectarray. A 3-D printer compatible material ABS 400 is is used as the structural medium, with a silver coating applied to both the inner and outer surfaces. The metal layer thickness is chosen to be sufficiently larger than the skin depth at the operating frequency, ensuring negligible conduction loss. The detailed dimensions are provided in the caption of Figure 7.7. The aperture blockage of the horn antenna used in the configuration is only 1.4% of the reflectarray

area, which is within acceptable limits and has negligible effect on gain or patterns. Moreover, the horn provides a well-defined illumination taper that reduces spillover and sidelobes, outweighing the minor blockage introduced.

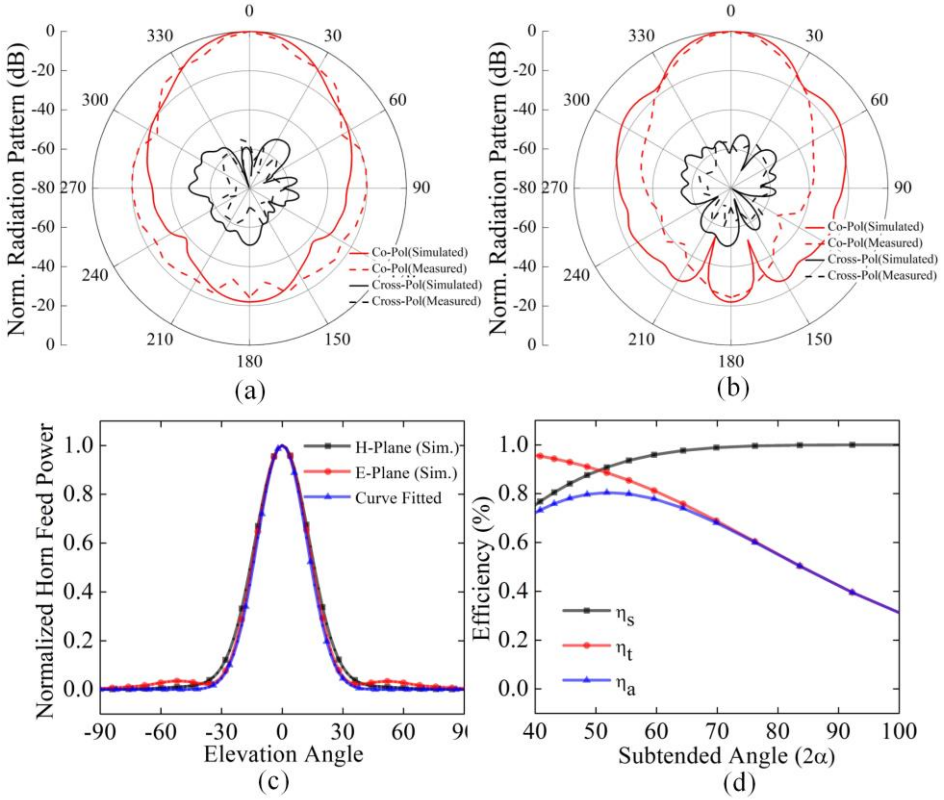

Figure 7.8. Simulated and measured normalized radiation pattern for the horn antenna in (a) E-plane and (b) H-lane at 28 GHz, (c) curve fitting of the normalized radiation pattern for the 3D printed horn feed antenna. (d) Spillover (η_s), edge taper (η_t), and aperture efficiency (η_{ap}) for various values of subtended angle (2α).

The antenna structure is analyzed using Ansys HFSS 2025 R1. The normalized radiation patterns in the E- and H-planes are shown in Figures 7.8(a) and 7.8(b), respectively, indicating a beamwidth of 32.3° in both planes. The far-field characteristics of the horn exhibit an axisymmetric power pattern approximated by $cos^n(\theta)$ [13], where *n* is a positive real number. In this design, *n* = 21, determined through curve fitting of the simulated results, as illustrated in Figure 7.8(c). The determination of an optimum angle subtended from centre of horn to the sides of reflectarray $\left(\alpha = tan^{-1}\left(\frac{D}{2F}\right)\right)$ is a crucial parameter to achieve the highest possible aperture efficiency (η_{ap}), which is a product of edge taper efficiency (η_t) and spillover efficiency (η_s). Maximizing η_t requires a broad feed pattern to ensure sufficient power at the reflectarray edges, but this increases spillover losses. Conversely, maximizing η_s demands a

narrower feed pattern to minimize power loss beyond the reflectarray, which reduces edge illumination, creating a trade-off. Different values of η_t, η_s, and therefore maximum η_{ap} corresponding to different α values are determined through the formulations [140] given in (7.6), (7.7) and plotted in Figure 7.8(d).

$$\eta_t = \frac{2n.\left(\frac{1}{tan^2(\alpha)}\right).\left(1-cos^{\left(\frac{n}{2}-1\right)}(\alpha)\right)^2}{\left(\frac{n}{2}-1\right)^2.(1-cos^n(\alpha))} \tag{7.6}$$

$$\eta_s = 1 - cos^{(n+1)}(\alpha) \tag{7.7}$$

Therefore, for the proposed horn feed, the maximum theoretical aperture efficiency (η_{ap}) is obtained at an optimal flare angle (α) of 25∘.

7.2.2 Design of Reflectarray with Feed Horn Antenna

The final design consists of an assembly of the reflectarray surface and the pyramidal horn antenna, where the feed is subtended at an angle of 2α to achieve the desired radiation. For broadside radiation (θ = 0°, ϕ = 0°), the aperture angle (2α) is set to 50°, whereas for ±20° beam steering operation, the horn is mechanically rotated to a position of 36°. The combined reflectarray–horn configuration is modeled in Ansys HFSS and analyzed using the finite element boundary integral (FEBI) technique.

7.3 Experimental Verification and Discussion

To demonstrate the beam-steering operation, the proposed configuration is fabricated using a hybrid technique. The reflectarray surface is constructed using an LPKF Protomat S104 PCB prototyping machine, while the horn antenna is fabricated using a 3D printing process. Initially, ABS-400 material is employed in an Ultimaker 2+ 3D printer to construct the antenna outline, after which the inner and outer surfaces are metallized with a silver-based conductive coating. Prior to metallization, the printed surface is cleaned, smoothened, and primed to ensure strong adhesion. A commercially available aerosol silver-conductive spray, consisting of silver particles suspended in a polymer matrix, is then applied in multiple thin layers to provide uniform coverage and adequate conductivity. Following the drying process, the metallized horn is tested with a multimeter to verify electrical continuity and low surface resistance. Figures 7.9(a) and 7.9(b) show the fabricated horn feed and planar reflectarray, respectively.

After fabrication, the feed antenna is mounted above the reflectarray surface using a 3D printed PLA-based framework. A built-in slider mechanism is incorporated to enable

mechanical movement of the horn antenna along the y-axis, thereby facilitating beam-steering in the YZ-plane from –20° to +20°. The measurement is performed inside an anechoic chamber, as shown in Figure 7.9(c). The input signal is supplied to the feed horn antenna (Tx), while the radiated signal is received by another wideband horn antenna (Rx). Both antennas are connected to an Anritsu S820E vector network analyzer (VNA) for data acquisition.

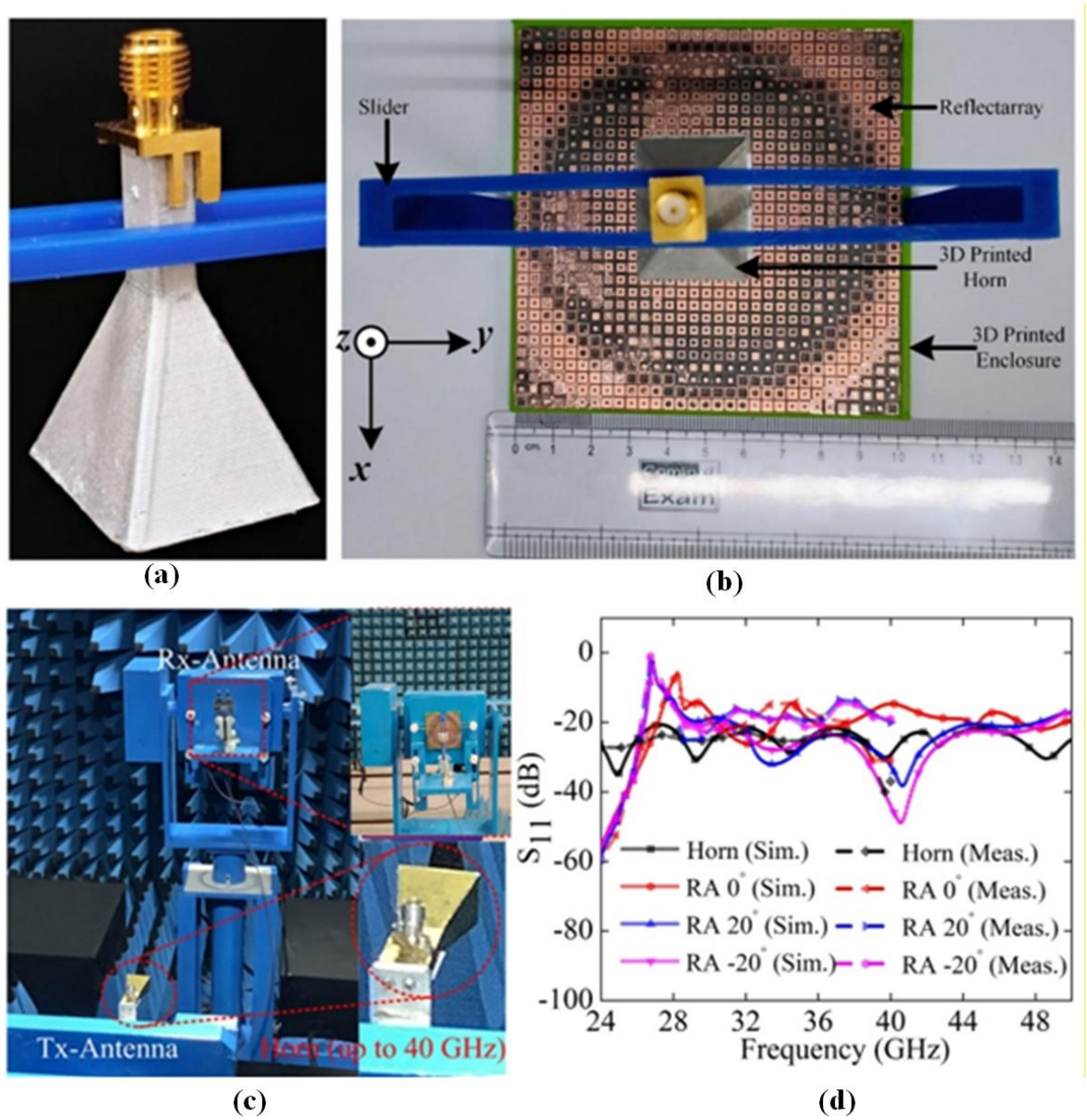

Figure 7.9: Fabricated Prototype of the (a) proposed horn antenna. (b) proposed reflect-array antenna. (c) Measurement setup inside an anechoic chamber. (d) Simulated (solid line) and measured (dashed line) reflection coefficients for feed source (Horn) and feed source with reflect-array for radiated beam at 0°, 20°, -20°.

Prior to evaluating the complete reflectarray configuration, the reflection characteristic of the 3D printed horn antenna is measured. A low reflection coefficient (S_{11} < -10 dB) is observed across a wide frequency band for both simulated and measured results at 0° as well as ±20° incidence angles, confirming the accuracy of the feed design. Subsequently, the normalized radiation patterns of the reflectarray antenna are measured and compared with simulations, as shown in Figures 7.10(a) and 7.10(b) for broadside radiation in the *yz*- and *xz*-planes, respectively. The measured 3-dB beamwidths are 5.8° and 5.76°, which are in close agreement with the simulated values.

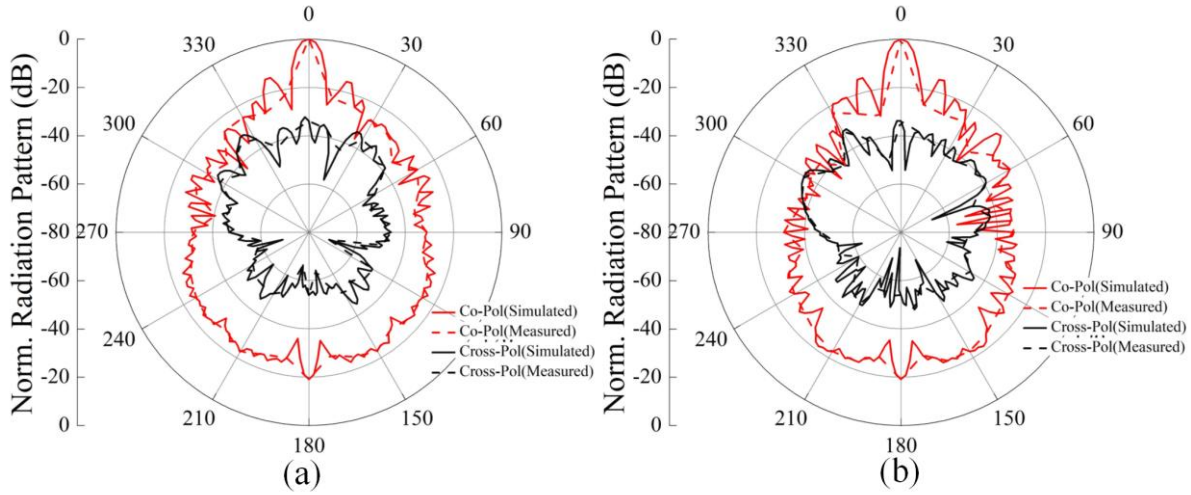

Figure 7.10: Simulated and measured normalized radiation pattern for feed source with reflect-array in (a) yz-plane and (b) xz-plane at 28 GHz for radiated beam at 0°; simulated result (solid line) and measured result (dashed line) for both co-polarized and cross-polarized components.

Compared with the 3-D printed horn feed patterns in Figures 7.8(a) and 7.8(b), the reflectarray exhibits a significantly narrower beam and enhanced directivity, achieving simulated and measured gain improvements of 12.6 dB and 12.4 dB, respectively. Some deviations between simulated and measured radiation patterns, particularly in the sidelobe regions, are observed in Figures 7.8 and 7.10. These discrepancies primarily arise from limitations in the measurement setup. The measurements were carried out in a compact antenna test range using a relatively coarse angular step size of 10°, with the antenna rotated manually. While this method is sufficient for capturing the main-beam characteristics, it produces fewer smooth curves and reduces the accuracy of sidelobe estimation. Additional factors, such as slight feed misalignment, environmental reflections, and the surface roughness of the 3-D printed horn, further contribute to the observed differences. Nevertheless, the main-lobe

characteristics, including beamwidth, pointing accuracy, and gain show close agreement with simulations, thereby validating the proposed design.

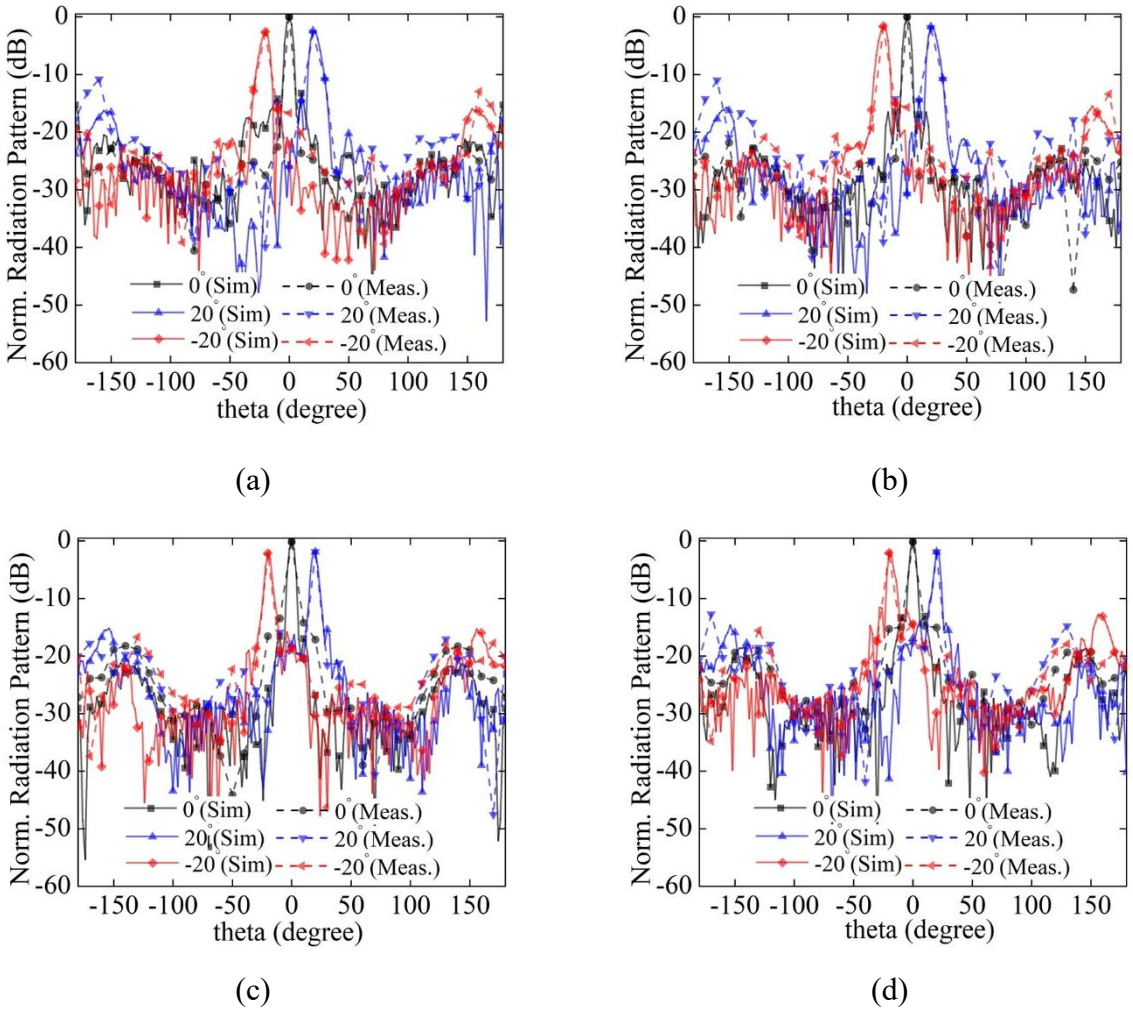

Figure 7.11: Measured and simulated far-field radiation pattern for radiated beam at 0°, 20°, -20° in YZ-plane at (a) 26.7 GHz, (b) 28 GHz (c) 33 GHz, and (d) 38 GHz.

Figure 7.11 compares the simulated and measured normalized radiation patterns in the YZ-plane for radiated beam at 26.7 GHz, 28 GHz, 33 GHz, and 38 GHz. Highly directive beams are generated along the broadside direction, as well as at ±20° in the E plane, with measured side lobe levels between -17 dB to -23 dB. The measured results closely align with the simulations, demonstrating the effectiveness of the design approach. This consistency is primarily attributed to the optimized unit cell design, which accounts for compact volume, polarization insensitivity, oblique incidence tolerance, and the precise determination of the optimum subtended angle (2α) based on the feed source's illumination pattern. Beam squint refers to the deviation of the main beam from its intended pointing direction as the operating frequency shifts away from the designed center frequency. This is inherently present in

wideband reflectarray antennas due to the frequency-dependent phase response of the unit cells. Beam squint in the proposed reflectarray is first evaluated using full-wave simulations. Experimental measurements are then performed manually with a 10° angular step because of limitations in the test setup. Due to this coarse step size, small deviations of less than 10° cannot be captured in the measurements. Even with this limitation, the measured beam directions agree well with the expected steering positions. Simulation results, shown in Figure 7.11, confirm that the maximum beam squint remains below 1.5° across the operational band (26.7 GHz–39.8 GHz), indicating that the proposed design maintains accurate beam pointing with minimal frequency-dependent deviation despite the large gain bandwidth.

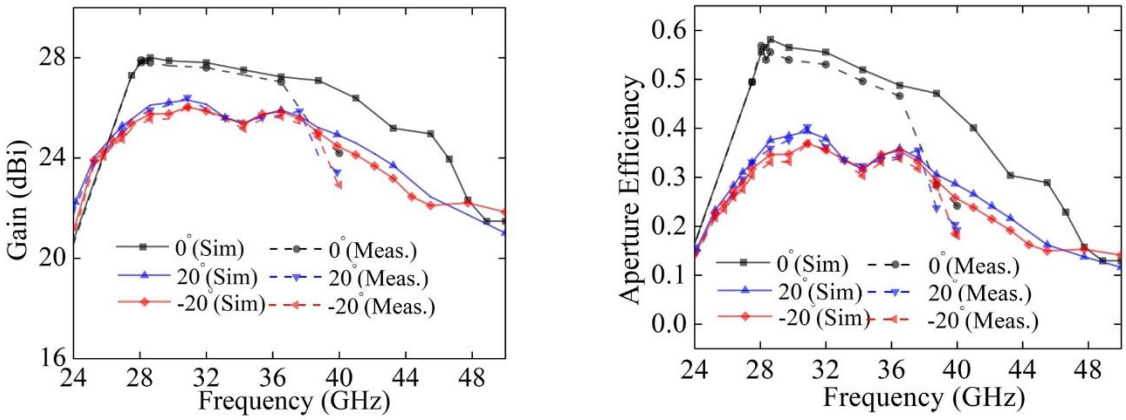

(a) (b)

Figure 7.12: Simulated and measured responses of the proposed reflectarray: (a) gain versus frequency, and (b) aperture efficiency versus frequency.

Figure 7.12(a) shows the simulated and measured gain versus frequency for the beam-steerable reflectarray antenna at broadside and at ±20° scan angles. The simulations predict a 3-dB gain bandwidth of 59.2% over the frequency range of 26.7–42 GHz. However, due to the limitations of the available measurement setup, experimental characterization could only be performed up to 40 GHz. Based on the measured data, the 3-dB gain bandwidth of the fabricated reflectarray antenna extends from 26.7 GHz to 39.8 GHz, corresponding to a measured fractional bandwidth of 46.8%. The proposed reflectarray antenna achieves a maximum measured broadside gain of 27.8 dBi at 28 GHz. The measured broadside gain is 0.2 dB lower than the simulated value, attributed to fabrication and free-space measurement errors. Additionally, the measured gains for beam directions of ±20° is 25.9 dBi, demonstrating a maximum scan loss of 1.9 dB at 28 GHz. In Fig. 12(b), the simulated and measured aperture efficiencies are compared across the operating frequency range of reflectarray.

The maximum gain (G_{max}) achievable by an antenna aperture (A_{eff}) can be calculated using (1.1). The calculated G_{max} with A_{eff} = (99.2 mm × 99.2 mm) at 28 GHz, assuming 100% radiation efficiency is 30.36 dB. Thus, the beam-switching reflectarray antenna with measured gain of 27.8 dB has 55.4% aperture efficiency. The measured gain of 27.8 dBi is 2.56 dB below the limit of 30.36 dB due to multiple contributing factors. Spillover and taper illumination losses, arising from the feed source placement, are estimated to be approximately 0.4 dB and 0.6 dB, respectively. The 3-bit phase quantization loss is estimated to be about 0.2 dB, while reflection and cross-polarization losses are expected to contribute an additional 0.3 dB, based on typical values reported in the literature for similar reflectarrays. The average insertion loss of the unit cells is around 0.86 dB, and the remaining 0.2 dB loss is attributed to fabrication tolerances, slight misalignments, and measurement uncertainties.

7.4 Conclusion

This chapter presents a cost-effective, high-performance planar 3-bit quantized reflectarray antenna for beam steering and gain enhancement in the n510, n511, and n512 frequency bands for non-terrestrial networks. Employing a 31×31 array of unit cells within a compact $9.27\lambda_0 \times 9.27\lambda_0$ aperture, and illuminated by a 3D-printed horn feed, the design achieves 1-D beam steering over a ±20° range with minimal scan loss. The fabricated prototype demonstrates a measured broadside gain of 27.8 dBi, a maximum aperture efficiency of 55.4%, and a wide -3 dB gain bandwidth of 46.78%. Table 7.2 presents a comparative analysis of the proposed reflectarray antenna with recent advancements in similar designs, and the proposed antenna stands out due to its high gain, enhanced aperture efficiency, and wider 3-dB gain bandwidth. Furthermore, the geometry demonstrates a significant improvement in aperture efficiency compared to previously reported designs, owing to the adoption of 3-bit, whereas earlier designs had higher quantization loss due to a smaller number of bits. The combination of improved performance metrics and cost-effective design positions the proposed antenna as a strong contender for establishing reliable, high-capacity communication links in the challenging non-terrestrial environments.

Table 7.2: Comparison with Reported Millimeter Wave Reflectarray Antennas

[Ref]	Aperture area (λ_0^2)	Freq. range (GHz)	F/D ratio	No. of layers	PRG (dBi)	Beam steering range	-3 dB Gain BW (%)	Scan Loss (dB)	Peak AE (%)	PR (bits)
[141]	$364.8\lambda_0^2$	27-31	0.61	3	29	±20°	11	3.9	20.1	1
[142]	$102\lambda_0^2$	26.6-29	1	2	24.2	±27°	4.7	3.7	24.5	-
[143]	40.7 λ_0^2	27.2-51	1	1	25	NA	28.6 (-2 dB)	NR	20	1
[144]	$87.23\lambda_0^2$	27-29	N.R.	3	21.3	±50°	N.R.	5.9	12.5	1
[145]	$232.2\lambda_0^2$	28-32	N.R.	5	27.8	±30°	13.3	3	23.2	2
[146]	87 λ_0^2	27.5-40	1	1	27.9	NA	35.7	NR	51.7	Cont
[147]	$282.7\lambda_0^2$	29-31	0.34	3D-P	25	±50°	N.R.	2.5	13	-
[148]	$250.9\lambda_0^2$	25.1-27.5	0.87	5	29.2	±50°	8 (-2 dB)	3	27.1	2
[149]	104.8 λ_0^2	29-35	0.66	3D-P	24	NA	18.7	NA	54	3
This work	**$85.9\lambda_0^2$**	**26.7-39.8**	**1.07**	**1**	**27.8**	**±20°**	**46.78**	**1.9**	**55.4**	**3**

PRG: Peak realized gain; PR: Phase Resolution; NR: Not Reported; NA: Not Available; 3D-P: 3D Printed

***

Chapter 8

Conclusions and Future Scope

This thesis has systematically addressed the design challenges associated with mm-wave antenna systems for both terrestrial and non-terrestrial networks envisioned in 5G and beyond-5G (B5G) communication frameworks. Starting from compact MIMO topologies and progressing toward high-gain reflectarray architectures, the research demonstrates a unified design approach that bridges device-scale integration and large-aperture beam steering within a single, coherent framework.

In the first phase, compact dual-band MIMO antennas employing SRR/CSRR loading were realized to achieve dual-frequency operation (28 GHz and 38 GHz) with high isolation and low envelope correlation. The subsequent AMC-backed and Fabry–Perot cavity-based designs achieved significant gain enhancement and aperture-efficiency improvement, validating the feasibility of low-profile high-gain antennas suitable for wearable and short-range 5G front ends. The development of a five-port hybrid MIMO antenna further advanced this work by incorporating polarization and pattern diversity, thereby improving link reliability under multipath fading and demonstrating robust diversity characteristics with enhanced isolation.

The final stage of this research introduced a wideband, high-gain 3-bit quantized reflectarray antenna for Ka-band NTN applications such as LEO/GEO satellites, UAVs, and high-altitude platforms (HAPs). The design achieved mechanical beam steering of ±20°, a peak gain of 27.8 dBi, and > 55% aperture efficiency. This configuration successfully demonstrated a low-cost, lightweight, and energy-efficient alternative to active phased arrays, bridging terrestrial and non-terrestrial communication domains within an integrated 5G/6G ecosystem.

Collectively, the work presented in this thesis contributes a set of compact, broadband, and high-efficiency antenna solutions that address key performance bottlenecks—mutual coupling, limited bandwidth, restricted scan dynamics, and fabrication complexity—while maintaining practical manufacturability at mm-wave frequencies. The experimental validations performed across multiple fabricated prototypes confirm the scalability and reliability of the proposed architectures for real-world deployment. Overall, the research establishes a solid foundation for next-generation antenna subsystems capable of enabling ubiquitous, high-capacity connectivity in both terrestrial and satellite-based communication infrastructures.

8.1 Future Scope

While the objectives outlined in this thesis have been successfully realized, several promising directions can extend the presented research toward the next phase of intelligent, reconfigurable, and sustainable antenna technologies:

1. Development of Electronically Reconfigurable Reflectarrays: The 3-bit quantized reflectarray antenna presented in Chapter 7 can be extended to an electronically tunable geometry by incorporating active phase-tuning elements such as p–i–n diodes, varactors, or MEMS switches. This modification will enable real-time electronic beam steering and adaptive beam shaping suitable for dynamic NTN payloads.
2. Design of Dual-Band or Multi-Band Reflectarray Architectures: Building upon the single-band Ka-band reflectarray, a dual-band or tri-band configuration can be developed to simultaneously cover Ka, Q, and V bands, thereby enhancing frequency agility and enabling broadband backhaul for 6G satellite communication systems.
3. Integration of Intelligent Control and AI-Based Optimization: Future work may explore intelligent reflecting surface enabled reflectarrays, where machine learning algorithms optimize phase distributions dynamically in response to channel conditions, enhancing link reliability and spectral efficiency in hybrid terrestrial-NTN environments.
4. Realization of Conformal and Flexible Reflectarrays: Extending the current planar prototype to flexible or conformal geometries using advanced substrate materials will facilitate integration with curved satellite panels, UAV fuselages, or wearable surfaces, ensuring structural adaptability without compromising performance.
5. Hybrid Beamforming and Massive MIMO Integration: The compact MIMO designs proposed in Chapters 4 and 6 can be scaled to massive MIMO or hybrid beamforming arrays, combining digital and analog control for high-capacity, spatially diverse links in dense 5G/6G deployments.
6. Polarization and Frequency Reconfigurable Antennas: Future antenna prototypes can be designed to achieve polarization switching between RHCP, LHCP, and LP states, or frequency reconfiguration across multiple mm-wave bands using tunable resonant structures and integrated bias networks.
7. System-Level Integration and Experimental Validation: The proposed antenna subsystems can be further validated by integrating them with RF front-end modules and baseband hardware, followed by over-the-air (OTA) performance evaluation under realistic NTN link conditions.

8.2 Closing Remarks

The progressive antenna designs developed in this thesis—from compact dual-band MIMO arrays to mechanically reconfigurable reflectarrays—collectively demonstrate that structural innovation, electromagnetic optimization, and practical fabrication can be harmonized to realize high-performance mm-wave antennas. The results advance the understanding of gain–bandwidth–compactness trade-offs, and provide experimentally verified pathways toward scalable and cost-effective Terrestrial/Non Terrestrial communication architectures.

As wireless networks evolve toward intelligent, autonomous, and globally integrated infrastructures, the concepts and methodologies established in this work are expected to play a pivotal role in shaping the antenna front-ends of future 6G communication systems—extending seamless connectivity across terrestrial, aerial, and space borne domains.

***

Bibliography

[1] W. Hong *et al.*, “The role of millimeter-wave technologies in 5G/6G wireless communications,” *IEEE Journal of Microwaves*, vol. 1, no. 1, pp. 101–122, Jan. 2021, doi: 10.1109/JMW.2020.3035541.

[2] T. S. Rappaport, S. Sun, R. Mayzus, H. Zhao, Y. Azar, K. Wang, G. N. Wong, J. K. Schulz, M. Samimi, and F. Gutierrez, “Millimeter wave mobile communications for 5G cellular: it will work!,” *IEEE Access*, vol. 1, pp. 335–349, May 2013, doi: 10.1109/ACCESS.2013.2260813.

[3] M. Marcus and B. Pattan, “Millimeter wave propagation: spectrum management implications,” *IEEE Microwave Magazine*, vol. 6, no. 2, pp. 54–62, Mar. 2005, doi: 10.1109/MMW.2005.1491267.

[4] S. J. Lee and W. Y. Lee, “Capacity of multiple beamformed spatial stream transmission in millimeter-wave communication channels,” *IET Communications*, vol. 7, no. 12, pp. 1263–1268, Aug. 2013, doi: 10.1049/iet-com.2012.0747.

[5] M. M. Saad, M. A. Tariq, M. T. R. Khan, and D. Kim, “Non-terrestrial networks: an overview of 3GPP release 17 & 18,” *IEEE Internet of Things Magazine*, vol. 7, no. 1, pp. 20–26, Jan. 2024, doi: 10.1109/IOTM.001.2300154.

[6] M. M. Azari *et al.*, “Evolution of non-terrestrial networks from 5G to 6G: a survey,” *IEEE Communications Surveys & Tutorials*, vol. 24, no. 4, pp. 2633–2672, Fourth Quarter 2022, doi: 10.1109/COMST.2022.3199901.

[7] H. Kim, G.-H. Gho, V. Va, H. Kim, S. Kim, and J. Ahn, “Race and challenges for developing direct satellite-to-smartphone communication systems,” *IEEE Communications Magazine*, vol. 63, no. 5, pp. 54–60, May 2025.

[8] S. Li, Q. Wu, R. Wang, and R. Lu, “Toward Networking and Routing in 6G satellite–terrestrial integrated networks: current issues and a potential solution,” *IEEE Communications Magazine*, vol. 63, no. 3, pp. 92–98, Mar. 2025.

[9] C. E. Shannon, “A mathematical theory of communication,” *Bell System Technical Journal*, vol. 27, no. 3, pp. 379–423, 1948, doi: 10.1002/j.1538-7305.1948.tb01338.x.

[10] D. T. Emerson, “The work of Jagadis Chandra Bose: 100 years of millimeter-wave research,” *IEEE Transactions on Microwave Theory and Techniques*, vol. 45, no. 12, pp. 2267–2273, Dec. 1997, doi: 10.1109/22.643830.

[11] M. Xiao *et al.*, “Millimeter wave communications for future mobile networks,” *IEEE Journal on Selected Areas in Communications*, vol. 35, no. 9, pp. 1909–1935, Sept. 2017, doi: 10.1109/JSAC.2017.2719924.

[12] International Telecommunication Union (ITU-R), “Frequency arrangements for the implementation of the terrestrial component of IMT in the bands 24.25–27.5 GHz and 27.5–29.5 GHz,” *ITU-R M.2109-1*, 2017. [Online]. Available: https://www.itu.int/hub/2020/01/wrc-19-identifies-additional-frequency-bands-for-5g/. [Accessed: Oct. 9, 2025].

[13] Reliance Jio Infocomm Ltd., “Jio completes acquisition of right to use spectrum in 700 MHz, 3300 MHz, and 26 GHz bands across all 22 circles,” *Press Release*, Aug. 2022. [Online]. Available: https://www.ril.com/sites/default/files/2023-01/media-release-01-august-2022.pdf. [Accessed: Oct. 9, 2025].

[14] 3GPP, “Specifications and technologies: release 18,” [Online]. Available: https://www.3gpp.org/specifications-technologies/releases/release-18. [Accessed: Oct. 9, 2025].

[15] Y. Ge, K. P. Esselle, and T. S. Bird, “The Use of Simple Thin Partially Reflective Surfaces with Positive Reflection Phase Gradients to Design Wideband, Low-Profile EBG resonator antennas,” *IEEE Transactions on Antennas and Propagation*, vol. 60, no. 2, pp. 743–750, Feb. 2012, doi: 10.1109/TAP.2011.2173113.

[16] J. H. Kim, C. Ahn, and J. Bang, “Antenna gain enhancement using a holey superstrate,” *IEEE Transactions on Antennas and Propagation*, vol. 64, no. 3, pp. 1164–1167, Mar. 2016, doi: 10.1109/TAP.2016.2518650.

[17] G. K. Pandey and M. K. Meshram, “Anisotropic artificial material with ENZ and high refractive index property for high-gain vivaldi antenna design,” in *Proceedings of the 2015*

IEEE 15th Mediterranean Microwave Symposium (MMS), pp. 1–4, 2015, doi: 10.1109/MMS.2015.7375382.

[18] M. U. Afzal and K. P. Esselle, "A low-profile printed planar phase correcting surface to improve directive radiation characteristics of electromagnetic band-gap resonator antennas," *IEEE Transactions on Antennas and Propagation*, vol. 64, no. 1, pp. 276–280, Jan. 2016, doi: 10.1109/TAP.2015.2493159.

[19] A. Lalbakhsh, M. U. Afzal, K. P. Esselle, and S. L. Smith, "Wideband near-field correction of a Fabry–Perot resonator antenna," *IEEE Transactions on Antennas and Propagation*, vol. 67, no. 3, pp. 1975–1980, Mar. 2019, doi: 10.1109/TAP.2019.2891230.

[20] T. Hayat, M. U. Afzal, A. Lalbakhsh, and K. P. Esselle, "3D-Printed phase-rectifying transparent superstrate for resonant-cavity antenna," *IEEE Antennas and Wireless Propagation Letters*, vol. 18, no. 7, pp. 1400–1404, Jul. 2019, doi: 10.1109/LAWP.2019.2917767.

[21] E. G. Larsson, O. Edfors, F. Tufvesson, and T. L. Marzetta, "Massive MIMO for next-generation wireless systems," *IEEE Communications Magazine*, vol. 52, no. 2, pp. 186–195, Feb. 2014.

[22] D. Liang, H. Choi, R. W. Heath Jr., and H. Lu, "Simulation of MIMO channel capacity with antenna polarization diversity," *IEEE Transactions on Wireless Communications*, vol. 4, no. 4, pp. 1869–1873, Jul. 2005.

[23] R. G. Vaughan, "Pattern translation and rotation in uncorrelated source distributions for multiple beam antenna design," *IEEE Transactions on Antennas and Propagation*, vol. 46, no. 7, pp. 982–990, Jul. 1998.

[24] J. G. Andrews, S. Buzzi, W. Choi, S. V. Hanly, A. Lozano, A. C. Soong, and J. C. Zhang, "What will 5G be?," *IEEE Journal on Selected Areas in Communications*, vol. 32, no. 6, pp. 1065–1082, Jun. 2014.

[25] M. Shafi *et al.*, "5G: A tutorial overview of standards, trials, challenges, deployment, and practice," *IEEE Journal on Selected Areas in Communications*, vol. 35, no. 6, pp. 1201–1221, Jun. 2017.

[26] H. Q. Ngo, E. G. Larsson, and T. L. Marzetta, “Energy and spectral efficiency of very large multiuser MIMO systems,” *IEEE Transactions on Communications*, vol. 61, no. 4, pp. 1436–1449, Apr. 2013.

[27] T. L. Marzetta, “Noncooperative cellular wireless with unlimited numbers of base station antennas,” *IEEE Transactions on Wireless Communications*, vol. 9, no. 11, pp. 3590–3600, Nov. 2010.

[28] L. Lu, G. Y. Li, A. L. Swindlehurst, A. Ashikhmin, and R. Zhang, “An overview of massive MIMO: benefits and challenges,” *IEEE Journal of Selected Topics in Signal Processing*, vol. 8, no. 5, pp. 742–758, Oct. 2014.

[29] A. Guidotti *et al.*, “Architectures and key technical challenges for 5G systems incorporating satellites,” *IEEE Transactions on Vehicular Technology*, vol. 68, no. 3, pp. 2624–2639, Mar. 2019.

[30] S. Kodheli *et al.*, “Satellite communications in the new space era: a survey and future challenges,” *IEEE Access*, vol. 8, pp. 183497–183523, 2020.

[31] A. Goldsmith, S. A. Jafar, N. Jindal, and S. Vishwanath, “Capacity limits of MIMO channels,” *IEEE Journal on Selected Areas in Communications*, vol. 21, no. 5, pp. 684–702, Jun. 2003.

[32] S. Sun, T. S. Rappaport, R. W. Heath, A. Nix, and S. Rangan, “MIMO for millimeter-wave wireless communications: beamforming, spatial multiplexing, or both?” *IEEE Communications Magazine*, vol. 52, no. 12, pp. 110–121, Dec. 2014, doi: 10.1109/MCOM.2014.6979962.

[33] O. E. Ayach, S. Rajagopal, S. Abu-Surra, Z. Pi, and R. W. Heath, “Spatially sparse precoding in millimeter-wave MIMO systems,” *IEEE Transactions on Wireless Communications*, vol. 13, no. 3, pp. 1499–1513, Mar. 2014.

[34] X. Zhang, A. F. Molisch, and S.-Y. Kung, “Variable-Phase-Shift-Based RF-baseband codesign for MIMO antenna selection,” *IEEE Transactions on Signal Processing*, vol. 53, no. 11, pp. 4091–4103, Nov. 2005, doi: 10.1109/TSP.2005.857024.

[35] C.-H. Wu, S.-L. Zuo, and C.-H. Chan, “Broadband planar inverted-F antenna for 5G millimeter-wave applications,” *IEEE Transactions on Antennas and Propagation*, vol. 69, no. 7, pp. 3895–3903, Jul. 2021.

[36] Y. Liu, X. Yang, Y. Jia, and Y. J. Guo, “A low correlation and mutual coupling MIMO antenna,” *IEEE Access*, vol. 7, pp. 127384–127392, 2019, doi: 10.1109/ACCESS.2019.2939270.

[37] A. Ramachandran, S. V. Pushpakaran, M. Pezholil, and V. Kesavath, “A four-port MIMO antenna using concentric square-ring patches loaded with CSRR for high isolation,” *IEEE Antennas and Wireless Propagation Letters*, vol. 15, pp. 1196–1199, 2016.

[38] D. Tse and P. Viswanath, *Fundamentals of Wireless Communication*. Cambridge, U.K.: Cambridge University Press, 2005.

[39] J. G. Proakis and M. Salehi, *Digital Communications*, 5th ed. New York: McGraw-Hill, 2008.

[40] S. M. Alamouti, “A simple transmit diversity technique for wireless communications,” *IEEE Journal on Selected Areas in Communications*, vol. 16, no. 8, pp. 1451–1458, Oct. 1998.

[41] A. F. Molisch and M. Z. Win, “MIMO systems with antenna selection,” *IEEE Microwave Magazine*, vol. 5, no. 1, pp. 46–56, Mar. 2004.

[42] I. Sesia, S. Toufik, and M. Baker, *LTE – The UMTS Long Term Evolution: From Theory to Practice*, 2nd ed. Hoboken, NJ: Wiley–IEEE Press, 2011.

[43] Y. Li and X. Chen, “Dual-polarized MIMO Antenna Design for 5G mobile terminals with high isolation and compact size,” *IEEE Transactions on Antennas and Propagation*, vol. 69, no. 5, pp. 2595–2605, May 2021.

[44] S. Zhang, A. Zhao, and G. F. Pedersen, “A compact pattern-diversity antenna array for MIMO terminals,” *IEEE Transactions on Antennas and Propagation*, vol. 65, no. 12, pp. 6413–6421, Dec. 2017.

[45] M. A. Jensen and J. W. Wallace, “A review of antennas and propagation for MIMO wireless communications,” *IEEE Transactions on Antennas and Propagation*, vol. 52, no. 11, pp. 2810–2824, Nov. 2004.

[46] M. S. Sharawi, “Printed multi-band MIMO antenna systems and their performance metrics,” *IEEE Antennas and Propagation Magazine*, vol. 55, no. 5, pp. 218–232, Oct. 2013.

[47] S. Blanch, J. Romeu, and I. Corbella, “Exact representation of antenna system diversity performance from input parameter description,” *Electronics Letters*, vol. 39, no. 9, pp. 705–707, May 2003.

[48] R. S. Kshetrimayum, M. Mishra, S. Aïssa, S. K. Koul, and M. S. Sharawi, “Diversity order and measure of MIMO antennas in single-user, multiuser, and massive MIMO wireless communications,” *IEEE Antennas and Wireless Propagation Letters*, vol. 22, no. 1, pp. 19–23, 2023.

[49] M. Manteghi and Y. Rahmat-Samii, “Multiport characteristics of a wide-band large-array antenna: performance metrics and design,” *IEEE Transactions on Antennas and Propagation*, vol. 57, no. 12, pp. 3839–3848, Dec. 2009.

[50] J. Thaysen, K. B. Jakobsen, and J. Appel-Hansen, “Antenna efficiency and channel capacity of MIMO antennas,” *IEEE Transactions on Antennas and Propagation*, vol. 57, no. 5, pp. 1559–1563, May 2009.

[51] K. Ogawa, T. Uwano, and T. Nishikawa, “An analysis of mean effective gain of mobile antennas in real environments,” *IEEE Transactions on Vehicular Technology*, vol. 48, no. 6, pp. 1617–1626, Nov. 1999.

[52] S. Khabba, S. Ibnyaich, and M. M. Hassani, “A compact 5G millimeter-wave MIMO antenna for ultra-wideband wireless applications,” *2019 International Conference on Systems of Collaboration, Big Data, Internet of Things & Security (SysCoBIoTS)*, pp. 1–4, 2019.

[53] R. C., D. S., D. G., C. S., J. Y. Siddiqui, and Y. M. M. Antar, “Four-element MIMO antenna system based on SRR-loaded printed monopoles for 28/38 GHz 5G applications,” *2020 International Symposium on Antennas & Propagation (APSYM)*, Cochin, India, pp. 36–39, 2020, doi: 10.1109/APSYM50265.2020.9350731.

[54] I. Elfergani, J. Rodriguez, A. Iqbal, M. Sajedin, C. Zebiri, and R. A. Abd-Alhameed, "Compact millimeter-wave MIMO antenna for 5G applications," *2020 14th European Conference on Antennas and Propagation (EuCAP)*, Copenhagen, Denmark, pp. 1–5, 2020, doi: 10.23919/EuCAP48036.2020.9136015.

[55] M. Singh and M. S. Parihar, "Gain improvement of Vivaldi MIMO antenna with pattern diversity using bi-axial anisotropic metasurface for millimeter-wave band applications," *IEEE Antennas and Wireless Propagation Letters*, vol. 22, no. 3, pp. 621–625, Mar. 2023, doi: 10.1109/LAWP.2022.3220710.

[56] J. Zhu, S. Li, S. Liao, and Q. Xue, "Wideband low-profile highly isolated MIMO antenna with artificial magnetic conductor," *IEEE Antennas and Wireless Propagation Letters*, vol. 17, no. 3, pp. 458–462, Mar. 2018, doi: 10.1109/LAWP.2018.2795018.

[57] H. Malekpoor and M. Hamidkhani, "Performance enhancement of low-profile wideband multi-element MIMO arrays backed by AMC surface for vehicular wireless communications," *IEEE Access*, vol. 9, pp. 166206–166222, 2021, doi: 10.1109/ACCESS.2021.3135447.

[58] A. Iqbal *et al.*, "Electromagnetic bandgap-backed millimeter-wave MIMO antenna for wearable applications," *IEEE Access*, vol. 7, pp. 111135–111144, 2019, doi: 10.1109/ACCESS.2019.2933913.

[59] Z. Briqech *et al.*, "High-gain antipodal tapered slot antenna with sine-shaped corrugation and fermi profile substrate slotted cut-out for millimeter-wave 5G," *Global Symposium on Millimeter Waves (GSMM)*, pp. 1–3, 2015.

[60] S. Gupta, Z. Briqech, A. R. Sebak, and T. A. Denidni, "Mutual-coupling reduction using metasurface corrugations for 28 GHz MIMO applications," *IEEE Antennas and Wireless Propagation Letters*, vol. 16, pp. 2763–2766, 2017.

[61] Z. Li, Z. Du, M. Takahashi, K. Saito, and K. Ito, "Reducing mutual coupling of MIMO antennas with parasitic elements for mobile terminals," *IEEE Transactions on Antennas and Propagation*, vol. 60, no. 2, pp. 473–481, Feb. 2012.

[62] M. Karaboikis, C. Soras, G. Tsachtsiris, and V. Makios, “Compact dual-printed inverted-F antenna diversity systems for portable wireless devices,” *IEEE Antennas and Wireless Propagation Letters*, vol. 3, pp. 9–14, 2004.

[63] S. D. Assimonis, T. V. Yioultsis, and C. S. Antonopoulos, “Design and optimization of uniplanar EBG structures for low-profile antenna applications and mutual coupling reduction,” *IEEE Transactions on Antennas and Propagation*, vol. 60, no. 10, pp. 4944–4949, Oct. 2012.

[64] D. A. Ketzaki and T. V. Yioultsis, “Metamaterial-based design of planar compact MIMO monopoles,” *IEEE Transactions on Antennas and Propagation*, vol. 61, no. 5, pp. 2758–2766, May 2013.

[65] Z. Xu and C. Deng, “High-isolated MIMO antenna design based on pattern diversity for 5G mobile terminals,” *IEEE Antennas and Wireless Propagation Letters*, vol. 19, no. 3, pp. 467–471, Mar. 2020.

[66] C. F. Ding, X. Y. Zhang, C.-D. Xue, and C.-Y.-D. Sim, “Novel pattern-diversity-based decoupling method and its application to multielement MIMO antenna,” *IEEE Transactions on Antennas and Propagation*, vol. 66, no. 10, pp. 4976–4985, Oct. 2018, doi: 10.1109/TAP.2018.2851380.

[67] L. Malviya, R. K. Panigrahi, and M. V. Kartikeyan, “A 2×2 dual-band MIMO antenna with polarization diversity for wireless applications,” *Progress in Electromagnetics Research C*, vol. 61, pp. 91–103, 2016.

[68] G. Das, A. Sharma, and R. K. Gangwar, “Dielectric resonator-based circularly polarized MIMO antenna with polarization diversity,” *Microwave and Optical Technology Letters*, vol. 60, no. 3, pp. 685–693, 2018.

[69] K. D. Ayinala and P. K. Sahu, “Isolation-enhanced compact dual-mode 4-Port MIMO design using slot-based switchable DGS decoupling filters,” *Wireless Personal Communications*, vol. 135, pp. 805–833, 2024.

[70] F. Taher, H. A. Hamadi, M. S. Alzaidi, H. Alhumyani, D. H. Elkamchouchi, Y. H. Elkamshoushy, M. T. Haweel, M. F. A. Sree, and S. Y. A. Fatah, “Design and analysis of

circularly polarized two-port MIMO antennas with various antenna element orientations," *Micromachines*, vol. 14, p. 380, 2023.

[71] U. Ullah, M. Al-Hasan, S. Koziel, and I. B. Mabrouk, "Series-slot-fed circularly polarized multiple-input–multiple-output antenna array enabling circular polarization diversity for 5G 28 GHz indoor applications," *IEEE Transactions on Antennas and Propagation*, vol. 69, no. 9, pp. 5607–5616, Sept. 2021, doi: 10.1109/TAP.2021.3066247.

[72] M. Ameen, R. K. Chaudhary, and S. Ghosh, "Millimeter-wave high-gain and highly isolated diversity MIMO array antenna for 5G wireless applications," *2022 IEEE Microwaves, Antennas, and Propagation Conference (MAPCON)*, Bangalore, India, pp. 1203–1208, 2022, doi: 10.1109/MAPCON56011.2022.10047611.

[73] G. von Trentini, "Partially reflecting sheet arrays," *IRE Transactions on Antennas and Propagation*, vol. 4, no. 4, pp. 666–671, 1956, doi: 10.1109/TAP.1956.1144455.

[74] A. Goudarzi, M. M. Honari, and R. Mirzavand, "Resonant cavity antennas for 5G communication systems: a review," *Electronics*, vol. 9, no. 7, p. 1080, Jul. 2020.

[75] J. James, S. Kinany, P. Peel, and G. Andrasic, "Leaky-wave multiple dichroic beamformers," *Electronics Letters*, vol. 25, no. 18, pp. 1209–1211, 1989, doi: 10.1049/el:19890811.

[76] A. P. Feresidis and J. Vardaxoglou, "High-gain planar antenna using optimized partially reflective surfaces," *IEE Proceedings – Microwaves, Antennas and Propagation*, vol. 148, no. 6, pp. 345–350, 2001, doi: 10.1049/ip-map:20010828.

[77] N. Alexopoulos and D. Jackson, "Fundamental superstrate (cover) effects on printed circuit antennas," *IEEE Transactions on Antennas and Propagation*, vol. 32, no. 8, pp. 807–816, 1984, doi: 10.1109/TAP.1984.1143433.

[78] D. R. Jackson and N. Alexopoulos, "Gain enhancement methods for printed circuit antennas," *IEEE Transactions on Antennas and Propagation*, vol. 33, no. 9, pp. 976–987, 1985, doi: 10.1109/TAP.1985.1143709.

[79] H. Attia, M. L. Abdelghani, and T. A. Denidni, “Wideband and high-gain millimeter-wave antenna based on FSS Fabry–Perot cavity,” *IEEE Transactions on Antennas and Propagation*, vol. 65, no. 10, pp. 5589–5594, Oct. 2017.

[80] Y. Wang and A. Zhang, “Dual circularly polarized Fabry–Perot resonator antenna employing a polarization conversion metasurface,” *IEEE Access*, vol. 9, pp. 44881–44887, 2021.

[81] Y. Zheng *et al.*, “Wideband gain enhancement and RCS reduction of Fabry–Perot resonator antenna with chessboard arranged metamaterial superstrate,” *IEEE Transactions on Antennas and Propagation*, vol. 66, no. 2, pp. 590–599, Feb. 2018.

[82] W. Wang and Y. Zheng, “Wideband gain enhancement of high-isolation Fabry–Perot antenna array with tandem circular parasitic patches and radial gradient PRS,” *IEEE Transactions on Antennas and Propagation*, vol. 69, no. 11, pp. 7959–7964, Nov. 2021, doi: 10.1109/TAP.2021.3083781.

[83] S. Angadi, Y. Sharma, N. S. Raghava, and T. Sabapathy, “A low-profile circularly polarized metasurface-based ultra-wideband 4×4 MIMO antenna for 5G NR band FR2 frequencies,” *AEU – International Journal of Electronics and Communications*, p. 155282, 2024.

[84] M. Akbari, H. A. Ghalyon, M. Farahani, A.-R. Sebak, and T. A. Denidni, “Spatial decoupling of CP antennas based on FSS for 30-GHz MIMO systems,” *IEEE Access*, vol. 5, pp. 6527–6537, 2017.

[85] P. Nayeri, F. Yang, and A. Z. Elsherbeni, “Beam-scanning reflectarray antennas: a technical overview and state of the art,” *IEEE Antennas and Propagation Magazine*, vol. 57, no. 4, pp. 32–47, 2015.

[86] A. Hu, K. Konno, and Q. Chen, “A 2-Bit 3D-printed reflectarray antenna using cylindrical rotation-based phase-tunable elements,” *IEEE Transactions on Antennas and Propagation*, vol. 72, no. 10, pp. 7774–7782, 2024.

[87] G.-B. Wu, S.-W. Qu, S. Yang, and C. H. Chan, “Low-cost 1-D beam-steering reflectarray with ±70° scan coverage,” *IEEE Transactions on Antennas and Propagation*, vol. 68, no. 6, pp. 5009–5014, 2020, doi: 10.1109/TAP.2019.2963572.

[88] G. Bashir, A. K. Singh, and A. Dubey, “Beam-switching digital metasurface reflectarray antenna with extreme offset illumination for satellite communications,” *IEEE Journal on Miniaturization for Air and Space Systems*, vol. 5, no. 4, pp. 221–227, 2024.

[89] G.-B. Wu, S.-W. Qu, and S. Yang, “Wide-angle beam-scanning reflectarray with mechanical steering,” *IEEE Transactions on Antennas and Propagation*, vol. 66, no. 1, pp. 172–181, 2018.

[90] R. Garg and I. J. Bahl, “Characteristics of coupled microstriplines,” *IEEE Transactions on Microwave Theory and Techniques*, vol. 27, no. 7, pp. 700–705, 1979.

[91] D. Berry, R. Malech, and W. Kennedy, “The reflectarray antenna,” *IEEE Transactions on Antennas and Propagation*, vol. 11, no. 6, pp. 645–651, 1963.

[91] P. Danuor, M. A. Salifu, J. Appiah-Kubi, and E. D. Adjei, “High-gain printed monopole antenna with dual-band characteristics for modern wireless applications,” *Scientific Reports*, vol. 13, no. 11546, pp. 1–10, 2023, doi: 10.1038/s41598-023-37186-x.

[92] M. Ameen, “Single split-ring resonator loaded self-decoupled dual-band MIMO antenna for 5G applications,” *AEU – International Journal of Electronics and Communications*, vol. 128, no. 153504, pp. 1–9, 2020, doi: 10.1016/j.aeue.2020.153504.

[93] C. Rahul *et al.*, “Four-element MIMO antenna system based on SRR-loaded printed monopoles for 28/38 GHz 5G applications,” *International Symposium on Antennas and Propagation (APSYM)*, pp. 36–39, 2020.

[94] W. Ahmad and W. T. Khan, “Small Form Factor Dual-Band (28/38 GHz) PIFA antenna for 5G applications,” *2017 IEEE MTT-S International Conference on Microwaves for Intelligent Mobility (ICMIM)*, pp. 21–24, 2017, doi: 10.1109/ICMIM.2017.7918846.

[95] D. T. T. Tu, N. G. Thang, N. T. Ngoc, N. T. B. Phuong, and V. V. Yem, “28/38 GHz dual-band MIMO antenna with low mutual coupling using novel round patch EBG cell for 5G

applications," *2017 International Conference on Advanced Technologies for Communications (ATC)*, pp. 64–69, 2017.

[96] H. M. Marzouk, M. I. Ahmed, and A. A. Shaalan, "A novel dual-band 28/38 GHz slotted microstrip MIMO antenna for 5G mobile applications," *2019 IEEE International Symposium on Antennas and Propagation and USNC-URSI Radio Science Meeting (APS-URSI)*, pp. 607–608, 2019.

[97] D. F. Sievenpiper, *High-Impedance Electromagnetic Surfaces*. Ph.D. dissertation, University of California, Los Angeles, 1999.

[98] L. Longzhao, L. Shixing, Y. Xin, and W. L. Tong, "Frequency-reconfigurable quasi-sierpinski antenna integrating with dual-band high-impedance surface," *IEEE Transactions on Antennas and Propagation*, vol. 62, pp. 4459–4467, 2014.

[99] R. Das and H. Yoo, "Application of a compact electromagnetic bandgap array in a phone case for suppression of mobile phone radiation exposure," *IEEE Transactions on Microwave Theory and Techniques*, vol. 66, no. 5, pp. 2363–2372, May 2018.

[100] "IEEE standard for safety levels with respect to human exposure to radio frequency electromagnetic fields, 3 kHz to 300 GHz amendment 1: specifies ceiling limits for induced and contact current, clarifies distinctions between localized exposure and spatial peak power density," *IEEE Standard C95.1a-2010 (Amendment to IEEE Std C95.1-2005)*, pp. 1–9, 2010, doi: 10.1109/IEEESTD.2010.5433227.

[101] A. Ahlbom, "Guidelines for limiting exposure to time-varying electric, magnetic, and electromagnetic fields (Up to 300 GHz)," *Health Physics*, vol. 74, no. 4, pp. 494–522, Apr. 1998.

[102] A. Verma, R. K. Arya, R. Bhattacharya, and S. N. Raghava, "Compact PIFA antenna with high gain and low SAR using AMC for WLAN/C-band/5G applications," *IETE Journal of Research*, 2021, doi: 10.1080/03772063.2021.1945958.

[103] R. L. McIntosh and V. Anderson, "A comprehensive tissue properties database provided for the thermal assessment of a human at rest," *Biophysical Reviews and Letters*, vol. 5, no. 3, pp. 129–151, 2010, doi: 10.1142/S1793048010001184.

[104] J. Bang and J. Choi, “A SAR-reduced mm-wave beam-steerable array antenna with dual-mode operation for fully metal-covered 5G cellular handsets,” *IEEE Antennas and Wireless Propagation Letters*, vol. 17, no. 6, pp. 1118–1122, Jun. 2018.

[105] T. Wu, T. S. Rappaport, and C. M. Collins, “Safe for generations to come: considerations of safety for millimeter waves in wireless communications,” *IEEE Microwave Magazine*, vol. 16, no. 2, pp. 65–84, Mar. 2015.

[106] W. H. Bailey, R. Bodemann, J. Bushberg, C. K. Chou, R. Cleveland, A. Faraone, K. R. Foster, K. E. Gettman, K. Graf, T. Harrington, and A. Hirata, “Synopsis of IEEE Std C95.1-2019: IEEE standard for safety levels with respect to human exposure to electric, magnetic, and electromagnetic fields, 0 Hz to 300 GHz,” *IEEE Access*, vol. 7, pp. 171346–171356, Nov. 2019.

[107] International Commission on Non-Ionizing Radiation Protection (ICNIRP), “Guidelines for limiting exposure to time-varying electric and magnetic fields (1 Hz to 100 kHz),” *Health Physics*, vol. 99, no. 6, pp. 818–836, 2010.

[108] S. X. Ta and I. Park, “Dual-band low-profile crossed asymmetric dipole antenna on dual-band AMC surface,” *IEEE Antennas and Wireless Propagation Letters*, vol. 13, pp. 587–590, 2014.

[109] Z. H. Jiang, D. E. Brocker, P. E. Sieber, and D. H. Werner, “A compact, low-profile metasurface-enabled antenna for wearable medical body area network devices,” *IEEE Transactions on Antennas and Propagation*, vol. 62, no. 8, pp. 4021–4030, Aug. 2014.

[110] Y.-S. Chen and T.-Y. Ku, “A low-profile wearable antenna using a miniature high-impedance surface for smartwatch applications,” *IEEE Antennas and Wireless Propagation Letters*, vol. 15, pp. 1144–1147, 2016.

[111] A. Y. I. Ashyap *et al.*, “Compact and low-profile textile EBG-based antenna for wearable medical applications,” *IEEE Antennas and Wireless Propagation Letters*, vol. 16, pp. 2550–2553, 2017.

[112] S. M. Saeed, C. A. Balanis, C. R. Birtcher, A. C. Durgun, and H. N. Shaman, “Wearable flexible reconfigurable antenna integrated with artificial magnetic conductor,” *IEEE Antennas and Wireless Propagation Letters*, vol. 16, pp. 2396–2399, 2017.

[113] A. Alemaryeen and S. Noghanian, “On-body low-profile textile antenna with artificial magnetic conductor,” *IEEE Transactions on Antennas and Propagation*, vol. 67, pp. 3649–3656, 2019.

[114] C. A. Balanis, *Antenna Theory: Analysis and Design*, 2nd ed. New York: John Wiley & Sons, 1997.

[115] C. A. Balanis, *Advanced Engineering Electromagnetics*, 2nd ed. New York: John Wiley & Sons, 2012.

[116] Y. Dong, H. Toyao, and T. Itoh, “Design and characterization of miniaturized patch antennas loaded with complementary split-ring resonators,” *IEEE Transactions on Antennas and Propagation*, vol. 60, no. 2, pp. 772–785, Feb. 2012.

[117] Z. Xu, Q. Zhang, and L. Guo, “A Printed Multiband MIMO antenna with decoupling element,” *International Journal of Microwave and Wireless Technologies*, vol. 11, no. 4, pp. 413–419, 2019.

[118] N. Nguyen and V. Vu, “Gain Enhancement for MIMO antenna using metamaterial structure,” *International Journal of Microwave and Wireless Technologies*, vol. 11, no. 8, pp. 851–862, 2019.

[119] Y. Zhang, J. Y. Deng, M. J. Li, D. Sun, and L. X. Guo, “A MIMO dielectric resonator antenna with improved isolation for 5G mm-wave applications,” *IEEE Antennas and Wireless Propagation Letters*, vol. 18, no. 4, pp. 747–751, Apr. 2019.

[120] Y. Sun and K. W. Leung, “Substrate-integrated two-port dual-frequency antenna,” *IEEE Transactions on Antennas and Propagation*, vol. 64, no. 8, pp. 3692–3697, Aug. 2016.

[121] N. Yoon and C. A. Seo, “28-GHz wideband 2×2 U-slot patch array antenna,” *Journal of Electromagnetic Engineering and Science*, vol. 17, pp. 133–137, 2017.

[122] M. S. Sharawi, S. K. Podilchak, M. T. Hussain, and Y. M. M. Antar, “Dielectric resonator-based MIMO antenna system enabling millimeter-wave mobile devices,” *IET Microwaves, Antennas & Propagation*, vol. 11, pp. 287–293, 2017.

[123] U. Ullah, S. Koziel, and A. P. Dabrowska, “Design and characterization of a planar structure wideband millimeter-wave antenna with wide beamwidth for wearable off-body communication applications,” *IEEE Antennas and Wireless Propagation Letters*, vol. 21, no. 10, pp. 2070–2074, Oct. 2022.

[124] H. Xue, Z. X. Shen, L. Wu, Y. Rong, and S. Peng, “A low-profile planar end-fire broadband antenna with wide beamwidth,” *IET Microwaves, Antennas & Propagation*, vol. 17, no. 5, pp. 378–385, 2023.

[125] W. Wang, Q. Cao, and Y. Zheng, “Bandstop frequency-selective structures based on stepped-impedance loop resonators: design, analysis, and measurement,” *IEEE Transactions on Antennas and Propagation*, vol. 67, no. 2, pp. 1053–1064, Feb. 2019.

[126] K. Konstantinidis, A. P. Feresidis, and P. S. Hall, “Multilayer partially reflective surfaces for broadband Fabry–Perot cavity antennas,” *IEEE Transactions on Antennas and Propagation*, vol. 62, no. 7, pp. 3474–3481, Jul. 2014.

[127] N. Hussain, M.-J. Jeong, J. Park, and N. Kim, “A broadband circularly polarized Fabry–Perot resonant antenna using a single-layered PRS for 5G MIMO applications,” *IEEE Access*, vol. 7, pp. 42897–42907, 2019.

[128] O. M. Haraz, A. Elboushi, S. A. Alshebeili, and A.-R. Sebak, “Dense dielectric patch array antenna with improved radiation characteristics using EBG ground structure and dielectric superstrate for future 5G cellular networks,” *IEEE Access*, vol. 2, pp. 909–913, 2014.

[129] D. A. Sehrai *et al.*, “Metasurface-based wideband MIMO antenna for 5G millimeter-wave systems,” *IEEE Access*, vol. 9, no. 1, pp. 125348–125357, 2021.

[130] S. Tariq, S. I. Naqvi, N. Hussain, and Y. Amin, “A metasurface-based MIMO antenna for 5G millimeter-wave applications,” *IEEE Access*, vol. 9, no. 1, pp. 51805–51817, 2021.

[131] S. Tariq, A. A. Rahim, W. T. Sethi, F. Faisal, and T. Djerafi, "Metasurface-based antenna array with improved performance for millimeter-wave applications," *AEU – International Journal of Electronics and Communications*, vol. 177, no. 1, p. 155195, 2024.

[132] J. Jung *et al.*, "Design of high-gain and low-mutual-coupling multiple-input multiple-output antennas based on PRS for 28 GHz applications," *Electronics*, vol. 12, no. 20, p. 4286, 2023.

[133] N. Hussain, M. J. Jeong, A. Abbas, and N. Kim, "Metasurface-based single-layer wideband circularly polarized MIMO antenna for 5G millimeter-wave systems," *IEEE Access*, vol. 8, pp. 130293–130304, 2020.

[134] M. Khalid, S. I. Naqvi, N. Hussain, M. Rahman, S. S. Mirjavadi, M. J. Khan, and Y. Amin, "4-Port MIMO Antenna With Defected Ground Structure for 5G millimeter-wave applications," *Electronics*, vol. 9, no. 1, p. 71, 2020.

[135] C. R. Jetti, T. Addepalli, S. R. Devireddy, G. K. Tanimki, A. J. A. Al-Gburi, Z. Zakaria, and P. Sunitha, "Design and analysis of modified U-Shaped Four-Element MIMO antenna for dual-band 5G millimeter-wave applications," *Micromachines*, vol. 14, p. 1545, 2023.

[136] K. D. Ayinala and P. K. Sahu, "Isolation-enhanced compact dual-mode 4-Port MIMO design using slot-based switchable DGS decoupling filters," *Wireless Personal Communications*, vol. 135, pp. 805–833, 2024.

[137] U. Ullah, M. A. Hasan, S. Koziel, and I. B. Mabrouk, "Series-slot-fed circularly polarized multiple-input–multiple-output antenna array enabling circular polarization diversity for 5G 28 GHz indoor applications," *IEEE Transactions on Antennas and Propagation*, vol. 69, no. 9, pp. 5607–5616, Sept. 2021.

[138] M. Ameen, R. K. Chaudhary, and S. Ghosh, "Millimeter-wave high-gain and highly isolated diversity MIMO array antenna for 5G wireless applications," in *IEEE Microwaves, Antennas, and Propagation Conference (MAPCON)*, pp. 1203–1208, 2022.

[139] F. Kiouach, M. E. Ghzaoui, S. Das, T. Islam, and B. T. P. Madhav, "A compact wideband printed 4×4 MIMO antenna with high gain and circular polarization characteristics for mm-

Wave 5G NR n260 applications," *Wireless Personal Communications*, vol. 133, pp. 1857–1886, 2023.

[140] D. M. Pozar, S. D. Targonski, and H. D. Syrigos, "Design of millimeter-wave microstrip reflectarrays," *IEEE Transactions on Antennas and Propagation*, vol. 45, no. 2, pp. 287–296, Feb. 1997.

[141] K. T. Pham, R. Sauleau, E. Fourn, F. Diaby, A. Clemente, and L. Dussopt, "Dual-band transmitarrays with dual-linear polarization at Ka-band," *IEEE Transactions on Antennas and Propagation*, vol. 65, no. 12, pp. 7009–7018, Dec. 2017.

[142] M. Jiang, Z. N. Chen, Y. Zhang, W. Hong, and X. Xuan, "Metamaterial-based thin planar lens antenna for spatial beamforming and multi-beam massive MIMO," *IEEE Transactions on Antennas and Propagation*, vol. 65, no. 2, pp. 464–472, Feb. 2017.

[143] J. Yin, Q. Lou, H. Wang, Z. N. Chen, and W. Hong, "Broadband dual-polarized single-layer reflectarray antenna with independently controllable 1-bit dual beams," *IEEE Transactions on Antennas and Propagation*, vol. 69, no. 6, pp. 3294–3302, Jun. 2021, doi: 10.1109/TAP.2020.3037686.

[144] X. Wan *et al.*, "Reconfigurable sum and difference beams based on a binary programmable metasurface," *IEEE Antennas and Wireless Propagation Letters*, vol. 20, no. 3, pp. 381–385, Mar. 2021.

[145] Q. Zhang *et al.*, "A low-profile beam-steering reflectarray with integrated leaky-wave feed and 2-bit phase resolution for Ka-band SatCom," *IEEE Transactions on Antennas and Propagation*, vol. 70, no. 3, pp. 1884–1894, Mar. 2022.

[146] J. Zhao, C. Fu, H. Li, F. Li, and X. Hu, "A single-layer broadband Ka-band reflectarray using novel windmill elements," *IEEE Transactions on Antennas and Propagation*, vol. 70, no. 11, pp. 11167–11171, Nov. 2022, doi: 10.1109/TAP.2022.3191442.

[147] Á. F. Vaquero *et al.*, "Design of low-profile transmitarray antennas with wide mechanical beam steering at millimeter-waves," *IEEE Transactions on Antennas and Propagation*, vol. 71, no. 4, pp. 3713–3718, Apr. 2023.

[148] E. Wang *et al.*, “A 1296-Cell reconfigurable reflectarray antenna with 2-bit phase resolution for Ka-Band applications,” *IEEE Transactions on Antennas and Propagation*, vol. 72, no. 4, pp. 3425–3437, Apr. 2024.

[149] O. S. Hassan, K. H. Ali, and M. A. Abou-Khousa, “A 3D-printed mm-wave reflectarray with coaxial unit cells,” *IEEE Transactions on Antennas and Propagation*, vol. 72, no. 12, pp. 9251–9258, Dec. 2024, doi: 10.1109/TAP.2024.3484148.

List of Publications

(A) Publications from PhD thesis work

A1. In refereed journals

1. **Priyank Mishra** and Saptarshi Ghosh, "High aperture efficiency millimeter-wave Fabry–Perot cavity MIMO antenna using unprinted and printed dielectric superstrates for n257 band 5G applications," *Frequenz*, vol. 80, no. 1-2, pp. 77-88, Jan. 2026.
2. **Priyank Mishra**, Akhila Gouda, Patinavalasa Megh Sainadh, and Saptarshi Ghosh, "Wideband high-gain beam-steerable reflectarray for millimeter-wave non-terrestrial networks," *Physica Scripta*, vol. 100, no. 10, p. 105509, Oct. 2025.
3. **Priyank Mishra**, Maharana Pratap Singh, and Saptarshi Ghosh., "A compact five-port millimeter-wave MIMO antenna with polarization and pattern diversity for 5G wireless communication," *Sādhanā*, vol. 50, 288, Oct. 2025.

A2. In refereed conferences

1. **Priyank Mishra**, Poonam Tiwari, Akhila Gouda and Saptarshi Ghosh, "A high-gain dual-band millimeter-wave MIMO antenna array for wireless body area networks," *IEEE Microwaves, Antennas, and Propagation Conference (MAPCON)*, Kochi, India, 14–18 December, 2025.
2. **Priyank Mishra**, Maharana Pratap Singh and Saptarshi Ghosh, "A Compact Dual Band Millimeter-Wave CSRR Loaded MIMO Antenna Array System for 5G Applications," *IEEE Microwaves, Antennas, and Propagation Conference (MAPCON), Bangalore, India,* pp. 1188-1192, 2022.
3. **Priyank Mishra**, Praneet Jain, Maharana Pratap Singh, and Saptarshi Ghosh, "Artificial Magnetic Conductor backed Printed Monopole MIMO Antenna for Millimeter-Wave 5G WBAN Applications," *URSI Regional Conference on Radio Science (USRI-RCRS), Indore, India,* pp. 1-4, 2022.
4. **Priyank Mishra**, Maharana Pratap Singh, Aditi. Sharma, Kumar Vaibhav Srivastava and Saptarshi Ghosh, "A Dual-Band Millimeter Wave SRR Loaded Printed Monopole with

Annular Slot MIMO Antenna for 5G Applications," *52nd European Microwave Conference (EuMC), Milan, Italy,* pp. 552-555, 2022.

(B) Other publications during PhD

B1. In refereed journals

1. Akhila Gouda, Munna Aziz, **Priyank Mishra**, and Saptarshi Ghosh, "A 3D-printed Multilayer Conformal FSS for Ultrawideband Electromagnetic shielding, "Wideband high-gain beam-steerable reflectarray for millimeter-wave non-terrestrial networks," Under revision in *IEEE Letters on Electromagnetic Compatibility Practice and Applications*.

B2. In refereed conferences

1. Akhila Gouda, Munna Aziz, **Priyank Mishra**, and Saptarshi Ghosh, "A 3D-printed monolithic conformal FSS with embedded spacer for ultrawideband electromagnetic shielding applications," *IEEE Microwaves, Antennas, and Propagation Conference (MAPCON)*, Kochi, India, 14–18 December, 2025.
2. Poonam Tiwari, **Priyank Mishra**, Akhila Gouda and Saptarshi Ghosh, "A CPW-fed frequency reconfigurable antenna with dual-band to wideband capabilities for millimeter-wave applications," *IEEE Microwaves, Antennas, and Propagation Conference (MAPCON)*, Kochi, India, 14–18 December, 2025.
3. P. Santhosh, Maharana Pratap Singh, Praneet Jain, **Priyank Mishra**, and Saptarshi Ghosh, "SIW-based hexagonal slot MIMO antenna array for 28 GHz millimeter-wave applications," *IEEE Microwaves, Antennas, and Propagation Conference (MAPCON)*, Ahmedabad, India, pp. 1–5, 2023.
4. Maharana Pratap Singh, **Priyank Mishra**, Jogesh Chandra Dash, Debdeep Sarkar, and Saptarshi Ghosh, "A Double Layer Wideband Circularly Polarized Antenna for Millimeter-Wave Application," *2023 Asia-Pacific Microwave Conference (APMC)*, Taipei, Taiwan, pp. 159-161, 2023.
5. Maharana Pratap Singh, **Priyank Mishra**, Jiro Hirokawa, and Saptarshi Ghosh, "SIW-based Circularly Polarized Slot Antenna Array for Millimeter-Wave Applications," *IEEE*

Microwaves, Antennas, and Propagation Conference (MAPCON), Bangalore, India, pp. 1318-1322, 2022.